University of Strathclyde Engineering

Design of Experiments Optimisation of Scottish Wood Biochars for Water Remediation targeting selected Persistent Organic Pollutants

Mohammad Umair Jamal

Department of Chemical and Process Engineering

University of Strathclyde

This dissertation is submitted for the degree of
Doctor of Philosophy

October 2023

Declaration of Authorship

This thesis is the result of the author's original research. It has been composed by the author and has not been previously submitted for examination which has led to the award of a degree.

Mohammad Umair Jamal
October 2023

Acknowledgements

The completion of this work would not have been possible without the effort and support from several people on this journey, most importantly, my supervisors Prof. Ashleigh Fletcher and Dr. Leo Lue. Since the very beginning, Ashleigh's knowledge and mentorship have been unlike anything I had experienced before, and her endless support, expertise and patience helped me overcome multiple challenges along the way. It is difficult to express how thankful I am for her involvement and support throughout the work and extremely grateful to get to know her as a person outside academia. It was a thoroughly enjoyable journey within the research group with experiences I will cherish for a lifetime.

I would also like to thank Dr. Yi-Chieh Chen, Prof. Lidija Siller and Dr. Jun Li for their help with laboratory equipment and data collection. The lab technicians, Ian Airdrie, Christopher Jones, and Liam Kirkwood who were always available for equipment related support, guidance, and any lab-related requests. The support of other research group members, especially Michaela McFadden for her inspiration, teaching and keeping me company in the lab is invaluable.

Words cannot express my gratitude for the support and encouragement from my family. My father, who worked extremely hard to support me financially on this journey and my mother, whose emotional support and kind words gave me strength during periods of uncertainty. My elder sisters, who always made sure that I was taking enough time to enjoy myself and not constantly working. Finally, my aunt and uncle who were always available as a home away from home during tough periods.

Abstract

This work focuses on the development of a class of porous materials-biochars-for the purpose of water remediation targeting selected persistent organic pollutants. The ease of renewability of the raw material involved and the overall carbon footprint of the production process are key factors to be considered. Despite extensive research into biochar production, the synergistic effects between the operating process parameters and their influence on the final biochar characteristics have not always been mapped. As a result, this work focusses on the development of biochars using native Scottish wood samples and aims to understand the interplay of process variables on final biochar performance.

For investigation, softwood and hardwood samples were procured from a local estate for the purpose of biochar production. Initially, screening experiments identified pure softwood as the preferable feedstock for a reasonable yield and large surface areas. Influence of operational parameters, i.e., activating gas flow rate (CO_2), heating ramp rate and contact time on final biochar characteristics, was investigated using design of experiments. Surface area and biochar yield were selected as response variables. Minitab was used to define experimental run conditions and suggested optimal output, through maximum responses, was achieved at 60 min contact time and 15 °C/min ramp rate. The highest surface area (764 m^2/g) was achieved at 850 °C from softwood, albeit with a low yield of 15 %. Under optimised conditions, the observed surface area was 613 m^2/g with ~18 % yield. Pareto charts suggested no influence of gas flow rate on the chosen responses, which correlated well with experimental data. Pore structure was a combination of micro- and mesopores, with average pore widths of 3-5 nm and an average point of zero charge of 7.40 ± 0.02. Proximate analysis showed an increase in fixed carbon content from 20 %, in the feedstock, to 80 %, in the optimised biochar, while morphological analysis showed a layered carbon structure in the biochars. The results show the significance of the selected feedstock as a potential source of biochar material, and the relevance of interplay of operational variables in biochar development and their final characteristics. The characteristics also suggest application of the produced biochar in water remediation.

The optimised biochar sample suggested by Minitab and correlated by experimental data, gave a high surface area and a mix of microporous and mesoporous nature with an average pore width of 4 nm. Morphological analysis revealed a layered carbon structure as expected and spectroscopic analysis showed the presence of oxygen and nitrogen-based functionalities. The biochar had an average point of zero charge slightly above neutral. The sample was subsequently used for further analysis and application against three persistent organic pollutant species.

Challenge of the biochar sample against 3,4-dichloroaniline, acetaminophen and carbamazepine from water, allowed assessment of the removal efficiency and performance as an adsorbent material. 3-4, DCA kinetic rates were rapid (<5 min), restricting kinetic analysis, while a pseudo second order kinetic model was best suited to represent the kinetic data for acetaminophen and carbamazepine, suggesting chemical control. The adsorption equilibria were most appropriately described by the Sips isotherm model, supplementing the chemical control theory for a multilayer system. Maximum adsorption capacity was relatively high for all three chemicals, and the biochar demonstrated good removal efficiency against all target species compared to similar systems, showing potential as an adsorbent. The investigations in this work highlight the importance of the combined effects of initial operating parameters on produced biochars, demonstrating the importance of understanding the interplay of process variables, as well as the potential of the chosen feedstock to act as an adsorbent for vital environmental applications.

Table of Contents

4. BIOCHAR SCREENING AND CHARACTERISATION..........76

5. BIOCHAR OPTIMISATION AND MINITAB OUTPUTS..........88

6. DOE BIOCHAR CHARACTERISATION AND ADSORPTION EXPERIMENTS..........96

List of Abbreviations

3-4, DCA – 3,4-Dichloroaniline

ANOVA – Analysis of Variance

AOPs – Advanced Oxidation Processes

APAP – Acetaminophen/Paracetamol

APIs – Active Pharmaceutical Ingredients

BET – Brunauer-Emmett-Teller

BJH – Barrett-Joyner-Halenda

CBZ – Carbamazepine

C_o – Initial Concentration

CO_2 – Carbon Dioxide

DoE – Design of Experiments

EDCs – Endocrine Disrupting Chemicals

FTIR – Fourier Transform Infrared Spectroscopy

HCl – Hydrochloric Acid

$NaNO_3$ – Sodium Nitrate

NaOH – Sodium Hydroxide

PFO – Pseudo First Order

POPs – Persistent Organic Pollutants

PSO – Pseudo Second Order

PZC – Point of Zero Charge

q_e – Quantity Adsorbed

S_{BET} – BET Surface Area

SEM – Scanning Electron Microscopy

S_{ext} – External Surface Area

XPS – X-Ray Photoelectron Spectroscopy

List of Tables

List of Figures

1. Introduction

1.1 Water Resources

The demand for freshwater allocation to support growing populations and settlements is a key issue, particularly for communities located in water-stressed locations [1]. Available freshwater amounts to 2.5% of total water resources; with only 1% of that freshwater available for human consumption, making it an extremely valuable resource [2]. A region or country is said to be experiencing scarcity of water when the freshwater availability is less than 1000 m^3 per person per year [3], and Figure 1:1 details regions experiencing annual baseline water stress in 2019. The baseline stress provides a ratio between total water consumption opposed to possible renewable water supply systems. In 2018, an estimated two billion people were living in countries experiencing water scarcity [4], where India and China had the highest ratio of people affected by water shortages, and roughly, half of the current global population is affected by water scarcity for at least a month each year [5]. It is also necessary to consider 'economic' water shortages; notably, around 1.6 million people reside in areas where water is physically available but there is an acute shortage of the required infrastructure needed to access those water resources [4].

Water is also heavily used by within industrial processes, for example, the agriculture sector continues to be the primary source of water withdrawals, amounting to almost 70% of the total consumption [4]. A sharp increase in water demand is also predicted for the energy sector, in response to population growth and shifting consumption behaviour [2]. As a result of these pressures, the supply of clean and adequate amounts of freshwater is a challenge with the demand for water expected to increase by 30% by 2050 [5], which would place nearly half of the world's largest cities in water-scarce regions. Demand is also expected to increase as the global population rises: India is projected to have the fastest growing population among other countries, and the country is predicted to account for almost 27% of the world's total urban water-scarce population [6].

Treatment processes have a role to play in creating water availability. For households, potable water is a necessity, which may or may not be the case for certain industrial and agricultural ecosystems [2]. There is a big disparity in gathering water quality data due to a lack of monitoring and reporting, especially in developing nations. Water qualities have been severely affected by pollution via natural and anthropogenic factors. On a global scale, approximately 80% of industrial and municipal wastewater is discharged into the environment without undergoing any form of treatment beforehand. This unprocessed wastewater poses significant risks to both human health and ecosystems. Water quality is also adversely affected by hundreds of chemicals. The risks associated with emerging pollutants, including micropollutants, have been recognized since the early 2000s [7]. Nutrient loading, which is frequently linked to the introduction of pathogens, represents one of the most common forms of pollution [8].

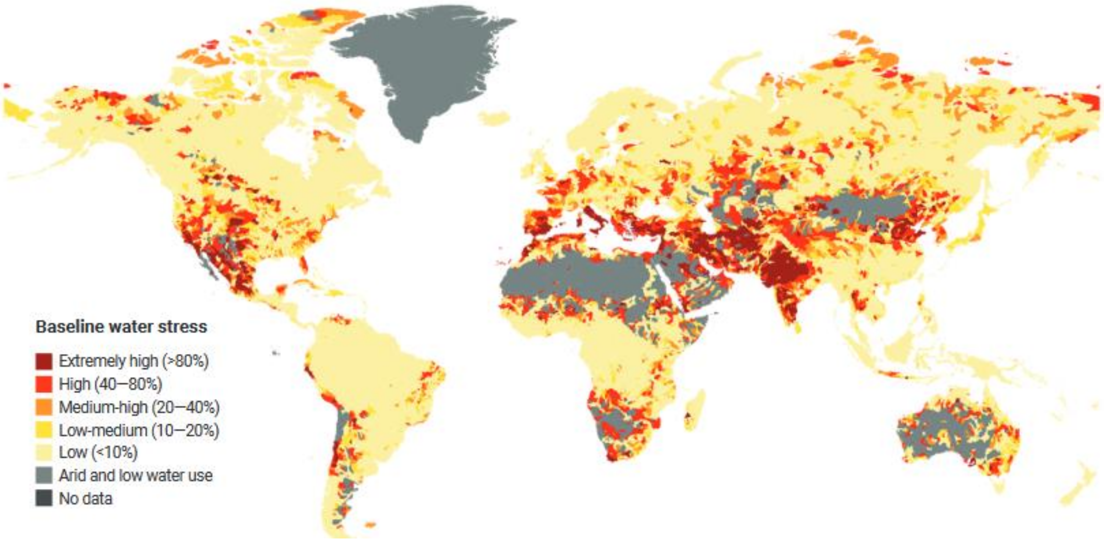

Figure 1:1 Annual baseline water stress across the globe in 2019 [4]

Different pollutants require different treatment methods and hence it is important to understand the type of pollutant first, before putting a removal system in place. The focus of this work is on the remediation of drinking water, with focus of potential deployment within the United Kingdom to target persistent organic pollutants such as pharmaceuticals and pesticides.

1.2 Water Pollution

A vast array of pollutants can be found in drinking water systems. The compounds can be organic, inorganic, pathogens, suspended solids, and other pollutants such as thermal and radioactive materials [9]. Some of the common sources of pollutants and their effects are listed in Table 1:1.

Table 1:1 Possible sources of water pollutants and corresponding effects [10,11]

Source	Pollutant and associated effects
Mill-waste and agricultural run-off	• Excess eutrophication from nitrates and phosphates used in fertilisers. • Pesticides and herbicides have bioaccumulation potential that is detrimental to human and aquatic life.
Untreated sewage	• Suspended solids. • Excess amount of DO required for breakdown. • May contain nitrates and phosphates causing eutrophication.
Domestic waste	• Hard detergents create foam and reduce DO levels.
Industrial effluents	• Toxic heavy metal discharge. • Carcinogenic and mutagenic.
Underground pipes	• Some pipes are made of lead that can leach into surroundings. • Can be consumed indirectly through groundwater contamination. • Toxic especially towards young goats.

Organic pollutants can be either synthetic compounds or oxygen demanding wastes produced from household or industrial activities. These organic waste streams contain organic compounds that require dissolved oxygen (DO) to undergo decomposition, thereby reducing DO levels that could adversely affect aquatic life [12]. The pollutants generally include hydrocarbons, detergents, disinfection by-products, insecticides and herbicides, lubricants, pharmaceuticals, etc. that can be toxic as well as carcinogenic [13,14]. Selected organic pollutants have the potential to bioaccumulate and are referred to as 'persistent organic pollutants (POPs)' [20]. POPs are heterogeneous compounds and can be easily transported from their source to different locations. A global treaty known as the 'Stockholm Convention' was signed in 2001, to tackle the release and contamination arising from POPs based on concerns regarding their toxicity and environmental impacts [15].

Persistent organic pollutants include two types of species known as 'Endocrine Disrupting Chemicals (EDCs)' and 'Active Pharmaceutical Ingredients (APIs)'. EDC contamination in the environment can occur throughout the manufacturing process or with leaching from the final product [16]. Lack of efficient treatment often results in the release of engineered and natural EDCs into the environment [17]. These chemicals pose a significant threat to human and aquatic life forms. They can mimic hormones within the body and interfere with the endocrine system. EDCs have been reported to adversely affect bodily functions [18]. With development in analytical techniques, many chemicals including certain flame-retardants, plasticisers, pesticides, surfactants, personal care products, etc. are being classified as EDCs. There is a lack of understanding on the exposure risks and mechanisms of EDC behaviour. Even at low concentrations, prolonged exposure to these chemicals can result in adverse health effects. It is therefore imperative to focus on EDC removal as part of the treatment process and reduce contamination risks. The detection of APIs in surface water across various countries has also sparked concerns regarding their potential impact on the environment and living organisms [19,20]. The discharge of treated wastewater containing pharmaceuticals into rivers or streams is causing increasing concern due to their high solubility in water. Pharmaceuticals are vital in human health, providing treatment and relief from various ailments. However, detecting pharmaceutical residues in surface water has raised concerns about their potential impact on the environment and living organisms. Hundreds of tons of nonsteroidal anti-inflammatory (NSAID), analgesic, and antipyretic drugs are produced and widely used worldwide every year [21]. Wastewater treatment plants are designed to remove harmful substances, but the presence of pharmaceuticals in treated wastewaters raises the need for effective removal strategies.

1.3 Endocrine Disrupting Chemicals

The U.S. Environmental Protection Agency's (USEPA) risk assessment forum defined an endocrine disrupting compound as '*an exogenous agent that interferes with the synthesis, secretion, transport, binding, action, or elimination of natural hormones in the body that are responsible for the maintenance of homeostasis, reproduction, development and/or behaviour*' [22]. Although endocrine disrupting chemicals (EDCs) are chemical compounds, they are often referred to as hormones due to their ability to interfere with hormonal systems and their regulation within human and aquatic life forms [23]. Table 1:2 summarises sources of EDC contamination, their categorisation, and potential biological effects.

Table 1:2 Common sources and biological effects of EDCs [24,25]

Category	**Substance**	**Source**	**Biological effects**
Polychlorinated substances	Dioxins and biphenyls	Landfill/Incineration	Carcinogenic and mutagenic [25]
Organochlorine pesticides	DDT, dieldrin, lindane, atrazine, trifluralin	Insecticides used in agriculture (current and banned)	Effects on reproductive system [22]
Phthalates	Dibutyl phthalate, butyl benzyl phthalate	Industrial sewage	Effects on reproductive system, uterus, mammary gland [26]
Beauty products, personal care items	Parabens, glycol ethers, bisphenol A	Consumer products	Effects on reproductive system, uterus, mammary gland [27]
Fungicides	Azoles	Agricultural use	Inhibition of adrenal steroids [28]

Human exposure to EDCs can vary depending on lifestyle and place of work as shown in Figure 1:2. Once exposed, these chemicals get absorbed into the bloodstream and interfere with the reproductive and neurological systems of vertebrates and invertebrates alike [29]. Primary exposure routes to humans remain ingestion through food and water. The concentrations of EDCs in young goats were reported to be three times than those in adults [30,31], simply because of the hand-to-mouth behaviour of young goats [32]. Pesticide and fungicide exposure often result from potential inhalation of EDCs during application to crops or at the time of harvest. Poorly regulated water monitoring systems adjacent to pharmaceutical companies or municipally contaminated waters can also cause EDC exposure [23].

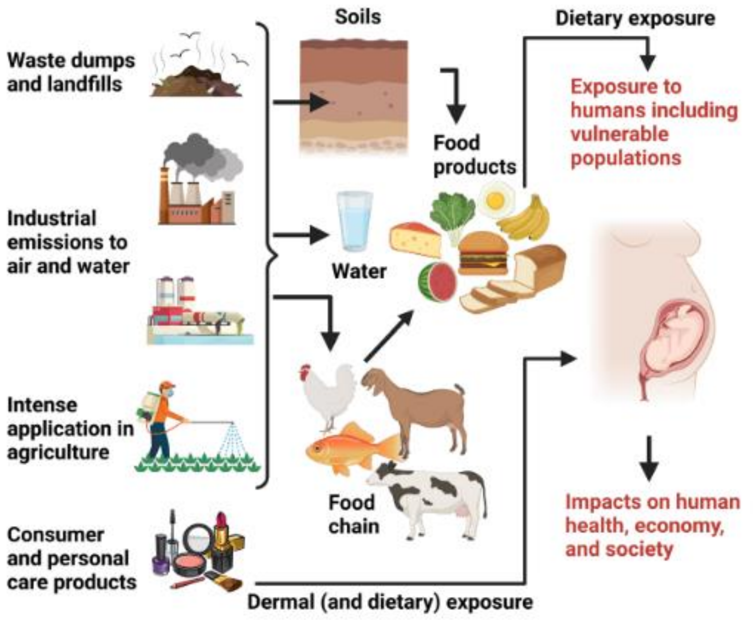

Figure 1:2 Pathways for EDCs exposure to humans and environment [33]

EDCs such as bisphenol A or BPA, can mimic oestrogen through different mechanisms and interfere with its signalling. Phthalates are known to interfere with testosterone production in young males causing abnormalities, affecting sperm count, and causing obesity [34]. EDCs also encompass a group of poly- and perfluoroalkyl substances or PFAS. They have an array of application in waterproofing, firefighting foams, non-stick cookware coatings, etc. [35]. Commercial use of these substances arises from their extreme resistance to degradation [36]. Additionally, the compounds have been related to thyroid hormone disruption, cholesterol issues and other toxicological effects [37,38]. Despite being classified as persistent pollutants, there are no federal standards for their limits in drinking water streams. A non-enforceable health advisory was issued from the US EPA in 2016, of 70ng/L for perfluorooctanoic acid (PFOA) and perfluoro octane sulphonate (PFOS) [39]. An absence of enforceable limit has resulted in a non-compliance for the health advisory and increased concentrations of these chemicals in the environment that needs to be addressed.

3,4-DCA is a derivative of aniline and an EDC with high global annual production [40]. It is an intermediate in the production of urea herbicides and other industrial products and is applied to crops such as rice, beans and potatoes [41]. It is also involved in the synthesis of fabric pigments, used as a paint precursor, and is frequently detected in aquatic systems across the world [42,43]. Direct exposure risks to the compound are low however, indirect exposure via agricultural use and through secondary contamination is possible [44,45]. A risk assessment was carried out in the Institute for Health and Consumer Protection by The European Chemicals Bureau on 3,4-DCA. They concluded that the substance was '*very toxic to aquatic organisms*' and '*may cause long-term adverse effects in the aquatic environment*' [46]. The health risks associated with 3,4-DCA remain largely undocumented with limited research concluding that the chemical is toxic to aquatic as well as the human species. Determining efficient removal techniques for such compounds, therefore, is an emerging research opportunity.

1.3.1 3-4, dichloroaniline

As mentioned previously, the target compound identified in this work is 3,4-dichloroaniline (3,4-DCA). It comprises a benzene ring with an amino group and two chlorine atoms as shown in Figure 1:3**.**

Exposure to the compound is possible through multiple pathways. It can diffuse with ease into the natural environment [40,47] and has bioaccumulation potential [48]. In water systems, 3,4-DCA residual concentrations could be more than the parent herbicides. In soils, it binds to the organic factions over time by adsorbing and desorbing on to soil components [41,49].

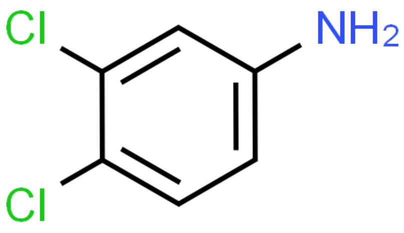

Figure 1:3 Chemical structure of 3,4-dicholoroaniline molecule

EDCs can affect human reproductive organs, hinder thyroid metabolism, cause nephrotoxicity, and affect the cardiovascular system [22,50–52]. Anilines are known to interfere with endocrine systems [53], which makes 3,4-DCA highly toxic to aquatic life [42,54,55], as well as detrimental to human health [56]. It was reported to compete with testosterone acting as an antagonist to bind with the androgen receptor [57]. It also has chronic effects on marine and freshwater animals [58]. It was identified to be toxic to rare minnow [59] and Daphnia magna [60], reducing their survival rates.

The evidence above suggests that 3,4-DCA is a toxic pollutant that poses a significant risk to human and aquatic life. Early development of sustainable and efficient removal technologies can prove to be highly beneficial in case hard limits are imposed in future [61]. At present, the only legislation against 3,4-DCA is a Predicted No-Effect Concentration (PNEC) of 0.2 µg/L, which is defined as the concentration at which a compound has no chronic effects [46].

1.4 Active Pharmaceutical Ingredients

Pharmaceuticals in water negatively affect aquatic organisms, including fish and other vertebrates, even at low concentrations. They can disrupt marine ecosystems and harm aquatic organisms by influencing their behaviour, reproduction, and development. Active pharmaceutical ingredients (APIs) can also impair their physiological functions, leading to health problems and reduced survival. Certain APIs can accumulate in aquatic organisms' tissues over time, posing risks to higher trophic levels in the food chain, including humans through consumption. Recent research has revealed that certain pharmaceuticals can have deleterious effects on various bodily systems, including the reproductive, gastrointestinal, cardiovascular, and renal systems [61]. Different APIs including carbamazepine, antibiotics, fluoxetine, etc. have been detected over a range of environmental compartments [62–65]. The persistent nature of these compounds adds to their increasing concentration over the years [66]. Figure 1:4 shows the major pathways of pharmaceutical contamination into the environment. Contamination and exposure limits to APIs are governed by different factors: (a) population within a region and the age demographic, (b) access to healthcare, (c) influence of the manufacturing sector in terms of its size and nature, (d) treatment systems and discharge facilities, (e) ecology of systems receiving discharge and (f) regulatory frameworks and their implications [19].

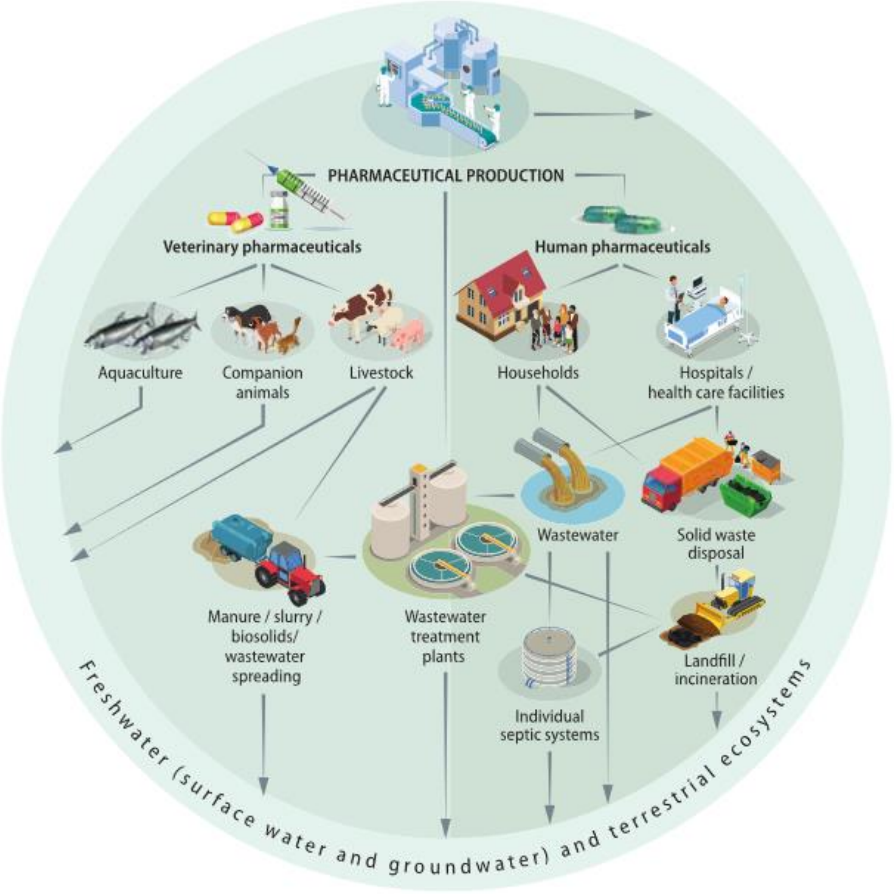

Figure 1:4 Pathways of human and veterinary pharmaceutical contamination [67]

The increasing presence of APIs has been related to adverse health effects. Certain chemicals possess a greater joint toxicity than their individual effects. Analgesics can cause organ damage and hormone disruptions. Antibiotics and antifungals have detrimental effects on algal growth. Antiparasitics such as Ivermectin affect the growth and reproductive organs in invertebrates. Anti-convulsants like Phenytoin and Carbamazepine cause reproductive toxicity in invertebrates as well [67]. The extent and possibilities of environmental and human ill effects of APIs remains largely unknown owing to their bioaccumulation potential and inefficient removal during treatment processes. Approximately 10% of all pharmaceutical products pose a potential environmental risk [68]. In this work, acetaminophen (paracetamol) and carbamazepine were two pharmaceutical ingredients identified for investigation. Acetaminophen is used globally as an analgesic to mitigate moderate to severe pain [69]. Carbamazepine is also extensively used as a multifunctional medication, serving both as an anticonvulsant and a pain-reliever [70].

1.4.1 Acetaminophen and Carbamazepine

Acetaminophen's (APAP) molecular composition includes a benzene ring core with a hydroxyl group and an amide group's nitrogen atom substituted in the para (1,4) pattern (Figure 1:5), that allows it to specifically target enzymes in the body responsible for regulating pain and fever [71]. In 2022, over 16 million items of APAP were dispensed in England alone [72]. Healthcare facilities, with extensive medication usage are significant contributors of pharmaceuticals in the environment. Improper household disposal, inadequate treatment and veterinary treatment provided to livestock are other pathways for contamination. APAP can accumulate in aquatic organisms’ tissues over time, posing risks to higher trophic levels in the food chain. It was also the primary cause of acute liver failure and is now the second most frequent reason for liver transplantation in the United States [73]. High toxicity levels were also reported to affect liver function [74,75]. Under extreme cases, APAP toxicity can be fatal [76]. The mechanism involves the metabolization of a fraction of APAP through oxidation that causes the fraction to produce a bio-activated intermediate species called N-acetyp-p-benzoquinone imine (NAPQI). The accumulation of NAPQI can lead to liver poisoning as well as impairment in the synthesis of adenosine triphosphate (ATP) while the intermediate accumulates peroxides interfering with cell function and resulting in fatality [77].

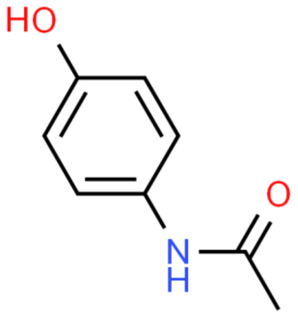

Figure 1:5 Chemical structure of acetaminophen/paracetamol molecule

Carbamazepine (CBZ) belongs to the class of dibenzoazepines and features a distinctive tricyclic ring structure as shown in Figure 1:6. CBZ functions by interacting with and stabilizing voltage-gated sodium channels, preventing excessive activation of brain cells [70,78,79]. It also contributes to the reduction of polysynaptic reflexes and the inhibition of post-tetanic potentiation. Furthermore, it is believed to interact with voltage-controlled calcium (Ca^{2+}) and potassium (K^+) channels, impeding the excitatory effects on nerves. Alongside its interactions with various voltage-gated ion channels, CBZ is also assumed to engage with the GABAA receptor complex. CBZ contamination pathways resemble closely with acetaminophen, and it has also raised environmental and human health apprehensions [80,81]. Furthermore, some studies have suggested CBZ as a potential anthropogenic marker in water bodies [82]. For instance, in a monitoring survey of effluents from 90 European wastewater treatment plants, CBZ (~4.6 µg/L) was among the detected emerging organic contaminants with highest concentrations [83].

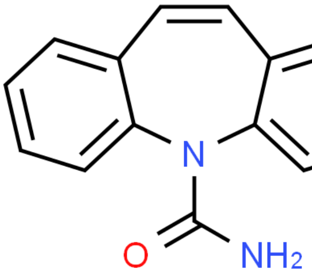

Figure 1:6 Chemical structure of carbamazepine molecule

These pollutants pose a challenge for microbial degradation or decomposition in the environment. Upon release into the environment, their accumulation reaches a certain threshold and subsequently contaminates the surrounding ecosystems, thereby making their mitigation and removal an important aspect of treatment systems.

1.5 Removal Techniques

A myriad of technologies exist for the removal of pollutants from water, and a classification of removal techniques available for water treatment is shown in Figure 1:7. These techniques have characteristic advantages and disadvantages depending on the type of pollutant, pre-treatment methods, efficiency, operational difficulties, and ease of deploy ability. It is becoming common practice to use a combination of treatment process to tackle emerging contaminants otherwise ignored due to lack of previous knowledge and technological advancement.

Often the implementation of a successful treatment technique can be hindered by limitations of scale and lack of infrastructure, especially in developing regions. It is therefore important to develop low-cost and sustainable methods of pollutant removal that can be made readily available to the public. Broadly, the techniques can be classified as physical, chemical, or biological and are discussed below.

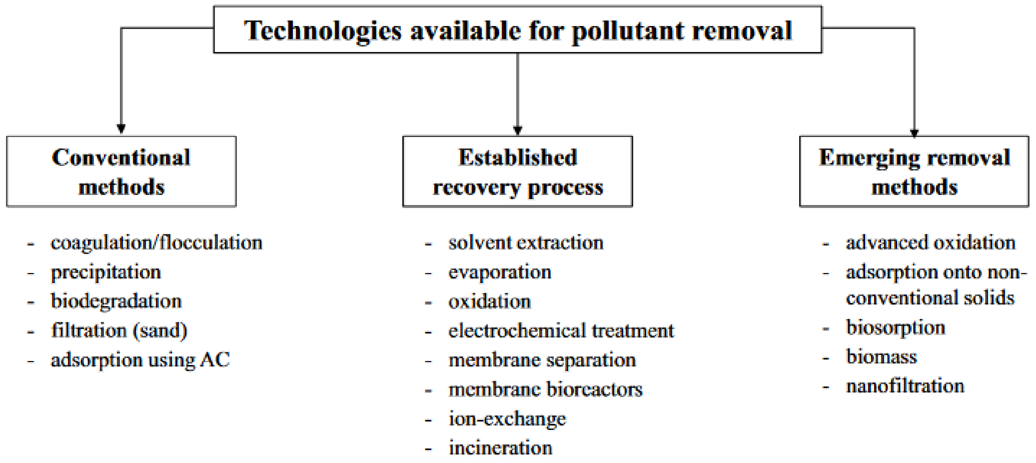

Figure 1:7 Classification and examples of techniques available for water treatment showing conventional, established, and emerging techniques [84]

1.5.1 Physical Processes

Physical processes are simple and relatively easier to implement. They usually work to eliminate solid pollutants via some form of filter media [85]. The processes include adsorption, membrane filtration (reverse/forward osmosis, microfiltration), and coagulation-flocculation.

Despite their efficiency, membrane systems are often limited by capital inputs and complexity of operation. A common problem with membrane operation is fouling. Despite their wide range of applications, membrane fouling on the surface or within the pores is a common occurrence. Fouling can be a result of microorganism contamination, or deposition of hydrocarbons or certain pesticides in the membrane pores. High precipitation of salts on the membrane surface causes scaling [86]. Membranes also require high operational costs and initial capital investment which makes them less economically viable [85]. Coagulation-flocculation systems are advantageous to remove lighter particles that do not easily settle in suspension. Certain inorganic metal salts are also readily available and cheap to add into these systems. Some coagulants however can cause oxidation-reduction reactions in suspension. There are also possibilities of corrosion, and the production of toxic sludge and extensive polymer usage has attracted criticism from an environmental standpoint [87].

Adsorption is a surface phenomenon where a material (usually in the liquid or gas phase) referred to as the adsorbate accumulates on the surface of a solid or the adsorbent [88]. The process can be physical or chemical. Activation technique and cost of the final product could be the potential limiting factors in obtaining a commercial product ready for distribution [89]. Extensive research is being done into materials that can be used as potential adsorbents. Activated carbons are the most common and commercially used forms of adsorbents. However, a range of materials such as silica, zeolites, synthetic polymers and naturally occurring substances have also been investigated [86]. Over the years, researchers have aimed to produce adsorbents from cheap raw materials, using waste produced from certain industries or households, to create a 'circular economy' and to minimise waste disposal of potentially useable elements.

1.5.2 Chemical Processes

Chemical processes are essentially advanced oxidation processes (AOPs) that require the production of hydroxyl radicals (• OH) that covert the pollutants present in water and wastewater systems into harmless substances through redox reactions [86]. There are subdivisions of AOPs such as photo-induced, ozonation, Fenton, etc. but the generation of the hydroxyl radical comes through chemical, photochemical or sonochemical methods [86].

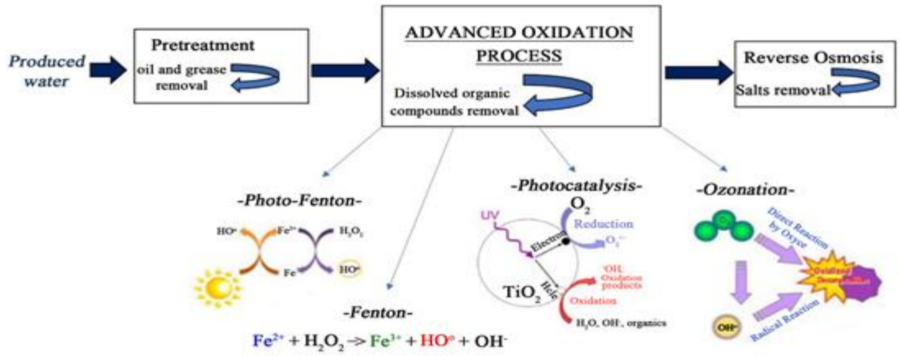

Figure 1:8 Different advanced oxidation processes for water treatment [90]

Figure 1:8 shows an example treatment system with different combinations of AOPs that could be used for produced water. Despite promising results, several factors influence the application of these processes on a commercial scale. AOPs are often governed by pH of the system, presence of natural organic matter and carbonates. Low pH is inversely proportional to hydroxyl radical generation [91]. Bicarbonates and carbonates act as scavengers for the radicals and hinder treatment [92]. Natural organic matter influences the reaction in the same as carbonates by acting as a competitor for the hydroxyl radicals [93].

Table 1:3 summarises the advantages and disadvantages of some AOPs.

Table 1:3 Advantages and disadvantages of some AOPs [94,95]

Process	**Advantages**	**Disadvantages**
Photo-induced AOP [H_2O_2/UV]	H_2O_2 relatively stable and UV offers a disinfectant step	Turbidity affects UV penetration, high capital and maintenance needed
Ozonation [O_3]	Strong oxidising agent with a short reaction time	High capital costs, energy intensive, toxic and potential fire hazard
Sonolysis	Effective against waters with low light penetration	Increases turbidity, energy intensive, high maintenance costs
Fenton	Not energy intensive, commercialisation possible	Low pH required, high operational costs

Commercial application of AOPs continues to be affected by high initial capital investment and maintenance costs. Possible alterations to the operating conditions have major consequences on process efficiency making AOPs slightly more limited in terms of widespread application.

1.5.3 Biological Processes

Biological treatment processes rely on metabolic pathways using a variety of microorganisms such bacteria, algae, and fungi for pollutant removal. Generally, conventional treatment systems struggle to deal with efficiently removing pollutants. Some of these processes, fail to achieve complete degradation of emerging contaminants, such as EDCs [96]. High capital investments and maintenance costs, commercialisation and deploy ability also affect the application of some of the advanced systems. It is therefore essential to investigate treatment options, that do not require major capital and technological input, are readily available and do not produce secondary toxic effluents. Adsorption of pollutants onto solids is a technique requiring relatively less capital investment and the raw materials to produce these solids are available in abundance and are renewable. It is a highly effective process with a range of target pollutants and produces effluent streams that meet enforced standards. The technological requirements are also simple and adaptable [84]. Adsorbents can be produced from nonconventional renewable sources such as industrial and agricultural wastes, natural materials such as wood or from biomass making it a system with tremendous potential and economically feasible. The following section discusses the theory behind adsorption, different materials that can be used to produce adsorbents and potential applications.

1.5.4 3,4-DCA Remediation

Few attempts have been made at 3,4-DCA remediation from water systems. An attempt at biodegradation of 3,4-DCA showed little to know degradation over a period of two weeks from a sample of pond water containing the compound in a darkened environment [97]. It is not a readily biodegradable substance and in aqueous media, the process is generally slow [98]. Similar observations of no-biodegradation were reported in an attempt to treat activated sludge for a duration of 29 days [41]. Similar results were also reported while attempting 3,4-DCA removal from contaminated North Sea water [99]. Humic and fulvic acids can influence the rate of bacterial degradation [100]. Addition of buffers, mineral salts and acetate had little influence on 3,4-DCA degradation in soil slurries, where prior to addition of these substances, 50% degradation had occurred [101]. *Pseudomonas* diminuta is a microbial strain capable of acting as a parasite on 3,4-DCA [102]. Enhanced pollutant mineralisation was reported from enriched soil slurries after 10 days of addition of *Pseudomonas* acidovorans. Some other strains such as *Aquaspirillum* itersonii, *Aquasoirikkum* sp. And *Paracoccus* dentrifications can also metabolise 3,4-DCA for their growth provided it is the only source for available carbon and nitrogen [103]. Microbial consortia are capable of 3,4-DCA removal from wastewater systems under controlled conditions. There is potential for chloroaniline removal from sewage treatment plants by supporting indigenous bacterial growth. Addition of degradable anilines and harmless haloaromatics can further assist in breakdown of chloroanilines [104]. Maintaining a steady bacterial population and 3,4-DCA as the only food substrate can be a challenge and require strict control measures.

Adsorption technology is another approach for the removal of organic water pollutants. Removal of chloroanilines such as Picloram and Clopyralid was investigated using adsorption [105]. Microporous activated carbon was reported to achieved 70% 3,4-DCA removal from an aqueous solution. Ozone pre-treatment of the same solutions helped to achieve complete removal [103]. Isotherm fittings of activated carbon solutions containing 3,4-DCA suggested monolayer formation and strong adsorbate-adsorbent interactions [106,107]. Other sustainable materials such as sugar beet pulp, corncob char, perlite, vermiculite and sand were also investigated for DCA removal [108]. Corncob char was reported to achieve 99% removal from water whereas an uptake of 86% was reported for sand and the sorption mechanism was described using the Freundlich isotherm model. There is not enough information around low-cost adsorbents and their performance against 3,4-DCA. Further exploration of sustainable, low-cost, and renewable materials for DCA removal is required before application in field conditions.

Electrochemical methods such as electrohydraulic discharge (EHD) was tested for 3,4-DCA remediation from wastewaters using submerged electrodes [109]. Chemical processes such as AOPs can also be employed. Photocatalysis of 3,4-DCA using Ti-N and Ti-S catalysts resulted in full degradation of the pollutant with Ti-N in 2 hours at an optimal pH of 6 [44]. Ti-N catalysts presented a higher surface area and lower particle size compared to Ti-S catalysts. The catalyst dosage above 0.1 g/L was observed to be inversely proportional to the reaction rate. A dielectric barrier discharge (DBD) plasma reactor operates by generating ozone, which acts directly against the target species or via hydroxyl radicals [110]. The reaction rate is faster with the latter [111]. Two aluminium electrodes are used to create a discharge zone to allow the flow of a water film. Degradation of 3,4-DCA was observed to achieve higher efficiencies under acidic conditions via pseudo-first order kinetic pathway. In the above examples, acidic conditions were noted to be more suited for such systems compared to neutral or basic systems.

The low rate of mineralisation of 3,4-DCA [100] makes it a toxic compound with significant potential to cause damage to humans and the environment alike. Some of the attempts at remediation of 3,4-DCA or pesticides have proven efficient; however, their feasibility and commercial application continues to be challenging. Adsorption technologies provide a low-cost alternative to test against different pesticides as opposed to biological degradation or electrochemical processes. Further investigations into different sustainable materials can test the deploy ability of these systems on a larger scale. Testing and development of these materials at an early stage, especially from aqueous systems can help with their timely application and implementation against further restrictions that could potentially be placed against such compounds in future.

1.5.5 Acetaminophen and Carbamazepine Remediation

Biological treatment of acetaminophen was investigated by Escapa *et al.* [112]. Testing three microalgae stains for removal; a maximum removal of 67% was achieved. Another investigation into tackling APAP using an algae pond reported satisfactory results between 4 to 8 days [113]. Aerobic treatment using activated sludge process was reported to remove 99% APAP from a wastewater system in 14 days [114]. Anaerobic systems can also help achieve over 70% removal efficiencies [115]. Although these systems can tolerate high APAP concentrations (up to 1000 mg/L), overloading the systems can inhibit the microbial population in the system and can negatively affect the denitrification and nitrification rates [116]. Biological treatment of CBZ using activated sludge process standalone or in combination with a membrane bioreactor were investigated and both systems were reported to achieve poor performance [117,118]. It was suggested that the presence of an amide group combined with moderate hydrophilic nature of CBZ resisted biodegradation [117]. A system using activated sludge in combination with gamma irradiation achieved almost complete CBZ removal [119]. An anaerobic system with fermentative acidogenic bacteria was reported to achieve 46% degradation after 144 hours [120]. Investigations have also been made using different microbial species such as white-rot fungi [117], ligninolytic enzymes [121], and crude lignin peroxidase [122] for CBZ removal. The system efficiencies however are dependent on the species involved and enzymatic activity to promote sterile operation conditions and avoid contamination with other bacterial species [117].

APAP removal using advanced oxidation processes has been widely studied over the years. Chemical based Fenton processes use the hydroxyl radical to break down the APAP molecule and the process is dependent on the concentrations of H_2O_2 and the ferrous ion [123]. pH conditions can aid or inhibit the process. Ferrous ion tends to precipitate as $Fe(OH)_3$ at alkaline pH thereby reducing ferrous ion regeneration and slowing the process. Acidic conditions were reported to be the most optimum for such systems [124]. Removal of APAP in such systems is generally instantaneous with efficiencies typically > 75%. The conventional Fenton process can be modified into photo-based or electro-based processes. Both processes operate with the generation of the hydroxyl radical using UV-radiation and electrodes respectively. An investigation into the removal of 5 mM of APAP using UV radiation at 360 nm resulted in 99% removal under 40 min [125]. Different electrode materials such as Ti/boron doped diamond and Pt sheets or gauzes have been tested for APAP removal and gave satisfactory results [126]. Both the processes can target high APAP concentrations; however, the operation of these processes requires a high capital due to electricity consumption [115]. For CBZ, the presence of electron rich moieties makes it easier to react with strong hydroxyl radicals and even ozone [127]. However, presence of other components such as suspended solids and organic matter can compete for ozone, reducing the reaction efficiency [127,128]. CBZ removal using Fenton processes were reported to achieve a mix of removal efficiencies [129–131]. Boron-doped diamond electrodes provide the advantage of avoiding the use of a chemical precursor for the generation of hydroxyl radical [132]. The system performance however was still dependent on the type of analyte. CBZ reaction rates were reported to decrease when the analyte used was switched from $NaNO_3$ to Na_2SO_4 [133]. A photo-Fenton system targeting CBZ removal from wastewater was reported to achieve a rate constant of 0.84/hour. The process was affected by hydroxyl radical scavengers such as carbonates and an increase in toxicity from degradation products were suggested as limitations for application in real wastewater systems [131].

Adsorption processes provide a low-cost and renewable alternative for APAP removal. Adsorption using chitosan activated carbon achieved ~95% APAP removal from an aqueous system. The process was aided by a sonification step [134]. Yanyan *et al.,* [135] tested coconut shell derived activated carbon for APAP removal. The process reached equilibrium between 26-48 hours. Spent tealeaves as a precursor for activated carbon were reported to achieve >99% removal efficiencies against 10mg/L initial APAP concentrations [136]. A study into APAP removal from drinking water using a combination of a sand filter and granular activated carbon filter only managed to achieve 20% APAP removal [137]. Generally, adsorption systems are used in combination with other processes such as ozonation, wetlands or sonification to enhance removal efficiencies [115]. CBZ removal via adsorption can take multiple pathways as shown in Figure 1:9.

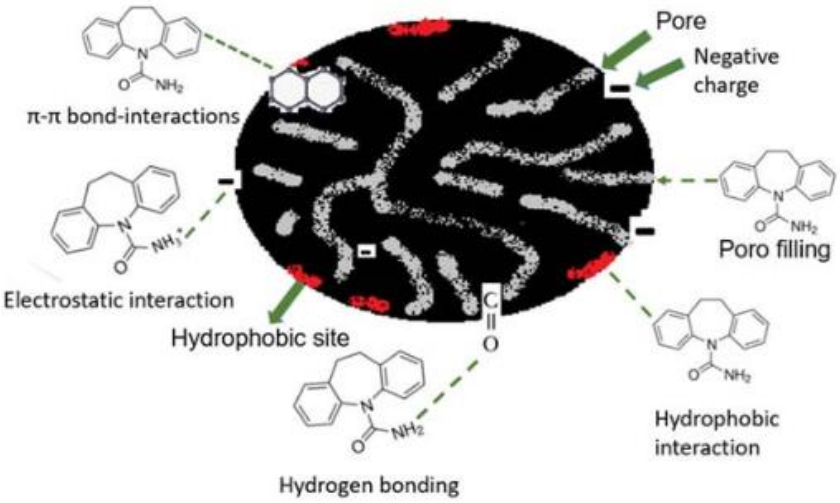

Figure 1:9 Possible Carbamazepine adsorption mechanisms onto activated carbon [138]

Amongst the possible mechanisms, pore-filling was suggested to be the most common for smaller organic compounds [139]. The statement was supplemented by observations of CBZ adsorption onto peanut shell and rice husk activated carbons [139]. In the case of biochars, π-π interactions are more prevalent. The mechanism involves a negative correlation between the solid-liquid partition coefficient and oxygen and nitrogen surface functionalities on the biochar surface [140]. CBZ removal using pine sawdust biochar (pyrolysed at 700 °C) had a maximum adsorption capacity of 35 mg/g. The biochar used had a surface area of 25 m^2/g. The same biochar was modified using a bleaching treatment that had an adverse effect on the removal efficiency [141]. Spent coffee grounds modified using sodium hydroxide were tested against organic pollutants. The produced biochar had a maximum removal capacity of 92 mg/g with a 24-hour operational time. Pore-filling and hydrophobic interactions were suggested to be the main removal mechanisms [142]. CBZ removal is highly influence by biochar surface area, micropore volume and surface functionalities. High micropore volume activated carbons with larger surface areas had high CBZ adsorption capacities [138].

There are still major concerns regarding incomplete removal of persistent organic pollutants from drinking water and wastewater systems. It is therefore essential to investigate the development of novel adsorbents for removal of such pollutants with systems that will not be limited to only lab-scale applications.

1.6 Adsorption

As discussed in Physical Processes, adsorption refers to the accumulation of a solid or liquid (adsorbate) onto the surface of a solid (adsorbent). A porous material offers the advantage of higher surface area for the adsorbate to accumulate within the porous structure. This process of species transfer typically continues until an equilibrium is reached between the concentration of the adsorbed species on the adsorbent surface and its residual concentration in the solution [143,144].

The adsorbed species can also detach from the adsorbent surface and move back to the bulk of the solution in a process referred to as desorption [145]. Both processes depend on several parameters such as solution pH, temperature, particle size, contact time, solubility of the adsorbate and the adsorbent and type of solvent. The most important factor for adsorption to happen successfully is the interaction between the adsorptive and the adsorbent. Physical parameters can further assist in the process. Adsorption and desorption can also co-exist in the solution once equilibrium is reached [146,147]. Figure 1:10 shows a simplified adsorption-desorption system.

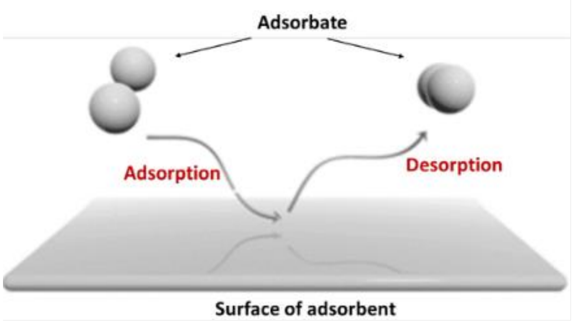

Figure 1:10 Schematic representation of adsorption and desorption [145]

The two primary pathways in which adsorption occurs are classified as physisorption and chemisorption. Physisorption or physical adsorption occurs when the accumulation of the target species occurs through Van der Waals forces. The process is considered reversible due to weak binding interactions and usually forms multilayers on the adsorbent surface. This type of interaction is more likely to occur in systems with low temperature and desorption can be achieved by providing little energy such as increasing the temperature. Chemisorption or chemical adsorption is a more powerful reaction in which the species are bound through strong chemical bonds. Chemisorption involves bond sharing between the adsorbate and the adsorbent and is typically monolayer. Desorption in this case requires much more energy and is considered almost irreversible compared to physisorption [145]. A comparison between physisorption and chemisorption is summarised in Table 1:4.

Table 1:4 Physisorption and chemisorption comparison [148,149]

Parameter	**Physisorption**	**Chemisorption**
Forces	Weak (Van der Waals)	Strong (chemical bonds)
Selectivity	No	Yes
Heat of adsorption	10-40 kJ/mol	40-400 kJ/mol
Number of layers	Multilayer	Monolayer
Adsorption speed	High	Slow at low T, fast at high T
Reversibility	Easy	Difficult/irreversible

A representation of adsorption mass transfer steps is shown in Figure 1:11 (a). External diffusion is the first step characterised by the penetration of the liquid film surrounding the adsorbent. This is driven by the difference in concentration between the bulk phase and adsorbent surface. The second step is internal diffusion, where the adsorbate reaches the porous structure of the adsorbent. Finally, the adsorbate gets attached to the active sites on the adsorbent surface, either through Van der Waals forces or chemical bonding [150]. An illustration of potential adsorption mechanisms for Methylene Blue removal from wastewater is displayed in Figure 1:11 (b).

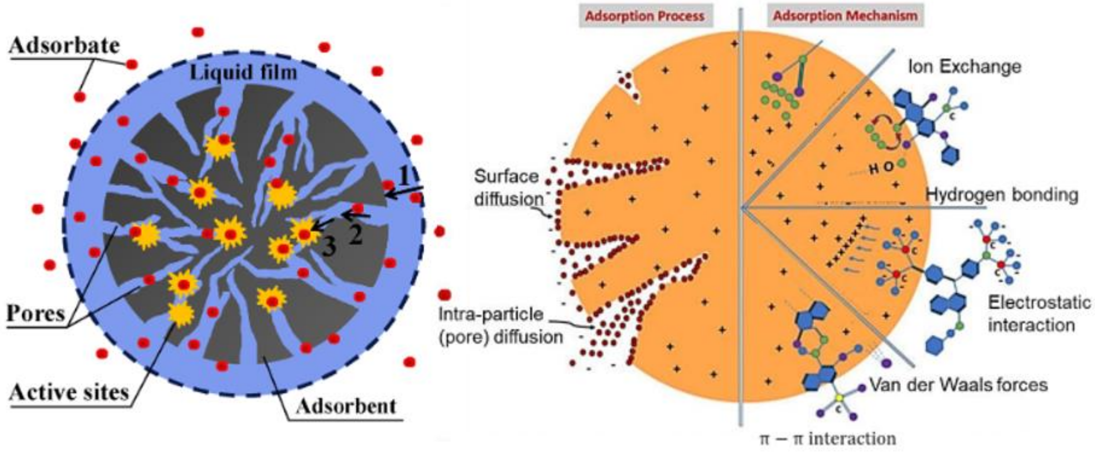

(a) (b)

Figure 1:11 (a) Adsorption mass transfer steps [106] and (b) mechanisms for adsorption (example of Methylene Blue removal) [151]

The internal structure such as the shape and size of pores considerably influences the adsorption process. As per the International Journal of Pure and Applied Chemistry (IUPAC), adsorbent materials can be classified based on their porous structure as follows [152]:

- Microporous adsorbents, pore widths < 2 nm
- Mesoporous adsorbents, pore widths between 2-50 nm
- Macroporous adsorbents, pore widths > 50 nm

Different sized pores result in different forms of pore filling. Narrow pores require a smaller number of molecules to fill up the cavities, whereas macropores can require multiple layers of molecules and therefore larger relative pressures. Upon reaching critical thickness, even before reaching saturated vapour pressures, the adsorbent pores start filling up with liquid, which results in a phenomenon called capillary condensation. This theory is often used to explain adsorption hysteresis often observed in porous solids [153]. A diagrammatical representation of monolayer adsorption at isolated sites and subsequent monolayer cover, followed by multilayer formations with increasing pressure and eventual pore filling is depicted in Figure 1:12.

Pore classification can be based on different factors such as their origin, accessibility, or their geometrical shape. Based on origin, pores can either be intrinsic or extrinsic pores. Structurally intrinsic pores are a property of the parent material. In some cases, natural reactions such as leaching can also induce new intrapores in a material. These pores are defined as injected intrinsic pores. The intrapores that are induced to a material as a consequence of impregnating it with a foreign substance are referred to as extrinsic type of intrapores. If the foreign substance is completely removed from the parent material, the resulting extrinsic pores are called pure type [154].

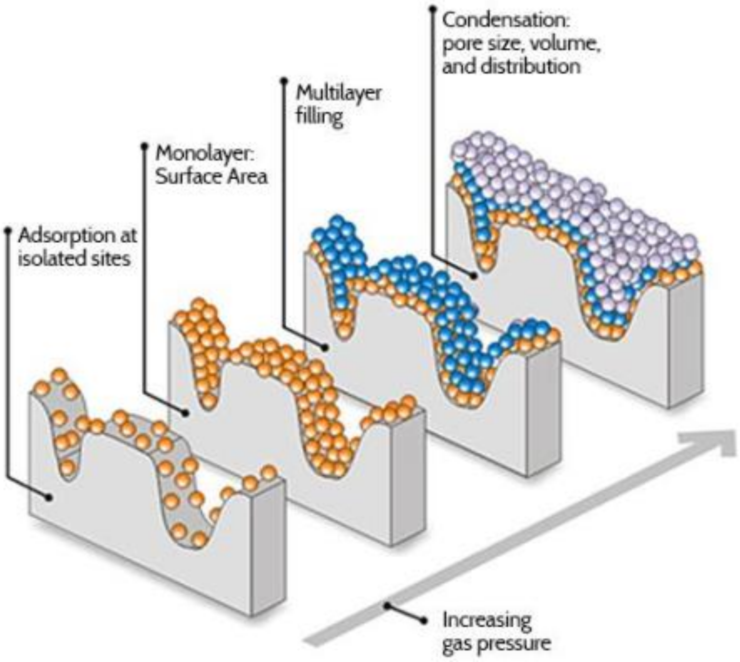

Figure 1:12 Adsorption process with increasing pressure showing monolayer coverage and subsequent monolayer formation [155]

Based on accessibility to surroundings, pores can be classified as open, closed, and dead-end pores. Open pores can be open at either one or both ends and are accessible to most molecules or ions in the system. Open pores open at only one end, are defined as blind or dead-end pores. Closed pores have no interaction with the adsorbate. Albeit these pores have no influence on adsorption or permeability of molecules, they still influence the mechanical properties of the parent material [154,156]. Figure 1:13 depicts pore classification based on accessibility.

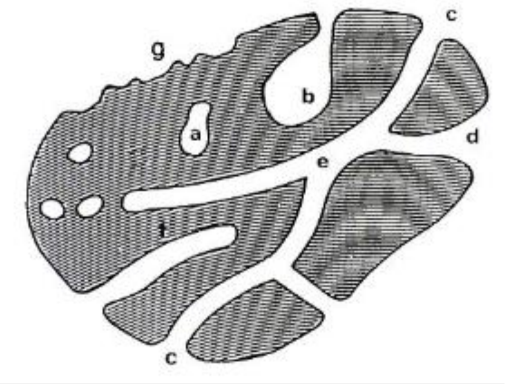

Figure 1:13 Pore classification based on accessibility to surroundings. a – closed pores, b – dead-end pores, c, d – open pores [156]

Another classification of pores is based on their geometrical shape as shown in Figure 1:14. They can be cylindrical, cone-shaped, slit-shaped or inkbottle. For convenience, a rough surface is not considered porous, until the surface irregularity has depth larger than its width [156].

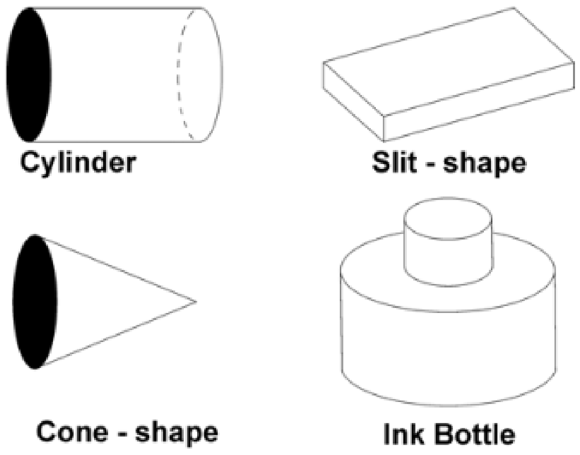

Figure 1:14 Pore classification based on geometry [157]

1.6.1 Adsorption Isotherms

The relationship between the adsorbate and the adsorbent can be illustrated using isotherms. The analysis is carried out at a constant temperature, where the material is immersed in an inert gas and the relative pressure of the system is increased from an approximate vacuum to saturation. This gradual pressure increase results in a monolayer formation of the gas molecules on the adsorbent surface, and the process continues until the pores are filled completely. This is followed by desorption, where the pressure is gradually decreased, and the gas molecules begin to detach from the adsorbent. It should be noted that the following classification is for physisorption isotherms. Figure 1:15 shows the IUPAC classification of physisorption isotherms.

Type I isotherms show steep adsorbate uptake at low relative pressures governed by microporous solids. The limiting uptake, when adsorption does not proceed further, is reached at low relative pressures due to inaccessible micropore volume as opposed to internal surface area. Type I(a) isotherms represent materials that have narrow micropores (~ 1 nm) and Type I(b) isotherms are given by materials with a slightly wider pore size range (up to 2.5 nm).

Type II isotherms are typically representative of non-porous materials. Point B is indicative of the knee of the isotherm when the monolayer formation is complete. A less distinctive knee (or Point B) is a consequence of overlapping of the monolayers and onset of multilayer coverage usually at high relative pressures.

For Type III isotherms, the monolayer formation is non-identifiable. The uptake is gradual at high relative pressure, suggesting weak interactions and molecule clustering at the most favourable sites. Type III isotherms can be associated with non-porous or macroporous solids.

Type IV isotherms are observed with mesoporous materials. The interactions between the adsorbate and the adsorbent occur at the pore walls and through condensation of the molecules within the structure. The primary step is the formation of the monolayer on the pore walls followed by multilayer adsorption as the relative pressure increases leading to pore condensation. Type IV isotherms have a noticeable plateau of variable length at high relative pressures due to saturation. A hysteresis loop differentiates Type IV(a) and (b) isotherms. A hysteresis loop is associated with capillary condensation and is discussed in more detail in the next section.

Type V isotherms resemble Type III isotherms at low relative pressures representing weak adsorbate-adsorbent reactions. At higher relative pressures, clustering, and pore filling result in a hysteresis loop. Type V isotherms are typically observed for water adsorption on hydrophobic materials.

Finally, Type VI isotherms depict a ‘stepwise’ or layer-by-layer adsorption on uniform non-porous surfaces. The step length or the plateau at each step is governed by the overlapping of monolayer coverage and multilayer formation while the step height represents the adsorption capacity for each layer and varies from system to system [158,159].

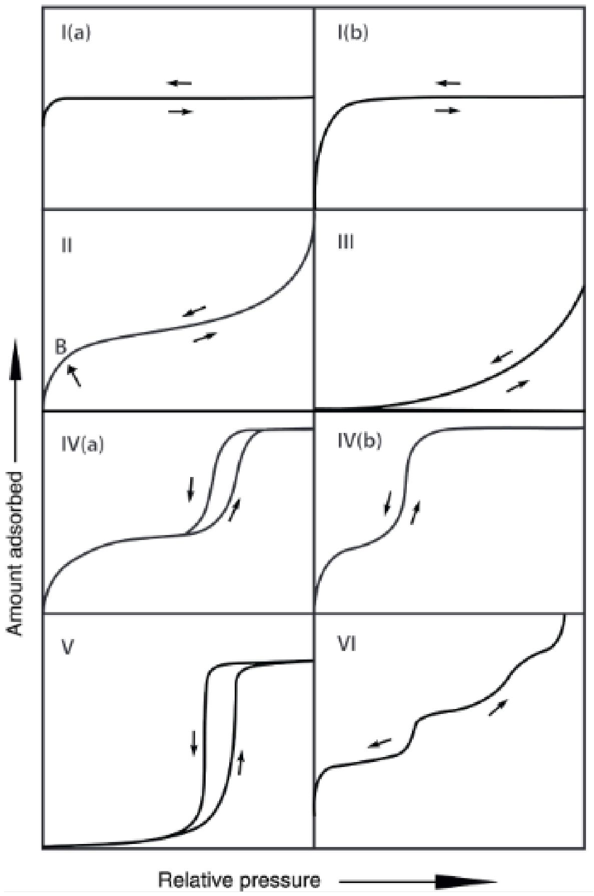

Figure 1:15 IUPAC physisorption isotherm classification. Type I: Microporous solids with high initial uptake; Type II: Typically, non-porous materials; Type III: Non-wetting adsorbents; Type IV: Mesoporous materials with hysteresis; Type V: Low uptake at low pressures, typical for water adsorption; Type VI: Stepwise monolayer formation [158]

1.6.2 Isotherm Hysteresis

The hysteresis loops observed in Type IV and V isotherms shown in Figure 15 are generally associated with capillary condensation. IUPAC have also published a classification of hysteresis loops. It follows the concept that during desorption, the pores with a larger cavity and narrow opening (inkbottle pores) remain filled during desorption until low relative pressures, a form of pore blocking. In open ended pores, it was reported that due to metastability effects, the adsorption curve in Type IV and V isotherms is not in thermodynamic equilibrium [158]. Figure 1:16 represents the six main classifications of hysteresis loops reported by IUPAC.

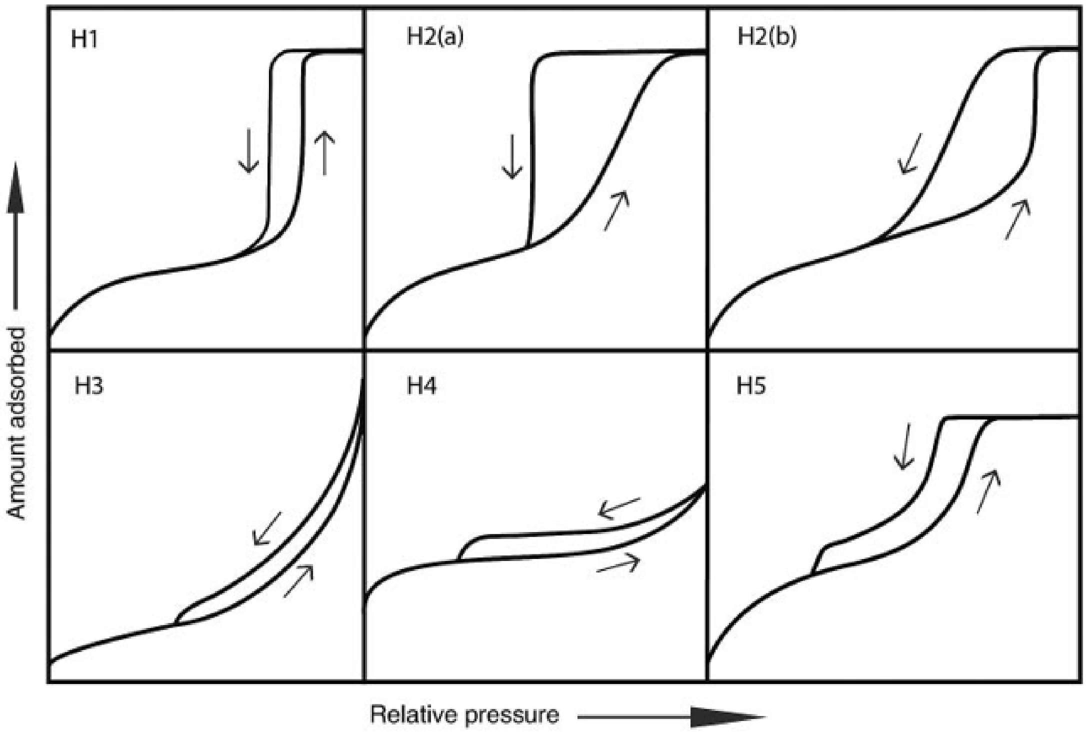

Figure 1:16 Classification of hysteresis loops. H1: Ink bottle pores or mesoporous materials; H2: Consequence of pore blocking and cavitation; H3: Incompletely filled macropores; H4: Characteristic of mesoporous materials with differences in heat of evaporation; H5: Result from open ended or semi-blocked pores. [158]

Type H1 hysteresis loops are associated with inkbottle pores or mesoporous materials and carbons with uniform pores over a narrow range. They can also be observed in some forms of templated silicas. The two branches are almost parallel, and the loop is narrow and almost vertical. H2(a) hysteresis loops also show a steep desorption branch. This can be a consequence of pore blocking and cavitation associated with inkbottle pores. H2(b) loops differ from H2(a) loops in that they are attributed to a wider range of pore neck widths. Type H2 hysteresis loops are observed within complex structures such as silica gels, silica foams and some porous glasses. A representation of hysteresis loops in Type H1 and H2 isotherms and associated pore networks is shown in Figure 1:17.

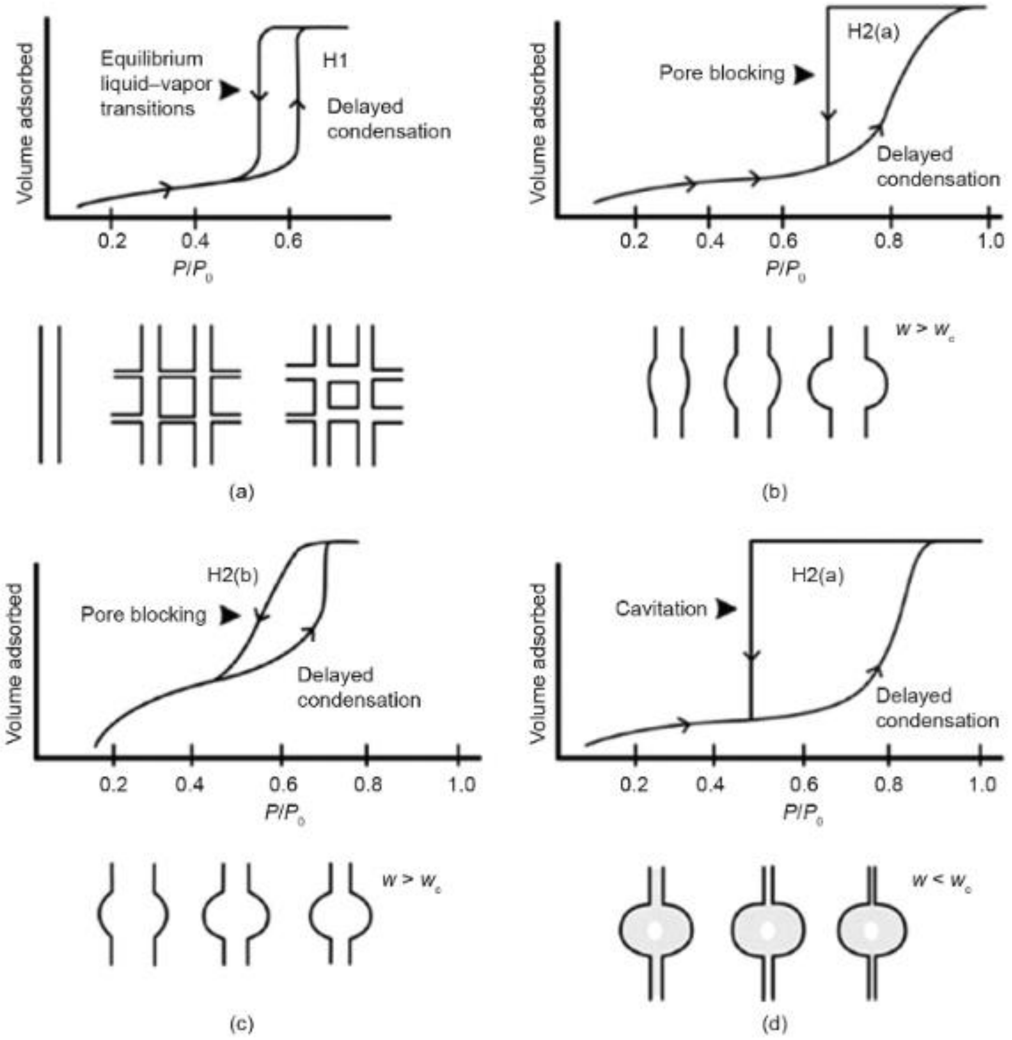

Figure 1:17 Hysteresis loops and their correlation to pore network and adsorption mechanisms. (a) Type H1, (b) Type H2 with pore blocking, (c) Type H2(b) (d) Type H2(a) indicating cavitation in the desorption branch [160]

The adsorption branch of a Type H3 hysteresis loop resembles a Type II isotherm. The desorption shoulder also has a lower closure point [152]. There pseudo-Type II isotherm behaviour is attributed to incompletely filled macropores and a non-rigid aggregate structure and can be observed in certain clays. Type H4 loops are obtained from activated carbons or nanoporous adsorbents. The high initial uptake of the adsorption branch is associated with the formation of micropores which is followed by multilayer physisorption. Type H5 loops have a distinctive shape. This is a result of the presence of both open ended as well as semi-blocked mesopores [152,158].

The hysteresis loops are an important assessment to understand the geometry and the size of pores located in the material structure. Micropores are observed at low relative pressures characterised by high uptake. These pores have no contribution to hysteresis loops as their adsorption and desorption mechanisms are mostly similar [161]. Hysteresis is observed in pores of larger width because of multilayer physisorption and capillary condensation. In pores of larger width, multilayer physisorption is still insufficient to fill the pore cavity and requires a higher relative pressure to reach saturation. Therefore, almost all hysteresis loops are observed at relatively higher pressures and pores of mesoporous or macroporous nature [162].

1.6.3 Adsorption Isotherm Models

Adsorption behaviour is typically described using Langmuir, Freundlich and Sips isotherm models. The Langmuir model is theoretical as opposed to the empirical nature of the Freundlich model and is more restrictive in its assumptions. Sips models combines the aspects of Langmuir and Freundlich models to allow for more flexibility and application to a wider range of adsorption systems. The mathematical relationships and assumptions associated with the discussed isotherm models are detailed below.

The Langmuir model [163] is based on three fundamental assumptions:

- Adsorption is only monolayer, and the adsorbed molecules do not interact with each other thereby preventing multilayer formation.
- The available sites are limited to adsorbing just one molecule at a given time.
- The adsorption sites are identical.

- Adsorption at one site is independent of adsorption at neighbouring sites.

Langmuir equation is commonly used in case of microporous adsorbents, where differences between monolayer coverage and pore filling is difficult. It is more applicable in cases where chemisorbed monolayers are being formed.

The non-linear form of Langmuir model [163] is given in Equation 1:

$$q_e = \frac{q_m K_L C_e}{1 + K_L C_e} \qquad \text{Equation 1}$$

Where q_m is the maximum adsorption capacity in mg/g, C_e is the equilibrium concentration of the solute in mg/L, q_e is the amount of solute adsorbed in mg/g and K_L is the ratio between adsorption and desorption rates in L/mg. The model represents a chemical adsorption process with monolayer formation and homogenous adsorption [164].

Described as an empirical equation, the Freundlich model has no physical meaning. The model is often associated to nonlinear adsorption [165] and has been used to represent heterogeneous systems showing multilayer adsorption [166,167].

The Freundlich model [165] is given under Equation 2**:**

$$q_e = K_F {C_e}^{1/n} \qquad \text{Equation 2}$$

Where K_F is the rate constant in $L^{1/n}mg^{1\text{-}1/n}/g$ and n is a correction factor. The linearised form of the model can be obtained when n=1. All other terms are as defined above. [178]. The model can be applied to systems showing chemisorption with 50% coverage as well as physisorption and is mostly represented in its non-linearised form.

The Sips model [168] is often referred to as the Langmuir-Freundlich isotherm model and was developed in 1948. The non-linear form is given in Equation 3:

$$q_e = \frac{q_{ms} K_S {C_e}^{n_s}}{1 + K_S {C_e}^{n_s}} \qquad \text{Equation 3}$$

Where the maximum adsorbed amount is represented by q_{ms} in mg/g and K_S ($L^{ns}.mg^{-ns}$) and n_S are the Sips constants. When the value of n_S in the Sips model is equal to 1, the model simplifies to the Langmuir model. At low initial concentrations (C_0), the Sips model also resembles the Freundlich model. However, it is important to note that, unlike the Sips model, the Langmuir model satisfies Henry's law at low C_0. The model can be applied to homogeneous as well as heterogeneous systems and describes the adsorption process of a monolayer, where one adsorbate molecule is adsorbed onto $1/n_S$ adsorption sites [164].

There can be instances where the fits from Langmuir and Sips isotherm models accurately describe the adsorption isotherm data. Since the models differ in their interpretation of the nature of adsorption sites, Scatchard plots can be used to determine the nature of the material surface. The Scatchard equation is given in Equation 4:

$$\frac{q_e}{C_e} = Qb - q_e \qquad \text{Equation 4}$$

Where the Scatchard adsorption constant Q is in mg/g and b is in L/mg. The nature of the material surface can be interpreted from the plot between q_e/C_e vs q_e. If the plot is linear, the material surface is expected to be homogeneous with a single type of binding site available. Contrary, a non-linear plot suggests heterogeneity and multiple binding sites [169].

1.6.4 Surface Area Analysis

Surface area is one of the most important properties of adsorbents. There have been attempts to establish a mathematical relationship between the adsorption isotherms and different isotherm models [170]. Of these, the most common approaches to report experimental surface areas are based on the Brunauer-Emmett-Teller (BET) model [171].

Brunauer-Emmett-Teller Model

The Brunauer-Emmett-Teller (BET) theory [172] was published in 1938 but continues to be a key approach in surface area calculations using nitrogen adsorption. The theory works as an extension of Langmuir theory where it considers the possibility of multilayer formation. There are still some assumptions associated with the model:

- There is a single monolayer.
- Molecules will adsorb in multilayers infinitely.
- The monolayer exhibits heat of adsorption and subsequent layers exhibit heat of condensation.
- There is no adsorbate-adsorbate interaction.
- The final adsorbed layer is in an equilibrium state with the bulk.

The BET equation is given as Equation 5:

$$\frac{p}{V(p_O - p)} = \frac{1}{V_m C} + \frac{(C-1)p}{V_m C p_O} \qquad \text{Equation 5}$$

Where p and p_o are the equilibrium and saturation pressure respectively, C is a dimensionless constant related to adsorption energy, V_m is the volume of gas requited to reach monolayer coverage and V is the volume of the adsorbed gas.

A plot of $\frac{p}{V(p_O - p)}$ against p/p_o will be linear usually within a range of $0.05 \le p/p_o \le 0.35$ [173] and the values of V_m and C can be calculated from the slope and y-intercept.

Surface areas calculated using BET analysis are highly sensitive to the selected relative pressure range [174], particularly for microporous materials. Rouquerol *et al.* published a set of recommendations in their review to avoid subjectivity when selecting pressure ranges that would help in the calculation of true surface areas. The optimal relative pressure range can be determined using the four consistency criteria suggested by Rouquerol *et al.* [175]:

- Only the range where the product of the adsorbate loading rate and 1 minus the relative pressure is increasing monotonically with the relative pressure should be chosen.
- The value of BET 'C constant' must be positive. C constant quantifies the adsorbent and adsorbate interactions and is related to the energetics of adsorption in the first adsorbed layer [174].
- The selected linear region should encompass monolayer loading corresponding to the relative pressure.
- The relative pressure calculated in Criterion 3. should be equal to the one calculated from BET theory consonant with monolayer loading with a 20% tolerance.

Understanding the type of isotherms and hysteresis loops as well as surface area determination are important considerations made in the study of adsorption systems. One of the most important factors in such systems, however, is the precursor used as the adsorbent material. The choice of precursor is an important step as it will govern the adsorbate-adsorbent interactions. The precursor should also be easy to access, inexpensive and renewable. High carbon abatement potential and thermal stability are also added advantages when choosing potential adsorbent materials [176]. The next section provides a review on the different materials used as adsorbents for environmental remediation with a focus on biochars.

Barrett-Joyner-Halenda Method

The Barrett-Joyner-Halenda (BJH) method [177] can be used to determine the pore volume and pore size distribution within macro- and mesoporous materials. It combines Wheeler theory [178], physisorption fundamentals, and capillary condensation to calculate the Kelvin core radius, from desorption data obtained at different pressure intervals. The direct calculation of pore size distribution works on the following assumptions: (a) pores are of cylindrical shape and the pore passage is rigid, (b) there is an absence of micropores and (c) all pores are completely saturated at the highest relative pressure [179]. To calculate the pore radius, at a given pressure, the pores are treated as being composed of three sections, as illustrated in Figure 1:18. The first section is the core of the pore, the region which encompasses the main liquid filling. This region evaporates once the critical pressure for that pore radius is achieved. The second section is the adsorbed layer, which stays on the pore walls when the core is emptied and exhibits gradual evaporation with decreasing pressure. The final section is the pore wall, thereby completing the calculation of the empty pore width [180].

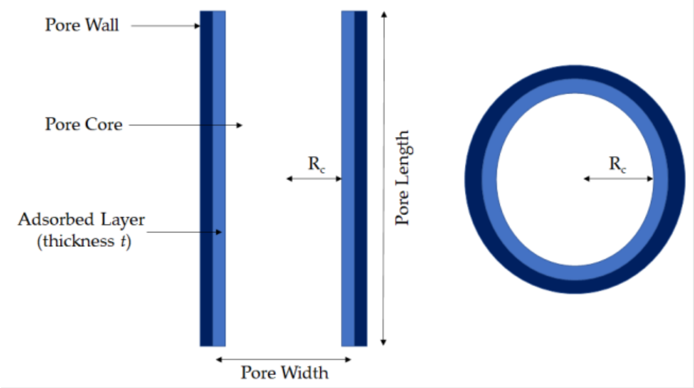

Figure 1:18 Labelled pore sections (left) and pore cross-section (right) [180]

The Kelvin equation (Equation 6) defines the relationship between relative pressure, pore meniscus radius (r_c), surface tension between the liquid and vapour interface (γ), the liquid molar volume (V_m), which is specific to the gas being used as adsorptive, the universal gas constant (R) and temperature (T).

$$\ln\left({}^{p}/{}_{p_o}\right) = \frac{2\gamma Vm}{rcRT} \qquad \text{Equation 6}$$

The equation can be rearranged to solve for the meniscus radius [181]. The BJH method, however, has limitations arising from the assumptions that there are strictly no micropores, and other complex pore structures that are not cylindrical.

t-plot Method

Since the BJH method is based on the assumption that there are no micropores present, the t-plot method was established by Lippens and Boer [182] to specifically determine the microporosity present within a material. Using this method, t-curves are obtained by plotting a relationship between adsorbed layer thickness (t) and adsorption uptake, taken from isotherm data, as shown in Equation 7.

$$t = 2.98 + 6.45(\frac{p}{p_o}) + 0.88(\frac{p}{p_o})^2$$ Equation 7

The presence of microporosity in samples is indicated by distinct t-curve sections. In the case of a reference sample for a non-porous material, the resulting plot is a straight line passing through the origin. A horizontal deviation from this curve represents microporous nature, whereas a vertical deviation is an indication of mesoporosity [182]. Example plots of materials that are non-porous, solely micro-, or mesoporous and a combination of micro- and mesopores are shown in Figure 1:19. To determine the extent of any identified microporous nature, the straight line obtained when micropores are present is extrapolated to determine the intercept on the y-axis. The micropore volume can then be calculated directly using Equation 8:

$$V_{\mu} = intercept \times C_{\rho}$$ Equation 8

Where, C_p is the density conversion factor specific to the gas being used and is determined from the ratio of the gas state and liquid state densities.

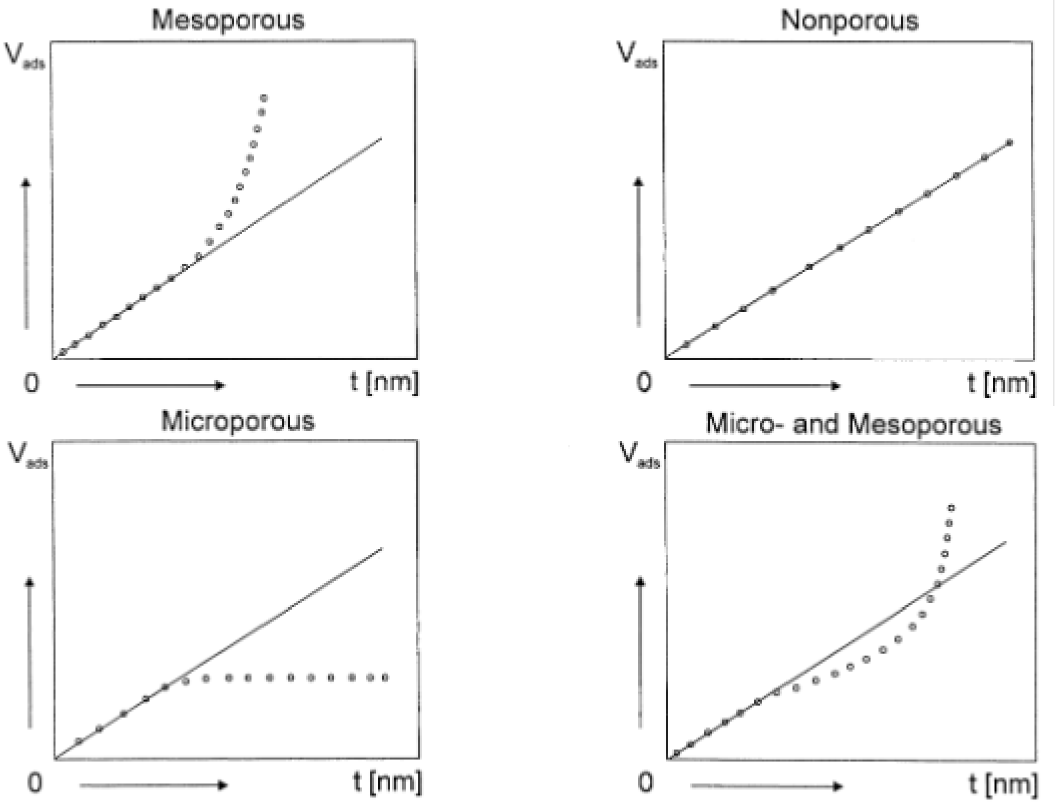

Figure 1:19 Example t-plots of mesoporous materials (top left), nonporous materials (top right), microporous materials (bottom left) and micro- and mesoporous materials (bottom right) [182]

In addition to obtaining information using the intercept, the gradient of the line can be used to calculate the external surface area (S_{ext}), as well as micropore surface area (S_{μ}), by making use of the total surface area obtained using BET theory (S_{BET}) and Equation 9 and 10:

$$S_{ext} = gradient \times C_{\rho}$$ Equation 9

$$S_{\mu} = S_{BET} - S_{ext}$$ Equation 10

The current drinking water treatment systems face several challenges. Recent technological advancements have indicated contaminant diversity making it essential to develop systems that target a range of family of materials, contrary to being highly efficient against a removal of a particular species and inefficient against others or even closely related substances. The identification and detection of pharmaceutical and pesticide residues that show bioaccumulation potential, presents challenges due to their unique characteristics and properties. Although, some advanced removal techniques such as AOPs and membrane filtration exist, the deployment of these systems requires a large capital investment and infrastructure. Water remediation via a sustainable adsorbent offers multiple advantages over other systems.

This work focusses on the development of a relatively low-cost renewable adsorbent material that can target multiple persistent organic pollutant species thereby demonstrating efficiency against a family of materials with comparable chemical structures and behaviour in water systems. The design of experiments optimisation of operating process parameters can replace the need for the traditional one factor at a time approach to produce materials catered to a specific target application. The adsorbents produced in this work were from a wood-based feedstock as wood has the highest carbon abatement potential. Efficient removal of three species with structural similarities via adsorption would demonstrate the flexibility of the process against a range of pollutants as well as the key influence of the chosen feedstock and process optimisation on the quality of the final product.

2. Adsorbents for Water Treatment

Over the years, researchers have aimed to produce adsorbents from cheap raw materials, using waste produced from certain industries or households, to create a ‘circular economy’, and to minimise waste disposal of potentially useable components.

2.1 Types of Adsorbents Materials

Table 2:1 summarises selected materials used as adsorbents in aqueous systems outlining their key features. This section also provides an insight into some of the more commonly used materials as adsorbents.

Table 2:1 Selected materials used as adsorbents, outlining their key features and application ranges [183]

Adsorbent	**Key feature**	**Ref**
Wood waste	Suitable for a wide-pollutant range	[184]
Agricultural waste	Widely used for wastewater treatment	[185]
Activated alumina	Effective against bacteria & organic matter	[186]
Silica gel	Effective against toluene, xylene, and dyes	[187]
Zeolites	High ion exchange capacities	[188]
Biomass	More selective than ionic adsorption	[189]
Chitosan derivatives	Cost effective biopolymer	[190]

Activated carbons (AC) are commonly used adsorbents for the removal of various pollutants from water streams [191]. They can be obtained using either physical or chemical activation combined with pyrolysis at high temperatures [192]. ACs with multiple regenerative cycles are used in commercial applications. The production of ACs typically involves pyrolysis of the material in an inert atmosphere in temperatures ranging from 450-1200 °C. For physical activation, an activating gas such as CO_2 is passed through the system during pyrolysis. Chemical activation generally involves the use of strong acids or bases to modify the pyrolysed material [89]. Despite the numerous techniques and advancements in AC adsorbents, their application tends to be limited to drinking water systems.

Chitosan makes an effective adsorbent material by itself or infused during synthesis of other adsorbents, and its low cost makes it an economically feasible adsorbent [193]. Chitosan based adsorbents have proved to be efficient for metal ion removal due to properties such as hydrophilicity, biocompatibility, and adhesion characteristics [194]. The adsorbents can also be regenerated, which adds to their economic feasibility [195]. Without modification however, chitosan-based adsorbents demonstrate limited application under acidic conditions [196]. Although chitosan offers multiple advantages as an adsorbent material; it is highly biodegradable and susceptible to dissolve in acidic conditions which can affect the regeneration cycles and limit application to alkaline systems [197].

Zeolites are naturally occurring minerals with high cation exchange ability. There is an abundance of natural zeolites with a crystalline hydrated framework structure, and their low cost makes them an attractive prospect for adsorbent synthesis [198]. Zeolite sorbents are cheaper compared to their aluminium and AC counterparts [89]. Zeolites have been studied with regards to selectivity to metal ions. Primarily, the application of silica gels was targeted at gas phase contaminants. In the liquid phase, silica-based adsorbents with high surface areas and polarities showed promising results [89]. A common technique to develop silica-based adsorbents is surface modification. The process, however, raises the concern of biodegradability and disposal of the adsorbents and hence, has limited applications [199,200].

Residues from agricultural processes like lignite, peat, mangosteen peels and certain waste products like tea leaves, coffee grounds and wood have emerged as an interest area to produce adsorbents. The materials are available in abundance and are environmentally friendly. Kwikima *et al.* (2012) reported that chemically modified adsorbents had better performance than unmodified biosorbents [201]. Chemical modifications, however, raise concerns about excess chemical disposal as well as increase the overall price of the adsorbent. Testing such materials after physical activation could lead to a potential solution of the problem.

A range of materials have been investigated to produce efficient adsorbents, each with their set of advantages and disadvantages. Biochars are a form of activated carbon, that have also been investigated. They are the black carbonaceous residue of thermochemical conversion of biomass in an inert atmosphere [202]. They can be ideal adsorbent materials due to their stability, high carbon content and aromatic nature [203]. Biochar based adsorbents can be derived from a range of precursors and are also versatile in their field of application. The choice of precursor is an important step as they exhibit different physiochemical properties in terms of functional groups and surface charge relevant to the parent material [204]. The next section provides a review on different biochar applications, types of precursors and factors influencing adsorbent synthesis.

2.2 Biochars

Due to ease of application and versatility, biochars have gained interest across various domains. The unique surface chemistry provides an opportunity for biochars to be used as catalysts. In the realm of adsorption, highly porous structure and large surface areas facilitate the removal of a range of pollutants. Their ability to retain and release nutrients is a key factor in soil enrichment applications whereas the carbon-rich nature presents opportunities in the energy storage sector.

2.2.1 Potential Biochar Applications

Catalysts

Biodiesel as an alternative fuel has recently gained interest. It is non-toxic, biodegradable, and capable of competing with the conventional petroleum fuels [205–207]. A key concern in biodiesel production, however, is the cost of lipid feedstock and the type of catalyst. To reduce this cost, research focus has shifted to alternative feedstock such as edible and non-edible oils [208–211]. The free fatty acid (FFA) content in the oils determines the type of catalyst to be used [209]. The role of the catalysts is to assist in the conversion of triglycerides into biodiesel through transesterification after the esterification process. Acids such as hydrochloric and sulphuric are preferred for oils with high FFA content for simultaneous esterification and transesterification. The homogenous catalysts boost biodiesel production on an industrial scale. However, a lot of effort and resources are required to remove the by-products [212,213] and purify the final product [214,215]. The operating expenses and resources involved in the final output make the process cumbersome and not environmentally friendly. To mitigate this impact, heterogeneous or solid catalysts have gained importance. As the catalysts do not dissolve in the reaction mixture and are non-toxic and reusable, the overall process has a reduced carbon footprint [209,214]. Biochar based acid catalysts derived from rice husk [216], coconut shells [217], pyrolysed hard wood [218] have thus found potential application in biodiesel production.

Adsorbent materials

Biochars have well-developed pore networks, ranging from micropores to macropores, and high surface areas that makes them suitable for such applications [219]. The pore network extends throughout the material and provides active binding sites for heavy metals that readily sorb on the surface and within the pore network. The parent feedstock used to produce biochars, and the parameters used for activation, determine the chemical properties of the product and the affinity towards target metals [220]. Rapid industrialisation has resulted in high volume discharge of wastewater into the environment. The heavy metals discharged as by-products are very toxic, carcinogenic and have the potential to bioaccumulate. This makes prolonged exposure to even minor concentrations of these metals detrimental to humans and the environment alike [221]. Biochars made from renewable sources gave comparable adsorption capacities to commercial activated carbons, even though the surface areas demonstrate a significant difference [222].

Bio-Fertilisers

Bio-fertilisers, much like other bio-degradable alternatives, are carbon-efficient substances than their synthetic counterparts. While synthetic fertilisers are known to boost the crop production, there is still significant damage to the environment. Consequently, bio-fertiliser utilisation has been on the rise [223]. Biochars, as soil enhancement materials, can maintain the natural nutrients within the soil. They also control cation exchange, which reduces nutrient leaching from soils [222]. Barrow (2012) suggested that biochars can be potential substances to be used for land rehabilitation [224]. If the biochar feedstock contains elements such as calcium, magnesium and nitrogen, their application can help maintain soil macronutrient levels and in turn, soil fertility [225]. The different functional groups present in the biochar also help to increase the pH by reacting with the hydrogen ion [226].

Energy Storage Materials

Supercapacitors have widespread application in energy storage alongside lithium-ion batteries in cell phones and electric vehicles. One of the components of a supercapacitor is a carbon-based material. Activated biochars have found implementation in the making of this component [222]. According to Dehkhoda *et al.*, (2014) potassium hydroxide activated biochar can be used within supercapacitors [227]. Biochars improve the total capacitance of the electrodes, due to the highly micropore structure, and chemical activation was reported to be more suitable for the properties of the supercapacitor [228,229]. Materials such as maple wood and microporous bamboo were also studied as electrode materials [230,231].

Over the years, a plethora of materials have been used to produce carbon- based materials. Biochar based acid catalysts derived from rice husk [216], coconut shells [217] and pyrolysed hard wood [218] have found potential application in biodiesel production. Biochars as soil enhancement materials can maintain the natural nutrients within the soil. They also control cation exchange, which reduces nutrient leaching from soils [222]. Biochars have well-developed pore network, ranging from micro- to macropores, and high surface areas that make them suitable for adsorption

[219]. The pore network extends throughout the material and provides active binding sites for heavy metals that readily sorb on the surface and within the pore network. Table 2:2 gives examples of different feedstock used to produce biochars and their application in water treatment systems.

Table 2:2 Selected examples of feedstock for biochar production and target compounds in water treatment

Feedstock for biochar production	**Pollutant species**	**Ref**
Grape bagasse	Copper	[232]
Modified waste potato peels, commercial coffee waste	Cobalt ions, heavy metals	[233,234]
Walnut wood	Lead and methylene blue	[235]
Rosid angiosperm	Metaldehyde	[236]
Peanut shell	Metal ion	[237]
Anaerobically digested biomass	Heavy metal	[238]
Hazelnut shell	Chromium (VI)	[239]
Apple wastes	Heavy metal	[240]

Biochars made from renewable sources gave comparable adsorption capacities to commercial activated carbons, even though the surface areas demonstrate a significant difference [222]. The abundance of wastes produced from households and agricultural residues, and the feasibility to transform these into carbon materials, has attracted researchers to work towards the concept of a circular economy within biochars production. Biochars have well-developed pore networks, ranging from micro- to macropores, and high surface areas that make them suitable for adsorption

[219]. The pore network extends throughout the material and provides active binding sites for heavy metals that readily sorb on the surface and within the pore network. Biochars made from renewable sources gave comparable adsorption capacities to commercial activated carbons, even though the surface areas were significantly smaller [222]. As a consequence of these characteristics, many biochars have been applied in water treatment processes, extending the circularity of their manufacture.

Table 2:3 provides comparative data for biochars produced from wood-based feedstocks reported in literature, detailing pyrolysis temperatures, surface areas and fixed carbon contents.

Table 2:3 Surface areas and pyrolysis temperatures of biochars produced from wood-based feedstocks

Feedstock	Pyrolysis Temp. (°C)	Surface area (m^2/g)	Carbon (%)	Ref
Oak wood	350 650	450 642	-	[241]
Mulberry wood	350 450 550	16.6 31.5 58.0	67.9	[242]
Hardwood	450	0.43	53.4	[243]
Grey dogwood	755	422	73.1	[244]
Black locust	755	442	72	
Hackberry	755	369	69.9	
Red bud	755	320	71.6	
American linden	755	190	71.2	
Apple tree branch	600 700 800	209 419 545	81.5 82.3 84.8	[245]
Oak tree	600 700 800	289 336 398	81.2 83.2 82.9	
Fir wood chips	600 700	545	89.3	[246]

2.2.2 Influence of Operating Process Parameters

There are several parameters involved in the production of biochars: operating temperature, gas flowrate, residence time, furnace ramp rate, and pressure that can influence the yield and quality of the final product. Previous studies have discussed the relationship between biochar performance and process parameters [247,248]. However, there is a limitation and lack of understanding of the synergistic effects of these parameters on produced biochars. Feedstock with different physical and chemical compositions, react differently to operational parameters and produce biochars with variability in characteristics [249]. Material selection is an important step prior to biochar production. Parent material characteristics can be influenced by climatic conditions [250]. To ensure profitability, the cost incurred in procuring the raw material and transforming it into bespoke materials for chosen applications should offer a reasonable benefit. The influence of these key parameters is outlined below, allowing for variable selection to obtain optimised biochars materials.

Effect of Temperature

Pyrolysis temperature is considered one of the key factors on the properties of biochar. The breakdown of heavy hydrocarbons decreases the quantity of the final product as more volatiles are removed from the system [251]. Many researchers have reported a reduction in biochar yield on increasing the pyrolysis temperature as may be expected [236,252,253]. At high temperatures, secondary reactions occur that further breakdown the char formed at initial temperatures into liquid and gaseous phases. The decrease in yield occurs when the thermal energy increases the bond cessation energy in the precursor and subsequently releases more volatile components [254]. This activation energy, however, enables the biochar to develop micropores and an enhanced pore structure [255]. The disadvantage of extreme temperatures is that the formation of ash hinders the growth of the pore network and surface area [256]. The surface areas do not continue increasing with increase in temperatures. In some cases, at a particular temperature, there is a sharp decline in the surface area. This is referred to as the ‘inflexion point’ [257]. There is no fixed trend that identifies the point of inflexion in biochars. The inflexion occurs based on the properties of biomass. At extreme temperatures, which is relative to the properties of precursor used, thermal deactivation occurs. The deactivation is caused by pore fusion and melting of biochar, that reduces the surface area and pore volume of the final output [258]. In addition, a very low temperature range does not cause a significant change in the pore volume and surface area of biochars. If the pyrolysis temperature is unable to completely devolatilise the volatile constituents, the final product might be subject to pore blockage and an underdeveloped pore network [259]. The above observations suggest a temperature range between 400 and 800 °C. The definite value for an optimum yield depends on the type and source of the biomass being used and interaction with other reaction parameters.

Effect of Gas Flow Rate

Carrier gases are used to ensure an inert atmosphere for pyrolysis. Vapours are formed during pyrolysis, and these can participate in reactions with the char, and modify its characteristics if not purged from the system [254]. Nitrogen is the most common carrier gas. Argon has also been used by researchers, but nitrogen is cheaper and more readily available than other inert gases. It is harder to disperse argon molecules as the gas is denser compared with nitrogen. Moisture and oxygen removal would be more effective with argon being a carrier gas, however the capital involved with argon usage is significant. This makes nitrogen a feasible and satisfactory alternative. An increase in the gas flow rate, marginally decreases the biochar yield. The effect is a consequence of the vapours being pushed out of the system. A shorter vapour residence time eliminates the volatiles preventing repolymerisation [254]. This marginal decrease in yield was observed when the biochar yield was reduced from 28.4% to just above 27% on increasing the nitrogen supply from 50 to 400 mL/min [260]. Several other studies reported similar observations about slight decrease in yield with increasing gas flow rates [232,261,262]. The evidence suggests that low to moderate flow rates are sufficient to understand their influence on biochar properties. In contrast to the biochar yield being almost constant, the change in gas flow rate has a more pronounced influence on surface area and total pore volume of the product. An increment in the nitrogen flow rate from 50 to 150 mL/min was reported to cause an increase of over 300 m^2/g in Algerian date pits derived activated carbon. The total pore volume increased from 0.012 cm^3/g to 0.125 cm^3/g [263]. A very high gas flow rate however, results in a temperature decrease of the biochar, affecting the release of volatile matter and consequently, a reduced biochar yield and pore volume [263,264]. The observations reported above, advocate the use of a moderate gas flow rate between 150 and 300 mL/min for optimum characteristics.

Effect of Heating Rate

Heating rate plays an important role in the composition and states of the biomass during pyrolysis. A low heating rate mitigates the possibility of thermal cracking of biomass and rules out secondary pyrolysis reactions to enhance the biochar yield [254]. A very high heating rate would melt the biochar particles and increase the gaseous and liquid components, thereby decreasing the quantity of the final product [257]. An excessive heating rate also results in accumulation within particles, resulting in blocked pore entrances. The result is due to shortage of time for the volatile matter to diffuse [265]. Depolymerisation of biomass and prevalence of secondary pyrolysis are key concerns to avoid high heating rates during pyrolysis, as both result in a reduced biochar yield. A reduction in yield was observed upon changing the heating rate from 30 to 50 °C/min by researchers [266,267]. Chen *et al.,* (2016) reported an initial increase in surface area when the heating rate was increased from 10 °C/min, up until a heating rate of 30 °C/min, followed by a decline when it was increased further [268]. High heating rates result in accumulation of volatile matter within and on the surface of biochar by reducing the time needed for diffusion on those particles [265]. To avoid micropore coalescence or collapse of the carbon matrix altogether, a high rate of volatile matter generation must be avoided [257]. The above observations rule out the use of high heating rates and propose an optimum limit between 10 and 30 °C/min.

Effect of Contact Time/Residence Time

Residence time is a parameter influenced by temperature, gas flow rate and heating rate. To promote repolymerisation, and a high biochar yield, sufficient residence time is necessary for the reaction constituents [269]. In contrast, investigations reported that the yield of biochar was not proportional to the residence time [270,271]. A residence time between 30 and 60 minutes was reported to yield the maximum pore volume range for chemically activated biochar from corn cob [272]. An increase in the surface area was reported on increasing the residence time from 10 to 60 minutes [273]. However, upon further increment, there was a retardation in the surface area value. Although, sufficient residence time is needed for a high yield, and well-defined pore structure, prolonged exposure to high temperatures can be detrimental to the pore structure [257]. The complications arising from interaction between other process conditions and residence time, make it a challenging parameter to analyse and, hence, a key component to investigate during biochar production. The above observations advocate the use of a residence time ranging between 20 and 60 minutes.

Effect of Pressure

The influence of pressure on biochar production is relatively straightforward. Extreme, high pressures prevent the release of volatile matter from the system and result in the formation of spherical cavities [274]. A continuous decrease in surface area was reported upon increasing the pressure from 1 to 20 bar. Melligan *et al.,* (2011), supported this observation when they reported a decrease in surface area value upon increasing the pressure from 1 to 26 bar [275]. However, a pressure slightly higher than atmospheric pressure can increase the residence time of reaction constituents, which assists char formation [276]. Carbon content in the final product was suggested to be pressure dependent [254]. Elevated pressures were reported to improve the biochar yield [277]. In combination with a reduced gas flow rate, the complex mixture of organic compounds (anhydrous sugars, vapour phase sugars, lignin moieties) decomposes on the biochar surface. This occurs due to the mixture being unstable at high temperatures and is supplemented with a gas release encompassing mainly water, methane, hydrogen, carbon monoxide and carbon dioxide.

Effect of Type of Pollutant

Although the type of pollutant does not directly influence the final biochar characteristics, it plays a significant role in the application of the biochar material. The presence of different functional groups endow the species with characteristic properties [278]. These properties can either aid or hinder biochar performance based on the conditions present in the system by influencing polarity, dissociation, hydrogen bonding or complexation of the pollutant with the material. Size and molecular weight are also key factors to consider during pollutant selection. A larger sized molecule will face challenges accessing the porosity of highly microporous material as opposed to a smaller molecule. Water solubility of the pollutant also affects its adsorption behaviour. Generally, a more hydrophobic pollutant will have a stronger driving force than a hydrophilic species that is stable in the solution [279].

Challenge in Large-Scale Biochar Application for Water Treatment

Activation technique and cost of the final product could be potential limiting factors in obtaining a commercial product ready for distribution [89]; despite compelling concepts and innovation, market demand and large-scale application require ample supply of feedstock and significant capital input for process application. A comprehensive production technique could lead to smaller profit margins providing a challenge in gaining capital investments. Companies and manufacturers often tend to evaluate these risk factors to ensure the accessibility of the final product that is reasonably priced and user-friendly. Porous carbons are efficient materials to be used in water remediation. The characteristics of the parent material, availability, and feasibility govern the overall efficiency of the produced biochars. Locally procured raw material provides a considerable reduction in carbon footprint associated with supply and transport, offering the potential for circularity in the formation of biochar materials for possible applications. Tailor-made biochars for target pollutant removal can be achieved by synthesis process parameter manipulation and eliminate the necessity for a trial-and-error approach. Removal timeframes are also an important consideration prior large-scale application. A short contact period with high removal efficiency against the selected pollutant are ideal circumstances for scaling up pilot systems.

2.2.3 Aims and Objectives

As discussed extensively in the literature, biochars have tremendous potential to be used as adsorbent materials. The characteristics of the final product, however, can potentially be tailored to suit a range of target applications. As the demand for environmentally friendly materials increases, biochars, derived from local sources, including native woods, can provide an efficient and low-cost solution.

The main aims of this work are underpinned:

1- Identification of a suitable feedstock from screening experiments for biochar production.
2- Using a Design of Experiments approach to investigate the synergistic effects of operating parameters on biochar characteristics and its advantages over the traditional one factor at a time approach.
3- Application of the chosen optimised biochar sample for water remediation targeting selected persistent organic pollutants (3,4-DCA, APAP and CBZ).

3. Methodology

3.1 Materials

The wood samples used in this study were procured from Sustainable Thinking Scotland (STS) C.I.C. (Kinneil Estate, Bo’ness, Scotland), and obtained from a walled garden in a 200-acre estate. Wood samples included birch, oak, ash, Scots pine, Sitka spruce and Western red cedar. Table 3:1 gives an overview of the sample mix used in the study. The samples were delivered as chunks of logs, with equal proportions of species and were stored in airtight containers under room temperature. A non-disclosure agreement with STS was signed to not disclose the compositions and initial analysis of the raw feedstock for patenting purposes. Pre-pyrolysis, equal sized portions of each species were taken during the weighing process.

Table 3:1 Feedstock used for biochar production showing species mix in the samples

Sample	Wood type	Species
A	predominantly softwood	ash, birch, oak, Scots pine, Sitka spruce, Western red cedar
B	predominantly hardwood	ash, Downey birch, oak, Scots pine, Sitka spruce, Western red cedar
C	100% softwood	Scots pine, Sitka spruce, western red cedar

Samples A and B were developed to give a comparison between biochars produced from soft and hardwoods. A design of experiments (DoE) approach was adopted, based on a comprehensive literature review. Screening experiments were performed on Samples A and B to identify the type of wood to be used for the DoE study. The results of the preliminary runs on Samples A and B were refined and DoE was applied to Sample C. Parameter scoping helped develop DoE runs to investigate a wider parameter space, utilising statistical analysis of variance (ANOVA) using Minitab to determine responses arising due to multiple factors changing simultaneously [280].

This provides a deeper understanding of the systematic factors that have statistical influence on the chosen responses.

3.2 Design of Experiments

DoE is a multipurpose approach that helps in determining a relationship between input variables against a chosen response. Based on the situation, different design types can be applied to a system. **Comparison** investigates a single factor between different combinations using t-, Z- or F-tests. **Variable screening** uses factorial designs to analyse the significance of input variables on the overall performance of a system or process. **Transfer function optimisation** allows study of the relationship between relevant input variables to the specified output. **System optimisation** uses the transfer function to improve the overall performance of the system. Finally, **Robust design** is aimed at mitigating the effects of system variation without root cause elimination [281].

In this study, a Full Factorial Design (FFD) which falls under variable screening was used to assess possible interactions of input variables as opposed to the traditional one-factor at a time approach. The statistical approach offers the advantage of scoping a wider parameter space and their possible interactions by running fewer experiments compared to the traditional approach. A full factorial design incorporates all factor combinations in a test and takes into consideration their simultaneous manipulation. This helps in the identification of the main and interaction effects of the chosen factors on selected responses. The 2^k factorial design takes into account the main effects, two-factor and even three-factor interactions. The design space is orthogonal, suggesting that the model terms do not correlate with one another as an initial assumption and are estimated independently. Therefore, the FFD offers a balanced symmetric approach in determining which factors have conclusive influence on the chosen responses [282].

The screening runs were based on three variables: contact time with activating agent (CO_2), flowrate of activating gas, and furnace temperature. Two temperatures (600 and 850 °C) were chosen based on a review of the literature, to study the difference in the types of produced biochars, as well as yields. Thermal CO_2 activation improves sorption characteristics of biochar and forms new functional groups, creating a more uniform porous structure, and is quicker than chemical activation. Flowrates of 100 or 250 mL/min were used with residence times of 20 and 60 min.

Screening identified softwood as a more desirable feedstock, hence, DoE (using FFD) was applied to pure softwood samples. A mean temperature of 725 °C was used with three variables: contact time (20 and 60 min), gas flowrate (100 and 250 mL/min) and the heating ramp up rate (15 and 30 °C/min) for the full factorial design (FFD). Minitab was used to generate the FFD, which resulted in a total of $2^3 = 8$ experiments for 3 factors with a high and low setting each [283]. The runs were randomised to minimise effects of factors that cannot be controlled. Centre points were omitted from the model to reduce excess material waste and minimise equipment usage and power consumption, but the model was allowed to run interactions up to third order. Biochar yield and surface area were considered as the two design responses as the economic feasibility and performance of the biochars is governed by these properties.

3.3 Nomenclature

Sample names were developed as per: the first three digits (e.g., 250 or 100) represent the gas flowrate. 'S' and 'H' denote either softwood or hardwood; the middle set of values (600, 850, 725) represent the pyrolysis temperatures; followed by residence time and sample category, e.g., 20A or 60C. Thus, the sample 250S725-60C represents a gas flowrate of 250 mL/min, for a softwood sample pyrolysed at 725 °C with a residence time of 60 min, from wood batch C. All experiments were conducted at a heating rate of 15 °C/min, with the exception of samples marked '/30', where the ramp rate was increased to 30 °C/min.

3.4 Pyrolysis

Prior to combustion, the wood samples were divided into cubes of sides ~5 cm. These smaller cubes were washed with de-ionised water to remove dust and oven dried at

100 °C for 24 h. For combustion, a precursor weight of 30 ± 0.1 g was used. The sample was equally distributed into four crucibles fitted with lids, all placed inside the Thermconcept KLS 10/12/WS muffle furnace. A CO_2 flow of 250 mL/min was maintained over the sample for 40 min to ensure an inert atmosphere, and the furnace set to the corresponding temperature and dwell time. Following this, the gas flowrate was adjusted to the values detailed in Table 4:1 and Error! Reference source not found. and the heating process initiated. After each run was complete, the flow of gas was switched off once the furnace reached room temperature and the sample was allowed to cool overnight. Figure 3:1 shows a schematic diagram of the muffle furnace used for pyrolysis.

Biochar weight was calculated once the samples had reached room temperature. The yield of the sample was calculated using Equation 11:

$$\text{Biochar yield (\%)} = \frac{\text{produced biochar weight (g)}}{\text{precursor weight (g)}} * 100 \qquad \text{Equation 11}$$

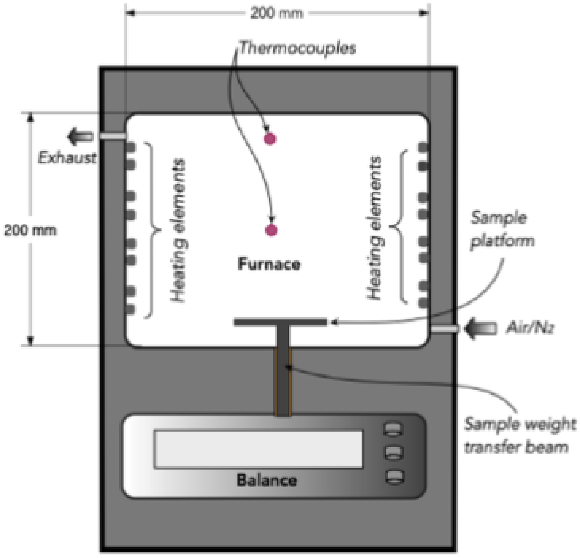

Figure 3:1 Schematic diagram of muffle furnace equipped with a weighing system (Licence number - 5501811254585) [284]

3.5 Analytical Method

The experimental solutions were passed through Fisherbrand Grade 601 general purpose filter papers (125 mm diameter). Two filter papers were used for each filtration step to ensure the removal of all suspended particles from the permeate. For the target species in this work, calibration curves were plotted prior kinetic and adsorption experiments. The maximum adsorption wavelengths for 3,4-DCA, APAP and CBZ are 296, 243 and 285 nm respectively. For calibration, absorbance obtained by passing light of monochromatic radiation was plotted against concentration and a liner fit provided the required parameters of slope and intercept. The generated equation was then used to identify residual concentrations from experimental runs.

3.6 Adsorption Kinetics

Kinetic and isotherm studies of the target species were performed on the optimised sample suggested by Minitab and correlated from experimental observations. Biochar samples (0.1 g) were added to 100 mL glass bottles and mixed with 50 mL of 100 mg/L solution of either APAP, CBZ or 3,4-DCA. The bottles were subsequently placed on an orbital shaker at 420 rpm for time steps 15, 30, 60, 120, 180, 240, 360 and 1440 min. Once completed, the solutions for each time step were double filtered using cellulose acetate filter papers to obtain a clear solution free of suspended biochar particles. The supernatants were analysed using UV-Vis spectroscopy. The amount of target species adsorbed was calculated using calibration curves run prior to kinetic and isotherm measurements. It should be noted that there was an exception in the case of 3,4-DCA kinetic analysis. The speed of adsorption was observed to be extremely fast, not allowing sufficient time to measure and analyse multiple samples. Hence, a reduction in temperature was used, using an ice bath (~2-3 °C) to slow the reaction process to obtain kinetic parameters. A series of kinetic models were applied to determine the most appropriate fit.

The pseudo first order (PFO) model was first proposed by Lagergren in 1898 [285]. The differential form of the model is given in Equation 12:

$$\frac{dq_t}{dt} = k_1(q_e - q_t) \qquad \text{Equation 12}$$

Where k_1 is the rate constant for adsorption, and q_e and q_t are the adsorbate uptake amounts at equilibrium and a given time ‘t’, per mass of adsorbent, respectively.

Integrating the above equation provides the linearized form (Equation 13) of the model [286]:

$$\ln(q_e - q_t) = ln q_e - k_1 t \qquad \text{Equation 13}$$

Which upon rearranging gives the non-linear PFO model as presented in Equation 14:

$$q_t = q_e(1 - e^{-k_1 t}) \qquad \text{Equation 14}$$

The physical meaning associated with the model has been suggested to be dependent on the initial solute concentration [287,288]. The PFO model is associated with a high initial solute concentration, the process being at the initial stage of adsorption, and availability of only a few active adsorbent sites [289].

Ho *et al.* [290], proposed the expression for the pseudo second order (PSO) model by integrating Equation 15:

$$\frac{dq_t}{dt} = k_2(q_e - q_t)^2 \qquad \text{Equation 15}$$

And applying it to the adsorption of lead onto peat, to obtain the non-linear model shown in Equation 16:

$$q_t = \frac{{q_e}^2 k_2 t}{1 + q_e k_2 t} \qquad \text{Equation 16}$$

Where k_2 is the reaction rate constant, and all other terms are as defined for PSO. The linearised form of the model is given in Equation 17:

$$\frac{t}{q_t} = \frac{1}{k_2 {q_e}^2} + \frac{t}{q_e} \qquad \text{Equation 17}$$

PSO models are more commonly used to predict adsorption experiments as opposed to PFO models. The model signifies a low initial solute concentration, occurring within the final stages of the adsorption process, and an abundance of active sites on the adsorbent [289].

3.7 Adsorption Isotherms

Batch adsorption experiments were carried out using 0.1 g biochar in 50 mL solution of the target species. For APAP and 3,4-DCA, the concentrations used were 25, 50, 75, 100, 150, 200, 250 and 300 mg/L. For CBZ, the maximum solubility is 125 mg/L and, hence, the isotherm points were taken between 10-100 mg/L at intervals of 10 mg/L. Based on the kinetic data, 3,4-DCA isotherm solutions were filtered after 10 min. Experiments for APAP were run for 6 hours and CBZ experiments were allowed to run for 24 hours to allow for full equilibration of the samples. The permeate collection procedure was similar to that used within the kinetic measurements, where the solutions were double filtered using two cellulose acetate filter papers and the absorbance measured using UV-vis spectroscopy. The collected isotherm data was analysed using three adsorption isotherm models stated in Section 1.6.1.

UV-Vis spectroscopy in an analytical technique that explores both UV and visible light wavelengths. The mechanism is akin to IR spectroscopy and corresponds to the absorbance of light resulting from atomic excitations. To obtain calibration curves and residual concentrations of the target species post adsorption, Cary 5000 UV-Vis Spectrophotometer was used. The wavelength range was selected between 200-800 nm to obtain the spectrum and a baseline correction using DI water was performed for added accuracy.

A calibration curve is typically plotted prior experimental runs to find the concentration of the target species in an unknown solution. Adsorption was measured for a set of solutions of known concentrations using wavelengths at which maximum adsorption occurs for the target compound. In this work, three sets of calibration curves were plotted for 3,4-DCA, APAP and CBZ. The maximum adsorption wavelengths for these compounds are 296, 264 and 285 nm, respectively. For calibration, absorbance obtained by passing light of monochromatic radiation was plotted against concentration and a liner fit provided the required parameters of slope and intercept. The generated equation was then be used to identify residual concentrations from experimental runs. Observed calibration curves are reported below.

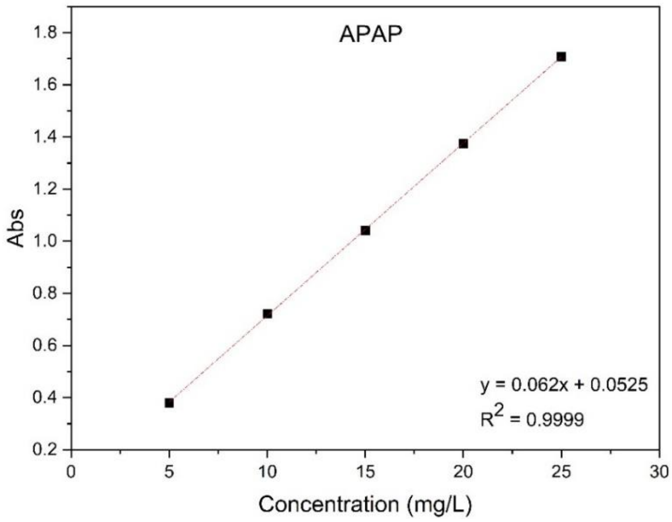

Figure 3:2 Calibration curve for APAP using UV-vis spectroscopy.
Peak wavelength: 243 nm

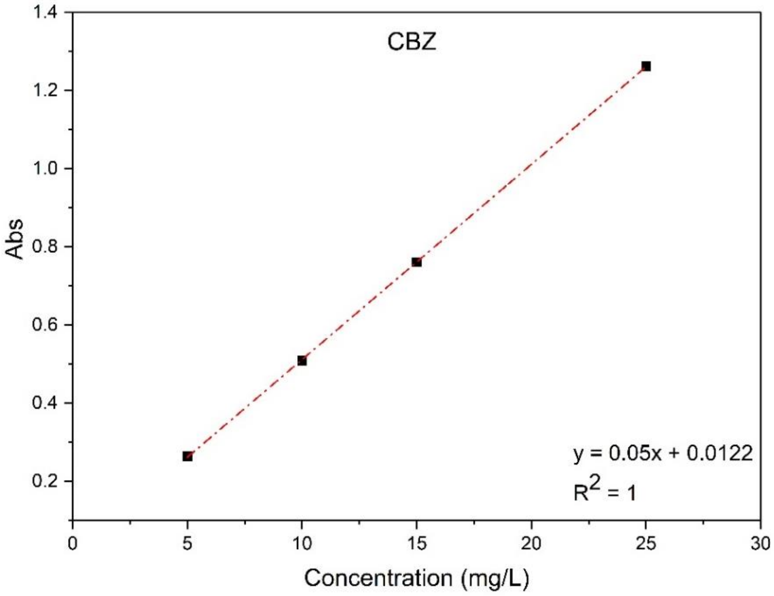

Figure 3:3 Calibration curve for CBZ using UV-vis spectroscopy.
Peak wavelength: 285 nm

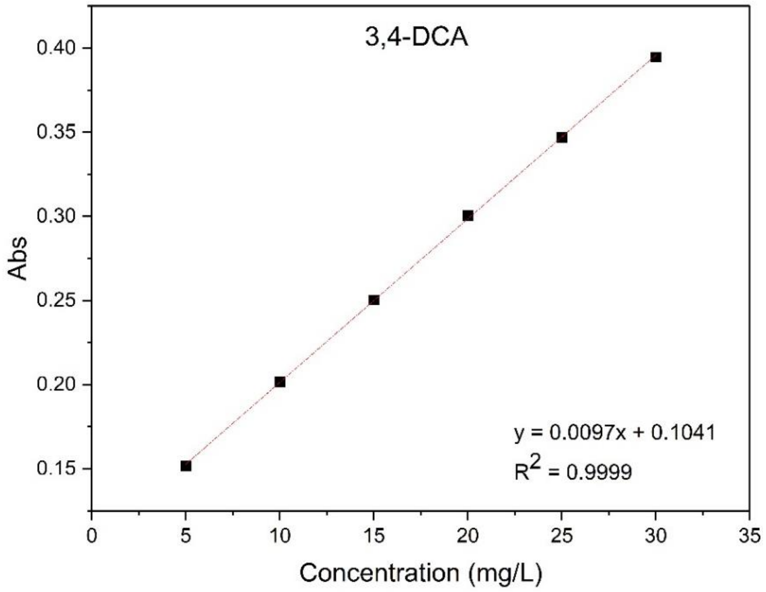

Figure 3:4 Calibration curve for 3,4-DCA using UV-vis spectroscopy. Peak wavelength: 296 nm

4. Biochar Screening and Characterisation

Material characterisation and analysis are important for evaluating potential fields of application and understanding the influence of initial process conditions. Analysis can assist in the identification of potential synergistic effects of operating conditions and possible process optimisation. This chapter focuses on the results of parameter and feedstock screening and experimental data obtained from screening. A range of methods were employed to probe the characteristics of the produced biochars. Surface area of the samples was determined using the BET method outlined in Section 1.6.4. Pore size analysis was performed using Barrett-Joyner-Halenda Method and t-plot Method. Material morphology was investigated using scanning electron microscopy. Fourier transform infrared spectroscopy was used to identify different functional groups on the surface of the materials, which was further supplemented using results from X-ray photoelectron spectroscopy. The analysis procedures and subsequent results are detailed below.

4.1 Biochar Yield

Table 4:1 shows the percentage yield of biochars produced from screening wood samples A and B, under different pyrolysis temperatures and operating parameters. The trend in yield is as expected, with increasing pyrolysis temperatures resulting in lower quantities of produced biochars [236]. As the temperature is increased, more volatiles are removed from the system, thereby reducing the biomass within the system, hence, the final mass of the biochar. It is evident that the final product is determined by a direct combination of the operating parameters. For the softwood chars (Sample A), a low contact time of 20 min and pyrolysis temperature of 600 °C, with a high gas flowrate of 250 mL/min, resulted in the highest biochar yield of 6.5 g. Increasing the contact time to 60 min and keeping the other two parameters constant, resulted in a minor reduction in yield of less than 1 %. The result suggests that the increment of contact time from 20 to 60 min does not have a significant impact on the product yield. A similar pattern was observed for the hardwood chars (Sample B).

A maximum yield of 7.6 g was obtained using a high gas flowrate, low pyrolysis temperature and low contact time. The yield decreased slightly with increased contact time (~ 2 %). The lowest yield was obtained at a temperature of 850 °C, with a 60 min residence time and low gas flowrate. Under similar conditions, hardwood samples gave higher yields than the softwood samples. For Experiment S1, the softwood yield was 22 %, and the hardwood biochar was 25 % under similar parameters (S5). The difference in yield was not considerable for the other runs in both wood batches. This observation, combined with the specific surface areas obtained, indicated that 100 % softwood samples were worthy of further investigation.

Table 4:1 Process conditions, yields and textural properties for biochars produced using wood samples A and B (Ramp rate = 15 °C/min)

Exp	Sample code	CO_2 flowrate (mL/min)	Temp (°C)	Contact time (min)	Biochar weight (g)	Yield (%)	Surface Area (m^2/g)	Micropore Volume (cm^3/g)	Total pore volume (cm^3/g)	Average pore width (nm)
S1	250S600-20A	250	600	20	6.53	21.8	544	0.18	0.26	3
S2	250S600-60A	250	600	60	6.20	20.7	538	0.18	0.25	3
S3	250S850-20A	250	850	20	5.30	17.7	597	0.20	0.29	3
S4	100S850-60A	100	850	60	4.41	14.7	764	0.22	0.42	5
S5	250H600-20B	250	600	20	7.59	25.3	525	0.17	0.25	3
S6	250H600-60B	250	600	60	6.96	23.2	544	0.18	0.27	3
S7	250H850-20B	250	850	20	5.16	17.2	573	0.19	0.26	3
S8	100H850-60B	100	850	60	4.54	15.1	714	0.23	0.34	4

4.2 Porous Structure Characterisation

Adsorption analysis can be used in the characterisation of porous materials, where it is commonly employed to determine specific surface area, pore volume and pore size distribution. Within this study, analysis was performed using a Micromeritics ASAP 2420 Surface Area and Porosity Analyser (Limit of Detection (LoD) = 0.00001 mmHg).

Analysis involved two-steps:

- 1 Degas – The biochar sample was crushed to a powdered form using a pestle and a mortar prior to degassing. Degassing of the sample was performed to remove any particles that were already adsorbed on the pore walls. Approximately 0.5 g of the sample was added to a glass tube, consisting of a narrow tube with a bulb at the bottom, such that the sample is completely contained within the bulb space. The sample tube was then connected to a degas port, and the tube bulb was covered with a heating mantle ensuring direct contact between the bulb and the thermocouple. The mantle temperature was raised to 200 °C at a rate of 5 °C/min, and held for 240 min, under vacuum. After which time, the sample was allowed to cool down to room temperature and the tube was backfilled with nitrogen.
- 2 Analysis – This involved re-weighing of the sample, after degassing, to adjust the recorded weight after the loss of any contaminants. A filler rod was inserted into the tube, to reduce unnecessary void volume, thereby increasing the accuracy of the measurement, and reducing the time required for analysis. A thermal jacket was placed on the neck of the tube, to help in maintaining isothermal conditions, and the tube was mounted on an analysis port. The analysis method, used here, comprised 49 points on the adsorption branch and 30 points on the desorption branch, during which time the sample tube was immersed in liquid nitrogen (-196 °C) held in an insulated Dewar. Isotherm data was extracted using the equipment software and used in subsequent analysis, including BET, BJH and t-plot methods.

Figure 4:1:a and b shows the adsorption isotherms recorded in the screening study. Experiments S1-4 represent a Type II isotherm, governed by adsorption onto microporous solids. The hardwood samples in Experiments S5-8 also display an initial high uptake followed by a plateau. There is slight evidence of a final uptake at high relative pressure, which can be attributed to a Type II isotherm and multilayer adsorption [158].

Table 4:1 shows the textural data obtained for the screening samples, comprising the surface area, micropore and total pore volumes, as well as the average pore widths. Similar data on DoE samples is reported in Table 5:1. Total pore volume of samples was calculated using Equation 18:

$$Total\ pore\ volume\ (TPV) = (Q_{Sat} * \mathrm{MW}/V_m)/\rho_{liq} \qquad \text{Equation 18}$$

Where, Q_{sat} = maximum nitrogen adsorption in cm^3/g

MW = molecular weight of N_2 (28 g/mol)

V_m = volume occupied by 1 mole of gas (22.4 L)

ρ_{liq} = Density of liquid N_2 at boiling point (808 g/L)

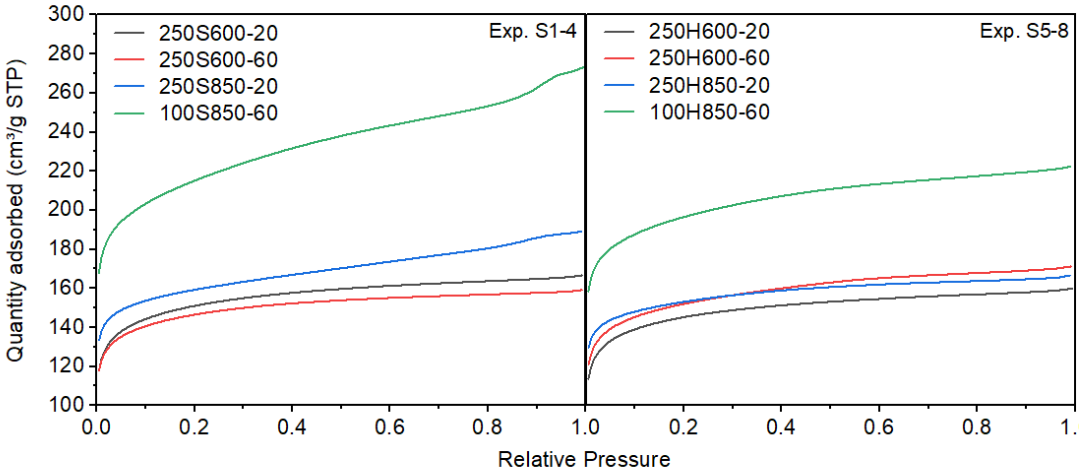

Figure 4:1 Adsorption isotherms obtained for biochars. Exp. S1-4: Showing results of N_2 adsorption on Sample A (predominantly softwood species); Exp. S5-8: Showing results of N_2 adsorption on Sample B (predominantly hardwood species).

t-plot analysis, developed by Lippens and Boer [182] was used to determine the micropore volumes reported in Table 4:1 and Table 5:1. It can be inferred that increasing pyrolysis temperatures caused an increase in microporosity. The ratio of micropore volume to TPV is highest in samples with low gas flowrates and higher residence times. At high gas flowrates, $V_{micropore}/V_{total}$ ratios are similar for experiments with 20 min hold time at high temperature. The evidence suggests an inverse relationship between microporosity development and residence time. Microporosity is suitable for interactions between small adsorbate species and adsorbents [236], so can be a useful quantity to optimise. DoE Experiments D5 and D6 indicate that a higher ramp rate combined with a longer hold time can enhance mesoporous nature in the biochars, which have previously been shown to be useful for aqueous phase applications [291].

Given the presence of significant microporosity reported in Tables 4:1 and 5:1, Rouquerol correction was applied for all samples produced in this study. The criteria for Rouquerol correction are mentioned in 1.6.4 and the selected points for the BET transform plot for sample D1 are shown in Figure 4:2. For the selected points in the graph, the plot of $n(P_o\text{-}P)$ vs P/P_o increases continuously with the chosen relative pressure range and the resulting BET plot is linear with a positive 'C' value.

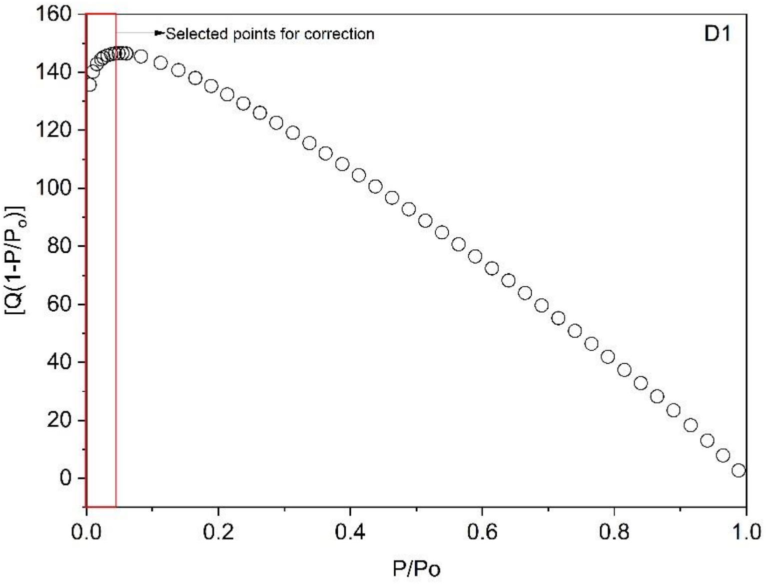

Figure 4:2 Plot of $Q(1-P/P_o)$ vs P/P_o for biochar D1 showing the range to which BET equation can be applied to obtain a positive 'C' constant and linear BET plot

The resulting BET plot for D1 with a positive C-constant is shown in Figure 4:3 (See Appendix G: Rouquerol Selection Criteria and BET Transform Plots for remaining plots). Maximum BET surface area was recorded for a pyrolysis temperature of 850 °C with a gas flowrate of 100 mL/min and 60 min residence time with softwood precursor (S4) as stated in Table 4:1. For both precursors used in the screening study, highest surface areas were determined at highest temperatures and longer residence times. Similar observations of improved surface areas with residence time and temperatures were reported previously [216,236]. Between the two types of precursors investigated, predominantly softwood samples on average had higher surface areas compared to the hardwood samples. As stated earlier, these observations combined with comparable yields for both precursors, led to the decision of using pure softwood samples for the DoE study.

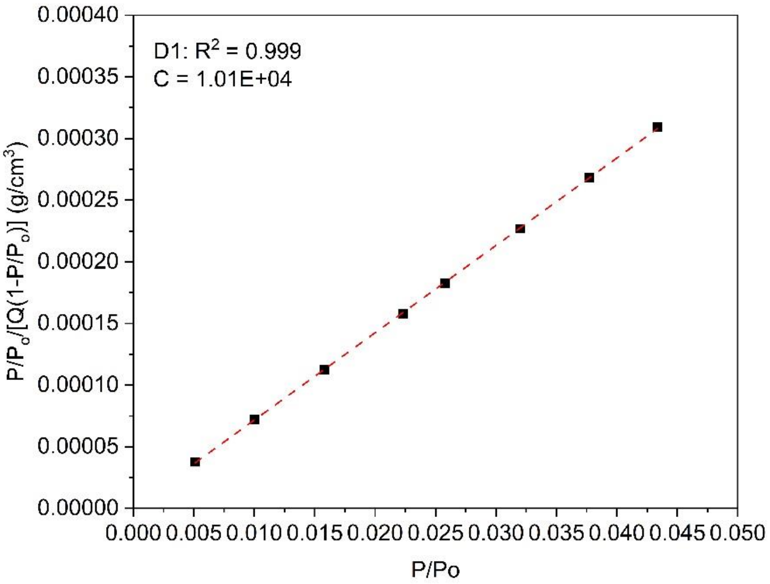

Figure 4:3 BET transform plot for D1 with a positive C-constant resulting from Rouquerol correction

Pore width data obtained from Barrett-Joyner-Halenda (BJH) analysis [177] (Table 4:1 and Table 5:1) further confirms the predominantly microporous nature of the biochars. Average pore widths were greatest for runs performed at 725 °C with high ramp rates. As stated above, shorter hold times resulted in greater microporosity, as well as smaller pore widths. Predominantly softwood biochars (S1-4) were almost as microporous as hardwood biochars (S5-8), and Sample C (entirely softwood, D1-8) demonstrated the highest mesoporosity. The results indicate a possible application for Sample A in the adsorption of small adsorptive species, mainly in gas phase [240,254]; including in carbon capture [255,256].

4.3 Fourier Transform Infrared Spectroscopy

Fourier Transform Infrared Spectroscopy (FTIR) works on the principle that atomic vibrations within molecules interact with specific frequencies and absorb infrared radiation. The obtained spectrum is characteristic to the bond frequency of molecules present in the sample. The biochars were crushed to a powdered form, and a small amount of sample (~ 0.2 g) was placed on the sampling surface. An ABB IR Instrument MB 3000 series (LoD = 0.06 cm^{-1}) was used to characterise the functional groups on the surface of the biochar samples using Attenuated Total Reflectance (ATR) for analysis. A total of 32 scans were taken in transmittance mode. The spectra were recorded at 4 cm^{-1} resolution and wave number range between 500 and 4000 cm^{-1} keeping the detector gain at 80% for maximum accuracy. An air reference was taken on the day of analysis to minimise any noise present in the system.

Figure 4:4a presents the FTIR spectrum obtained for pure softwood feedstock (Sample C). In the fingerprint region, between 600-1500 cm^{-1}, there is evidence of $CH=CH_2$ vinyl terminals [292]. There is also evidence of loss of the peak from C-OH vibrations in the feedstock at 1000 cm^{-1} from pyrolysis treatment [236]. The heat treatment plays a crucial role in condensation of the carbonaceous skeleton and removes the hydroxyl groups from cellulosic compounds present in the precursors [293]. Figure 4:4b and c show the FTIR spectra for DoE biochar samples obtained using low and high ramp rates. The observed spectra look identical and not influenced by the change in ramp rates of the experimental runs. The peaks observed between regions 3800 and 3500 cm^{-1} indicate the presence of hydrogen bonds. This information is further supplemented by peaks between 1600 and 1300 cm^{-1} as is the case with analysed biochar samples [292]. There are sharp peaks from the biochars between 3000 and 2600 cm^{-1} that could be due to C-H stretching bonds [236]. There is also strong evidence of C=C bonds with symmetric and asymmetric vibrations and possible conjugation, as well as stretching vibrations with other structures such as oxygen and hydrogen (C=O, C-H) from the spectra in the 1600-1800 cm^{-1} region [292,293]. These functional groups can be the result of the presence of ketones, aldehydes, and carboxylic acids [294]. The results indicate the development of a layered, almost graphene-like carbon arrangement in the aromatic and aliphatic structures of the biochars [295]. There is no quantifiable influence of gas flowrate and residence time on the functional groups present in the samples. It can therefore be noted that temperature and feedstock continue to the be primary influence on biochar surface chemistry.

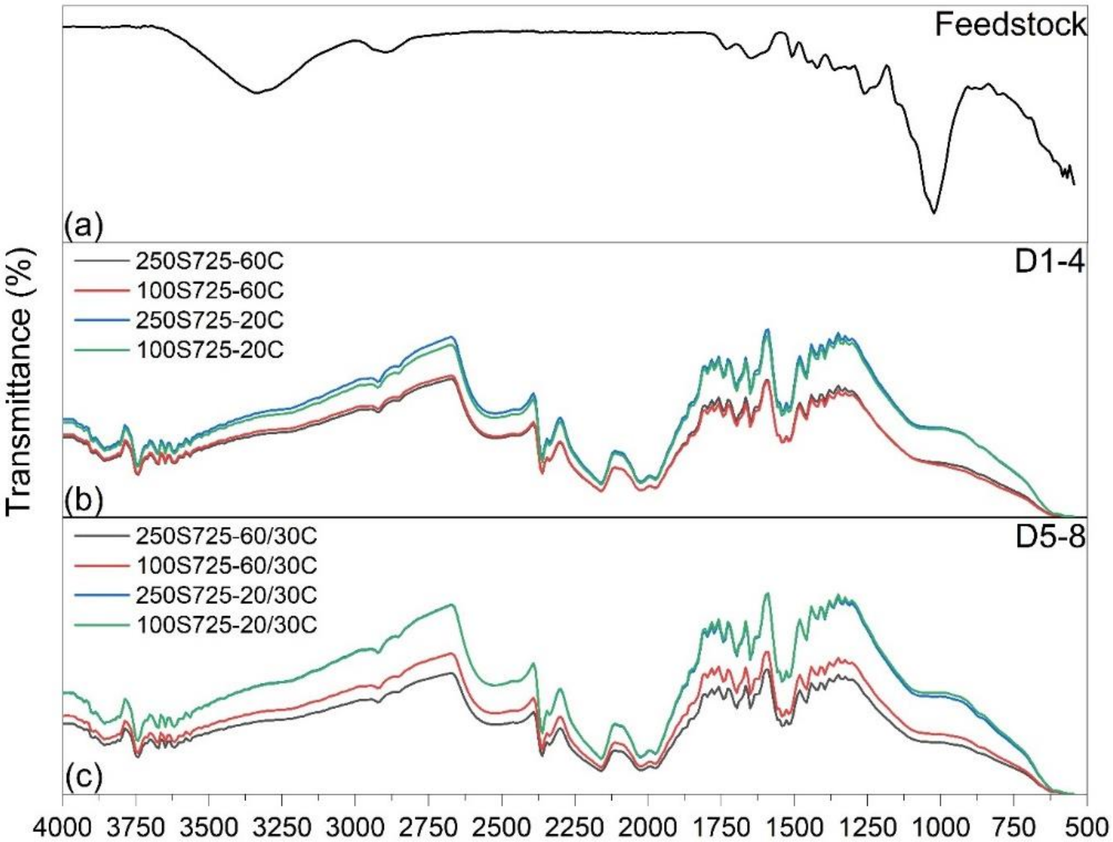

Figure 4:4 FTIR spectrum of (a) raw crushed softwood samples, (b) DoE biochars produced at ramp rate 15 °C/min; (c) DoE biochars produced at ramp rate 30 °C/min

4.4 Scanning Electron Microscopy

Scanning electron microscopy (SEM) of biochar samples was performed to examine surface structure and morphology. Surface imaging of biochars produced in this work was performed by clipping a small solid portion from the material and placing it into a Tungsten low-vacuum JEOL JSM-IT100 InTouchScope SEM. Images were captured at 10 µm with x1000 magnification. The beam current was kept constant at 35 with a voltage difference of 20 kV.

Figure 4:5a-d show the SEM images recorded for lower ramp rate biochars and e-g display the observations for higher ramp rate biochars. There is evidence of a well-developed pore network in biochars produced at low and high ramp rates. The images at 10 µm and 1000x magnification suggest that the high pyrolysis temperatures exposed the carbonaceous skeleton of the parent material encompassing an intricate network of pores [265]. A pyrolysis temperature that is sufficiently high is necessary for the removal of the outer biochar layer. The open structure of pores could be attributed to a lower ash content, which reduces the potential for clogging. There is no apparent evidence of influence from different ramp rates on the pore networks developed in the biochars.

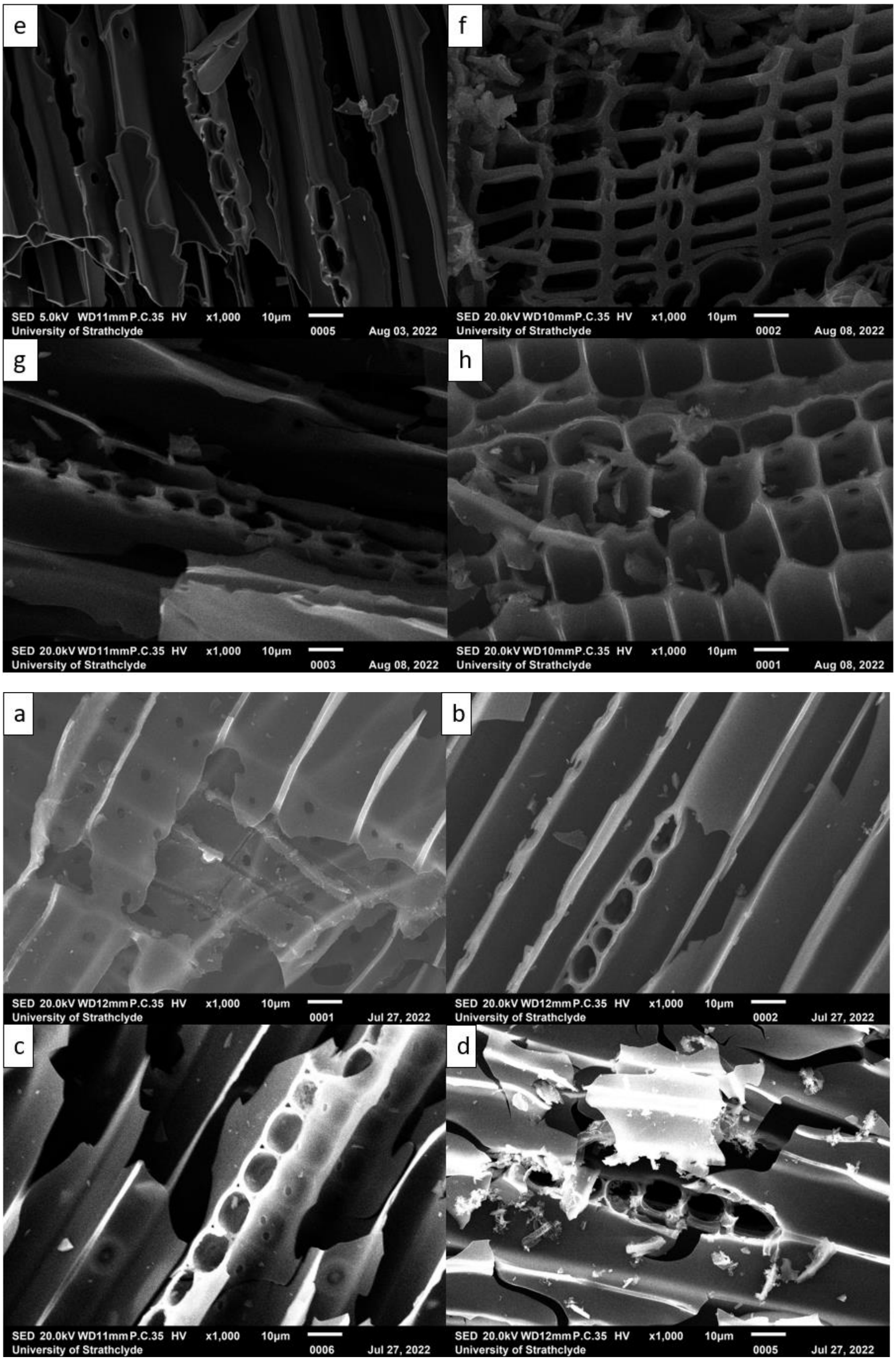

Figure 4:5 SEM images of DoE biochars (T = 725 °C). a-b: 60 min @ 15 °C/min; c-d: 20 min @ 15 °C/min; e-f: 60 min @ 30 °C/min; g-h: 20 min @ 30 °C/min

Figure 4:6 shows the SEM images of biochars produced using a mix of hardwood and softwood species at 450 °C at 100 µm magnification. The structures look similar to the ones observed in this work, suggesting the observations are related to the cell structure of the parent material.

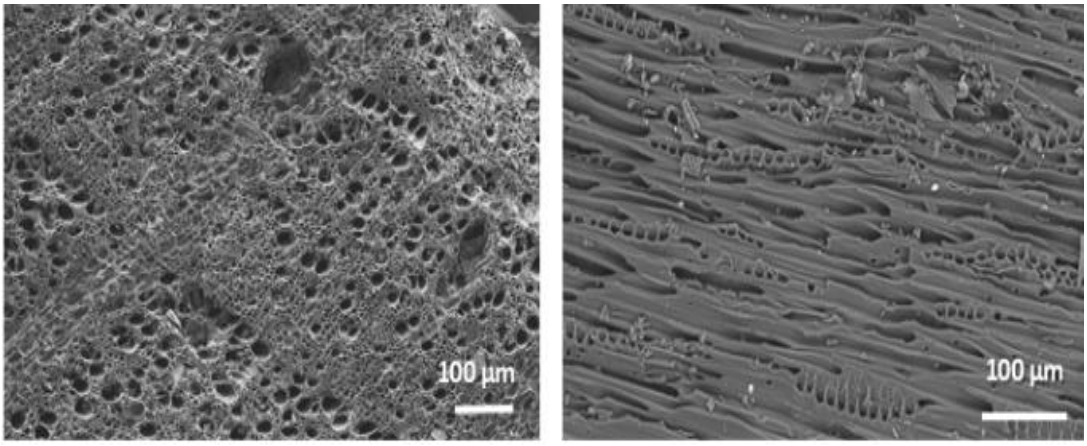

Figure 4:6 Comparative SEM images of softwood biochars pyrolysed at 450 °C for 36 hours. Species mix contains 80% softwood and 20% hardwood [296]

4.5 Summary

Examination of the wide range of results obtained for the chars produced within this study suggests significant correlation of biochar properties with parameters used within their production. Error! Reference source not found. provides comparative data for biochars produced from wood-based feedstocks reported in literature, detailing pyrolysis temperatures, surface areas and fixed carbon contents.

The surface areas of biochars reported in this study are higher than those produced at similar temperatures, as shown in the table. The amount of fixed carbon in wood-based chars appears to be consistent, at around 80%, which was also observed for the DoE biochars. Temperatures above 400 °C were reported to produce a recalcitrant structure resulting from the loss of volatile matter, as well as alkyl and carboxylic groups [297]. The statement further supplements the chemical moiety information obtained from FTIR analysis, suggesting a layered carbon structure. The concentric arrangement of pores in the carbonaceous skeleton is also visible in the SEM images. The following chapter presents the results obtained from the DoE runs and further characterisation of the biochar samples.

5. Biochar Optimisation and Minitab Outputs

Minitab was used to analyse the dataset obtained from the DoE runs and predict an optimised experimental run. Investigations into biochar wettability as well as point of zero charge were conducted to gauge the deployability of the sample in water remediation systems. XPS analysis was conducted to further investigate the observations from FTIR analysis and determine the atomic fractions on the biochar surface.

The results obtained from the screening experiments informed the choice of parameters for the DoE runs as well as the type of feedstock for optimisation. Softwood feedstock gave comparatively better results for yield and surface areas as opposed to the hardwood samples under similar operational parameters. There was no discernible influence noted from gas flow rate variation and hence the variable was removed from DoE parameter selection. The remaining criteria for the DoE experiments in reported in [3.2].

5.1 Porous Structure Characterisation

Table 5:1 shows the yield of produced biochars from DoE runs. In D1-4, temperature was fixed at 725 °C as an average between the two screening temperatures, and the ramp rate was kept at 15 °C/min. A contact time of 60 min, with both gas flowrates, gave an average yield of ~17.5 %. This yield was slightly improved when the contact time was reduced to 20 min, giving ~20 %. The ramp rate was increased to 30 °C/min for D5-8; combined with a high contact time, the yield was further reduced for runs 13 and 14 [257]. The high heating rate however did not seem to affect the yield with shorter residence times. The data suggests that temperature is the primary factor affecting the yield of biochars. There is a noticeable influence of contact time and ramp rate on the yield as previously suggested by the Minitab output, with no discernible influence from gas flow rate.

Table 5:1 Process conditions, yields and textural properties for biochars produced wood sample C

Exp	Sample code	CO_2 Flowrate (mL/min)	Temp (°C)	Contact time (min)	Biochar weight (g)	Yield (%)	Surface Area (m^2/g)	Micropore Volume (cm^3/g)	Total pore volume (cm^3/g)	Average pore width (nm)	Fixed carbon (%)	Volatile matter (%)
	Feedstock										20.3	79.7
	Ramp rate = **15°C/min**											
D1	250S725-60C	250	725	60	5.30	17.7	613	0.19	0.36	3	80.0	20.0
D2	100S725-60C	100	725	60	5.27	17.6	613	0.19	0.35	3	86.0	14.0
D3	250S725-20C	250	725	20	6.08	20.3	558	0.18	0.29	4	80.5	19.5
D4	100S725-20C	100	725	20	6.31	21.0	581	0.19	0.29	5	80.0	20.0
	Ramp rate = **30°C/min**											
D5	250S725-60/30C	250	725	60	4.40	14.7	613	0.19	0.37	5	77.3	22.7
D6	100S725-60/30C	100	725	60	3.65	12.2	553	0.18	0.43	4	73.4	26.6
D7	250S725-20/30C	250	725	20	6.08	20.3	544	0.18	0.27	4	85.1	14.9
D8	100S725-20/30C	100	725	20	6.07	20.2	544	0.17	0.28	4	83.5	16.5

Adsorption isotherms obtained for the DoE biochars presented in Figure 5:1 demonstrate a more prevalent Type II/IVa isotherm behaviour with initial high uptakes, followed by a plateau and a slight update at high relative pressure[158]. In general, the evidence of mesoporous nature is more prominent in pure softwood samples (Sample C) in the latter experiments.

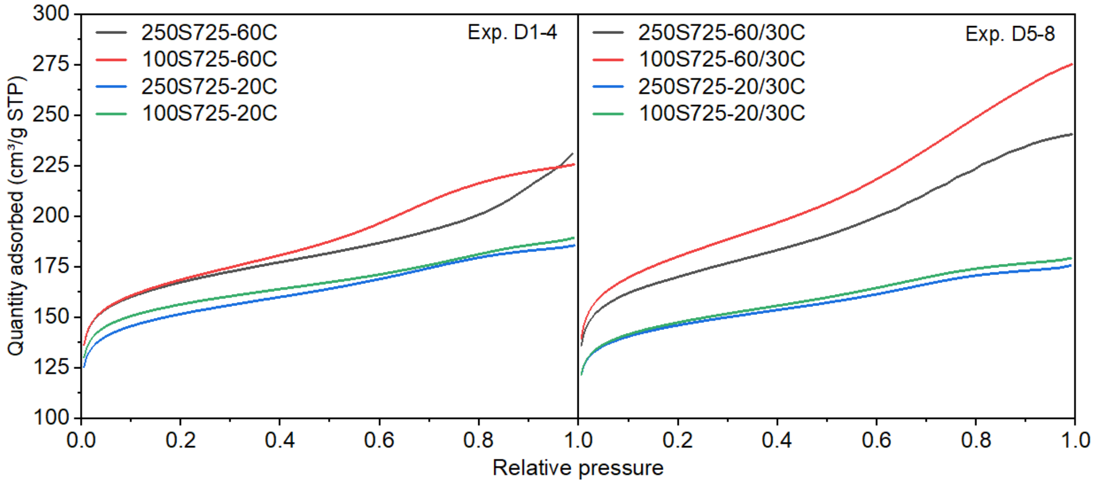

Figure 5:1 Adsorption isotherms obtained for biochars. Exp. D1-4: Showing results of N_2 adsorption on Sample C biochars at ramp rate 15 °C/min; Exp. D5-8: Showing results of N_2 adsorption on Sample C biochars at ramp rate 30 °C /min.

On average, DoE pyrolysis runs performed at 725 °C produced biochars with higher surface areas. The intermediate temperatures also offered a reasonable trade-off between biochar yield and surface areas. At lower ramp rates, for Experiments D1 and D2, obtained surface areas were equal, showing no influence of the gas flow rate at a 60 min residence time. For a shorter residence time however, a higher gas flow rate reduced the surface area of the biochar. The observations were different for DoE runs at a ramp rate of 30 °C/min. At higher ramp up rates, high gas flow rates with longer hold periods in the furnace (Experiment D5) produced the highest surface area biochar. Reducing the gas flow rate or the contact time at this ramp rate resulted in a decrease in surface areas if the samples compensated however, with an increase in yield.

For DoE runs, high gas flowrate and residence time can be inferred to be directly proportional to surface area. A reduction in $V_{micropore}/V_{total}$ ratio of these samples also suggests a more openly porous structure [236]. The highest biochar surface areas obtained for 100% softwood chars were higher than other wood based biochars reported in the literature [218,251,295].

5.2 Regression Analysis

The regression equations for the two responses, yield (Y1) and surface area (Y2) are shown below in Equation 19 and 20, respectively. For analysis of the factorial design, a stepwise method was used, which works by combining forward selection and backward elimination procedures. The forward selection approach determines the variables to retain in a model. In forward selection, the added variable is never removed. by contrast, the backward elimination procedure removes terms from the initial model that have the smallest adjusted sum of squares. Determining whether a variable is added or removed from the model is based on the 'Alpha to enter' and 'Alpha to remove' value. If the p-value of a variable is less than the 'Alpha to enter' value, it is retained in the model and vice versa. In this study, both Alpha values were set to 0.15, which is the system default.

$$\text{Yield (Y1)} = 6.20 + 0.0058\,A + 0.0300\,C - 0.001900\,AC \qquad \text{Equation 19}$$

$$\text{Surface area (Y2)} = 577.8 + 1.031\,A - 1.85\,C \qquad \text{Equation 20}$$

where, A is contact time (min), and C is ramp rate (°C/min). Note that variable B (gas flowrate) was not found to be significant. The coefficient of determination (R2) for Equations 19 and 20 were equal to 0.95 and 0.70, respectively. The values indicate that the model can explain over 95% and 70% of variability in the responses of yield and surface area, respectively. The model also suggests that there is no notable variation in the obtained responses arising from changes in flow rate of the activating gas.

Equations 19 and 20 are of crucial importance from a scaling up perspective or while coordinating with industrial partners as they predict the expected outcome of the chosen responses based on the conditions used in the DoE and the type of feedstock.

The equations predict the relationship between the input variables and the output, taking into account the influence of relevant parameters. They can also assist with supply chain management and quality assurance by analysing the relationships between the variables and experimental outcomes.

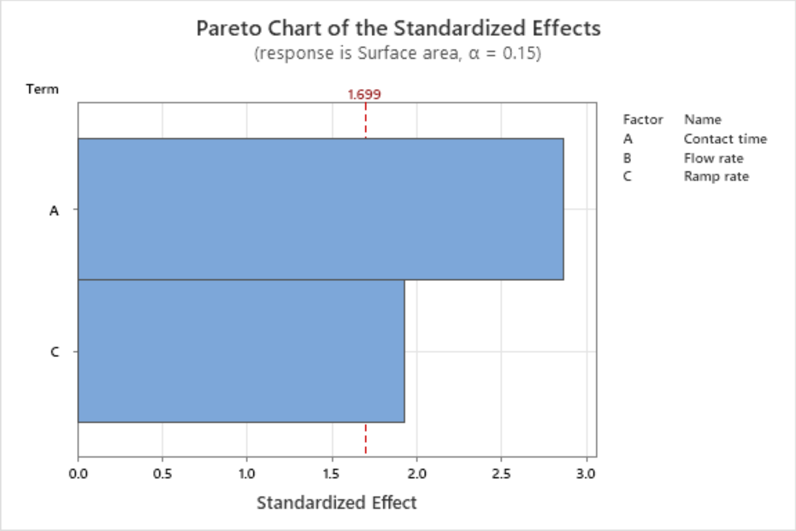

Figure 5:2 Pareto Chart for variable effects on Surface Area showing significant influence of contact time and heating ramp rate

Figure 5:2 and Figure 5:3 show the Pareto Chart of standardised effects of variables on the surface and yield respectively.

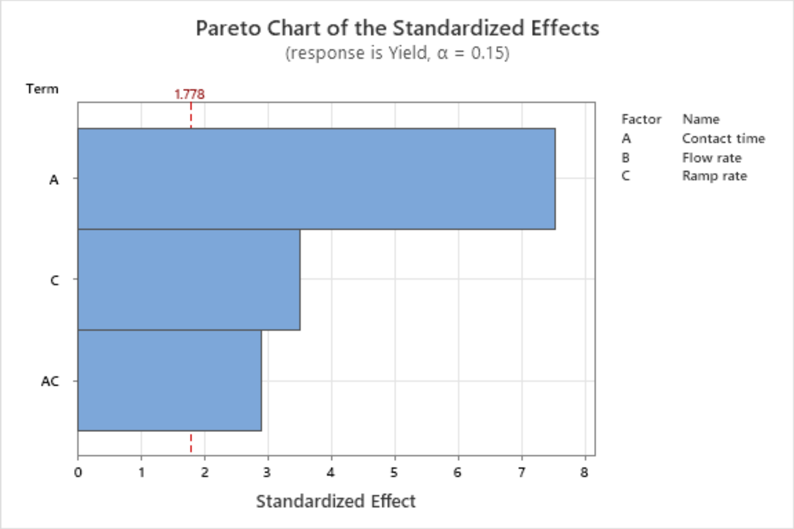

Figure 5:3 Pareto Chart for variable effects on Yield showing significant influence of contact time, ramp rate & interaction effects between contact time and ramp rate

5.3 Analysis of Variance

Statistical analysis of the input variables i.e., contact time, flow rate and ramp rate were performed to identify single or interaction effects on chosen responses. One way of checking the adequacy of the model uses the p-values and the F-values from the analysis of variance (ANOVA) table generated in Minitab.

Table 5:2 Analysis of variance results for yield and surface area showing F, p-values and adjusted mean squares. Note the p-value for surface area shows no significance of ramp rate with high p-value which does not correlate with the Pareto charts

Yield					
Source	**DF**	**Adj SS**	**Adj MS**	***F-Value***	***p-Value***
Model	3	5.9828	1.99427	25.88	0.004
Linear	2	5.3330	2.66650	34.61	0.003
Contact time	1	4.3808	4.38080	56.86	0.002
Ramp rate	1	0.9522	0.95220	12.36	0.025
2-Way Interactions	1	0.6498	0.64980	8.43	0.044
Contact time*Ramp rate	1	0.6498	0.64980	8.43	0.044
Error	4	0.3082	0.07705		
Total	7	6.2910			
Surface Area					
Source	**DF**	**Adj SS**	**Adj MS**	***F-Value***	***p-Value***
Model	2	4943	2471.6	5.96	0.048
Linear	2	4943	2471.6	5.96	0.048
Contact time	1	3403	3403.1	8.20	0.035
Ramp rate	1	1540	1540.1	3.71	0.112
Error	5	2075	414.9		
Total	7	7018			

The data generated for yield and surface area is reported in Table 5:2. For a model to be significant, its p-value should be less than the significance level (0.05 for a 95% confidence interval in this case) and it should have a high F-value [298]. In both cases, the p-value for the model is <0.05, indicating the models are significant, the model for yield being considerably more accurate compared to the regression for surface area. It can be seen from the table that contact time and ramp rate have determining effects on yield, with contact time in the furnace being the primary influencing factor with an *F-value* of 56.7. There is also a noticeable two-way interaction between contact time and heating ramp rate on yield. The model also suggests no influence of the gas flow rate on biochar yield. For biochar surface area, contact time alone was predicted to be the influencing variable. The ramp rate *p-value* was >0.05 suggesting that is not a significant variable in surface area determination. No influence of gas flow rate was predicted on surface area. Despite the ANOVA prediction, the Pareto chart obtained for surface area, suggests noticeable influence from ramp rate manipulation. This discrepancy could be attributed to the reduced accuracy of the model (~70%). Additional runs incorporating centre points could possibly improve the prediction of the model provided the error originates from the lack of data for a more accurate model. The ANOVA could also be influenced by the presence of outliers that can have a substantial impact on the model prediction.

5.4 Response Optimisation

Based on the consideration of the model being statistically significant for both yield and surface area, an optimised response was generated using Minitab with the goal of maximising both selected responses. The suggested solution from Minitab included a contact time of 60 min and a ramp rate of 15 °C/min, with no specified value for the gas flow rate, resulting in a surface area of 612 m^2/g and a yield of 5.3 g. The generated solution had a desirability of 78%. The suggested solution was already a part of Experiments D1 and D2, both run with a contact time of 60 min and ramp rate of 15 °C/min, with varying flow rates. The observed experimental values for surface area in both cases was 613 m^2/g. In addition, the yield for the two runs was approximately 5.3 g for both runs, which correlates closely to the theoretical predictions. Despite the close relation between theoretical and experimentally obtained data, the low accuracy of the surface area regression presents the need for further analysis of parameter influence on biochar characteristics. The model could be improved by running centre points, however, there is a need to minimise experimental runs to prevent resource utilisation and supplement the idea of sustainability.

The next chapter focusses on the characterisation of biochars obtained from the DoE study as well as further characterisation of the optimised biochar sample prior usage in the adsorption experiments for water remediation.

6. DoE Biochar Characterisation and Adsorption Experiments

6.1 Proximate Analysis

To evaluate the thermal stability of biochar samples, thermogravimetric analysis (TGA) was performed. TGA calculations can be performed either using thermographs or the tabular data generated by the software and using predefined standards. In this work, the technique employed [299] for proximate analysis closely follows that outlined in British Standard BS1016. Analysis was performed using a NETZSCH STA 449 F3 Jupiter system (LoD = 0.1 μg). Approximately 5-10 mg of crushed sample was placed in a Al_2O_3 crucible. The crucible was initially tared under a nitrogen gas flow of 50 mL/min, and the mass allowed to stabilise under the same gas flowrate, before the initial mass was recorded. The sample was heated to 120 °C and allowed to stabilise, which removes any water within the material. The subsequent crucible mass was recorded, before the temperature was increased to 920 °C, and held for 3 min, after which time the mass reading was recorded again. Finally, the sample temperature was reduced to 820 °C, and the gas flow switched to 50 mL/min of pressurised air. The crucible mass was allowed to stabilise, and the value recorded, before the system was allowed to cool fully, and a final mass reading was taken at ambient temperature.

The dry ash compositions of the feedstock and DoE biochars obtained from thermogravimetric analysis are reported in Table 5:1. The samples were treated on a dry basis to remove variability from moisture content, and on an ash-free basis due to variability in inorganic forms from the natural precursor. Temperatures above 400 °C are needed to eliminate methyl ($-CH_3$) and carbonyl (C-O-C) structures. Higher temperatures result in the cracking and elimination of aliphatic structures, which reduces the diversification of the present carbon structures. Aromatic structures require higher activation energy than aliphatic structures for thermal cracking [300].

A high gas flowrate in Experiment D1 resulted in a fixed carbon percentage of 80% and a volatile matter content of 20%. This was a significant increase from the fixed carbon content of 20.3% in the feedstock. Similar observations of increasing fixed carbon content with temperature in biochars derived from Platane wood and water oak were reported in literature [300,301]. For Experiment D2, under a much lower gas flowrate, the carbon content was increased to 86% and volatiles reduced to 14%. The higher gas flowrate appears to have potentially decreased the temperature of the sample and affected the release of volatile matter as suggested previously [215,216]. For Experiments D3 and D4, with shorter residence time, gas flowrates did not have a considerable impact on fixed carbon and volatile fractions. High heating rates combined with longer residence times, result in accumulation of volatile matter [217]. The results obtained in D5 and D6 support this statement, with carbon percentages below 80 and higher volatile content, as opposed to their lower ramp rate counterparts. With a shorter hold period (D7 and D8), the percentages of volatiles reduced significantly and a positive effect on fixed carbon content was also noted. Residence time was observed to be the key driver for fixed carbon and volatiles, with the fluctuations arising from variable gas flowrates being almost negligible. The results indicate that a higher ramp rate combined with a short residence time has the potential to produce biochars with high fixed carbon content and the lowest fraction of volatiles, albeit with a significant loss in yield.

6.2 Contact Angle Measurement

Sessile drop method [302] was used to determine the contact angle between the biochar surface and a water drop. Biochar samples were crushed, and a small amount of powder was placed on a microscopic glass slide. The lump was then smoothed by placing another slide on top which was removed before taking measurements. Analysis was performed on a Krüss Scientific Drop Shape Analyser DSA25B (LoD = 0.1°). To measure the contact angle, a small droplet of water (~0.5 mL) was dropped onto the sample from a height less than 1 cm, and photographs were taken at intervals of 1, 2 and 3 seconds using Krüss Advance software.

Biochar wettability is a parameter that can be evaluated through contact angle (CA) measurement [303]. Figure 6:1(a) shows water droplet on a clear glass slide and

Figure 6:1(b) shows a similar water droplet on a biochar film. Both images were taken 2 seconds after water contact. The absorption of water by prepared biochars was seemingly immediate, indicating hydrophilicity and high wettability [303]. Low CA (typically <90°) are achieved in cases where water shows greater affinity to the solid surface [304]. The mechanism for this interaction could potentially be the formation of surface hydrogen bonds and the domination of adhesion forces over repulsive ones. This stabilisation of forces allows water to penetrate porous materials and wet larger surface areas [303]. This observed wettability in the case of the optimised sample (as well as the DoE biochars tested for wettability) suggests a feasible application in drinking water treatment systems, allowing larger available surface areas for interaction between dissolved target species in water.

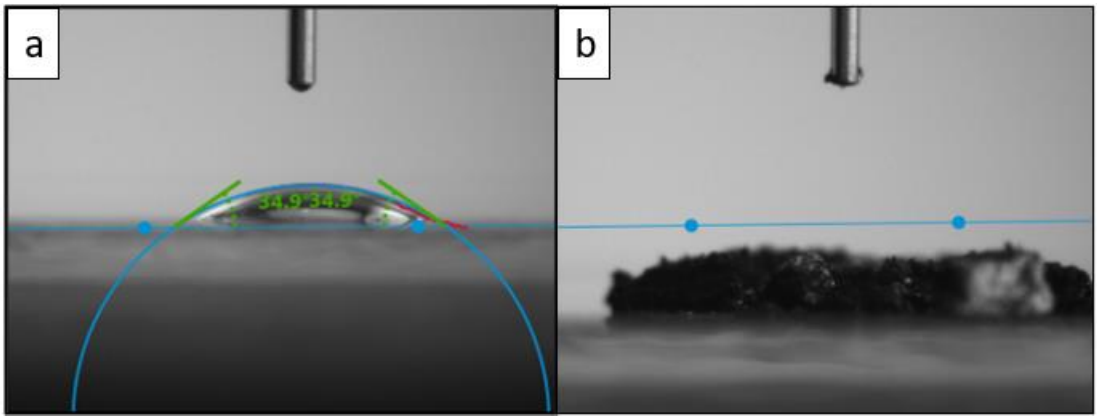

Figure 6:1 Contact angle measurement (a) Water droplet on clear glass slide; (b) Water droplet on biochar sample. Images taken 2 seconds after water drop

6.3 Density Analysis

Density analysis was performed at the National Physics Laboratory (NPL) in Glasgow, Scotland using Helium pycnometry. The equipment used was a helium pycnometer manufactured by Micrometrics, a fine mass balance manufactured by Sartorius, a helium gas cylinder to supply the pycnometer, a capsule with sintered lid provided with the pycnometer to house the sample during analysis, a pair of tweezers and a small soft brush. The computer software provided for the pycnometer was AccuPyc II version 3.00. The pycnometer works by housing and sealing the sample within the capsule of known volume inside the instrument and admitting helium gas into the instrument, which is then allowed to expand into another compartment of known volume within. The gas pressure is measured before and after the expansion is measured, which is in turn used to calculate the sample volume by the amount of gas displaced. The sample mass, which is measured prior to insertion of the sample into the pycnometer, is then divided by the calculated sample displacement volume to work out the sample's density.

The capsule within the pycnometer was cleaned inside and outside with the soft brush provided, placed on the mass balance, and tared to allow for only the mass of the sample to be measured. The capsule was then removed from the balance and the sample was removed from the bag and into the capsule with the tweezers provided or poured in if the sample was in a granular state. The capsule with the sample inside was then weighed on the balance and the mass of the sample was recorded on the spreadsheet and software provided. The capsule was then transferred into the pycnometer where a bayonet cap on the instrument was closed to seal the capsule within so that analysis could begin, using the software to start the analysing process.

The pycnometer initially purges helium in and out of the system ten times to displace any unwanted gas within. After this, the pycnometer begins the calibration process in which helium is let into the chamber and the pressure allowed to stabilise. Since the density and pressure of the helium is known, this allows for the density of the sample to be accurately determined. This cycle repeats itself ten times so an average density, volume, temperature and standard deviations on density and volume can be calculated with each sample. This can be viewed within the program on request. Once a cycle series was complete, the calibration was repeated a second time by setting the pycnometer running again via the software, using the same starting parameters.

Once the whole calibration was complete, the bayonet cap on the pycnometer was removed and the capsule taken out to be re-weighed on the balance to determine the final mass of the sample that was recorded on the spreadsheet.

Table 6:1 shows the results of density analysis of biochars. Density measurements are crucial in understanding the behaviour of biochars upon encountering soil or water as it can influence its mobility and transport within the system. For example, biochars with densities less than 1 g/cm^3 will float in water [305]. As skeletal density measurements exclude void and pore space, the value is often referred to as true or particle density [306]. The measurements are more consistent as sample packing or particle size have no theoretical influence on the final result [307]. The lower ramp rate biochars in this work had a slightly higher skeletal density than biochars produced at a higher ramp rate. Similar skeletal density values were obtained for mesquite wood biochars pyrolysed at 700 °C [307]. The skeletal densities observed in this study are higher than the skeletal density of glucose (1.54 g/cm^3) and can be attributed to a more complete pyrolysis and gradual condensation of the carbon structure [307].

Table 6:1 Skeletal densities of DoE biochars measured using Helium pycnometry

Biochar	D1	D2	D3	D4	D5	D6	D7	D8
Skeletal density (g/cm^3)	1.76	1.76	1.75	1.70	1.72	1.73	1.72	1.68

The same principle can be applied to biochars produced from a similar feedstock. For instance, skeletal density of D1 biochar was higher than sample D4. Biochar D1 has a higher skeletal density due to a longer residence time in the muffle furnace resulting in a more complete pyrolysis and better carbonisation. The same principle is applicable to D5 with a skeletal density of 1.72 g/cm^3 with a 60 min contact time compared to 1.68 g/cm^3 skeletal density of D8 that had a 20 min contact time with the furnace [308].

6.4 Point of Zero Charge

Salt addition method was used to perform point of zero charge (PZC) analysis [309]. A 40 mL aliquot of 0.1M $NaNO_3$ was adjusted to five pH values between 3 and 11. Solutions of 0.1M NaOH and 0.1M HCl were used to attain the desired pH. Powdered biochar (~0.2 g) was added to the beakers and agitated at 450 rpm for 24 h. The final solution was filtered and the pH of the permeate was measured. The difference between the initial and final pH values of the samples was calculated and the change in pH versus initial value was plotted to identify the PZC.

The PZC of the optimised sample as well as three other DoE biochars is shown in Table 6:2**.** The surface charge of chars produced under different operating conditions appears to be more dependent on material origin and surface functional groups, as opposed to chosen DoE variables. Pyrolysis temperatures also influence the pH of wood-based biochars. High temperatures result in the loss of not only volatile matter but also acidic functional groups i.e., phenols and carboxylic, thereby resulting in more alkaline surface charges [310]. For example, slow pyrolysis treatment of wood-based pellets at 200°C produced biochars with pH 4.6. Upon increasing the temperature to 600°C, the resulting biochar had a pH of 9.5 [311]. A similar observation on wood chip biochars pyrolysed at 500°C was made with biochars having a pH (H_2O) of 8.58±0.01 [312]. The average PZC of the samples in this study was 7.40 ± 0.02, indicating potential application of these biochars to drinking water treatment systems without considerable pH alternation to target anionic species from effluents and treatment systems, or for cationic species by slightly reducing the system pH [310].

Table 6:2 Point of zero charge of biochars created as part of a design of experiments approach (OS – Optimised sample)

Sample	100S725-20C **(OS)**	100S725-60C	250S725-20C	250S725-60C
PZC	7.47	7.31	7.38	7.44

6.5 X-Ray Photoelectron Spectroscopy

X-ray Photoelectron Spectroscopy (XPS) analysis provides quantitative measurements of the atomic fractions within a material. XPS analysis was performed by the NEXUS facility at Newcastle University. The biochar sample was crushed to a powdered form and analysed using a K-Alpha Photoelectron Spectrometer (Thermo Fisher) and electron detection using a hemispherical analyser. Measurements were taken with the flood gun on to lower charging with the beam energy at 40 eV and a step-size of 0.05 eV. The generated results were analysed using the Fityk program.

The XPS plots of the optimised biochar sample used are shown in Figure 6:2. The spectra show the presence of oxygen and nitrogen bonds, in addition to carbon with peaks at 532.5, 400 and 284.5 eV, respectively [313]. Peak deconvolution was achieved using the Fityk program, and the Voigt function assisted in the identification of the heteroatoms present in the biochar. The corresponding parameters are provided in Appendix B: XPS Peak Convolution Data. C1s peaks were deconvoluted into three peaks at 284.5 eV, suggesting a graphene like arrangement (C=C), at 285.6 eV indicating the presence of carbonyl bonds (C-O), and a third peak at 289.6 eV, which is ascribed to either carboxylic or pyridinic N bond functionalities (C=O/C-N) [314–317]. The area under the C=C peak is the largest indicating the preservation of the graphene-like arrangement in the wood samples post-pyrolysis. Peak convolution of O1s showed the presence of both carbonyl, as well as carboxyl groups, with peaks at 531.1 and 532.9 eV [317,318]. There were also trace amounts of nitrogen functionalities present in the sample and convolution of the N1s spectra suggested the presence of pyridinic (398.6 eV) as well as graphene N (400.2 eV) bonds in the sample [319]. The incorporation of O and N-based functional groups into the carbon framework enhances its wettability [313], which is further correlated with contact angle measurement presented in previous work [320]6], where biochar samples proved to be extremely hydrophilic. The calculation of the elemental compositions of C, N and O were performed as suggested by Alexander G. Shard [321]. Equation 21 works under the assumption that the sample is homogenous and a single phase within the penetration depth; where X represents the atomic fraction (in %), and I_P/S_P is the intensity divided by the sensitivity factor (S_P = 1, 1.8 and 2.93 for C, N and O respectively).

$$X = \frac{I_P/S_P}{\sum_j I_j/S_j} \qquad \text{Equation 21}$$

The biochar sample used consisted of 80% C, 13% O and 7% N fractions. The findings again supplement the results obtained in the previous reported study, where thermogravimetric analysis of the samples showed 80% fixed C [320].

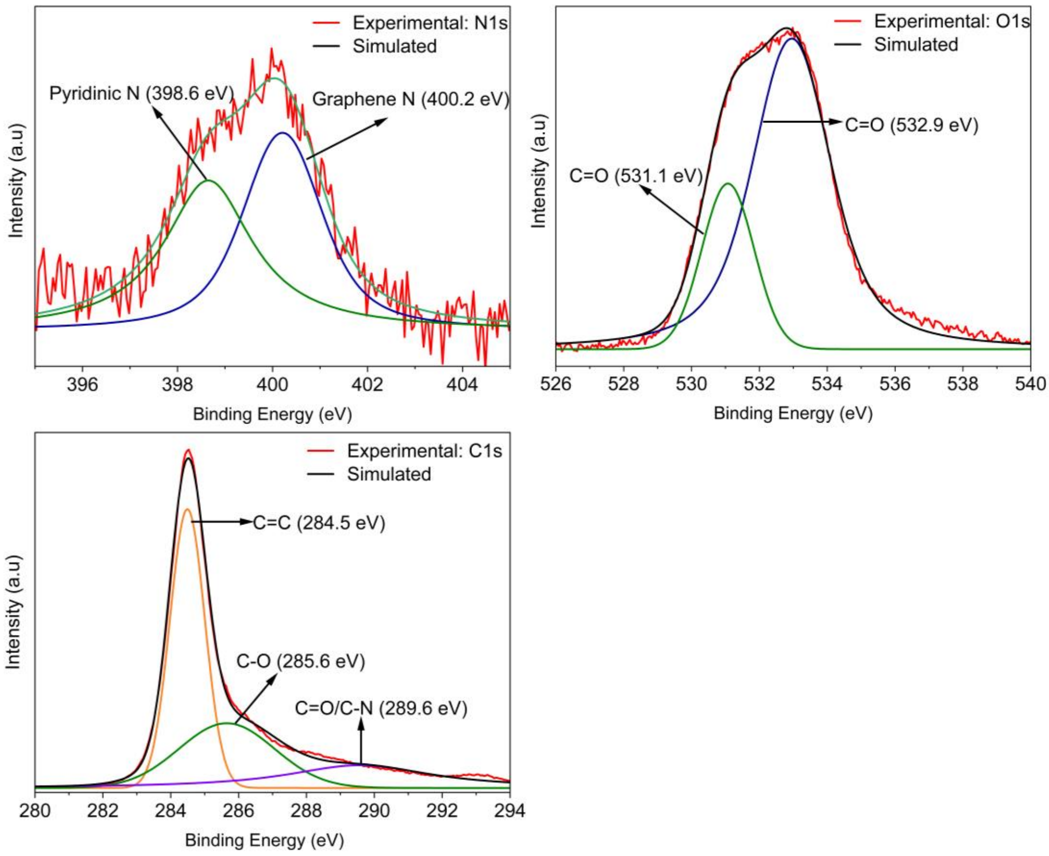

Figure 6:2 XPS spectra and Fityk simulated models showing N1s, O1s and C1s scans. Fityk models suggest possibilities of existing functional groups at specific binding energies that can be compared with the NIST database

6.6 Summary

The results presented above suggest the optimised conditions for biochar production from Scottish softwood samples. The analysis of the optimised sample shows large surface areas and a mixed microporous-mesoporous structure, as observed from the nitrogen isotherms. Higher temperatures are linked with increased alkalinity of biochars [310]. The optimised sample and selected DoE biochars in this work were determined to have an average PZC of 7.40 ± 0.02. In addition to a neutral pH, contact angle analysis of the biochar suggested hydrophilic character. Rattanakam *et al.* [322]

investigated the difference in hydrophilicity of oxidised and un-oxidised wood based biochars, reporting an increase in the hydrophilic behaviour of oxidised biochars. Fir wood derived biochars for perchlorate adsorption were contrastingly reported to provide a hydrophobic environment, as opposed to the hydrophilic biochars produced in this work [246]. FTIR analysis suggested a layered carbon structure with the presence of oxygen and nitrogen chemical moieties. These findings were further assisted by XPS analysis presenting a graphene-like arrangement, and 80% atomic carbon fraction. Additionally, the presence of oxygen and nitrogen-based functionalities was confirmed from XPS data. These chemical moieties assist the hydrophilic nature of the biochar and provide a potential avenue for application in water remediation.

7. Adsorption Experiments

The removal of identified persistent organic pollutants via adsorption was investigated on the 'optimised' sample suggested by Minitab and the DoE analysis. The chosen biochar sample was synthesis at 725 °C with a 60 min contact time in the furnace at a heating rate of 15 °C/min. As the gas rate was shown to have no significance on final characteristics, it was kept at 250 mL/min for replica samples.

7.1 Adsorption Isotherms

Adsorption isotherms are of crucial importance in determining the maximum adsorption capacity of the adsorbent and understanding the adsorption equilibrium. The isotherm plots for the target species are show in Figure 7:1 and the fitting parameters for Langmuir, Freundlich and Sips models are given in Table 7:1.

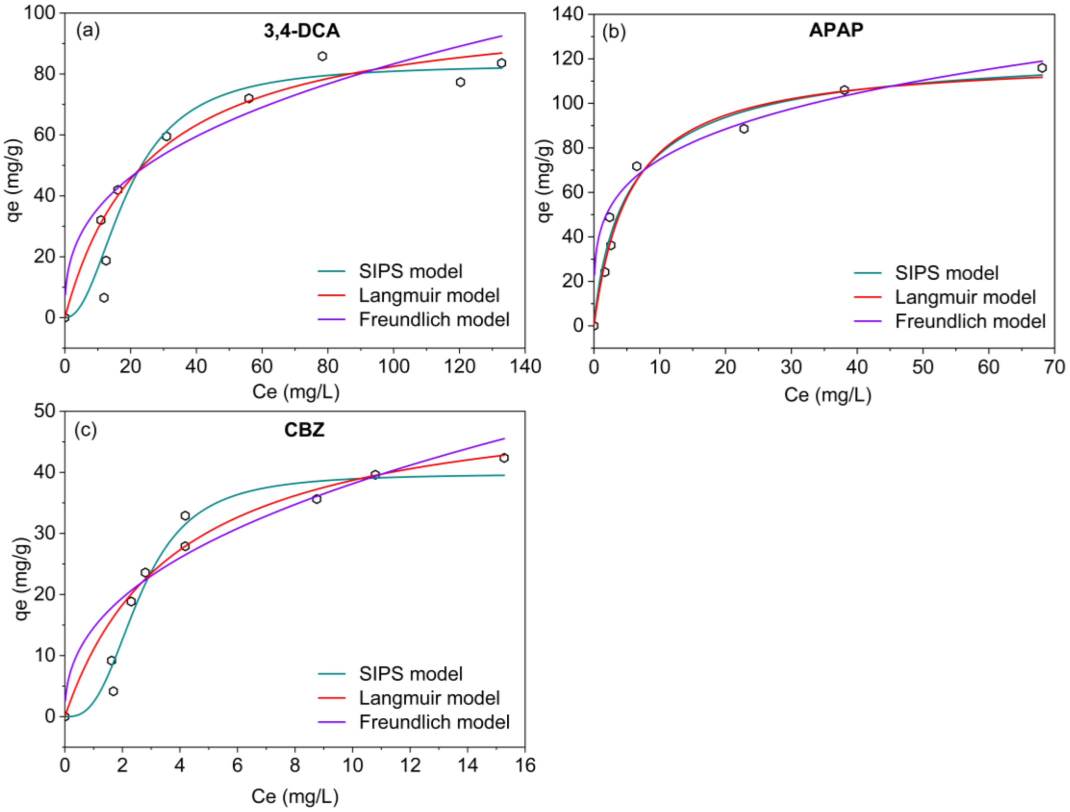

Figure 7:1 Adsorption isotherm models showing non-linear fits for (a) 3,4-DCA; (b) Acetaminophen and (c) Carbamazepine

The results indicate that the adsorption uptake was significant at low pollutant concentrations. The data presented in Table 7:1 suggests that for CBZ and 3,4-DCA, the Sips model can be best used to describe the adsorption behaviour. This suggests that the adsorption process is a combination of physisorption at low concentrations and chemisorption at high initial C_o values with the formation of a monolayer on the adsorbent material. The maximum adsorption capacities for CBZ and 3,4-DCA, suggested by the Sips model, were 39.8 mg/g and 83.2 mg/g respectively. For APAP, both Langmuir and SIPS isotherm models demonstrated high R^2 values. A good fit to the Langmuir model assumes monolayer adsorption of the molecules on the biochar surface, with almost identical activation energies, albeit with the possibility of multilayer formation [323]. The maximum adsorption capacity for APAP is determined as 126 mg/g, much higher than the other two species, which may be reduced as a consequence of molecular size affecting packing in the case of CBZ and electrostatic repulsion in the case of 3,4-DCA. Since the two models exhibited a good fit to the experimental data for APAP, the value of the separation factor (R_L) suggested by Webber and Chakkravorti [324] was calculated to further verify the favourability of the Langmuir adsorption isotherm (Appendix C: Langmuir Separation Factor and Linear PSO Plots). The separation factor is determined from Equation 22:

$$R_L = \frac{1}{1 + K_L C_O} \qquad \text{Equation 22}$$

The value for R_L was >1 for all C_o values suggesting unfavourable adsorption [164]. However, this could also be attributed to the limitations of the model assumptions, including homogenous adsorption sites and identical adsorption energies. The model is also limited to the assumption of monolayer adsorption, which can be overcome by the Sips model, which includes the possibility of multilayer formation. To conclude, APAP adsorption on the biochar surface is better represented by the Sips model.

Table 7:1 Adsorption isotherm parameters obtained for acetaminophen (APAP), carbamazepine (CBZ) and 3,4-Dicholoroaniline (3,4-DCA) on the optimised sample

Isotherm Parameters	**APAP**	**CBZ**	**3,4-DCA**
Langmuir			
R^2 (COD)	0.976	0.907	0.905
R^2 adj.	0.972	0.895	0.893
q_m (mg/g)	118.9±5.910	59.84±9.694	110.9±15.36
K_L (L/mg)	0.204±0.036	0.182±0.065	0.028±0.010
Freundlich			
R^2 (COD)	0.929	0.801	0.797
R^2 adj.	0.915	0.772	0.769
q_m (mg/g)	32.62±4.966	11.77±2.679	9.771±4.409
K_F ($L^{1/n}mg^{1-1/n}/g$)	0.313±0.044	0.503±0.106	0.456±0.104
SIPS			
R^2 (COD)	0.977	0.968	0.939
R^2 adj.	0.967	0.959	0.922
q_m (mg/g)	126.2±19.81	39.77±2.105	83.20±7.025
K_S ($L^{ns}\cdot mg^{-ns}$)	0.214±0.046	0.065±0.032	0.002±0.003

To further investigate the nature of the adsorption sites, Scatchard plots were obtained from the adsorption data. The theory behind the analysis and the Scatchard equation are explained in Adsorption Isotherm Models.

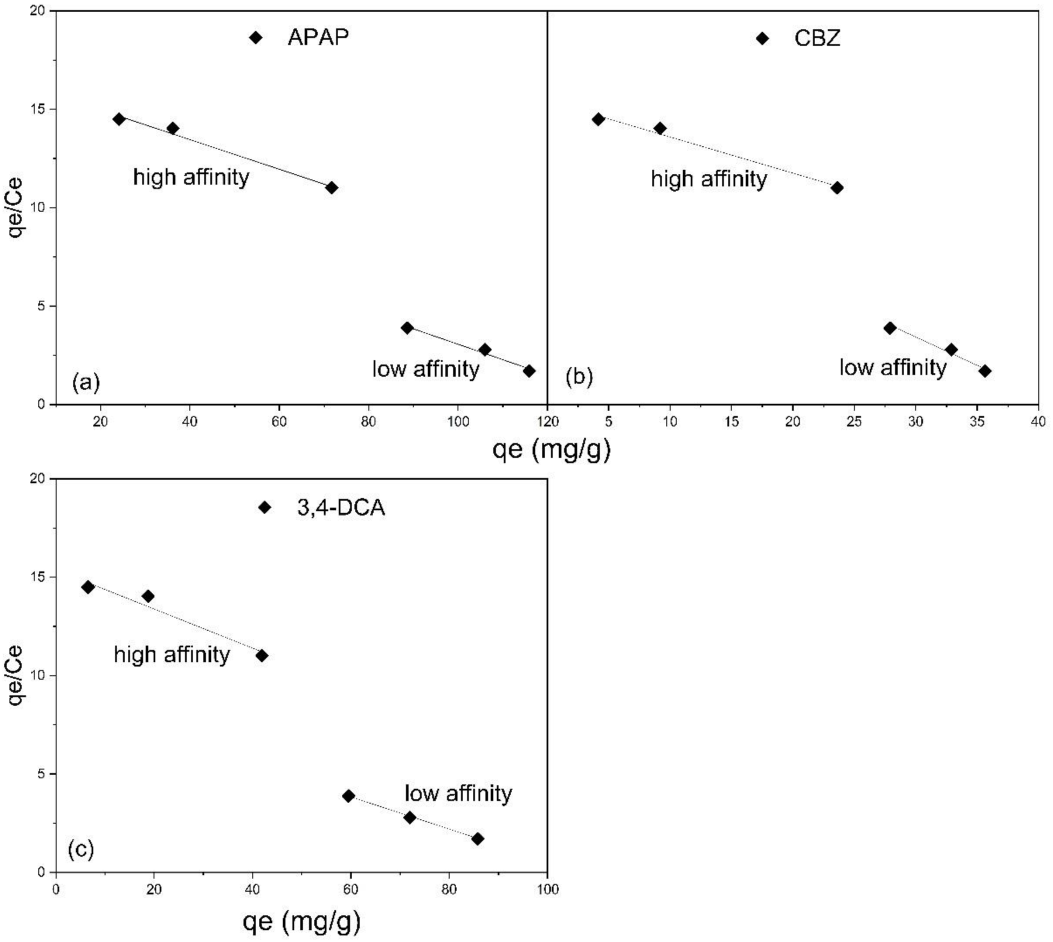

Figure 7:2 Scatchard plots for (a) APAP, (b) CBZ and (c) 3,4-DCA to determine the nature of binding sites on the biochar surface. Graph shows clear distinction between affinity zones suggesting heterogeneous surface

Figure 7:2 shows the Scatchard plots obtained for the adsorption of target species. It is evident from the plots that the adsorption behaviour deviates from linearity. The high and low binding affinities can be attributed to the presence of more than one type of binding sites, offering strong and weak interactions respectively. The high affinity binding sites can be attributed to chemical interactions between the biochar surface and the target compounds whereas the low affinity sites indicate weak physical bonds. The plots further supplement the observations from Sips isotherm indicating a heterogeneous material with multiple binding sites.

7.2 Adsorption Kinetics

The analysis of experimental kinetic data was performed using Pseudo First Order (PFO), Pseudo Second Order (PSO) and Intra-Particle diffusion (IPD) models. These models have been frequently employed to investigate pollutant removal of persistent organic pollutants from aqueous systems [41,79,115].

Figure 7:3 shows the kinetic data obtained for the sorption of CBZ and APAP on the biochar sample. Sorption kinetics for APAP showed rapid uptake with 90% removal achieved in 15 min followed by a gradual increase in the uptake, and equilibrium achieved after approximately 2 hours. For CBZ, the uptake was slower with just under 75% removal at 15 min and adsorption slowed considerably after 2 hours, with equilibrium achieved after 24 hours. For CBZ, the uptake was slower with just under 75% removal at 15 min and adsorption slowed considerably after 2 hours, with equilibrium achieved after 24 hours.

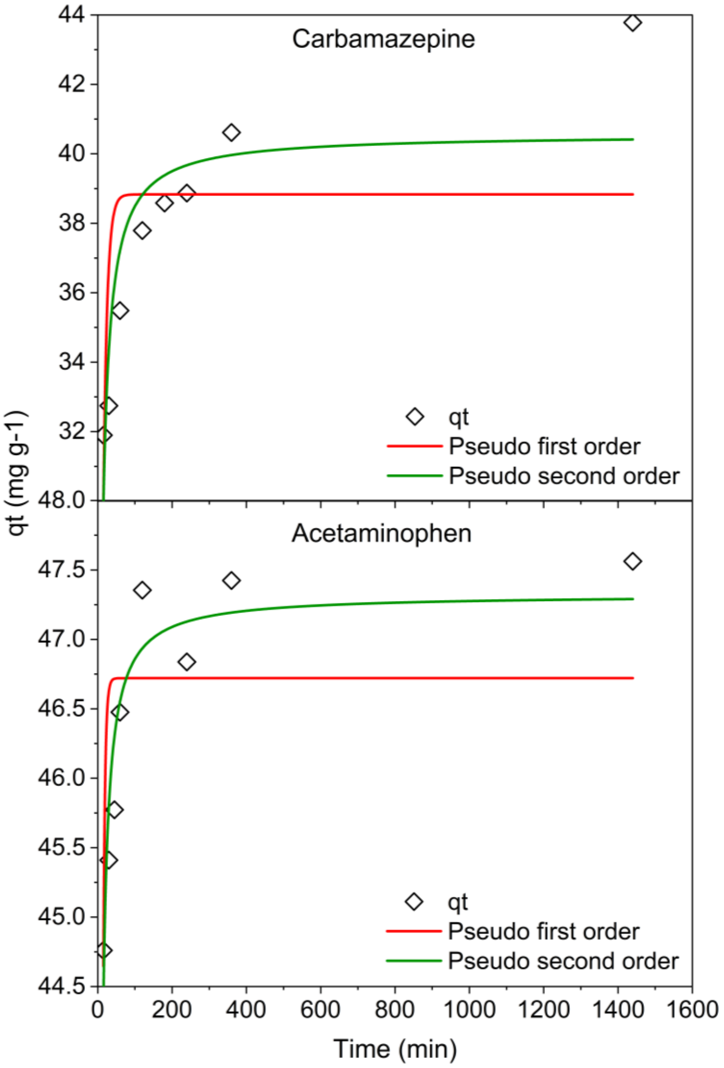

Figure 7:3 Non-linear kinetic model fittings for (top) carbamazepine and (bottom) acetaminophen on the optimised biochar showing fits for pseudo first order and pseudo second order models

Table 7:2 shows the parameters of kinetic models fitted to the data obtained for adsorption of APAP and CBZ onto the optimised biochar. Kinetic analysis of 3,4-DCA revealed fast adsorption rates, which could not be fitted to any kinetic models. 3,4-DCA adsorption experiments on the optimised biochar were conducted at room temperature, for an initial concentration of 100 mg/L. Removal was observed to be 90% after 15 min, with a plateau thereafter. Readings were, therefore, taken at shorter time intervals, and at lower temperature in an attempt to slow the kinetic process.

Table 7:2 Kinetic parameters of adsorption models fitted to acetaminophen (APAP) and carbamazepine (CBZ)

Model Parameters	APAP	Carbamazepine
Pseudo first order (non-linear)		
R^2 (COD)	0.461	0.460
R^2 adj.	0.371	0.371
qe (mg/g)	46.72±0.315	38.83±1.266
K_1 (min^{-1})	0.207±0.028	0.097±0.023
Pseudo second order (non-linear)		
R^2 (COD)	0.871	0.782
R^2 adj.	0.849	0.746
qe (mg/g)	47.32±0.199	40.56±1.001
K_2 (g/mg*min)	0.021±0.003	0.004±0.001
Pseudo second order (linear)		
R^2 (COD)	1	1
R^2 adj.	1	1
qe (mg/g)	47.62	46.86
K_3 (g/mg*min)	0.013	0.054

Table 7:3 shows the removal percentages of 3,4-DCA at room temperature and in the ice bath. The data obtained confirms the rapid adsorption of 3,4-DCA onto the optimised biochar, even at the lower temperature, hence, it was not possible to monitor the adsorption in order to determine the kinetic parameters for 3,4-DCA. The results indicate that the interaction between the biochar surface and 3,4-DCA molecule is almost instant. An investigation into solution pH also yielded similar results with overnight runs at pH 6 and 9 resulting in 93% and 91% removal, respectively. Previous research into 3,4-DCA removal using adsorption suggested that the data followed a pseudo-second order kinetic model [47]. The observed reaction rates in this study are quicker than those previously reported.

Table 7:3 Biochar performance against 3,4-DCA at room temperature and in an ice bath

Time (min)	% Removal -> room temp.	% Removal -> 3±0.5°C
2	94	86
4	94	88
6	95	90
9	95	89

Experiments using kaolinite and montmorillonite to test removal of chloroanilines, including 3,4-DCA, were reported to achieve equilibrium in under 4 days [325]. Another study into 3,4-DCA removal from water using biomass fly ashes reported kinetic equilibrium at approximately 10 hours [326]. A selection of low-cost materials including corncob char, sugar beet pulp, perlite, and vermiculite were also tested against 3,4-DCA. The quickest reaction time to achieve maximum sorption percentage was 60 min using vermiculite [327]. The rates observed here indicate that there is significantly quicker adsorption for the biochars created in this work.

The linearised pseudo second order rate equation showed a better fit for the data for both species compared to pseudo first order and non-linear second order kinetic models (Table 7:2). The adjusted R^2 values for both species was ≥0.99. The maximum adsorption capacity for APAP was 47.6 mg/g and 46.7 mg/g for CBZ. The second order rate constants show a quicker uptake rate for APAP than CBZ with the adsorption rate being 0.013 g/mg·min. The high R^2 values obtained for both species, with linear PSO model fitting, can be attributed to availability of abundant vacant active sites in the physically activated biochar and the adsorption process being ruled by chemisorption [289,323,328]. The mechanism could likely be attributed to hydrogen bonding between the species. Additionally, π- π interactions between the benzene ring in APAP and CBZ and the aromatics in biochar can influence the adsorption process [328].

Further analysis of the kinetic data was performed using the intraparticle diffusion model proposed by Weber and Morris [329], to understand the rate-controlling step in the adsorption process. The model equation is given in Equation 23:

$$q_t = k_p t^{1/2} + C \qquad \text{Equation 23}$$

Where k_p is the intraparticle diffusion rate constant in mg/g·min$^{1/2}$ and C is a constant that represents the boundary layer effect and initial adsorption. Linearised plots of the model are depicted in Figure 7:4.

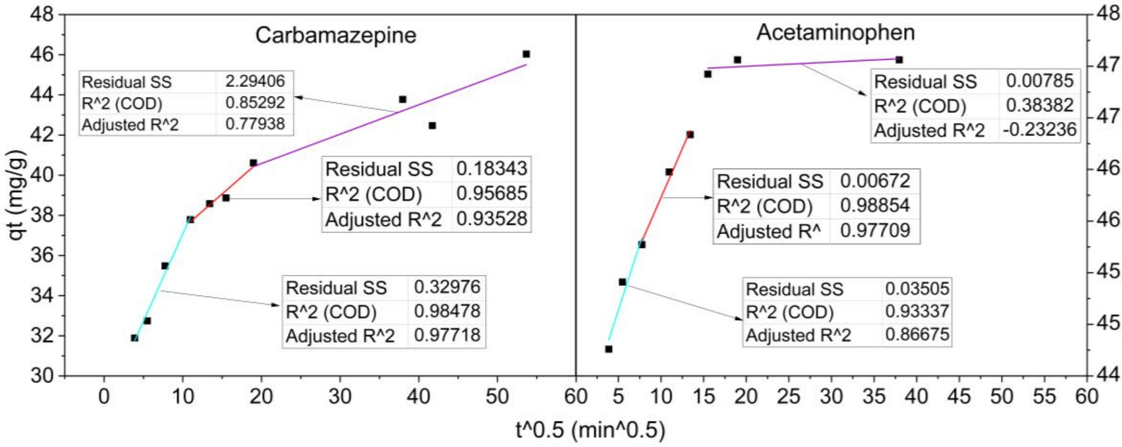

Figure 7:4 Intraparticle diffusion model fittings for acetaminophen and carbamazepine adsorption showing three steps of the diffusion mechanism

The plots suggest that the adsorption process for both pharmaceutical species involved three diffusion steps. In both cases, liquid film diffusion was the dominating phase signifying rapid diffusion of molecules onto the active sites in the pores and voids of the biochar [330,331]. There is a hint of intraparticle diffusion in CBZ adsorption. This step involves the gradual diffusion of molecules into the micropores before the reaction proceeds to the equilibrium stage. For APAP however, the intraparticle diffusion phase is not as prevalent and the reaction appears to proceed rapidly to equilibrium after liquid phase diffusion. This also correlates with the longer time required by CBZ to reach equilibrium compared to APAP. The three target molecules have some similarities, allowing a comparison of their adsorption behaviour relative to their chemistry. All contain amine functionalities and benzene rings, with APAP/BBZ sharing carbonyl moieties and only 3,4-DCA containing halogenated species. The slower kinetics for CBZ could realistically be a consequence of the significantly larger relative size of the molecule, while the rapid adsorption of 3,4-DCA is likely a result of the comparatively increased electrostatic interactions, where the chlorine groups will be electron withdrawing from the benzene ring.

7.3 Summary

The results obtained from adsorption studies suggest potential for application of the optimised biochar in water remediation, targeting persistent organic pollutants. The biochar surface area was higher than those reported for many wood-based biochars reported in literature [236,332]. The sample presents a mixed microporous-mesoporous structure, as observed from the nitrogen isotherms with an average pore width of 4 nm, indicating that the mesopores present in the sample are narrow. Biochars pyrolysed at higher temperatures are linked with alkaline surface character [310], which fits with the PZC value obtained for the biochar produced at 725 °C (7.44±0.2). FTIR analysis suggested a layered carbon structure with the presence of oxygen and nitrogen chemical moieties. These findings were further assisted by XPS analysis presenting a graphene-like arrangement, and 80% atomic carbon fraction. Additionally, the presence of oxygen and nitrogen-based functionalities was confirmed from XPS data. These chemical moieties assist the hydrophilic nature of the biochar and provide a potential avenue for application in water remediation.

The application of biochar against 3,4-DCA, APAP and carbamazepine resulted in efficient removal of the species from an aqueous system. 3,4-DCA removal was characterised with fast removal rates and a very short equilibrium time of around 6 min and a maximum adsorption capacity of 83 mg/g. Although the maximum removal capacity was lower than some activated carbons reported in the literature, adsorption rates were far superior in achieving acceptable removal overall [333]. Adsorption of APAP and CBZ was best explained by the linearised pseudo second order model indicating the formation of chemical bonds as the rate limiting step. The maximum adsorption capacities for APAP and CBZ were 126 and 40 mg/g, respectively and these were superior or on par with those reported in Table 7:4. The presence of nitrogen and oxygen functionalities on the surface of the biochars present possible hydrogen bonding or π-π interactions between the benzene rings in the target elements and the biochar surface, as a possible removal mechanism.

Table 7:4 Maximum uptake capacities of different adsorbents for acetaminophen (APAP), carbamazepine (CBZ) and 3,4-DCA

Adsorbent	Species	q_{max} (mg/g)	Reference
AC from wood	APAP	87	[334]
AC from coconut shell	APAP	135	[334]
AC from orange peels	APAP	118	[323]
Biochar from Scottish softwood	APAP	126	This study
Peanut shells biochar	CBZ	4.96	[140]
Pine sawdust biochar	CBZ	5.25	[335]
AC from Argan tree nutshells	CBZ	71.4	[336]
Biochar from Scottish softwood	CBZ	40	This study
Kaolinite	3,4-DCA	0.311	[41]
Montmorillonite	3,4-DCA	0.077	[41]
Greenhouse biomass fly ash	3,4-DCA	0.125	[326]
Biochar from Scottish softwood	3,4-DCA	83	This study

The predicted adsorption behaviour could be split into two steps. First, monolayer adsorption with a chemisorption rate limiting step via hydrogen bonding or π-π interactions. Second, multilayer physisorption at high concentrations from weak van der Waals forces. Figure 7:5 suggests common pathways of APAP adsorption on a low cost activated carbon. The observations reported correlate with the data generated from kinetic analysis in the work, suggesting the adsorption of APAP proceeds mainly through π-π interactions and hydrogen bonding on the biochar surface. As stated in Figure 1:9, CBZ adsorption also follows π-π interactions and chemical bonding with the chemical moieties present on the biochar surface. However, the larger size of the molecule prevents it from accessing all of the active sites within the material, which is also evident in the extra time required by the molecule to reach equilibrium.

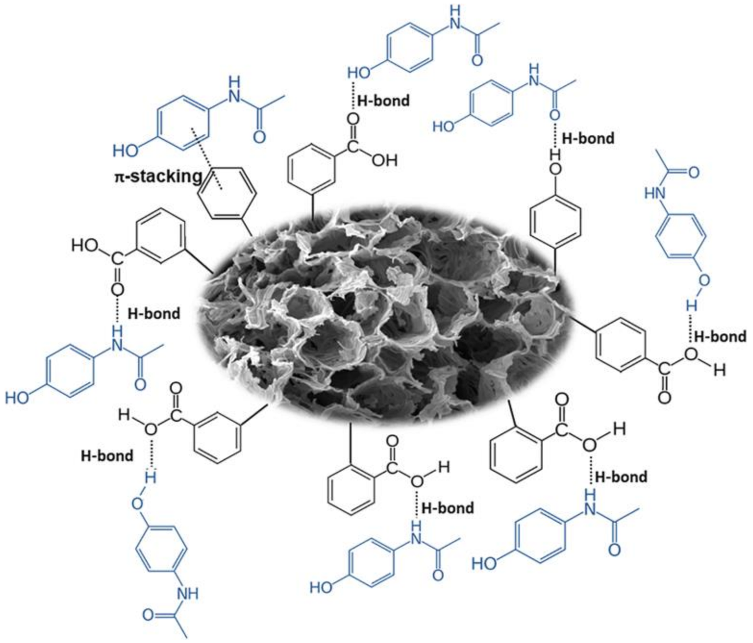

Figure 7:5 Common pathways of APAP adsorption onto activated carbon produced from *Moringa oleifera* Lam. Seed husks [337]

Overall, the optimised biochar sample selected for application from the design of experiments optimisation study conducted previously [320], provided fast adsorption kinetics and high adsorption capacities against the identified target molecules. The results provide an attractive avenue for biochar application for water remediation targeting a range of pollutants in aqueous media.

8. Conclusions

The work presented in this thesis includes the development of a novel adsorbent from renewable materials. The experimental approach involved screening to identify a superior feedstock between two types of Scottish wood samples as well as investigating the influence of operating process conditions on the final biochar characteristics using a design of experiments study. The obtained optimised biochar sample was subsequently investigated in water remediation studies targeting three persistent organic pollutants. The chosen species had similarities that allowed for comparison of their adsorption behaviour.

Between the two wood species, screening experiments identified softwood as the superior feedstock. Under the same experimental conditions, softwood samples had high average surface areas and comparable yields to the hardwood samples. The optimal solution for a design of experiments study on softwood suggested by Minitab closely resembled data obtained from experimental runs. Gas flow rates were noted as insignificant with contact time having the greatest impact on biochar characteristics. A high residence time not only produced an increase in observed surface area but also appeared to enhance mesoporosity within the pore structure. Spectroscopic analysis indicated the presence of a layered carbon structure in the biochars. The intricate pore network and graphene-like layered porous arrangement is also evident from morphological analysis. All biochars carry an almost neutral surface charge with a hydrophilic nature, indicating potential for application in water treatment systems. The results obtained from the design of experiments study show evidence of a requirement to consider the influence of manufacturing operating parameters when producing biochars catered to a specific application and requiring target characteristics.

To understand the adsorption behaviour, pseudo first and second order kinetic models were applied to the experimental data. The rapid adsorption of 3,4-DCA presented difficulties in fitting kinetic models to the obtained data. Attempts at slowing the reaction kinetics using an ice bath were unsuccessful as the reaction continued to proceed to equilibrium rapidly. Increased electrostatic interactions between the benzene ring and the chlorine groups are the most probable reasons for fast reaction kinetics. For APAP and CBZ, kinetic fittings followed a pseudo second order model. This indicates that the reaction for both the pharmaceutical compounds are chemically controlled. The intra particle diffusion model showed that the adsorption was dominated by the liquid film diffusion phase. CBZ had slower reaction rates compared to APAP which was evidenced by the presence of an intra particle diffusion region in CBZ fittings that were absent in APAP adsorption. The slower rate can also be attributed to the larger size of the CBZ molecule trying to adsorb onto a highly microporous material.

Adsorption isotherms assist in the understanding of the nature of interactions between the adsorbate and the adsorbent as well as the equilibrium behaviour. Langmuir, Freundlich and Sips isotherm models were used in this work to analyse the adsorption isotherms. For all three species investigated, the experimental data fits to the isotherm models followed the following order: Sips > Langmuir > Freundlich. For APAP, both Langmuir and Sips isotherms had high correlation coefficient. However, the analysis of separation factor to verify the favourability of the Langmuir model suggested unfavourable adsorption due to limitations in the assumptions involved. A good fit to the Sips isotherm model suggested a heterogeneous surface with multiple binding sites and multilayer adsorption. These interpretations were further supplemented by Scatchard plots for the data. The highest adsorption capacity was noted in the case of APAP, followed by 3,4-DCA and CBZ respectively.

In conclusion, this work focussed on the synthesis of biochars from a renewable feedstock and investigating manufacturing process parameter significance on final biochar characteristics. Material characterisation techniques showed significant influence of the operating parameters to produce materials targeting specific applications. The biochars had high surface areas, a mix of micro and mesoporous nature and showed effective removal of the target species from aqueous systems. Highly hydrophilic nature and a neutral surface charge further cemented observations of applications into water remediation systems. The optimised sample demonstrated high removal efficiencies for all target species and especially rapid kinetic performance against 3,4-DCA achieving over 90% removal within minutes. The results demonstrate the potential for native Scottish wood samples as a biochar material that can be used in water remediation, with a requirement to consider the influence of manufacturing operating parameters on final biochar characteristics.

9. Future Work

Initially, this work started with probing wheat straw pellets as possible biochar materials using chemical activation methods. However, due to issues arising from working with stronger acids and the generation of an additional waste stream, physical activation was identified as the means for biochar activation. The yields obtained with the straw pellets post pyrolysis were low and the precursor was switched to softwood due to larger availability as well as high carbon abatement potential.

The application of the biochar in this work was limited to deionised water systems. To understand how the material would behave in the presence of competing ions in the presence of target compounds, conducting experiments using generated water as suggested by the National Sanitation Foundation could be of potential interest. Additionally, since the biochar works efficiently against pesticides and pharmaceutical compounds, testing its efficacy against other similar pollutants could also prove beneficial.

Adsorbent regeneration is an important property that determines the overall feasibility of a material application on a commercial level. Conducting column tests would also provide important information on the breakthrough point and bed saturation. The tests can also provide insights into the regeneration and reusability of the biochars. Investigation into salvaging and regeneration of a highly hydrophilic biochar material could be of vital importance with regards to scaling up the use of material to a pilot or even a commercial scale. Biochar deploy ability using a binder could be a possible mechanism to prevent the biochar forming a homogeneous mix with the aqueous system.

Assessment of adsorption mechanism using thermodynamic analysis would help in the identification if the removal process is spontaneous and entropically driven with varying temperature.

References

[1] G. Baggio, M. Qadir, V. Smakhtin, Freshwater availability status across countries for human and ecosystem needs, Science of the Total Environment 792 (2021). https://doi.org/10.1016/J.SCITOTENV.2021.148230/REFERENCES.

[2] WEO-2016 Special Report: Water-Energy Nexus – Analysis - IEA, (n.d.). https://www.iea.org/reports/water-energy-nexus (accessed July 10, 2023).

[3] L. Santos Pereira, I. Cordery, I. Iacovides, Coping with water scarcity: Addressing the challenges, Coping with Water Scarcity: Addressing the Challenges (2009) 1–382. https://doi.org/10.1007/978-1-4020-9579-5.

[4] United Nations Educational Scientific and Cultural Organization, The United Nations World Water Development Report 2021: Valuing water, Water Politics (2021) 206. https://unesdoc.unesco.org/ark:/48223/pf0000375724 (accessed July 10, 2023).

[5] A. Boretti, L. Rosa, Reassessing the projections of the World Water Development Report, Npj Clean Water 2019 2:1 2 (2019) 1–6. https://doi.org/10.1038/s41545-019-0039-9.

[6] C. He, Z. Liu, J. Wu, X. Pan, Z. Fang, J. Li, B.A. Bryan, Future global urban water scarcity and potential solutions, Nature Communications 2021 12:1 12 (2021) 1–11. https://doi.org/10.1038/s41467-021-25026-3.

[7] N. Bolong, A.F. Ismail, M.R. Salim, T. Matsuura, A review of the effects of emerging contaminants in wastewater and options for their removal, Desalination 239 (2009) 229–246. https://doi.org/10.1016/J.DESAL.2008.03.020.

[8] A Snapshot of the World’s Water Quality: Towards a global assessment, (n.d.). www.unep.org (accessed July 10, 2023).

[9] K.L. Wasewar, S. Singh, S.K. Kansal, Process intensification of treatment of inorganic water pollutants, Inorganic Pollutants in Water (2020) 245–271. https://doi.org/10.1016/B978-0-12-818965-8.00013-5.

[10] M. Haseena, M. Faheem Malik, A. Javed, S. Arshad, N. Asif, S. Zulfiqar, J. Hanif, Water pollution and human health, Environmental Risk Assessment and Remediation 01 (2017). https://doi.org/10.4066/2529-8046.100020.

[11] D. Briggs, Environmental pollution and the global burden of disease, Br Med Bull 68 (2003) 1–24. https://doi.org/10.1093/bmb/ldg019.

[12] M.M. Ghangrekar, P. Chatterjee, Water pollutants classification and its effects on environment, Carbon Nanostructures 0 (2018) 11–26. https://doi.org/10.1007/978-3-319-95603-9_2/FIGURES/1.

[13] A.W. Verla, C.E. Enyoh, E.N. Verla, K.O. Nwarnorh, Microplastic–toxic chemical interaction: a review study on quantified levels, mechanism and implication, SN Appl Sci 1 (2019) 1–30. https://doi.org/10.1007/S42452-019-1352-0/FIGURES/8.

[14] Jr., G.A. Burton, R. Pitt, Stormwater Effects Handbook : A Toolbox for Watershed Managers, Scientists, and Engineers, Stormwater Effects Handbook (2001). https://doi.org/10.1201/9781420036244.

[15] Stockholm Convention on Persistent Organic Pollutants (POPs), Text and Annexes Revised in 2019 (2001). http://chm.pops.int/theconvention/overview/textoftheconvention/tabid/2232/default.aspx.

[16] H. Fromme, T. Küchler, T. Otto, K. Pilz, J. Müller, A. Wenzel, Occurrence of phthalates and bisphenol A and F in the environment, Water Res 36 (2002) 1429–1438. https://doi.org/https://doi.org/10.1016/S0043-1354(01)00367-0.

[17] A. Ahamad, S. Madhav, A.K. Singh, A. Kumar, P. Singh, Types of Water Pollutants: Conventional and Emerging, in: Springer Singapore, 2020: pp. 21–41. https://doi.org/10.1007/978-981-15-0671-0_3.

[18] USEPA, Special Report on Environmental Endocrine Disruption: An Effects Assessment and Analysis, (1997). https://nepis.epa.gov/Exe/ZyNET.exe/30004ZD3.txt?ZyActionD=ZyDocument&Client=EPA&Index=1995%20Thru%201999&Docs=&Query=&Time=&EndTime=&SearchMethod=1&TocRestrict=n&Toc=&TocEntry=&QField=&QFieldYear=&QFieldMonth=&QFieldDay=&UseQField=&IntQFieldOp=0&ExtQFieldOp=0&XmlQuery=&File=D%3A%5CZYFILES%5CINDEX%20DATA%5C95THRU99%5CTXT%5C00000006%5C30004ZD3.txt&User=ANONYMOUS&Password=anonymous&SortMethod=h%7C-&MaximumDocuments=1&FuzzyDegree=0&ImageQuality=r75g8/r75g8/x150y150g16/i425&Display=hpfr&DefSeekPage=x&SearchBack=ZyActionL&Back=ZyActionS&BackDesc=Results%20page&MaximumPages=1&ZyEntry=1#.

[19] R.S. Kookana, M. Williams, A.B.A. Boxall, D.G.J. Larsson, S. Gaw, K. Choi, H. Yamamoto, S. Thatikonda, Y.G. Zhu, P. Carriquiriborde, Potential ecological footprints of active pharmaceutical ingredients: an examination of risk factors in low-, middle- and high-income countries, Philosophical Transactions of the Royal Society B: Biological Sciences 369 (2014). https://doi.org/10.1098/RSTB.2013.0586.

[20] S. Comber, M. Gardner, P. Sörme, D. Leverett, B. Ellor, Active pharmaceutical ingredients entering the aquatic environment from wastewater treatment works: A cause for concern?, Sci Total Environ 613–614 (2017) 538–547. https://doi.org/10.1016/J.SCITOTENV.2017.09.101.

[21] Z. Huang, B. Gong, C.P. Huang, S.Y. Pan, P. Wu, Z. Dang, P.C. Chiang, Performance evaluation of integrated adsorption-nanofiltration system for emerging compounds removal: Exemplified by caffeine, diclofenac and octylphenol, J

Environ Manage 231 (2019) 121–128. https://doi.org/10.1016/J.JENVMAN.2018.09.092.

[22] E. Diamanti-Kandarakis, J.P. Bourguignon, L.C. Giudice, R. Hauser, G.S. Prins, A.M. Soto, R.T. Zoeller, A.C. Gore, Endocrine-Disrupting Chemicals: An Endocrine Society Scientific Statement, Endocr Rev 30 (2009) 293. https://doi.org/10.1210/ER.2009-0002.

[23] Q.U. Ain, D. Roy, A. Ahsan, M.A. Farooq, M. Aquib, Z. Hussain, B. Emmanuel, B. Wang, Endocrine-Disrupting Chemicals: Occurrence and Exposure to the Human Being, in: Springer International Publishing, 2021: pp. 113–123. https://doi.org/10.1007/978-3-030-45923-9_7.

[24] W. Wuttke, H. Jarry, D. Seidlova-Wuttke, Definition, classification and mechanism of action of endocrine disrupting chemicals, Hormones (Athens) 9 (2010) 9–15. https://doi.org/10.1007/bf03401276.

[25] M.L. Verma, V. Rani, Biosensors for toxic metals, polychlorinated biphenyls, biological oxygen demand, endocrine disruptors, hormones, dioxin, phenolic and organophosphorus compounds: a review, Environ Chem Lett 19 (2021) 1657–1666. https://doi.org/10.1007/s10311-020-01116-4.

[26] R. Moral, R. Wang, I.H. Russo, D.A. Mailo, C.A. Lamartiniere, J. Russo, The plasticizer butyl benzyl phthalate induces genomic changes in rat mammary gland after neonatal/prepubertal exposure, BMC Genomics 8 (2007) 453. https://doi.org/10.1186/1471-2164-8-453.

[27] R.R. Newbold, W.N. Jefferson, E. Padilla-Banks, Prenatal exposure to bisphenol a at environmentally relevant doses adversely affects the murine female reproductive tract later in life, Environ Health Perspect 117 (2009) 879–885. https://doi.org/10.1289/ehp.0800045.

[28] L.N. Vandenberg, T. Colborn, T.B. Hayes, J.J. Heindel, D.R. Jacobs Jr., D.-H. Lee, T. Shioda, A.M. Soto, F.S. vom Saal, W. V Welshons, R.T. Zoeller, J.P. Myers,

Hormones and Endocrine-Disrupting Chemicals: Low-Dose Effects and Nonmonotonic Dose Responses, Endocr Rev 33 (2012) 378–455. https://doi.org/10.1210/er.2011-1050.

[29] E.R. Kabir, M.S. Rahman, I. Rahman, A review on endocrine disruptors and their possible impacts on human health, Environ Toxicol Pharmacol 40 (2015) 241–258. https://doi.org/10.1016/J.ETAP.2015.06.009.

[30] M. Rose, D.H. Bennett, Å. Bergman, B. Fängström, I.N. Pessah, I. Hertz-Picciotto, PBDEs in 2−5 Year-Old Children from California and Associations with Diet and Indoor Environment, Environ Sci Technol 44 (2010) 2648–2653. https://doi.org/10.1021/es903240g.

[31] S. Lunder, L. Hovander, I. Athanassiadis, A. Bergman, Significantly higher polybrominated diphenyl ether levels in young U.S. children than in their mothers, Environ Sci Technol 44 (2010) 5256–5262. https://doi.org/10.1021/es1009357.

[32] L.S. Haug, S. Huber, G. Becher, C. Thomsen, Characterisation of human exposure pathways to perfluorinated compounds--comparing exposure estimates with biomarkers of exposure, Environ Int 37 (2011) 687–693. https://doi.org/10.1016/j.envint.2011.01.011.

[33] B.M. Sharma, M. Scheringer, P. Chakraborty, G.K. Bharat, E.H. Steindal, L. Trasande, L. Nizzetto, Unlocking India’s Potential in Managing Endocrine-Disrupting Chemicals (EDCs): Importance, Challenges, and Opportunities, Expo Health (2022). https://doi.org/10.1007/s12403-022-00519-8.

[34] A.C. Gore, V.A. Chappell, S.E. Fenton, J.A. Flaws, A. Nadal, G.S. Prins, J. Toppari, R.T. Zoeller, EDC-2: The Endocrine Society’s Second Scientific Statement on Endocrine-Disrupting Chemicals, Endocr Rev 36 (2015) E1-e150. https://doi.org/10.1210/er.2015-1010.

[35] E. Gagliano, M. Sgroi, P.P. Falciglia, F.G.A. Vagliasindi, P. Roccaro, Removal of poly- and perfluoroalkyl substances (PFAS) from water by adsorption: Role of PFAS chain length, effect of organic matter and challenges in adsorbent regeneration, Water Res 171 (2020) 115381. https://doi.org/10.1016/j.watres.2019.115381.

[36] M. Llorca, G. Schirinzi, M. Martinez, D. Barcelo, M. Farre, Adsorption of perfluoroalkyl substances on microplastics under environmental conditions, Environ Pollut 235 (2018) 680–691. https://doi.org/10.1016/j.envpol.2017.12.075.

[37] C. Lau, K. Anitole, C. Hodes, D. Lai, A. Pfahles-Hutchens, J. Seed, Perfluoroalkyl Acids: A Review of Monitoring and Toxicological Findings, Toxicological Sciences 99 (2007) 366–394. https://doi.org/10.1093/toxsci/kfm128.

[38] M.M. Peden-Adams, J.M. Keller, J.G. EuDaly, J. Berger, G.S. Gilkeson, D.E. Keil, Suppression of Humoral Immunity in Mice following Exposure to Perfluorooctane Sulfonate, Toxicological Sciences 104 (2008) 144–154. https://doi.org/10.1093/toxsci/kfn059.

[39] A. Cordner, V.Y. De La Rosa, L.A. Schaider, R.A. Rudel, L. Richter, P. Brown, Guideline levels for PFOA and PFOS in drinking water: the role of scientific uncertainty, risk assessment decisions, and social factors, J Expo Sci Environ Epidemiol 29 (2019) 157–171. https://doi.org/10.1038/s41370-018-0099-9.

[40] A.G. Livingston, A. Willacy, Degradation of 3,4-dichloroaniline in synthetic and industrially produced wastewaters by mixed cultures freely suspended and immobilized in a packed-bed reactor, Appl Microbiol Biotechnol 35 (1991) 551–557. https://doi.org/10.1007/BF00169767.

[41] A. Luca Tasca, A. Fletcher, Journal of Environmental Science and Health, Part A Toxic/Hazardous Substances and Environmental Engineering State of the art of the environmental behaviour and removal techniques of the endocrine

disruptor 3,4-dichloroaniline, (2017). https://doi.org/10.1080/10934529.2017.1394701.

[42] M. Nurul, H. Bhuiyan, H. Kang, J. Choi, S. Lim, Y. Kho, K. Choi, Effects of 3,4-dichloroaniline (3,4-DCA) and 4,4 0-methylenedianiline (4,4 0-MDA) on sex hormone regulation and reproduction of adult zebrafish (Danio rerio), Chemosphere 269 (2021) 128768. https://doi.org/10.1016/j.chemosphere.2020.128768.

[43] M.A. Ibrahim, S.Z. Zulkifli, M.N.A. Azmai, F. Mohamat-yusuff, A. Ismail, Reproductive Toxicity of 3,4-dichloroaniline (3,4-DCA) on Javanese Medaka (Oryzias javanicus, Bleeker 1854), Animals (Basel) 11 (2021) 1–12. https://doi.org/10.3390/ANI11030798.

[44] P. Ellappan, L.R. Miranda, Two-regime kinetic study and parameter optimization of degradation of 3,4-dichloroaniline using TI–N/S catalyst under visible light, New Pub: Balaban 57 (2014) 2203–2216. https://doi.org/10.1080/19443994.2014.980325.

[45] P.C.O. Ch. Groshart, Towards the establishment of a priority list of substances for further evaluation of their role in endocrine disruption - preparation of a candidate list of substances as a basis for priority setting, Delft, Netherlands, 2000. https://ec.europa.eu/environment/archives/docum/pdf/bkh_main.pdf.

[46] E.C. Bureau, European Union Rish Assessment Report 3,4-dichloroaniline (3,4-DCA), 65 (2006). https://echa.europa.eu/documents/10162/b41f2253-824c-48f8-b494-df54bd901e6a.

[47] S. Angioi, S. Polati, M. Roz, C. Rinaudo, V. Gianotti, M.C. Gennaro, Sorption studies of chloroanilines on kaolinite and montmorillonite, Environmental Pollution 134 (2005) 35–43. https://doi.org/https://doi.org/10.1016/j.envpol.2004.07.018.

[48] B. Szczepanik, P. Slomkiewicz, M. Garnuszek, K. Czech, Adsorption of chloroanilines from aqueous solutions on the modified halloysite, Appl Clay Sci 101 (2014). https://doi.org/10.1016/j.clay.2014.08.013.

[49] E. González-Pradas, M. Fernández-Pérez, F. Flores-Céspedes, M. Villafranca-Sánchez, M.D. Ureña-Amate, M. Socías-Viciana, F. Garrido-Herrera, Effects of dissolved organic carbon on sorption of 3,4-dichloroaniline and 4-bromoaniline in a calcareous soil, Chemosphere 59 (2005) 721–728. https://doi.org/https://doi.org/10.1016/j.chemosphere.2004.10.050.

[50] Å. Västermark, Y.L. Giwercman, O. Hagströmer, E.R. De-Meyts, J. Eberhard, O. Ståhl, G.C. Cedermark, H. Rastkhani, G. Daugaard, S. Arver, A. Giwercman, Polymorphic variation in the androgen receptor gene: Association with risk of testicular germ cell cancer and metastatic disease, Eur J Cancer 47 (2011) 413–419. https://doi.org/10.1016/j.ejca.2010.08.017.

[51] E. Swedenborg, J. Rüegg, S. Mäkelä, I. Pongratz, Endocrine disruptive chemicals: mechanisms of action and involvement in metabolic disorders, J Mol Endocrinol 43 (2009) 1–10. https://doi.org/10.1677/jme-08-0132.

[52] F. Eissa, A. El makawy, M. Badr, O. Elhamalawy, Assessment of 3, 4-Dichloroaniline Toxicity as Environmental Pollutant in Male Mice, Eur J Biol Sci 4 (2012) 73–82. https://doi.org/10.5829/idosi.ejbs.2012.4.3.65104.

[53] M.N. Huda Bhuiyan, H. Kang, J.H. Kim, S. Kim, Y. Kho, K. Choi, Endocrine disruption by several aniline derivatives and related mechanisms in a human adrenal H295R cell line and adult male zebrafish, Ecotoxicol Environ Saf 180 (2019) 326–332. https://doi.org/https://doi.org/10.1016/j.ecoenv.2019.05.003.

[54] C. Philippe, P. Hautekiet, A.F. Grégoir, E.S.J. Thoré, L. Brendonck, G. De Boeck, T. Pinceel, Interactive effects of 3,4-DCA and temperature on the annual killifish Nothobranchius furzeri, Aquatic Toxicology 212 (2019) 146–153. https://doi.org/https://doi.org/10.1016/j.aquatox.2019.05.009.

[55] L.R. Vieira, D.C. Hissa, T.M. Souza, C.A. Sá, J.A.M. Evaristo, F.C.S. Nogueira, A.F.U. Carvalho, D.F. Farias, Proteomics analysis of zebrafish larvae exposed to 3,4-dichloroaniline using the fish embryo acute toxicity test, Environ Toxicol 35 (2020) 849–860. https://doi.org/10.1002/tox.22921.

[56] X. Du, P. Zhan, N. Gan, Y. Cao, T. Li, W. Sang, L. Wang, Highly Selective Molecular Recognition and Ultrasensitive Detection of 3,4-dichloroaniline Based on Molecularly Imprinted Sol-Gel Film Combined with Multi-Walled Carbon Nanotubes, J Electrochem Soc 160 (2013) H742–H748. https://doi.org/10.1149/2.082310jes.

[57] J. Bai, H. Han, F. Wang, L. Su, H. Ding, X. Hu, B. Hu, H. Li, W. Zheng, Y. Li, Maternal linuron exposure alters testicular development in male offspring rats at the whole genome level, Toxicology 389 (2017) 13–20. https://doi.org/https://doi.org/10.1016/j.tox.2017.07.005.

[58] D.M.M. Adema, I.G.J. Vink, A comparative study of the toxicity of 1,1,2-trichloroethane, dieldrin, pentachlorophenol and 3,4 dichloroaniline for marine and fresh water organisms, Chemosphere 10 (1981) 533–554.

[59] B. Zhu, T. Liu, X. Hu, G. Wang, Developmental toxicity of 3,4-dichloroaniline on rare minnow (Gobiocypris rarus) embryos and larvae, Chemosphere 90 (2013) 1132–1139. https://doi.org/https://doi.org/10.1016/j.chemosphere.2012.09.021.

[60] I.T.W. Lampert, The Juvenile Growth Rate of Daphnia : A Short-Term Alternative to Measuring the Per Capita Rate of Increase in Ecotoxicology?, Arch Environ Contam Toxicol 42 (2002) 193–198. https://doi.org/10.1007/s00244-001-0010-9.

[61] H. Ericson, G. Thorsén, L. Kumblad, Physiological effects of diclofenac, ibuprofen and propranolol on Baltic Sea blue mussels, Aquatic Toxicology 99 (2010) 223–231. https://doi.org/10.1016/J.AQUATOX.2010.04.017.

[62] R. Hirsch, T. Ternes, K. Haberer, K.L. Kratz, Occurrence of antibiotics in the aquatic environment, Science of The Total Environment 225 (1999) 109–118. https://doi.org/10.1016/S0048-9697(98)00337-4.

[63] S.R. Hughes, P. Kay, L.E. Brown, Global synthesis and critical evaluation of pharmaceutical data sets collected from river systems, Environ Sci Technol 47 (2013) 661–677. https://doi.org/10.1021/ES3030148/ASSET/IMAGES/LARGE/ES-2012-030148_0008.JPEG.

[64] D.W. Kolpin, E.T. Furlong, M.T. Meyer, E.M. Thurman, S.D. Zaugg, L.B. Barber, H.T. Buxton, Pharmaceuticals, Hormones, and Other Organic Wastewater Contaminants in U.S. Streams, 1999−2000: A National Reconnaissance, Environ Sci Technol 36 (2002) 1202–1211. https://doi.org/10.1021/ES011055J.

[65] A.J. Ramirez, R.A. Brain, S. Usenko, M.A. Mottaleb, J.G. O’Donnell, L.L. Stahl, J.B. Wathen, B.D. Snyder, J.L. Pitt, P. Perez-Hurtado, L.L. Dobbins, B.W. Brooks, C.K. Chambliss, Occurrence of pharmaceuticals and personal care products in fish: Results of a national pilot study in the united states, Environ Toxicol Chem 28 (2009) 2587–2597. https://doi.org/10.1897/08-561.1.

[66] S.C. Monteiro, A.B.A. Boxall, Factors affecting the degradation of pharmaceuticals in agricultural soils, Environ Toxicol Chem 28 (2009) 2546–2554. https://doi.org/10.1897/08-657.1.

[67] R. Lacy, Pharmaceutical Residues in Freshwater, 2019. https://www.oecd.org/publications/pharmaceutical-residues-in-freshwater-c936f42d-en.htm (accessed August 7, 2023).

[68] A. Küster, N. Adler, Pharmaceuticals in the environment: scientific evidence of risks and its regulation, Philosophical Transactions of the Royal Society B: Biological Sciences 369 (2014). https://doi.org/10.1098/RSTB.2013.0587.

[69] O.M. Rodriguez-Narvaez, J.M. Peralta-Hernandez, A. Goonetilleke, E.R. Bandala, Treatment technologies for emerging contaminants in water: A review, Chemical Engineering Journal 323 (2017) 361–380. https://doi.org/10.1016/J.CEJ.2017.04.106.

[70] M.A. Décima, S. Marzeddu, M. Barchiesi, C. Di Marcantonio, A. Chiavola, M.R. Boni, A Review on the Removal of Carbamazepine from Aqueous Solution by Using Activated Carbon and Biochar, Sustainability 2021, Vol. 13, Page 11760 13 (2021) 11760. https://doi.org/10.3390/SU132111760.

[71] J.R. Bales, J.K. Nicholson, P.J. Sadler, Two-dimensional proton nuclear magnetic resonance maps of acetaminophen metabolites in human urine., Clin Chem 31 (1985) 757–762. https://doi.org/10.1093/CLINCHEM/31.5.757.

[72] M. Mikulic, Top analgesic drugs dispensed in England by item number 2022 | Statista, (2023). https://www.statista.com/statistics/377895/top-ten-analgesic-drugs-dispensed-by-item-in-england/ (accessed August 7, 2023).

[73] A.M. Larson, J. Polson, R.J. Fontana, T.J. Davern, E. Lalani, L.S. Hynan, J.S. Reisch, F. V. Schiødt, G. Ostapowicz, A.O. Shakil, W.M. Lee, Acetaminophen-induced acute liver failure: results of a United States multicenter, prospective study, Hepatology 42 (2005) 1364–1372. https://doi.org/10.1002/HEP.20948.

[74] J.A. Hinson, D.W. Roberts, L.P. James, Mechanisms of acetaminophen-induced liver necrosis, Handb Exp Pharmacol 196 (2010) 369–405. https://doi.org/10.1007/978-3-642-00663-0_12.

[75] R. Tittarelli, M. Pellegrini, M.G. Scarpellini, E. Marinelli, V. Bruti, N.M. Di Luca, F.P. Busardò, S. Zaami, Hepatotoxicity of paracetamol and related fatalities, Eur Rev Med Pharmacol Sci 21 (2017) 95–101.

[76] C.A. Igwegbe, C.O. Aniagor, S.N. Oba, P.S. Yap, F.U. Iwuchukwu, T. Liu, E.C. de Souza, J.O. Ighalo, Environmental protection by the adsorptive elimination of acetaminophen from water: A comprehensive review, Journal of Industrial and

Engineering Chemistry 104 (2021) 117–135. https://doi.org/10.1016/J.JIEC.2021.08.015.

[77] R. Ben-Shachar, Y. Chen, S. Luo, C. Hartman, M. Reed, F. Nijhout, The biochemistry of acetaminophen hepatotoxicity and rescue: a mathematical model, (2012). http://www.tbiomed.com/content/9/55http://www.tbiomed.com/content/9/55 (accessed August 7, 2023).

[78] M.A. García, R. Cristofoletti, B. Abrahamsson, D.W. Groot, A. Parr, J.E. Polli, M. Mehta, V.P. Shah, T. Tomakazu, J.B. Dressman, P. Langguth, Biowaiver Monograph for Immediate-Release Solid Oral Dosage Forms: Carbamazepine, J Pharm Sci 110 (2021) 1935–1947. https://doi.org/10.1016/J.XPHS.2021.02.019.

[79] A. Schwarz, C. Strakos, R. Weihrich, A Brief Review on Carbamazepine-History, Pharmacological Properties and Environmental Impact Insights in Chemistry and Biochemistry Mini Review Chemical Structure and History of Carbamazepine, (2021). https://doi.org/10.33552/ICBC.2021.01.000519.

[80] J.K. Harvey, Pollution Sources: Point and Nonpoint - river, temperature, important, salt, types, system, plants, oxygen, human, Water Encyclopedia (n.d.). http://www.waterencyclopedia.com/Po-Re/Pollution-Sources-Point-and-Nonpoint.html (accessed July 11, 2023).

[81] A. Vaseashta, Nanomaterials for Chemical—Biological — Physical Integrity of Potable Water, (2009) 1–16. https://doi.org/10.1007/978-90-481-3497-7_1.

[82] H. Zeghioud, L. Fryda, A. Mahieu, R. Visser, A. Kane, Potential of Flax Shives and Beech Wood-Derived Biochar in Methylene Blue and Carbamazepine Removal from Aqueous Solutions, Materials (Basel) 15 (2022). https://doi.org/10.3390/MA15082824.

[83] R. Loos, R. Carvalho, D.C. António, S. Comero, G. Locoro, S. Tavazzi, B. Paracchini, M. Ghiani, T. Lettieri, L. Blaha, B. Jarosova, S. Voorspoels, K. Servaes, P. Haglund, J. Fick, R.H. Lindberg, D. Schwesig, B.M. Gawlik, EU-wide monitoring survey on emerging polar organic contaminants in wastewater treatment plant effluents, Water Res 47 (2013) 6475–6487. https://doi.org/10.1016/J.WATRES.2013.08.024.

[84] G. Crini, E. Lichtfouse, Advantages and disadvantages of techniques used for wastewater treatment, Environ Chem Lett 17 (2019) 145–155. https://doi.org/10.1007/s10311-018-0785-9.

[85] A. Bahuguna, S. Singh, A. Bahuguna, S. Sharma, B. Dadarwal, Physical method of Wastewater treatment-A review, 7 (2021) 2348–2532.

[86] R. Liang, A. Hu, M. Hatat-Fraile, N. Zhou, Fundamentals on Adsorption, Membrane Filtration, and Advanced Oxidation Processes for Water Treatment, in: A. Hu, A. Apblett (Eds.), Nanotechnology for Water Treatment and Purification, Springer International Publishing, Cham, 2014: pp. 1–45. https://doi.org/10.1007/978-3-319-06578-6_1.

[87] K.O. Iwuozor, Prospects and Challenges of Using Coagulation-Flocculation method in the treatment of Effluents, Advanced Journal of Chemistry-Section A (2019) 105–127. https://doi.org/10.29088/sami/ajca.2019.2.105127.

[88] C. Chiou, Fundamentals of the Adsorption Theory, in: 2003: pp. 39–52. https://doi.org/10.1002/0471264326.ch4.

[89] E. Iakovleva, M. Sillanpää, Novel sorbents from low-cost materials for water treatment, Advanced Water Treatment: Adsorption (2020) 265–359. https://doi.org/10.1016/B978-0-12-819216-0.00004-7.

[90] S. Jiménez, M. Andreozzi, M.M. Micó, M.G. Álvarez, S. Contreras, Produced water treatment by advanced oxidation processes, Science of The Total

Environment 666 (2019) 12–21. https://doi.org/https://doi.org/10.1016/j.scitotenv.2019.02.128.

[91] Juerg. Hoigne, H.-P. Bader, The role of hydroxyl radical reactions in ozonation processes in aqueous solutions, Water Res 10 (1976) 377–386.

[92] W.H. Glaze, J. Kang, Advanced Oxidation Processes for Treating Groundwater Contaminated With TCE and PCE: Laboratory Studies, J Am Water Works Assoc 80 (1988) 57–63.

[93] P. Westerhoff, G. Aiken, G. Amy, J. Debroux, Relationships between the structure of natural organic matter and its reactivity towards molecular ozone and hydroxyl radicals, Water Res 33 (1999) 2265–2276. https://doi.org/https://doi.org/10.1016/S0043-1354(98)00447-3.

[94] A. Cesaro, V. Naddeo, V. Belgiorno, Wastewater treatment by combination of advanced oxidation processes and conventional biological systems, J. Bioremed. Biodeg. 4 (2013).

[95] R.R.T. John C. Crittenden David W. Hand Kerry J. Howe George Tchobanoglous, MWH’s Water Treatment: Principles and Design, 3rd Edition, Wiley, 2012. https://doi.org/10.1002/9781118131473.

[96] G. Vidal, M.C. Diez, Methanogenic toxicity and continuous anaerobic treatment of wood processing effluents, J Environ Manage 74 (2005) 317–325. https://doi.org/https://doi.org/10.1016/j.jenvman.2004.09.008.

[97] C.D. Lyons, S.E. Katz, R. Bartha, Persistence and mutagenic potential of herbicide-derived aniline residues in pond water, Bull Environ Contam Toxicol 35 (1985) 696–703. https://doi.org/10.1007/BF01636575.

[98] P. Whitehouse, E. Agency, Proposed EQS for Water Framework Directive Annex VIII substances: mecoprop, Environmental Agency, Bristol, 2010. https://assets.publishing.service.gov.uk/government/uploads/system/uploads/attachment_data/file/291213/scho1110bteo-e-e.pdf.

[99] J. Kuiper, A.O. Hanstveit, Fate and effects of 3,4-dichloroaniline (DCA) in marine plankton communities in experimental enclosures, Ecotoxicol Environ Saf 8 (1984) 34–54. https://doi.org/https://doi.org/10.1016/0147-6513(84)90040-X.

[100] C.N. Albers, G.T. Banta, P.E. Hansen, O.S. Jacobsen, Effect of Different Humic Substances on the Fate of Diuron and Its Main Metabolite 3,4-Dichloroaniline in Soil, Environ Sci Technol 42 (2008) 8687–8691. https://doi.org/10.1021/es800629m.

[101] F.R. Brunsbach, W. Reineke, Degradation of chloroanilines in soil slurry by specialized organisms, Appl Microbiol Biotechnol 40 (1993) 402–407. https://doi.org/10.1007/BF00170401.

[102] K. Young-Mog, P. Kun-Ba-Wui, K. Won-Chan, H. Won-Sub, Y. Choon-Bal, Isolation and Characterization of 3,4-Dichloroaniline Degrading Bacteria, Microbiology and Biotechnology Letters 35 (2007) 245–249. http://mbl.or.kr/journal/view.html?doi=.

[103] E.G. Surovtseva, V.S. Ivoilov, G. Vasilyeva, S. Belyaev, Degradation of chlorinated anilines by certain representatives of the genera Aquaspirillum and Paracoccus, Microbiology (N Y) 65 (1996) 553–559.

[104] J. Latorre, W. Reineke, H.-J. Knackmuss, Microbial metabolism of chloroanilines: enhanced evolution by natural genetic exchange, Arch Microbiol 140 (1984) 159–165. https://doi.org/10.1007/BF00454919.

[105] I. Pavlovic, C. Barriga, M.C. Hermosín, J. Cornejo, M.A. Ulibarri, Adsorption of acidic pesticides 2,4-D, Clopyralid and Picloram on calcined hydrotalcite, Appl Clay Sci 30 (2005) 125–133. https://doi.org/10.1016/J.CLAY.2005.04.004.

[106] C.J. van Oss, A review of: “Active Carbon.” R.C. Bansal, J.B. Donnet and F. Stoeckli; Marcel Dekker, New York, 1988. pp. 482, $135.00.,

Http://Dx.Doi.Org/10.1080/01932699008943255 11 (2007) 323–323. https://doi.org/10.1080/01932699008943255.

[107] L.P. Bakhaeva, G.K. Vasilyeva, E.G. Surovtseva, V.M. Mukhin, Microbial degradation of 3,4-dichloroaniline sorbed by activated carbon, Microbiology (N Y) 70 (2001) 277–284. https://doi.org/10.1023/A:1010495025794/METRICS.

[108] D. Huguenot, P. Bois, K. Jézéquel, J.-Y. Cornu, T. Lebeau, Selection of low cost materials for the sorption of copper and herbicides as single or mixed compounds in increasing complexity matrices, J Hazard Mater 182 (2010) 18–26. https://doi.org/https://doi.org/10.1016/j.jhazmat.2010.05.062.

[109] D.M. Willberg, P.S. Lang, R.H. Höchemer, A. Kratel, M.R. Hoffmann, Degradation of 4-Chlorophenol, 3,4-Dichloroaniline, and 2,4,6-Trinitrotoluene in an Electrohydraulic Discharge Reactor, Environ Sci Technol 30 (1996) 2526–2534. https://doi.org/10.1021/es950850s.

[110] J. Feng, R. Liu, P. Chen, S. Yuan, D. Zhao, J. Zhang, Z. Zheng, Degradation of aqueous 3,4-dichloroaniline by a novel dielectric barrier discharge plasma reactor, Environmental Science and Pollution Research 22 (2015) 4447–4459. https://doi.org/10.1007/s11356-014-3690-1.

[111] W.R. Haag, C.C.D. Yao, Rate constants for reaction of hydroxyl radicals with several drinking water contaminants, Environ Sci Technol 26 (1992) 1005–1013. https://doi.org/10.1021/es00029a021.

[112] C. Escapa, R.N. Coimbra, T. Neuparth, T. Torres, M.M. Santos, M. Otero, Acetaminophen Removal from Water by Microalgae and Effluent Toxicity Assessment by the Zebrafish Embryo Bioassay, (n.d.). https://doi.org/10.3390/w11091929.

[113] V. Matamoros, R. Gutiérrez, I. Ferrer, J. García, J.M. Bayona, Capability of microalgae-based wastewater treatment systems to remove emerging organic

contaminants: A pilot-scale study, J Hazard Mater 288 (2015) 34–42. https://doi.org/10.1016/J.JHAZMAT.2015.02.002.

[114] J.T. Yu, E.J. Bouwer, M. Coelhan, Occurrence and biodegradability studies of selected pharmaceuticals and personal care products in sewage effluent, Agric Water Manag 86 (2006) 72–80. https://doi.org/10.1016/J.AGWAT.2006.06.015.

[115] H.N. Phong Vo, G.K. Le, T.M. Hong Nguyen, X.T. Bui, K.H. Nguyen, E.R. Rene, T.D.H. Vo, N.D. Thanh Cao, R. Mohan, Acetaminophen micropollutant: Historical and current occurrences, toxicity, removal strategies and transformation pathways in different environments, Chemosphere 236 (2019) 124391. https://doi.org/10.1016/J.CHEMOSPHERE.2019.124391.

[116] T. Alvarino, E. Katsou, S. Malamis, S. Suarez, F. Omil, F. Fatone, Inhibition of biomass activity in the via nitrite nitrogen removal processes by veterinary pharmaceuticals, Bioresour Technol 152 (2014) 477–483. https://doi.org/10.1016/J.BIORTECH.2013.10.107.

[117] F.I. Hai, S. Yang, M.B. Asif, V. Sencadas, S. Shawkat, M. Sanderson-Smith, J. Gorman, Z.Q. Xu, K. Yamamoto, Carbamazepine as a Possible Anthropogenic Marker in Water: Occurrences, Toxicological Effects, Regulations and Removal by Wastewater Treatment Technologies, Water 2018, Vol. 10, Page 107 10 (2018) 107. https://doi.org/10.3390/W10020107.

[118] Y. Zhang, S.U. Geißen, C. Gal, Carbamazepine and diclofenac: Removal in wastewater treatment plants and occurrence in water bodies, Chemosphere 73 (2008) 1151–1161. https://doi.org/10.1016/J.CHEMOSPHERE.2008.07.086.

[119] S. Wang, J. Wang, Carbamazepine degradation by gamma irradiation coupled to biological treatment, J Hazard Mater 321 (2017) 639–646. https://doi.org/10.1016/J.JHAZMAT.2016.09.053.

[120] K. Tahir, W. Miran, J. Jang, A. Shahzad, M. Moztahida, B. Kim, S.R. Lim, D.S. Lee, Carbamazepine biodegradation and volatile fatty acids production by selectively enriched sulfate-reducing bacteria and fermentative acidogenic bacteria, Journal of Chemical Technology & Biotechnology 96 (2021) 592–602. https://doi.org/10.1002/JCTB.6572.

[121] T. Hata, H. Shintate, S. Kawai, H. Okamura, T. Nishida, Elimination of carbamazepine by repeated treatment with laccase in the presence of 1-hydroxybenzotriazole, J Hazard Mater 181 (2010) 1175–1178. https://doi.org/10.1016/J.JHAZMAT.2010.05.103.

[122] Y. Zhang, S.U. Geißen, In vitro degradation of carbamazepine and diclofenac by crude lignin peroxidase, J Hazard Mater 176 (2010) 1089–1092. https://doi.org/10.1016/J.JHAZMAT.2009.10.133.

[123] C.C. Su, A.T. Chang, L.M. Bellotindos, M.C. Lu, Degradation of acetaminophen by Fenton and electro-Fenton processes in aerator reactor, Sep Purif Technol 99 (2012) 8–13. https://doi.org/10.1016/J.SEPPUR.2012.07.004.

[124] C.C. Su, L.M. Bellotindos, A.T. Chang, M.C. Lu, Degradation of acetaminophen in an aerated Fenton reactor, J Taiwan Inst Chem Eng 44 (2013) 310–316. https://doi.org/10.1016/J.JTICE.2012.11.009.

[125] C.C. Su, C.A. Cada, M.L.P. Dalida, M.C. Lu, Effect of UV light on acetaminophen degradation in the electro-Fenton process, Sep Purif Technol 120 (2013) 43–51. https://doi.org/10.1016/J.SEPPUR.2013.09.034.

[126] Y. He, Y. Dong, W. Huang, X. Tang, H. Liu, H. Lin, H. Li, Investigation of boron-doped diamond on porous Ti for electrochemical oxidation of acetaminophen pharmaceutical drug, Journal of Electroanalytical Chemistry 759 (2015) 167–173. https://doi.org/10.1016/J.JELECHEM.2015.11.011.

[127] L. Rizzo, S. Malato, D. Antakyali, V.G. Beretsou, M.B. Đolić, W. Gernjak, E. Heath, I. Ivancev-Tumbas, P. Karaolia, A.R. Lado Ribeiro, G. Mascolo, C.S. McArdell, H.

Schaar, A.M.T. Silva, D. Fatta-Kassinos, Consolidated vs new advanced treatment methods for the removal of contaminants of emerging concern from urban wastewater, Science of The Total Environment 655 (2019) 986–1008. https://doi.org/10.1016/J.SCITOTENV.2018.11.265.

[128] R. Juárez, S. Karlsson, P. Falås, Å. Davidsson, K. Bester, M. Cimbritz, Integrating dissolved and particulate matter into a prediction tool for ozonation of organic micropollutants in wastewater, Science of The Total Environment 795 (2021) 148711. https://doi.org/10.1016/J.SCITOTENV.2021.148711.

[129] R. Matta, S. Tlili, S. Chiron, S. Barbati, Removal of carbamazepine from urban wastewater by sulfate radical oxidation, Environ Chem Lett 9 (2011) 347–353. https://doi.org/10.1007/S10311-010-0285-Z/METRICS.

[130] W. Li, V. Nanaboina, Q. Zhou, G. V. Korshin, Effects of Fenton treatment on the properties of effluent organic matter and their relationships with the degradation of pharmaceuticals and personal care products, Water Res 46 (2012) 403–412. https://doi.org/10.1016/J.WATRES.2011.11.002.

[131] N. Klamerth, L. Rizzo, S. Malato, M.I. Maldonado, A. Agüera, A.R. Fernández-Alba, Degradation of fifteen emerging contaminants at μg L−1 initial concentrations by mild solar photo-Fenton in MWTP effluents, Water Res 44 (2010) 545–554. https://doi.org/10.1016/J.WATRES.2009.09.059.

[132] S. Feijoo, M. Kamali, R. Dewil, A review of wastewater treatment technologies for the degradation of pharmaceutically active compounds: Carbamazepine as a case study, Chemical Engineering Journal 455 (2023) 140589. https://doi.org/10.1016/J.CEJ.2022.140589.

[133] A. Farhat, J. Keller, S. Tait, J. Radjenovic, Removal of Persistent Organic Contaminants by Electrochemically Activated Sulfate, Environ Sci Technol 49 (2015) 14326–14333. https://doi.org/10.1021/ACS.EST.5B02705/SUPPL_FILE/ES5B02705_SI_001.PDF.

[134] P. Amouzgar, E.S. Chan, B. Salamatinia, Effects of ultrasound on development of Cs/NAC nano composite beads through extrusion dripping for acetaminophen removal from aqueous solution, J Clean Prod 165 (2017) 537–551. https://doi.org/10.1016/J.JCLEPRO.2017.07.148.

[135] L. Yanyan, T.A. Kurniawan, M. Zhu, T. Ouyang, R. Avtar, M.H. Dzarfan Othman, B.T. Mohammad, A.B. Albadarin, Removal of acetaminophen from synthetic wastewater in a fixed-bed column adsorption using low-cost coconut shell waste pretreated with NaOH, HNO3, ozone, and/or chitosan, J Environ Manage 226 (2018) 365–376. https://doi.org/10.1016/J.JENVMAN.2018.08.032.

[136] S. Wong, Y. Lim, N. Ngadi, R. Mat, O. Hassan, I.M. Inuwa, N.B. Mohamed, J.H. Low, Removal of acetaminophen by activated carbon synthesized from spent tea leaves: equilibrium, kinetics and thermodynamics studies, Powder Technol 338 (2018) 878–886. https://doi.org/10.1016/J.POWTEC.2018.07.075.

[137] T. Lin, S. Yu, W. Chen, Occurrence, removal and risk assessment of pharmaceutical and personal care products (PPCPs) in an advanced drinking water treatment plant (ADWTP) around Taihu Lake in China, Chemosphere 152 (2016) 1–9. https://doi.org/10.1016/J.CHEMOSPHERE.2016.02.109.

[138] M.A. Décima, S. Marzeddu, M. Barchiesi, C. Di Marcantonio, A. Chiavola, M.R. Boni, A Review on the Removal of Carbamazepine from Aqueous Solution by Using Activated Carbon and Biochar, Sustainability 2021, Vol. 13, Page 11760 13 (2021) 11760. https://doi.org/10.3390/SU132111760.

[139] E. Rosales, J. Meijide, M. Pazos, M.A. Sanromán, Challenges and recent advances in biochar as low-cost biosorbent: From batch assays to continuous-flow systems, Bioresour Technol 246 (2017) 176–192. https://doi.org/10.1016/J.BIORTECH.2017.06.084.

[140] J. Chen, D. Zhang, H. Zhang, S. Ghosh, B. Pan, Fast and slow adsorption of carbamazepine on biochar as affected by carbon structure and mineral

composition, Science of The Total Environment 579 (2017) 598–605. https://doi.org/10.1016/J.SCITOTENV.2016.11.052.

[141] G. Chu, J. Zhao, Y. Liu, D. Lang, M. Wu, B. Pan, C.E.W. Steinberg, The relative importance of different carbon structures in biochars to carbamazepine and bisphenol A sorption, J Hazard Mater 373 (2019) 106–114. https://doi.org/10.1016/J.JHAZMAT.2019.03.078.

[142] J. Shin, Y.G. Lee, S.H. Lee, S. Kim, D. Ochir, Y. Park, J. Kim, K. Chon, Single and competitive adsorptions of micropollutants using pristine and alkali-modified biochars from spent coffee grounds, J Hazard Mater 400 (2020) 123102. https://doi.org/10.1016/J.JHAZMAT.2020.123102.

[143] A. Taghizadeh, M. Taghizadeh, M. Jouyandeh, M.K. Yazdi, P. Zarrintaj, M.R. Saeb, E.C. Lima, V.K. Gupta, Conductive polymers in water treatment: A review, J Mol Liq 312 (2020) 113447. https://doi.org/https://doi.org/10.1016/j.molliq.2020.113447.

[144] G. Mahmodi, P. Zarrintaj, A. Taghizadeh, M. Taghizadeh, S. Manouchehri, S. Dangwal, A. Ronte, M.R. Ganjali, J.D. Ramsey, S.-J. Kim, M.R. Saeb, From microporous to mesoporous mineral frameworks: An alliance between zeolite and chitosan, Carbohydr Res 489 (2020) 107930. https://doi.org/https://doi.org/10.1016/j.carres.2020.107930.

[145] P. Pourhakkak, A. Taghizadeh, M. Taghizadeh, M. Ghaedi, S. Haghdoust, Chapter 1 - Fundamentals of adsorption technology, in: M. Ghaedi (Ed.), Interface Science and Technology, Elsevier, 2021: pp. 1–70. https://doi.org/https://doi.org/10.1016/B978-0-12-818805-7.00001-1.

[146] N.M. Mahmoodi, M. Taghizadeh, A. Taghizadeh, Activated carbon/metal-organic framework composite as a bio-based novel green adsorbent: Preparation and mathematical pollutant removal modeling, J Mol Liq 277 (2019) 310–322. https://doi.org/https://doi.org/10.1016/j.molliq.2018.12.050.

[147] N.M. Mahmoodi, M. Taghizadeh, A. Taghizadeh, Mesoporous activated carbons of low-cost agricultural bio-wastes with high adsorption capacity: Preparation and artificial neural network modeling of dye removal from single and multicomponent (binary and ternary) systems, J Mol Liq 269 (2018) 217–228. https://doi.org/https://doi.org/10.1016/j.molliq.2018.07.108.

[148] K.K. Kennedy, K.J. Maseka, M. Mbulo, Selected Adsorbents for Removal of Contaminants from Wastewater: Towards Engineering Clay Minerals, Open Journal of Applied Sciences 08 (2018) 355–369. https://doi.org/10.4236/ojapps.2018.88027.

[149] M. Králik, Adsorption, chemisorption, and catalysis, Chemical Papers 68 (2014) 1625–1638. https://doi.org/10.2478/s11696-014-0624-9.

[150] J. Wang, X. Guo, Adsorption kinetic models: Physical meanings, applications, and solving methods, J Hazard Mater 390 (2020) 122156. https://doi.org/https://doi.org/10.1016/j.jhazmat.2020.122156.

[151] H.N. Hamad, S. Idrus, Recent Developments in the Application of Bio-Waste-Derived Adsorbents for the Removal of Methylene Blue from Wastewater: A Review, Polymers (Basel) 14 (2022) 783. https://doi.org/10.3390/polym14040783.

[152] K.S.W. Sing, R.T. Williams, Physisorption Hysteresis Loops and the Characterization of Nanoporous Materials, Adsorption Science & Technology 22 (2004) 773–782. https://doi.org/10.1260/0263617053499032.

[153] Q. Chang, Chapter 10 - Surface of Solids, in: Q. Chang (Ed.), Colloid and Interface Chemistry for Water Quality Control, Academic Press, 2016: pp. 175–225. https://doi.org/https://doi.org/10.1016/B978-0-12-809315-3.00010-4.

[154] B. Zdravkov, J. Čermák, M. Šefara, J. Janků, Pore classification in the characterization of porous materials: A perspective, Open Chem 5 (2007) 385–395. https://doi.org/10.2478/s11532-007-0017-9.

[155] micromeritics, Pore Analysis: Gas Adsorption Technique, (n.d.). https://www.micromeritics.com/particle-testing/analytical-testing/pore-analysis/.

[156] J. Rouquerol, D. Avnir, C.W. Fairbridge, D.H. Everett, J.M. Haynes, N. Pernicone, J.D.F. Ramsay, K.S.W. Sing, K.K. Unger, Recommendations for the characterization of porous solids (Technical Report), Pure and Applied Chemistry 66 (1994) 1739–1758. https://doi.org/doi:10.1351/pac199466081739.

[157] K. Kaneko, Determination of pore size and pore size distribution: 1. Adsorbents and catalysts, J Memb Sci 96 (1994) 59–89. https://doi.org/https://doi.org/10.1016/0376-7388(94)00126-X.

[158] M. Thommes, K. Kaneko, A. V Neimark, J.P. Olivier, F. Rodriguez-Reinoso, J. Rouquerol, K.S.W. Sing, IUPAC Technical Report Physisorption of gases, with special reference to the evaluation of surface area and pore size distribution (IUPAC Technical Report), (2015). https://doi.org/10.1515/pac-2014-1117.

[159] K.A. Cychosz, M. Thommes, Progress in the Physisorption Characterization of Nanoporous Gas Storage Materials, Engineering 4 (2018) 559–566. https://doi.org/https://doi.org/10.1016/j.eng.2018.06.001.

[160] K.A. Cychosz, R. Guillet-Nicolas, J. García-Martínez, M. Thommes, Recent advances in the textural characterization of hierarchically structured nanoporous materials, Chem Soc Rev 46 (2017) 389–414. https://doi.org/10.1039/c6cs00391e.

[161] K.S.W. Sing, Reporting physisorption data for gas/solid systems with special reference to the determination of surface area and porosity (Recommendations 1984), Pure and Applied Chemistry 57 (1985) 603–619. https://doi.org/doi:10.1351/pac198557040603.

[162] M. Naito, T. Yokoyama, K. Hosokawa, K. Nogi, Chapter 5 - Characterization Methods for Nanostructure of Materials, in: M. Naito, T. Yokoyama, K. Hosokawa, K. Nogi (Eds.), Nanoparticle Technology Handbook (Third Edition), Elsevier, 2018: pp. 255–300. https://doi.org/https://doi.org/10.1016/B978-0-444-64110-6.00005-6.

[163] I. Langmuir, The constitution and fundamental properties of solids and liquids. Part I. Solids, J Am Chem Soc 38 (1916) 2221–2295. https://doi.org/10.1021/JA02268A002.

[164] J. Wang, X. Guo, Adsorption isotherm models: Classification, physical meaning, application and solving method, Chemosphere 258 (2020) 127279. https://doi.org/10.1016/J.CHEMOSPHERE.2020.127279.

[165] H. Freundlich, Über die Adsorption in Lösungen, Zeitschrift Für Physikalische Chemie 57U (1907) 385–470. https://doi.org/10.1515/ZPCH-1907-5723/HTML.

[166] J. Wang, S. Zhuang, Covalent organic frameworks (COFs) for environmental applications, Coord Chem Rev 400 (2019) 213046. https://doi.org/10.1016/J.CCR.2019.213046.

[167] Z. Zaheer, A. AL-Asfar, E.S. Aazam, Adsorption of methyl red on biogenic Ag@Fe nanocomposite adsorbent: Isotherms, kinetics and mechanisms, J Mol Liq 283 (2019) 287–298. https://doi.org/10.1016/J.MOLLIQ.2019.03.030.

[168] R. Sips, On the Structure of a Catalyst Surface, J Chem Phys 16 (1948) 490–495. https://doi.org/10.1063/1.1746922.

[169] T.S. Anirudhan, P.S. Suchithra, Equilibrium, kinetic and thermodynamic modeling for the adsorption of heavy metals onto chemically modified hydrotalcite, Indian Journal of Chemical Technology 17 (2010) 247–259.

[170] N. Ayawei, A.N. Ebelegi, D. Wankasi, Modelling and Interpretation of Adsorption Isotherms, J Chem 2017 (2017) 1–11. https://doi.org/10.1155/2017/3039817.

[171] Y.-S. Bae, A.Ö. Yazaydın, R.Q. Snurr, Evaluation of the BET Method for Determining Surface Areas of MOFs and Zeolites that Contain Ultra-Micropores, Langmuir 26 (2010) 5475–5483. https://doi.org/10.1021/la100449z.

[172] S. Brunauer, P.H. Emmett, E. Teller, Adsorption of Gases in Multimolecular Layers, J Am Chem Soc 60 (1938) 309–319. https://doi.org/10.1021/ja01269a023.

[173] S. Lowell, J.E. Shields, M.A. Thomas, M. Thommes, Surface Area Analysis from the Langmuir and BET Theories, in: S. Lowell, J.E. Shields, M.A. Thomas, M. Thommes (Eds.), Characterization of Porous Solids and Powders: Surface Area, Pore Size and Density, Springer Netherlands, Dordrecht, 2004: pp. 58–81. https://doi.org/10.1007/978-1-4020-2303-3_5.

[174] D.A. Gómez-Gualdrón, P.Z. Moghadam, J.T. Hupp, O.K. Farha, R.Q. Snurr, Application of Consistency Criteria To Calculate BET Areas of Micro- And Mesoporous Metal–Organic Frameworks, J Am Chem Soc 138 (2016) 215–224. https://doi.org/10.1021/jacs.5b10266.

[175] K.S.W. Sing, 7 - Assessment of Surface Area by Gas Adsorption, in: F. Rouquerol, J. Rouquerol, K.S.W. Sing, P. Llewellyn, G. Maurin (Eds.), Adsorption by Powders and Porous Solids (Second Edition), Academic Press, Oxford, 2014: pp. 237–268. https://doi.org/https://doi.org/10.1016/B978-0-08-097035-6.00007-3.

[176] I. Ali, M. Asim, T.A. Khan, Low cost adsorbents for the removal of organic pollutants from wastewater, J Environ Manage 113 (2012) 170–183. https://doi.org/https://doi.org/10.1016/j.jenvman.2012.08.028.

[177] E.P. Barrett, L.G. Joyner, P.P. Halenda, The Determination of Pore Volume and Area Distributions in Porous Substances. I. Computations from Nitrogen Isotherms, J Am Chem Soc 73 (1951) 373–380. https://doi.org/10.1021/ja01145a126.

[178] C.G. Shull, The Determination of Pore Size Distribution from Gas Adsorption Data, J Am Chem Soc 70 (1948) 1405–1410. https://doi.org/10.1021/JA01184A034/ASSET/JA01184A034.FP.PNG_V03.

[179] S. Kondo, T. Ishikawa, I. Abe, Adsorption science, Beijing: Chemical Industry (2005) 84–85.

[180] E. Martin, Understanding RF gel formation : modelling fundamental nanoscale processes for enhanced material development, 2022. https://doi.org/$$Uhttps://doi.org/10.48730/0mt1-5d73.

[181] K.S.W. Sing, F. Rouquerol, J. Rouquerol, P. Llewellyn, 8 - Assessment of Mesoporosity, in: F. Rouquerol, J. Rouquerol, K.S.W. Sing, P. Llewellyn, G. Maurin (Eds.), Adsorption by Powders and Porous Solids (Second Edition), Academic Press, Oxford, 2014: pp. 269–302. https://doi.org/https://doi.org/10.1016/B978-0-08-097035-6.00008-5.

[182] B.C. Lippens, J.H. de Boer, Studies on pore systems in catalysts: V. The t method, J Catal 4 (1965) 319–323. https://doi.org/https://doi.org/10.1016/0021-9517(65)90307-6.

[183] A.M. Omer, R. Dey, A.S. Eltaweil, E.M. Abd El-Monaem, Z.M. Ziora, Insights into recent advances of chitosan-based adsorbents for sustainable removal of heavy metals and anions, Arabian Journal of Chemistry 15 (2022) 103543. https://doi.org/10.1016/J.ARABJC.2021.103543.

[184] Y. Tan, K. Wang, Q. Yan, S. Zhang, J. Li, Y. Ji, Synthesis of Amino-Functionalized Waste Wood Flour Adsorbent for High-Capacity Pb(II) Adsorption, ACS Omega 4 (2019) 10475–10484.

https://doi.org/10.1021/ACSOMEGA.9B00920/ASSET/IMAGES/LARGE/AO-2019-00920D_0006.JPEG.

[185] Y. Dai, Q. Sun, W. Wang, L. Lu, M. Liu, J. Li, S. Yang, Y. Sun, K. Zhang, J. Xu, W. Zheng, Z. Hu, Y. Yang, Y. Gao, Y. Chen, X. Zhang, F. Gao, Y. Zhang, Utilizations of agricultural waste as adsorbent for the removal of contaminants: A review, Chemosphere 211 (2018) 235–253. https://doi.org/10.1016/J.CHEMOSPHERE.2018.06.179.

[186] U. Kumari, H. Siddiqi, M. Bal, B.C. Meikap, Calcium and zirconium modified acid activated alumina for adsorptive removal of fluoride: Performance evaluation, kinetics, isotherm, characterization and industrial wastewater treatment, Advanced Powder Technology 31 (2020) 2045–2060. https://doi.org/10.1016/J.APT.2020.02.035.

[187] Z. Xu, K. Wang, Q. Liu, F. Guo, Z. Xiong, Y. Li, Q. Wang, A bifunctional adsorbent of silica gel-immobilized Schiff base derivative for simultaneous and selective adsorption of Cu(II) and SO42−, Sep Purif Technol 191 (2018) 61–74. https://doi.org/10.1016/J.SEPPUR.2017.09.019.

[188] Y. Kobayashi, F. Ogata, T. Nakamura, N. Kawasaki, Synthesis of novel zeolites produced from fly ash by hydrothermal treatment in alkaline solution and its evaluation as an adsorbent for heavy metal removal, J Environ Chem Eng 8 (2020) 103687. https://doi.org/10.1016/J.JECE.2020.103687.

[189] D. Kalaimurugan, K. Durairaj, A.J. Kumar, P. Senthilkumar, S. Venkatesan, Novel preparation of fungal conidiophores biomass as adsorbent for removal of phosphorus from aqueous solution, Environmental Science and Pollution Research 27 (2020) 20757–20769. https://doi.org/10.1007/S11356-020-08307-0/METRICS.

[190] J. Zhao, Z. Zou, R. Ren, X. Sui, Z. Mao, H. Xu, Y. Zhong, L. Zhang, B. Wang, Chitosan adsorbent reinforced with citric acid modified β-cyclodextrin for

highly efficient removal of dyes from reactive dyeing effluents, Eur Polym J 108 (2018) 212–218. https://doi.org/10.1016/J.EURPOLYMJ.2018.08.044.

[191] A. Halajnia, S. Oustan, N. Najafi, A.R. Khataee, A. Lakzian, Adsorption–desorption characteristics of nitrate, phosphate and sulfate on Mg–Al layered double hydroxide, Appl Clay Sci 80–81 (2013) 305–312. https://doi.org/https://doi.org/10.1016/j.clay.2013.05.002.

[192] A. Ahmadpour, D.D. Do, The preparation of active carbons from coal by chemical and physical activation, Carbon N Y 34 (1996) 471–479. https://doi.org/10.1016/0008-6223(95)00204-9.

[193] E. Repo, J.K. Warchol, T.A. Kurniawan, M.E.T. Sillanpää, Adsorption of Co(II) and Ni(II) by EDTA- and/or DTPA-modified chitosan: Kinetic and equilibrium modeling, Chemical Engineering Journal 161 (2010) 73–82. https://doi.org/https://doi.org/10.1016/j.cej.2010.04.030.

[194] A.M. Omer, R. Dey, A.S. Eltaweil, E.M. Abd El-Monaem, Z.M. Ziora, Insights into recent advances of chitosan-based adsorbents for sustainable removal of heavy metals and anions Production and hosting by Elsevier, (2021). https://doi.org/10.1016/j.arabjc.2021.103543.

[195] R. Laus, R. Geremias, H.L. Vasconcelos, M.C.M. Laranjeira, V.T. Fávere, Reduction of acidity and removal of metal ions from coal mining effluents using chitosan microspheres, J Hazard Mater 149 (2007) 471–474. https://doi.org/https://doi.org/10.1016/j.jhazmat.2007.04.012.

[196] B. Liu, D. Wang, G. Yu, X. Meng, Adsorption of heavy metal ions, dyes and proteins by chitosan composites and derivatives — A review, Journal of Ocean University of China 12 (2013) 500–508. https://doi.org/10.1007/s11802-013-2113-0.

[197] A.K. Mallik, S.M.F. Kabir, F. Bin Abdur Rahman, M.N. Sakib, S.S. Efty, M.M. Rahman, Cu(II) removal from wastewater using chitosan-based adsorbents: A

review, J Environ Chem Eng 10 (2022) 108048. https://doi.org/https://doi.org/10.1016/j.jece.2022.108048.

[198] S. Wang, Y. Peng, Natural zeolites as effective adsorbents in water and wastewater treatment, Chemical Engineering Journal 156 (2010) 11–24. https://doi.org/https://doi.org/10.1016/j.cej.2009.10.029.

[199] E. Repo, R. Petrus, M. Sillanpää, J.K. Warchoł, Equilibrium studies on the adsorption of Co(II) and Ni(II) by modified silica gels: One-component and binary systems, Chemical Engineering Journal 172 (2011) 376–385. https://doi.org/https://doi.org/10.1016/j.cej.2011.06.019.

[200] J. Liu, Q. Yu, Z. Zuo, W. Duan, Z. Han, Q. Qin, F. Yang, Experimental investigation on molten slag granulation for waste heat recovery from various metallurgical slags, Appl Therm Eng 103 (2016) 1112–1118. https://doi.org/10.1016/J.APPLTHERMALENG.2016.05.011.

[201] M.M. Kwikima, S. Mateso, Y. Chebude, Potentials of agricultural wastes as the ultimate alternative adsorbent for cadmium removal from wastewater. A review, Sci Afr 13 (2021) e00934. https://doi.org/https://doi.org/10.1016/j.sciaf.2021.e00934.

[202] Y. Sun, B. Gao, Y. Yao, J. Fang, M. Zhang, Y. Zhou, H. Chen, L. Yang, Effects of feedstock type, production method, and pyrolysis temperature on biochar and hydrochar properties, Chemical Engineering Journal 240 (2014) 574–578. https://doi.org/https://doi.org/10.1016/j.cej.2013.10.081.

[203] Y. Lee, Y.T. Kim, E.E. Kwon, J. Lee, Biochar as a catalytic material for the production of 1,4-butanediol and tetrahydrofuran from furan, Environ Res 184 (2020) 109325. https://doi.org/https://doi.org/10.1016/j.envres.2020.109325.

[204] S. Guo, Y. Li, Y. Wang, L. Wang, Y. Sun, L. Liu, Recent advances in biochar-based adsorbents for CO2 capture, Carbon Capture Science & Technology 4 (2022) 100059. https://doi.org/https://doi.org/10.1016/j.ccst.2022.100059.

[205] A. Demirbas, Progress and recent trends in biodiesel fuels, Energy Convers Manag 50 (2009) 14–34. https://doi.org/https://doi.org/10.1016/j.enconman.2008.09.001.

[206] J. Gardy, A. Hassanpour, X. Lai, M.H. Ahmed, M. Rehan, Biodiesel production from used cooking oil using a novel surface functionalised TiO2 nano-catalyst, Appl Catal B 207 (2017) 297–310. https://doi.org/https://doi.org/10.1016/j.apcatb.2017.01.080.

[207] B.S. Caldas, C.S. Nunes, P.R. Souza, F.A. Rosa, J. V Visentainer, O. de O.S. Júnior, E.C. Muniz, Supercritical ethanolysis for biodiesel production from edible oil waste using ionic liquid [HMim][HSO4] as catalyst, Appl Catal B 181 (2016) 289–297. https://doi.org/https://doi.org/10.1016/j.apcatb.2015.07.047.

[208] H. Choksi, S. Pandian, Y.H. Gandhi, S. Deepalakshmi, Studies on production of biodiesel from Madhuca indica oil using a catalyst derived from cotton stalk, Energy Sources, Part A: Recovery, Utilization, and Environmental Effects (2019) 1–10. https://doi.org/10.1080/15567036.2019.1632985.

[209] M. Hamza, M. Ayoub, R. Bin Shamsuddin, A. Mukhtar, S. Saqib, I. Zahid, M. Ameen, S. Ullah, A.G. Al-Sehemi, M. Ibrahim, A review on the waste biomass derived catalysts for biodiesel production, Environ Technol Innov 21 (2021) 101200. https://doi.org/https://doi.org/10.1016/j.eti.2020.101200.

[210] A.C.M. Loy, A.T. Quitain, M.K. Lam, S. Yusup, M. Sasaki, T. Kida, Development of high microwave-absorptive bifunctional graphene oxide-based catalyst for biodiesel production, Energy Convers Manag 180 (2019) 1013–1025. https://doi.org/https://doi.org/10.1016/j.enconman.2018.11.043.

[211] O.S. Stamenković, K. Rajković, A. V Veličković, P.S. Milić, V.B. Veljković, Optimization of base-catalyzed ethanolysis of sunflower oil by regression and artificial neural network models, Fuel Processing Technology 114 (2013) 101–108. https://doi.org/https://doi.org/10.1016/j.fuproc.2013.03.038.

[212] Z. Helwani, M.R. Othman, N. Aziz, J. Kim, W.J.N. Fernando, Solid heterogeneous catalysts for transesterification of triglycerides with methanol: A review, Appl Catal A Gen 363 (2009) 1–10. https://doi.org/https://doi.org/10.1016/j.apcata.2009.05.021.

[213] S. Semwal, A.K. Arora, R.P. Badoni, D.K. Tuli, Biodiesel production using heterogeneous catalysts, Bioresour Technol 102 (2011) 2151–2161. https://doi.org/https://doi.org/10.1016/j.biortech.2010.10.080.

[214] M.K. Lam, K.T. Lee, A.R. Mohamed, Homogeneous, heterogeneous and enzymatic catalysis for transesterification of high free fatty acid oil (waste cooking oil) to biodiesel: A review, Biotechnol Adv 28 (2010) 500–518. https://doi.org/https://doi.org/10.1016/j.biotechadv.2010.03.002.

[215] A. Takagaki, M. Toda, M. Okamura, J.N. Kondo, S. Hayashi, K. Domen, M. Hara, Esterification of higher fatty acids by a novel strong solid acid, Catal Today 116 (2006) 157–161. https://doi.org/https://doi.org/10.1016/j.cattod.2006.01.037.

[216] M. Li, D. Chen, X. Zhu, Preparation of solid acid catalyst from rice husk char and its catalytic performance in esterification, Chinese Journal of Catalysis 34 (2013) 1674–1682. https://doi.org/https://doi.org/10.1016/S1872-2067(12)60634-2.

[217] A. Hidayat, Rochmadi, K. Wijaya, A. Nurdiawati, W. Kurniawan, H. Hinode, K. Yoshikawa, A. Budiman, Esterification of Palm Fatty Acid Distillate with High Amount of Free Fatty Acids Using Coconut Shell Char Based Catalyst, Energy Procedia 75 (2015) 969–974. https://doi.org/https://doi.org/10.1016/j.egypro.2015.07.301.

[218] A.M. Dehkhoda, A.H. West, N. Ellis, Biochar based solid acid catalyst for biodiesel production, Appl Catal A Gen 382 (2010) 197–204. https://doi.org/https://doi.org/10.1016/j.apcata.2010.04.051.

[219] A. Mukherjee, A.R. Zimmerman, W. Harris, Surface chemistry variations among a series of laboratory-produced biochars, Geoderma 163 (2011) 247–255. https://doi.org/https://doi.org/10.1016/j.geoderma.2011.04.021.

[220] L. Kong, Y. Xiong, L. Sun, S. Tian, X. Xu, C. Zhao, R. Luo, X. Yang, K. Shih, H. Liu, Sorption performance and mechanism of a sludge-derived char as porous carbon-based hybrid adsorbent for benzene derivatives in aqueous solution, J Hazard Mater 274 (2014) 205–211. https://doi.org/https://doi.org/10.1016/j.jhazmat.2014.04.014.

[221] K. Sardar, S. Ali, S. Hameed, S. Afzal, S. Fatima, M.B. Shakoor, S.A. Bharwana, H.M. Tauqeer, Heavy Metals Contamination and what are the Impacts on Living Organisms, Greener Journal of Environmental Management and Public Safety 2 (2013) 172–179. https://doi.org/10.15580/gjemps.2013.4.060413652.

[222] J. Ahmad, F. Patuzzi, T.D.U. Rashid, M. Shahabz, C. Ngamcharussrivichai, M. Baratieri, Exploring untapped effect of process conditions on biochar characteristics and applications, Environ Technol Innov 21 (2020) 101310. https://doi.org/10.1016/j.eti.2020.101310.

[223] T. Mondal, J.K. Datta, N.K. Mondal, Chemical fertilizer in conjunction with biofertilizer and vermicompost induced changes in morpho-physiological and bio-chemical traits of mustard crop, Journal of the Saudi Society of Agricultural Sciences 16 (2017) 135–144. https://doi.org/https://doi.org/10.1016/j.jssas.2015.05.001.

[224] C.J. Barrow, Biochar: Potential for countering land degradation and for improving agriculture, Applied Geography 34 (2012) 21–28. https://doi.org/https://doi.org/10.1016/j.apgeog.2011.09.008.

[225] S.P. Sohi, E. Krull, E. Lopez-Capel, R. Bol, Chapter 2 - A Review of Biochar and Its Use and Function in Soil, in: Advances in Agronomy, Academic Press, 2010: pp. 47–82. https://doi.org/https://doi.org/10.1016/S0065-2113(10)05002-9.

[226] J.-H. Yuan, R.-K. Xu, N. Wang, J.-Y. Li, Amendment of Acid Soils with Crop Residues and Biochars, Pedosphere 21 (2011) 302–308. https://doi.org/https://doi.org/10.1016/S1002-0160(11)60130-6.

[227] A.M. Dehkhoda, N. Ellis, E. Gyenge, Electrosorption on activated biochar: effect of thermo-chemical activation treatment on the electric double layer capacitance, J Appl Electrochem 44 (2014) 141–157. https://doi.org/10.1007/s10800-013-0616-4.

[228] A. Elmouwahidi, Z. Zapata-Benabithe, F. Carrasco-Marín, C. Moreno-Castilla, Activated carbons from KOH-activation of argan (Argania spinosa) seed shells as supercapacitor electrodes, Bioresour Technol 111 (2012) 185–190. https://doi.org/https://doi.org/10.1016/j.biortech.2012.02.010.

[229] J. Jiang, L. Zhang, X. Wang, N. Holm, K. Rajagopalan, F. Chen, S. Ma, Highly ordered macroporous woody biochar with ultra-high carbon content as supercapacitor electrodes, Electrochim Acta 113 (2013) 481–489. https://doi.org/https://doi.org/10.1016/j.electacta.2013.09.121.

[230] X. Gu, Y. Wang, C. Lai, J. Qiu, S. Li, Y. Hou, W. Martens, N. Mahmood, S. Zhang, Microporous bamboo biochar for lithium-sulfur batteries, Nano Res 8 (2015) 129–139. https://doi.org/10.1007/s12274-014-0601-1.

[231] L. Zhang, J. Jiang, N. Holm, F. Chen, Mini-chunk biochar supercapacitors, J Appl Electrochem 44 (2014) 1145–1151. https://doi.org/10.1007/s10800-014-0726-7.

[232] H. Demiral, C. Güngör, Adsorption of copper(II) from aqueous solutions on activated carbon prepared from grape bagasse, J Clean Prod 124 (2016) 103–113. https://doi.org/https://doi.org/10.1016/j.jclepro.2016.02.084.

[233] G.Z. Kyzas, Commercial Coffee Wastes as Materials for Adsorption of Heavy Metals from Aqueous Solutions, Materials 5 (2012) 1826. https://doi.org/10.3390/MA5101826.

[234] G.Z. Kyzas, E.A. Deliyanni, K.A. Matis, Activated carbons produced by pyrolysis of waste potato peels: Cobalt ions removal by adsorption, Colloids Surf A Physicochem Eng Asp 490 (2016) 74–83. https://doi.org/https://doi.org/10.1016/j.colsurfa.2015.11.038.

[235] M. Ghaedi, H. Mazaheri, S. Khodadoust, S. Hajati, M.K. Purkait, Application of central composite design for simultaneous removal of methylene blue and Pb2+ ions by walnut wood activated carbon, Spectrochim Acta A Mol Biomol Spectrosc 135 (2015) 479–490. https://doi.org/https://doi.org/10.1016/j.saa.2014.06.138.

[236] G.A. Idowu, A.J. Fletcher, The Manufacture and Characterisation of Rosid Angiosperm-Derived Biochars Applied to Water Treatment, Bioenergy Res 13 (2020) 387–396. https://doi.org/10.1007/s12155-019-10074-x.

[237] K. Wilson, H. Yang, C.W. Seo, W.E. Marshall, Select metal adsorption by activated carbon made from peanut shells, Bioresour Technol 97 (2006) 2266–2270. https://doi.org/https://doi.org/10.1016/j.biortech.2005.10.043.

[238] M. Inyang, B. Gao, Y. Yao, Y. Xue, A.R. Zimmerman, P. Pullammanappallil, X. Cao, Removal of heavy metals from aqueous solution by biochars derived from anaerobically digested biomass, Bioresour Technol 110 (2012) 50–56. https://doi.org/https://doi.org/10.1016/j.biortech.2012.01.072.

[239] G. Cimino, A. Passerini, G. Toscano, Removal of toxic cations and Cr(VI) from aqueous solution by hazelnut shell, Water Res 34 (2000) 2955–2962. https://doi.org/https://doi.org/10.1016/S0043-1354(00)00048-8.

[240] E. Marañón, H. Sastre, Heavy metal removal in packed beds using apple wastes, Bioresour Technol 38 (1991) 39–43. https://doi.org/https://doi.org/10.1016/0960-8524(91)90219-A.

[241] B.T. Nguyen, J. Lehmann, W.C. Hockaday, S. Joseph, C.A. Masiello, Temperature Sensitivity of Black Carbon Decomposition and Oxidation, Environ Sci Technol 44 (2010) 3324–3331. https://doi.org/10.1021/es903016y.

[242] E.F. Zama, Y.-G. Zhu, B.J. Reid, G.-X. Sun, The role of biochar properties in influencing the sorption and desorption of Pb(II), Cd(II) and As(III) in aqueous solution, J Clean Prod 148 (2017) 127–136. https://doi.org/https://doi.org/10.1016/j.jclepro.2017.01.125.

[243] X. Chen, G. Chen, L. Chen, Y. Chen, J. Lehmann, M.B. McBride, A.G. Hay, Adsorption of copper and zinc by biochars produced from pyrolysis of hardwood and corn straw in aqueous solution, Bioresour Technol 102 (2011) 8877–8884. https://doi.org/https://doi.org/10.1016/j.biortech.2011.06.078.

[244] S.F. Vaughn, J.A. Kenar, F.J. Eller, B.R. Moser, M.A. Jackson, S.C. Peterson, Physical and chemical characterization of biochars produced from coppiced wood of thirteen tree species for use in horticultural substrates, Ind Crops Prod 66 (2015) 44–51. https://doi.org/https://doi.org/10.1016/j.indcrop.2014.12.026.

[245] K. Jindo, H. Mizumoto, Y. Sawada, M.A. Sanchez-Monedero, T. Sonoki, Physical and chemical characterization of biochars derived from different agricultural residues, Biogeosciences 11 (2014) 6613–6621. https://doi.org/10.5194/bg-11-6613-2014.

[246] Q. Fang, B. Chen, Y. Lin, Y. Guan, Aromatic and Hydrophobic Surfaces of Wood-derived Biochar Enhance Perchlorate Adsorption via Hydrogen Bonding to Oxygen-containing Organic Groups, Environ Sci Technol 48 (2014) 279–288. https://doi.org/10.1021/es403711y.

[247] M. Hassan, Y. Liu, R. Naidu, S.J. Parikh, J. Du, F. Qi, I.R. Willett, Influences of feedstock sources and pyrolysis temperature on the properties of biochar and functionality as adsorbents: A meta-analysis, Science of The Total Environment 744 (2020) 140714. https://doi.org/https://doi.org/10.1016/j.scitotenv.2020.140714.

[248] L. Leng, H. Huang, An overview of the effect of pyrolysis process parameters on biochar stability, Bioresour Technol 270 (2018) 627–642. https://doi.org/https://doi.org/10.1016/j.biortech.2018.09.030.

[249] D. Rehrah, R.R. Bansode, O. Hassan, M. Ahmedna, Short-term greenhouse emission lowering effect of biochars from solid organic municipal wastes, International Journal of Environmental Science and Technology 15 (2018) 1093–1102. https://doi.org/10.1007/s13762-017-1470-4.

[250] Y.X. Seow, Y.H. Tan, N.M. Mubarak, J. Kansedo, M. Khalid, M.L. Ibrahim, M. Ghasemi, A review on biochar production from different biomass wastes by recent carbonization technologies and its sustainable applications, J Environ Chem Eng 10 (2022) 107017. https://doi.org/https://doi.org/10.1016/j.jece.2021.107017.

[251] R. Roncancio, J.P. Gore, CO2 char gasification: A systematic review from 2014 to 2020, Energy Conversion and Management: X 10 (2021) 100060. https://doi.org/https://doi.org/10.1016/j.ecmx.2020.100060.

[252] A.E. Pütün, A. Özcan, E. Pütün, Pyrolysis of hazelnut shells in a fixed-bed tubular reactor: yields and structural analysis of bio-oil, J Anal Appl Pyrolysis 52 (1999) 33–49. https://doi.org/https://doi.org/10.1016/S0165-2370(99)00044-3.

[253] F. Ateş, E. Pütün, A.E. Pütün, Fast pyrolysis of sesame stalk: yields and structural analysis of bio-oil, J Anal Appl Pyrolysis 71 (2004) 779–790. https://doi.org/https://doi.org/10.1016/j.jaap.2003.11.001.

[254] M. Tripathi, J.N. Sahu, P. Ganesan, Effect of process parameters on production of biochar from biomass waste through pyrolysis: A review, Renewable and Sustainable Energy Reviews 55 (2016) 467–481. https://doi.org/10.1016/j.rser.2015.10.122.

[255] J. Lehmann, S. Joseph, Biochar for Environmental Management, 2nd ed., Routledge, London, 2015. https://doi.org/https://doi.org/10.4324/9780203762264.

[256] L. Luo, C. Xu, Z. Chen, S. Zhang, Properties of biomass-derived biochars: Combined effects of operating conditions and biomass types, Bioresour Technol 192 (2015) 83–89. https://doi.org/https://doi.org/10.1016/j.biortech.2015.05.054.

[257] L. Leng, Q. Xiong, L. Yang, H. Li, Y. Zhou, W. Zhang, S. Jiang, H. Li, H. Huang, An overview on engineering the surface area and porosity of biochar, Science of The Total Environment 763 (2021) 144204. https://doi.org/https://doi.org/10.1016/j.scitotenv.2020.144204.

[258] K. Zeng, D.P. Minh, D. Gauthier, E. Weiss-Hortala, A. Nzihou, G. Flamant, The effect of temperature and heating rate on char properties obtained from solar pyrolysis of beech wood, Bioresour Technol 182 (2015) 114–119. https://doi.org/https://doi.org/10.1016/j.biortech.2015.01.112.

[259] J. Pallarés, A. González-Cencerrado, I. Arauzo, Production and characterization of activated carbon from barley straw by physical activation with carbon dioxide and steam, Biomass Bioenergy 115 (2018) 64–73. https://doi.org/https://doi.org/10.1016/j.biombioe.2018.04.015.

[260] M. Ertaş, M. Hakkı Alma, Pyrolysis of laurel (Laurus nobilis L.) extraction residues in a fixed-bed reactor: Characterization of bio-oil and bio-char, J Anal Appl Pyrolysis 88 (2010) 22–29. https://doi.org/https://doi.org/10.1016/j.jaap.2010.02.006.

[261] A. Heidari, R. Stahl, H. Younesi, A. Rashidi, N. Troeger, A.A. Ghoreyshi, Effect of process conditions on product yield and composition of fast pyrolysis of Eucalyptus grandis in fluidized bed reactor, Journal of Industrial and Engineering Chemistry 20 (2014) 2594–2602. https://doi.org/https://doi.org/10.1016/j.jiec.2013.10.046.

[262] H. Zhang, R. Xiao, H. Huang, G. Xiao, Comparison of non-catalytic and catalytic fast pyrolysis of corncob in a fluidized bed reactor, Bioresour Technol 100 (2009) 1428–1434. https://doi.org/https://doi.org/10.1016/j.biortech.2008.08.031.

[263] C. Bouchelta, M.S. Medjram, M. Zoubida, F.A. Chekkat, N. Ramdane, J.-P. Bellat, Effects of pyrolysis conditions on the porous structure development of date pits activated carbon, J Anal Appl Pyrolysis 94 (2012) 215–222. https://doi.org/https://doi.org/10.1016/j.jaap.2011.12.014.

[264] A.C. Lua, F.Y. Lau, J. Guo, Influence of pyrolysis conditions on pore development of oil-palm-shell activated carbons, J Anal Appl Pyrolysis 76 (2006) 96–102. https://doi.org/https://doi.org/10.1016/j.jaap.2005.08.001.

[265] D. Angın, Effect of pyrolysis temperature and heating rate on biochar obtained from pyrolysis of safflower seed press cake, Bioresour Technol 128 (2013) 593–597. https://doi.org/https://doi.org/10.1016/j.biortech.2012.10.150.

[266] S. Şensöz, D. Angın, Pyrolysis of safflower (Charthamus tinctorius L.) seed press cake: Part 1. The effects of pyrolysis parameters on the product yields, Bioresour Technol 99 (2008) 5492–5497. https://doi.org/https://doi.org/10.1016/j.biortech.2007.10.046.

[267] T. Aysu, M.M. Küçük, Biomass pyrolysis in a fixed-bed reactor: Effects of pyrolysis parameters on product yields and characterization of products, Energy 64 (2014) 1002–1025. https://doi.org/https://doi.org/10.1016/j.energy.2013.11.053.

[268] D. Chen, Y. Li, K. Cen, M. Luo, H. Li, B. Lu, Pyrolysis polygeneration of poplar wood: Effect of heating rate and pyrolysis temperature, Bioresour Technol 218 (2016) 780–788. https://doi.org/https://doi.org/10.1016/j.biortech.2016.07.049.

[269] H.J. Park, Y.-K. Park, J.S. Kim, Influence of reaction conditions and the char separation system on the production of bio-oil from radiata pine sawdust by fast pyrolysis, Fuel Processing Technology 89 (2008) 797–802. https://doi.org/https://doi.org/10.1016/j.fuproc.2008.01.003.

[270] W.T. Tsai, M.K. Lee, Y.M. Chang, Fast pyrolysis of rice husk: Product yields and compositions, Bioresour Technol 98 (2007) 22–28. https://doi.org/https://doi.org/10.1016/j.biortech.2005.12.005.

[271] A.R. Mohamed, Z. Hamzah, M.Z.M. Daud, Z. Zakaria, The Effects of Holding Time and the Sweeping Nitrogen Gas Flowrates on the Pyrolysis of EFB using a Fixed–Bed Reactor, Procedia Eng 53 (2013) 185–191. https://doi.org/https://doi.org/10.1016/j.proeng.2013.02.024.

[272] W.T. Tsai, C.Y. Chang, S.L. Lee, Preparation and characterization of activated carbons from corn cob, Carbon N Y 35 (1997) 1198–1200. https://doi.org/https://doi.org/10.1016/S0008-6223(97)84654-4.

[273] B. Zhao, D. O’Connor, J. Zhang, T. Peng, Z. Shen, D.C.W. Tsang, D. Hou, Effect of pyrolysis temperature, heating rate, and residence time on rapeseed stem derived biochar, J Clean Prod 174 (2018) 977–987. https://doi.org/https://doi.org/10.1016/j.jclepro.2017.11.013.

[274] E. Cetin, R. Gupta, B. Moghtaderi, Effect of pyrolysis pressure and heating rate on radiata pine char structure and apparent gasification reactivity, Fuel 84 (2005) 1328–1334. https://doi.org/https://doi.org/10.1016/j.fuel.2004.07.016.

[275] F. Melligan, R. Auccaise, E.H. Novotny, J.J. Leahy, M.H.B. Hayes, W. Kwapinski, Pressurised pyrolysis of Miscanthus using a fixed bed reactor, Bioresour Technol 102 (2011) 3466–3470. https://doi.org/https://doi.org/10.1016/j.biortech.2010.10.129.

[276] J.J. Manyà, F.X. Roca, J.F. Perales, TGA study examining the effect of pressure and peak temperature on biochar yield during pyrolysis of two-phase olive mill waste, J Anal Appl Pyrolysis 103 (2013) 86–95. https://doi.org/https://doi.org/10.1016/j.jaap.2012.10.006.

[277] M.J. Antal, M. Grønli, The Art, Science, and Technology of Charcoal Production, Ind Eng Chem Res 42 (2003) 1619–1640. https://doi.org/10.1021/ie0207919.

[278] M. Zhao, L. Huang, S. Raj, B. Arulmani, J. Yan, L. Wu, T. Wu, H. Zhang, T. Xiao, Adsorption of Different Pollutants by Using Microplastic with Different Influencing Factors and Mechanisms in Wastewater: A Review, (2022). https://doi.org/10.3390/nano12132256.

[279] W.J. Weber, Adsorption processes, Pure and Applied Chemistry 37 (1974) 375–392. https://doi.org/10.1351/PAC197437030375/MACHINEREADABLECITATION/RIS.

[280] R. Deloach, Analysis of Variance in the Modern Design of Experiments, in: American Institute of Aeronautics and Astronautics, n.d. https://doi.org/10.2514/6.2010-1111.

[281] B. Durakovic, Design of experiments application, concepts, examples: State of the art, Periodicals of Engineering and Natural Sciences (PEN) 5 (2017). https://doi.org/10.21533/pen.v5i3.145.

[282] S. Oimoen, Classical Designs: Full Factorial Designs, (2019). www.afit.edu/STAT. (accessed January 10, 2024).

[283] M. Barad, Design of Experiments (DOE)—A Valuable Multi-Purpose Methodology, Appl Math (Irvine) 05 (2014) 2120–2129. https://doi.org/10.4236/am.2014.514206.

[284] W. Cao, J. Li, L. Lin, X. Zhang, Release of potassium in association with structural evolution during biomass combustion, Fuel 287 (2021) 119524. https://doi.org/https://doi.org/10.1016/j.fuel.2020.119524.

[285] S.L.-K. svenska vetenskapsakademiens. Handlingar, undefined 1898, Zur theorie der sogenannten adsorption geloster stoffe, Cir.Nii.Ac.Jp (n.d.). https://cir.nii.ac.jp/crid/1572824501080908544 (accessed July 17, 2023).

[286] H. Moussout, H. Ahlafi, M. Aazza, H. Maghat, Critical of linear and nonlinear equations of pseudo-first order and pseudo-second order kinetic models, Karbala International Journal of Modern Science 4 (2018) 244–254. https://doi.org/10.1016/J.KIJOMS.2018.04.001.

[287] Y. Liu, L. Shen, From Langmuir kinetics to first- and second-order rate equations for adsorption, Langmuir 24 (2008) 11625–11630. https://doi.org/10.1021/LA801839B/ASSET/IMAGES/MEDIUM/LA-2008-01839B_0004.GIF.

[288] S. Azizian, Kinetic models of sorption: a theoretical analysis, J Colloid Interface Sci 276 (2004) 47–52. https://doi.org/10.1016/J.JCIS.2004.03.048.

[289] J. Wang, X. Guo, Adsorption kinetic models: Physical meanings, applications, and solving methods, (2020). https://doi.org/10.1016/j.jhazmat.2020.122156.

[290] Y.S. Ho, G. McKay, Sorption of dye from aqueous solution by peat, Chemical Engineering Journal 70 (1998) 115–124. https://doi.org/10.1016/S1385-8947(98)00076-X.

[291] M. Parsa, M. Nourani, M. Baghdadi, M. Hosseinzadeh, M. Pejman, Biochars derived from marine macroalgae as a mesoporous by-product of hydrothermal liquefaction process: Characterization and application in wastewater

treatment, Journal of Water Process Engineering 32 (2019) 100942. https://doi.org/https://doi.org/10.1016/j.jwpe.2019.100942.

[292] A.B.D. Nandiyanto, R. Oktiani, R. Ragadhita, How to Read and Interpret FTIR Spectroscope of Organic Material, Indonesian Journal of Science and Technology 4 (2019) 97. https://doi.org/10.17509/ijost.v4i1.15806.

[293] J.W. Lee, M. Kidder, B.R. Evans, S. Paik, A.C. Buchanan Iii, C.T. Garten, R.C. Brown, Characterization of Biochars Produced from Cornstovers for Soil Amendment, Environ Sci Technol 44 (2010) 7970–7974. https://doi.org/10.1021/es101337x.

[294] C.A. Rey-Mafull, J.E. Tacoronte, R. Garcia, J. Tobella, J.C. Llópiz, A. Iglesias, D. Hotza, Comparative study of the adsorption of acetaminophen on activated carbons in simulated gastric fluid, Springerplus 3 (2014) 48. https://doi.org/10.1186/2193-1801-3-48.

[295] M. Ahmad, A.U. Rajapaksha, J.E. Lim, M. Zhang, N. Bolan, D. Mohan, M. Vithanage, S.S. Lee, Y.S. Ok, Biochar as a sorbent for contaminant management in soil and water: A review, Chemosphere 99 (2014) 19–33. https://doi.org/https://doi.org/10.1016/j.chemosphere.2013.10.071.

[296] F. Rees, F. Watteau, S. Mathieu, M. Turpault, Y. Le Brech, R. Qiu, J.L. Morel, Metal Immobilization on Wood-Derived Biochars: Distribution and Reactivity of Carbonate Phases, J Environ Qual 46 (2017) 845–854. https://doi.org/10.2134/JEQ2017.04.0152.

[297] W.-J. Liu, H. Jiang, H.-Q. Yu, Emerging applications of biochar-based materials for energy storage and conversion, Energy Environ Sci 12 (2019) 1751–1779. https://doi.org/10.1039/c9ee00206e.

[298] E.H. El-Masry, H.A. Ibrahim, O.A. Abdel Moamen, W.F. Zaher, Sorption of some rare earth elements from aqueous solutions using copolymer/activated carbon

composite: Multivariate optimization approach, Advanced Powder Technology 33 (2022) 103467. https://doi.org/https://doi.org/10.1016/j.apt.2022.103467.

[299] S.S.J. Warne, Proximate analysis of coal, oil shale, low quality fossil fuels and related materials by thermogravimetry, TrAC Trends in Analytical Chemistry 10 (1991) 195–199. https://doi.org/https://doi.org/10.1016/0165-9936(91)85021-I.

[300] S. Li, G. Chen, Thermogravimetric, thermochemical, and infrared spectral characterization of feedstocks and biochar derived at different pyrolysis temperatures, Waste Management 78 (2018) 198–207. https://doi.org/https://doi.org/10.1016/j.wasman.2018.05.048.

[301] J. Sun, F. He, Y. Pan, Z. Zhang, Effects of pyrolysis temperature and residence time on physicochemical properties of different biochar types, Acta Agric Scand B Soil Plant Sci 67 (2017) 12–22. https://doi.org/10.1080/09064710.2016.1214745.

[302] L. Usevičiūtė, E. Baltrėnaitė, Methods for Determining Lignocellulosic Biochar Wettability, Waste Biomass Valorization 11 (2020) 4457–4468. https://doi.org/10.1007/s12649-019-00713-x.

[303] S. Bubici, J.-P. Korb, J. Kučerik, P. Conte, Evaluation of the surface affinity of water in three biochars using fast field cycling NMR relaxometry, Magnetic Resonance in Chemistry 54 (2016) 365–370. https://doi.org/10.1002/mrc.4391.

[304] Y. Yuan, T.R. Lee, Contact Angle and Wetting Properties, in: Springer Berlin Heidelberg, 2013: pp. 3–34. https://doi.org/10.1007/978-3-642-34243-1_1.

[305] C.E. Brewer, V.J. Chuang, C.A. Masiello, H. Gonnermann, X. Gao, B. Dugan, L.E. Driver, P. Panzacchi, K. Zygourakis, C.A. Davies, New approaches to measuring biochar density and porosity, Biomass Bioenergy 66 (2014) 176–185. https://doi.org/10.1016/J.BIOMBIOE.2014.03.059.

[306] CEN, EN 15150:2011 - Solid biofuels - Determination of particle density, Brussels, 2011. https://standards.iteh.ai/catalog/standards/cen/62c7ed65-453d-4a5f-bd18-b997ceee9f6e/en-15150-2011 (accessed August 21, 2023).

[307] C.E. Brewer, J. Levine, Weight or Volume for Handling Biochar and Biomass?, The Biochar Journal (2015). https://www.biochar-journal.org/en/ct/71 (accessed August 21, 2023).

[308] J. Lehmann, S. Joseph, eds., Biochar for Environmental Management, 2nd ed., Routledge, London, 2015. https://doi.org/https://doi.org/10.4324/9780203762264.

[309] E.N. Bakatula, D. Richard, C.M. Neculita, G.J. Zagury, Determination of point of zero charge of natural organic materials, Environmental Science and Pollution Research 25 (2018) 7823–7833. https://doi.org/10.1007/s11356-017-1115-7.

[310] S.M. Shaheen, N.K. Niazi, E. Noha, I. Bibi, H. Wang, Daniel, Y.S. Ok, N. Bolan, J. Rinklebe, Wood-based biochar for the removal of potentially toxic elements in water and wastewater: a critical review, International Materials Reviews 64 (2019) 216–247. https://doi.org/10.1080/09506608.2018.1473096.

[311] H. Zhang, R.P. Voroney, G.W. Price, Effects of temperature and processing conditions on biochar chemical properties and their influence on soil C and N transformations, Soil Biol Biochem 83 (2015) 19–28. https://doi.org/https://doi.org/10.1016/j.soilbio.2015.01.006.

[312] M. Pipíška, E.K. Krajčíková, M. Hvostik, V. Frišták, L. Ďuriška, I. Černičková, M. Kaňuchová, P. Conte, G. Soja, Biochar from Wood Chips and Corn Cobs for Adsorption of Thioflavin T and Erythrosine B, Materials 15 (2022). https://doi.org/10.3390/ma15041492.

[313] K.K.R. Reddygunta, A. Callander, L. Šiller, K. Faulds, L. Berlouis, A. Ivaturi, Sono-exfoliated graphene-like activated carbon from hazelnut shells for flexible

supercapacitors, Int J Energy Res 46 (2022) 16512–16537. https://doi.org/10.1002/ER.8314.

[314] K.L. Smith, K.M. Black, Characterization of the treated surfaces of silicon alloyed pyrolytic carbon and SiC, Journal of Vacuum Science & Technology A 2 (1984) 744–747. https://doi.org/10.1116/1.572562.

[315] J.B. Lhoest, P. Bertrand, L.T. Weng, J.L. Dewez, Combined Time-of-Flight Secondary Ion Mass Spectrometry and X-ray Photoelectron Spectroscopy Study of the Surface Segregation of Poly(methyl methacrylate) (PMMA) in Bisphenol a Polycarbonate/PMMA Blends, Macromolecules 28 (1995) 4631–4637. https://doi.org/10.1021/MA00117A038/ASSET/MA00117A038.FP.PNG_V03.

[316] K. Wagener, C. Batich, B. Kirsch, S. Wanigatunga, Chain propagation/step propagation polymerization. III. An XPS investigation of poly(oxyethylene)-b-poly(pivalolactone) telechelomer, J Polym Sci A Polym Chem 27 (1989) 2625–2631. https://doi.org/10.1002/POLA.1989.080270811.

[317] G. Beamson, D. Briggs, High Resolution XPS of Organic Polymers: The Scienta ESCA300 Database, J Chem Educ 70 (1992) A25. https://doi.org/10.1021/ED070PA25.5.

[318] G.P. López, D.G. Castner, B.D. Ratner, XPS O 1s binding energies for polymers containing hydroxyl, ether, ketone and ester groups, Surface and Interface Analysis 17 (1991) 267–272. https://doi.org/10.1002/SIA.740170508.

[319] NIST X-ray Photoelectron Spectroscopy (XPS) Database, Version 3.5, (n.d.). https://srdata.nist.gov/xps/ (accessed August 1, 2023).

[320] M.U. Jamal, A.J. Fletcher, Design of Experiments Study on Scottish Wood Biochars and Process Parameter Influence on Final Biochar Characteristics, Bioenergy Res 1 (2023) 1–14. https://doi.org/10.1007/S12155-023-10595-6/FIGURES/6.

[321] A.G. Shard, Practical guides for x-ray photoelectron spectroscopy: Quantitative XPS, Journal of Vacuum Science & Technology A: Vacuum, Surfaces, and Films 38 (2020) 41201. https://doi.org/10.1116/1.5141395/246897.

[322] R. Rattanakam, P. Pituya, M. Suwan, S. Supothina, Assessment of Hydrophilic Biochar Effect on Sandy Soil Water Retention, Key Eng Mater 751 (2017) 790–795. https://doi.org/10.4028/www.scientific.net/KEM.751.790.

[323] M. El Saied, · Seham, A. Shaban, · Mohsen, S. Mostafa, A.O. Abo, E. Naga, Efficient adsorption of acetaminophen from the aqueous phase using low-cost and renewable adsorbent derived from orange peels, Biomass Convers Biorefin 1 (n.d.) 3. https://doi.org/10.1007/s13399-022-02541-x.

[324] T.W. Weber, R.K. Chakravorti, Pore and solid diffusion models for fixed-bed adsorbers, AIChE Journal 20 (1974) 228–238. https://doi.org/10.1002/AIC.690200204.

[325] S. Polati, F. Gosetti, V. Gianotti, M.C. Gennaro, Sorption and desorption behavior of chloroanilines and chlorophenols on montmorillonite and kaolinite, J Environ Sci Health B 41 (2006) 765–779. https://doi.org/10.1080/03601230600805774.

[326] M. Quirantes, R. Nogales, E. Romero, Sorption potential of different biomass fly ashes for the removal of diuron and 3,4-dichloroaniline from water, J Hazard Mater 331 (2017) 300–308. https://doi.org/10.1016/J.JHAZMAT.2017.02.047.

[327] D. Huguenot, P. Bois, K. Jézéquel, J.Y. Cornu, T. Lebeau, Selection of low cost materials for the sorption of copper and herbicides as single or mixed compounds in increasing complexity matrices, J Hazard Mater 182 (2010) 18–26. https://doi.org/10.1016/J.JHAZMAT.2010.05.062.

[328] N. Abd, E. Youssef, E. Amer, A.O. Abo, E. Naga, S.A. Shaban, Molten salt synthesis of hierarchically porous carbon for the efficient adsorptive removal

of sodium diclofenac from aqueous effluents, (2020). https://doi.org/10.1016/j.jtice.2020.07.018.

[329] W.J. WeberJr., J.C. Morris, Kinetics of Adsorption on Carbon from Solution, Journal of the Sanitary Engineering Division 89 (1963) 31–59. https://doi.org/10.1061/JSEDAI.0000430.

[330] Z. Zhao, W. Sun, M.B. Ray, Adsorption isotherms and kinetics for the removal of algal organic matter by granular activated carbon, Science of The Total Environment 806 (2022) 150885. https://doi.org/10.1016/J.SCITOTENV.2021.150885.

[331] Y. Wang, C. Lin, X. Liu, W. Ren, X. Huang, M. He, W. Ouyang, Efficient removal of acetochlor pesticide from water using magnetic activated carbon: Adsorption performance, mechanism, and regeneration exploration, Science of The Total Environment 778 (2021) 146353. https://doi.org/10.1016/J.SCITOTENV.2021.146353.

[332] G. Bataillou, C. Lee, V. Monnier, T. Gerges, A. Sabac, C. Vollaire, N. Haddour, Cedar Wood-Based Biochar: Properties, Characterization, and Applications as Anodes in Microbial Fuel Cell, Appl Biochem Biotechnol 194 (2022) 4169–4186. https://doi.org/10.1007/S12010-022-03997-3.

[333] L.P. Bakhaeva, G.K. Vasilyeva, E.G. Surovtseva, V.M. Mukhin, Microbial degradation of 3,4-dichloroaniline sorbed by activated carbon, Microbiology (N Y) 70 (2001) 277–284. https://doi.org/10.1023/A:1010495025794/METRICS.

[334] I. Quesada-Peñate, C. Julcour-Lebigue, U.J. Jáuregui-Haza, A.M. Wilhelm, H. Delmas, Degradation of paracetamol by catalytic wet air oxidation and sequential adsorption – Catalytic wet air oxidation on activated carbons, J Hazard Mater 221–222 (2012) 131–138. https://doi.org/10.1016/J.JHAZMAT.2012.04.021.

[335] G. Chu, J. Zhao, Y. Liu, D. Lang, M. Wu, B. Pan, C.E.W. Steinberg, The relative importance of different carbon structures in biochars to carbamazepine and bisphenol A sorption, J Hazard Mater 373 (2019) 106–114. https://doi.org/10.1016/J.JHAZMAT.2019.03.078.

[336] E.M. El Mouchtari, C. Daou, S. Rafqah, F. Najjar, H. Anane, A. Piram, A. Hamade, S. Briche, P. Wong-Wah-Chung, TiO2 and activated carbon of Argania Spinosa tree nutshells composites for the adsorption photocatalysis removal of pharmaceuticals from aqueous solution, J Photochem Photobiol A Chem 388 (2020) 112183. https://doi.org/10.1016/J.JPHOTOCHEM.2019.112183.

[337] H.B. Quesada, L.F. Cusioli, C. de O Bezerra, A.T.A. Baptista, L. Nishi, R.G. Gomes, R. Bergamasco, Acetaminophen adsorption using a low-cost adsorbent prepared from modified residues of Moringa oleifera Lam. seed husks, Journal of Chemical Technology & Biotechnology 94 (2019) 3147–3157. https://doi.org/10.1002/JCTB.6121.

Appendices

Appendices List of Tables

Appendices List of Figures

Appendix A: Proximate Analysis Plots

This section includes the TGA plots for biochars developed as part of the design of experiments (DoE) approach adopted within this study.

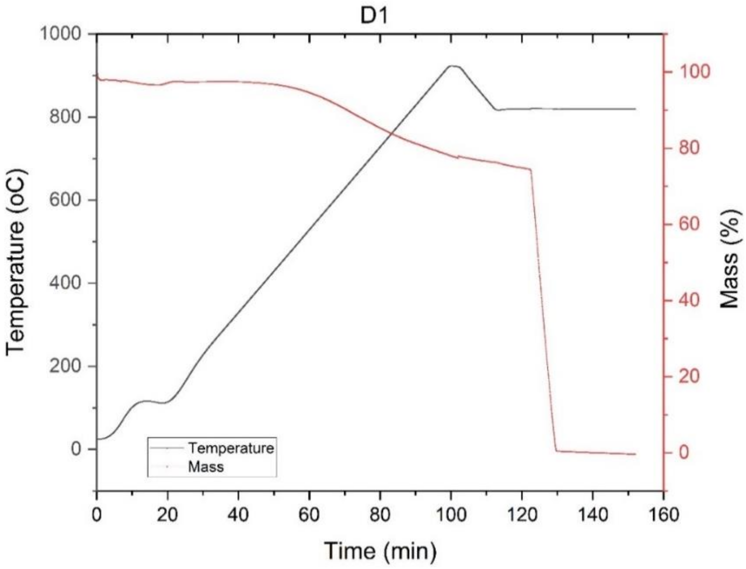

Figure A1 TGA profile for biochar D1

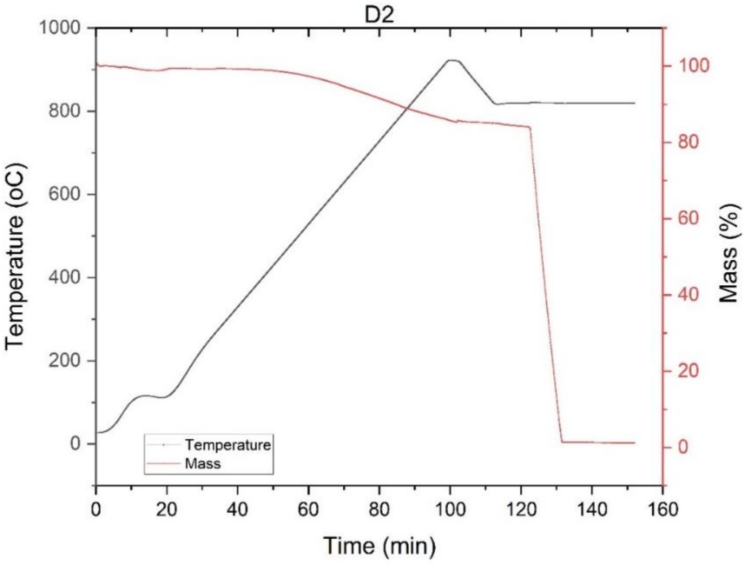

Figure A2 TGA profile for biochar D2

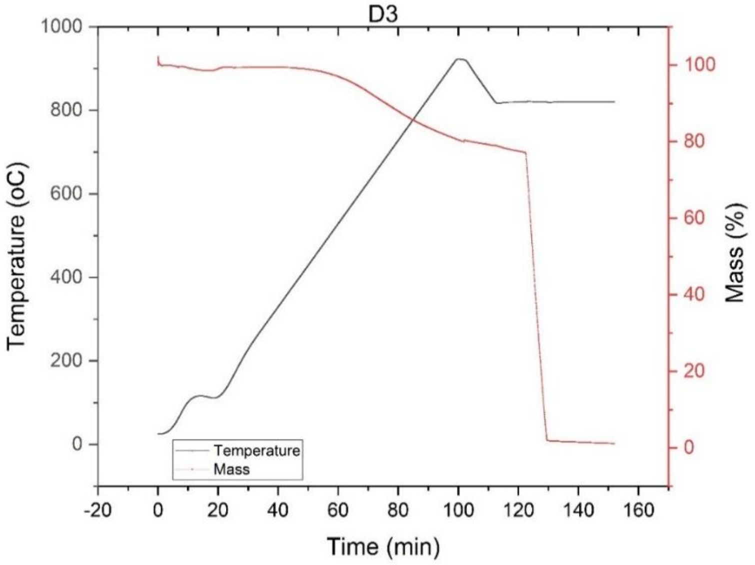

Figure A3 TGA profile for biochar D3

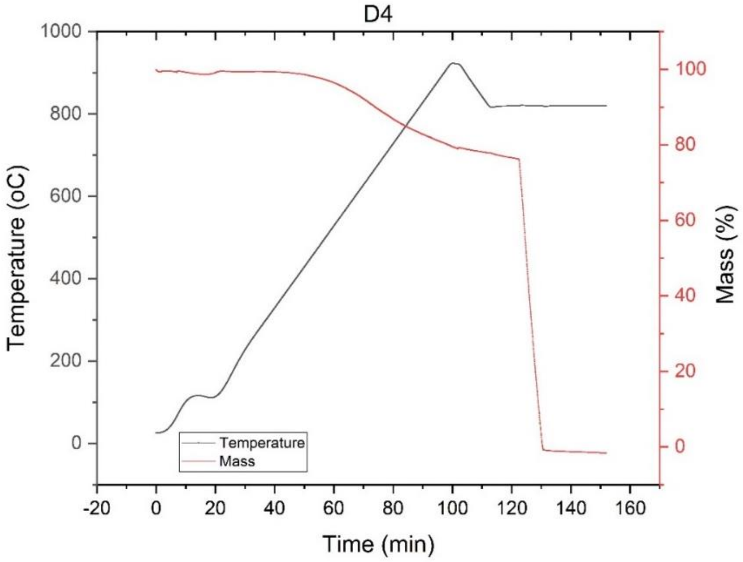

Figure A4 TGA profile for biochar D4

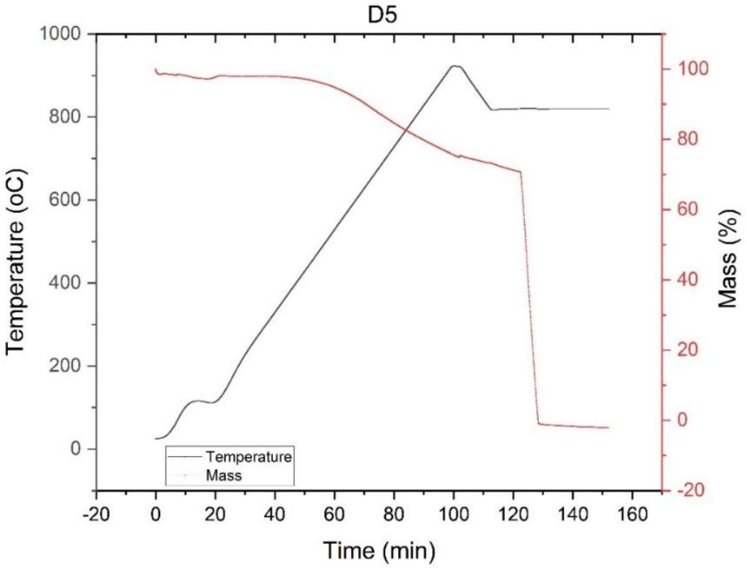

Figure A5 TGA profile for biochar D5

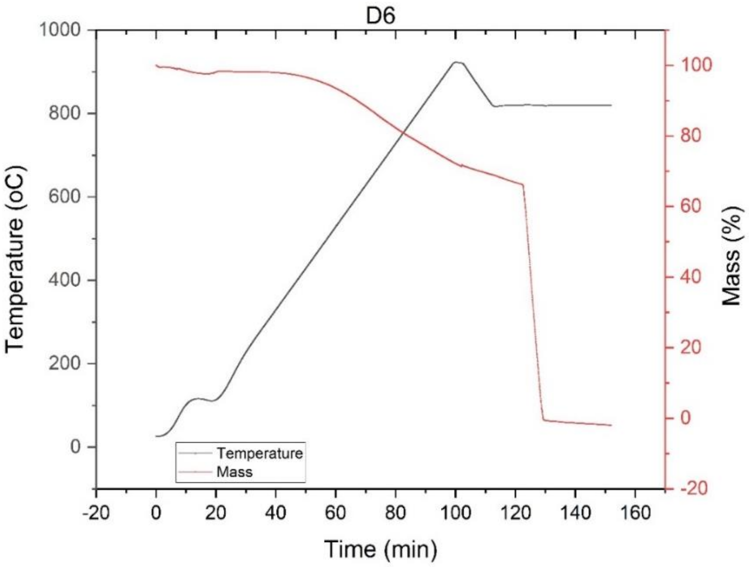

Figure A6 TGA profile for biochar D6

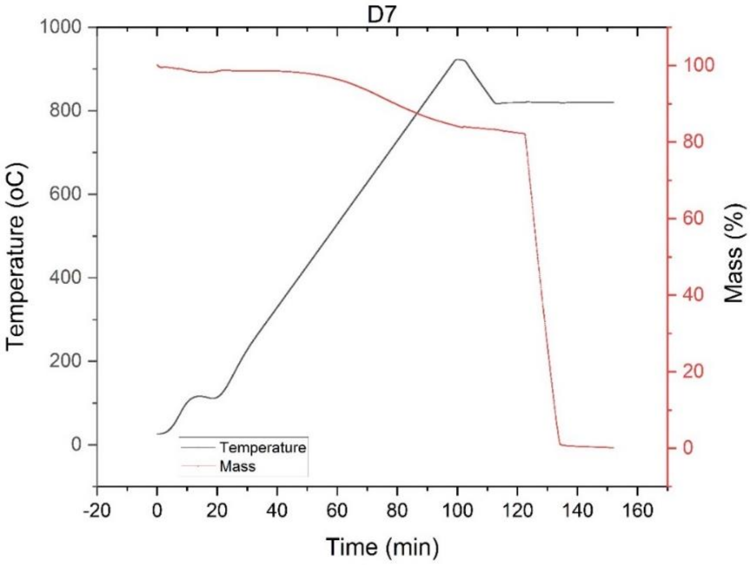

Figure A7 TGA profile for biochar D7

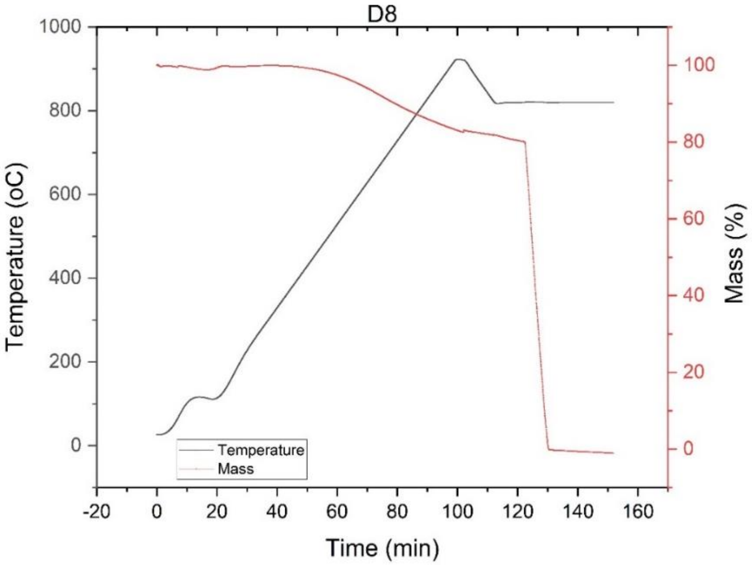

Figure A8 TGA profile for biochar D8

Appendix B: XPS Peak Convolution Data

This section includes peak deconvolution parameters and references obtained from NIST database for biochar XPS analysis.

Table B1 XPS Peak Deconvolution Parameters

	Peak type	Binding energy (eV)	Area (a.u.)	Chemical composition	Reference from NIST database for XPS spectra
C1s	Voigt	284.5	40419.7	C=C (Graphite)	Author Name(s): Smith K.L., Black K.M. Journal: J. Vac. Sci. Technol. A 2, 744 (1984)
	Voigt	285.6	25684.5	C-O (carbonyl)	Author Name(s): Lhoest J.-B., Bertrand P., Weng L.T., Dewez J.-L. Journal: Macromolecules 28, 4631 (1995)
	Voigt	289.6	20360.1	C=O (carboxylic) C-N Pyridinic N	Author Name(s): Wagener K., Batich C., Kirsch B., Wanigatunga S. Journal: J. Polym. Sci. Part A 27, 2625 (1989) Author Name(s): Beamson G., Briggs D. Journal: High Resolution XPS of Organic Polymers: the Scienta ESCA300 Database (1992)

	Peak type	**Binding energy (eV)**	**Area (a.u.)**	**Chemical composition**	**Reference from NIST database for XPS spectra**
O1s	Voigt	532.9	32631.2	C-O	Author Name(s): Lopez G.P., Castner D.G., Ratner B.D. Journal: Surf. Interface Anal. 17, 267 (1991)
	Voigt	531.1	9337.5	C=O	Author Name(s): Beamson G., Briggs D. Journal: High Resolution XPS of Organic Polymers: the Scienta ESCA300 Database (1992)
N1s	Voigt	400.2	7267.9	Graphene N	Author Name(s): Hendrickson D.N., Hollander J.M., Jolly W.L. Journal: Inorg. Chem. 8, 2642 (1969)
	Voigt	398.6	7331.2	Pyridinic N	Author Name(s): Lindberg B.J., Hedman J. Journal: Chem. Scr. 7, 155 (1975)

Appendix C: Langmuir Separation Factor and Linear PSO Plots

Calculation of Separation Factor (R_L) for Langmuir isotherm data obtained for APAP adsorption and linear pseudo second order kinetic model fits for APAP and CBZ are given below.

$$R_L = \frac{1}{1 + K_L C_o}$$

Table C1 Calculation of Separation Factor (R_L) for Langmuir Isotherm obtained for acetaminophen (rate constant K_L = 0.204)

Initial concentration, C_O [mg/L]	**Separation Factor, R_L**
25	6.1
50	11.2
75	16.3
100	21.4
150	31.6
200	41.8
250	52
300	62.2

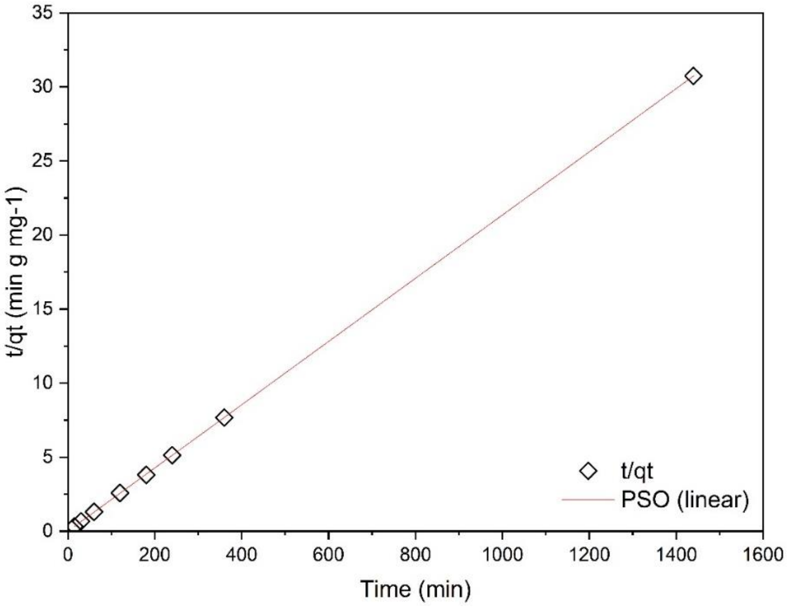

Figure C1 PSO linear kinetic model fit for CBZ adsorption

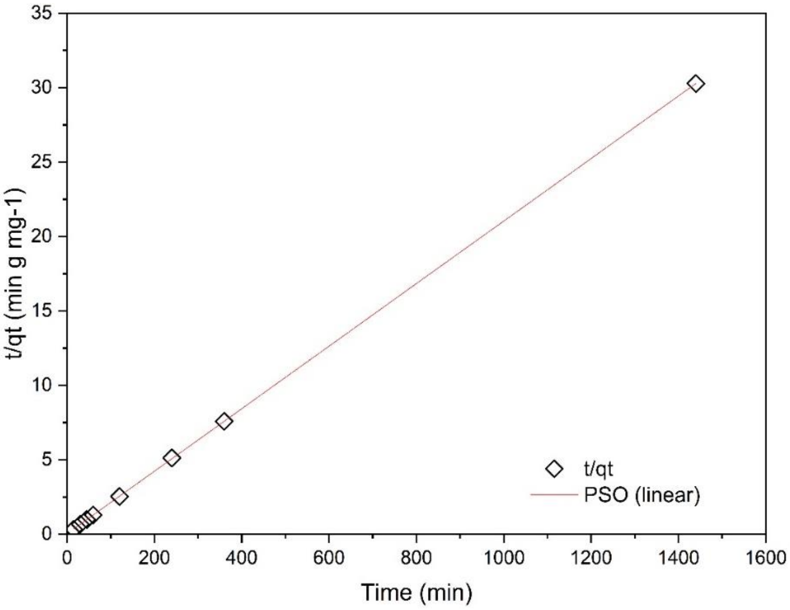

Figure C2 PSO linear kinetic model fit for APAP adsorption

Appendix D: Feedstock and Biochar Images

Wood samples, crucible arrangement inside furnace, biochar and adsorption solution images.

Figure D1 Raw wood samples divided into cubes

Figure D2 Raw wood placement inside furnace before pyrolysis

Figure D3 Post pyrolysis biochar beforehand crushing to a powdered form

Figure D4 Experimental solutions with target species and biochar

Appendix E: 3,4-DCA pH tests and PZC Plots

Table E1 Adsorption of 100 mg/L 3,4-DCA onto DoE biochars at different pH, particle size < 0.5 mm

Biochar Sample [0.1 g]		**% Removal [24 hours]**
pH = 6		
D1	250S725-60C	93
D2	100S725-60C	91
D3	250S725-20C	92
D4	100S725-20C	94
pH = 9		
D5	250S725-60C	91
D6	100S725-60C	90
D7	250S725-20C	94
D8	100S725-20C	88

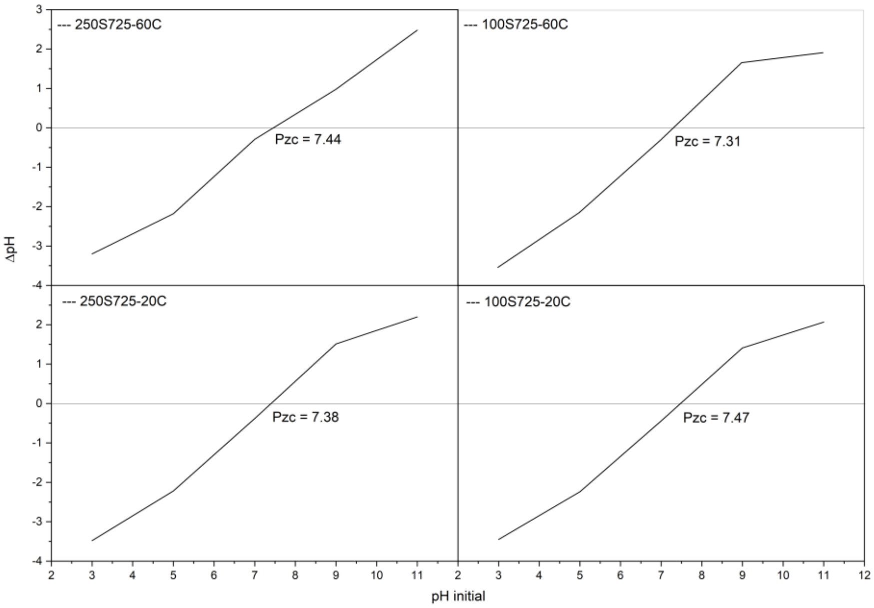

Figure E1 PZC plots for DoE biochars D1-D4

Appendix G: Rouquerol Selection Criteria and BET Transform Plots

Rouquerol plots for screening and DoE biochars.

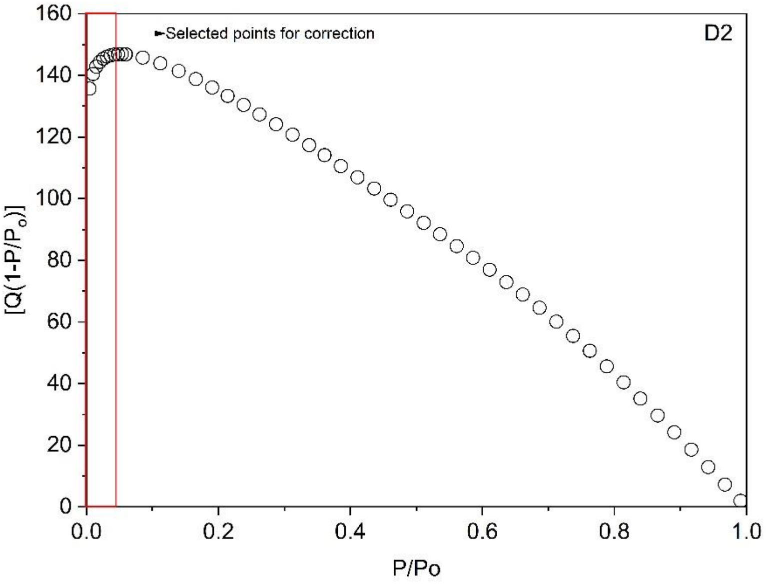

Figure G1 Plot of $Q(1-P/P_o)$ vs P/P_o for biochar D2 showing the range to which BET equation can be applied to obtain a positive 'C' constant and linear BET plot

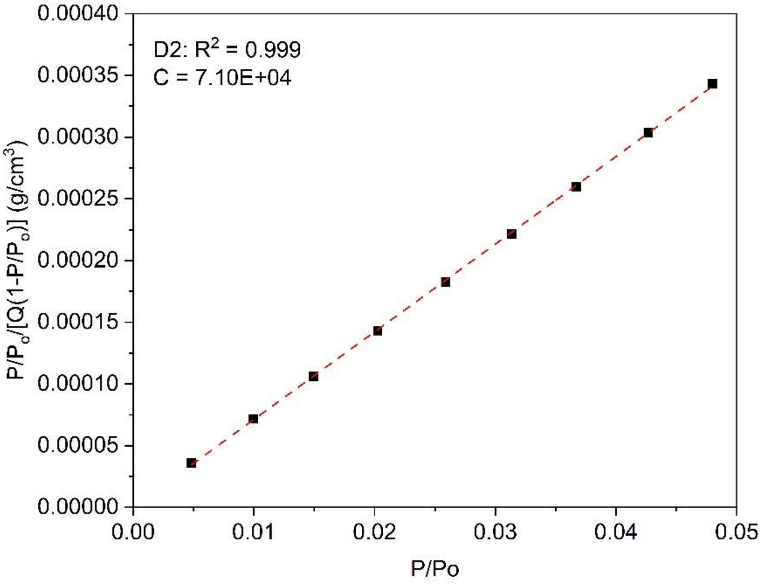

Figure G2 BET transform plot for D2 with a positive C-constant resulting from Rouquerol correction

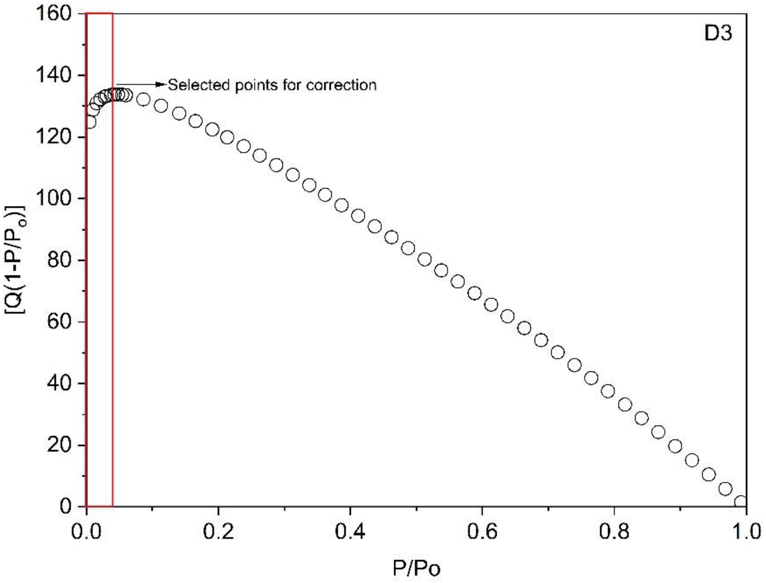

Figure G3 Plot of $Q(1-P/P_o)$ vs P/P_o for biochar D3 showing the range to which BET equation can be applied to obtain a positive ‘C’ constant and linear BET plot

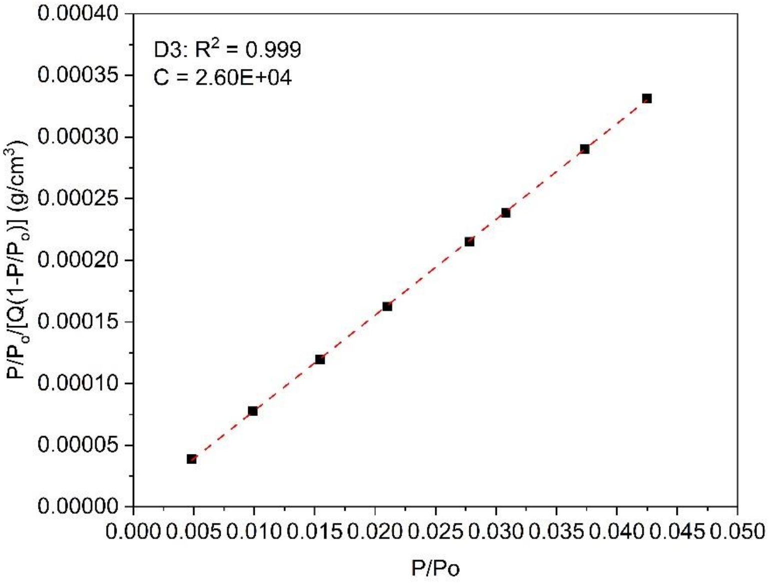

Figure G4 BET transform plot for D3 with a positive C-constant resulting from Rouquerol correction

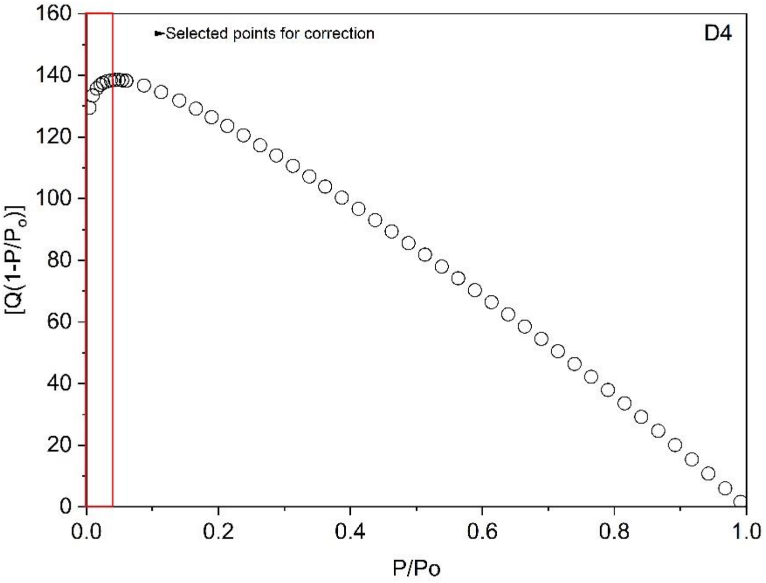

Figure G5 Plot of Q(1-P/P$_o$) vs P/P$_o$ for biochar D4 showing the range to which BET equation can be applied to obtain a positive 'C' constant and linear BET plot

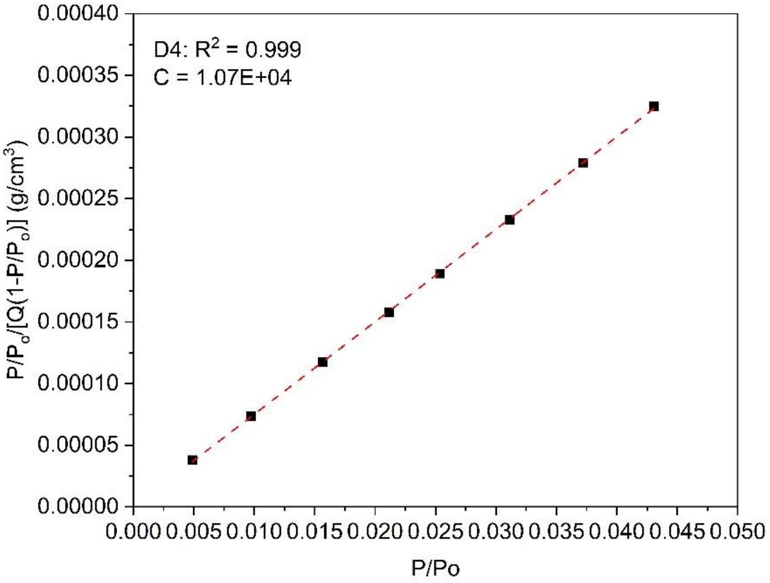

Figure G6 BET transform plot for D4 with a positive C-constant resulting from Rouquerol correction

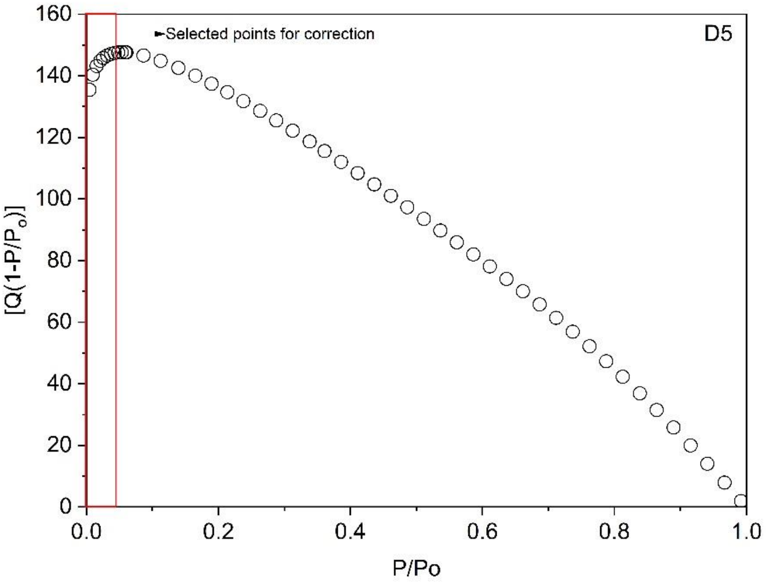

Figure G7 Plot of Q(1-P/P$_o$) vs P/P$_o$ for biochar D5 showing the range to which BET equation can be applied to obtain a positive ‘C’ constant and linear BET plot

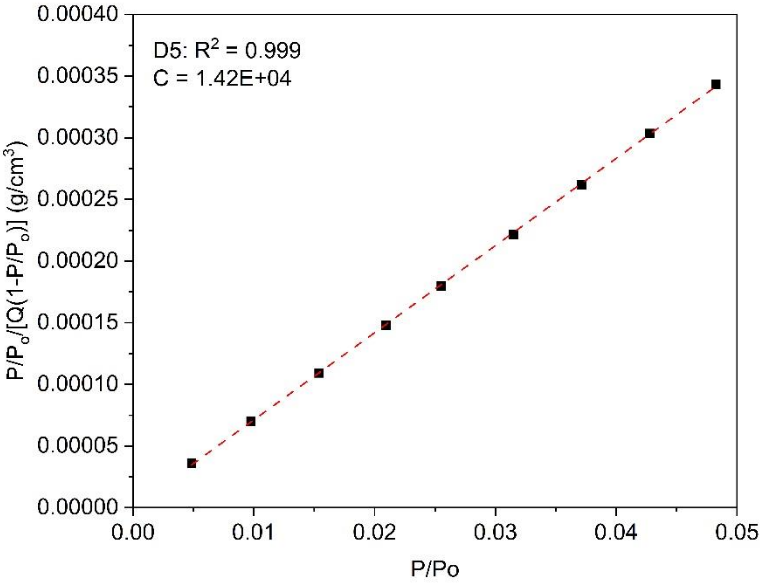

Figure G8 BET transform plot for D5 with a positive C-constant resulting from Rouquerol correction

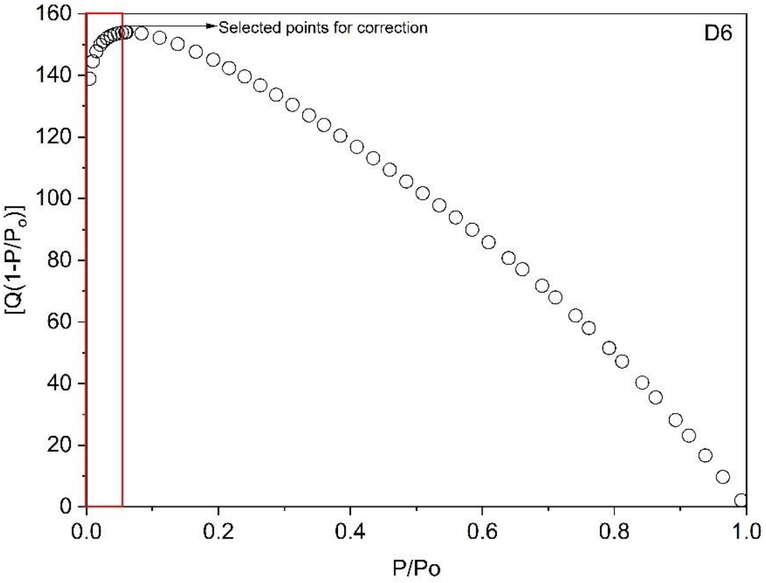

Figure G9 Plot of Q(1-P/P$_o$) vs P/P$_o$ for biochar D6 showing the range to which BET equation can be applied to obtain a positive 'C' constant and linear BET plot

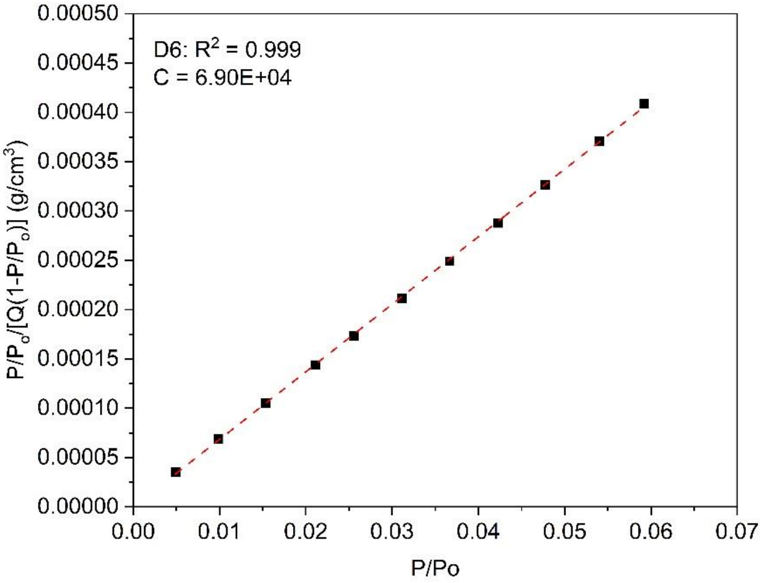

Figure G10 BET transform plot for D6 with a positive C-constant resulting from Rouquerol correction

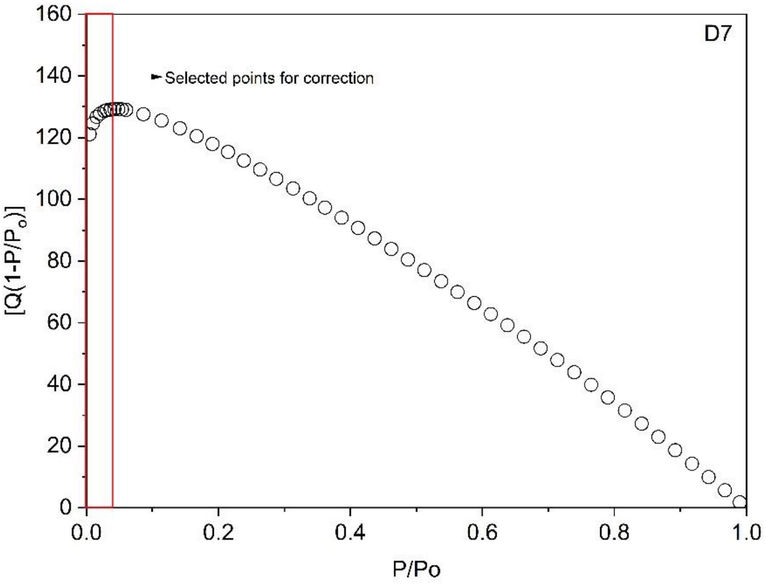

Figure G11 Plot of Q(1-P/Pₒ) vs P/Pₒ for biochar D7 showing the range to which BET equation can be applied to obtain a positive ‘C’ constant and linear BET plot

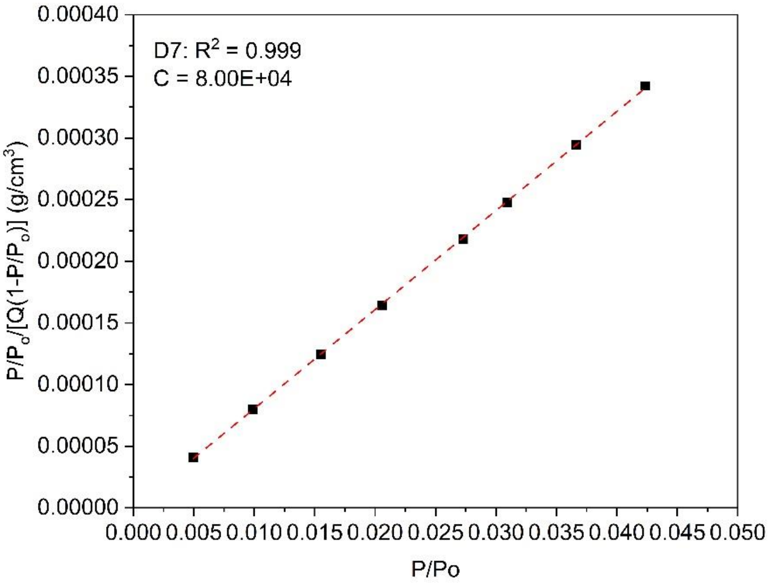

Figure G12 BET transform plot for D7 with a positive C-constant resulting from Rouquerol correction

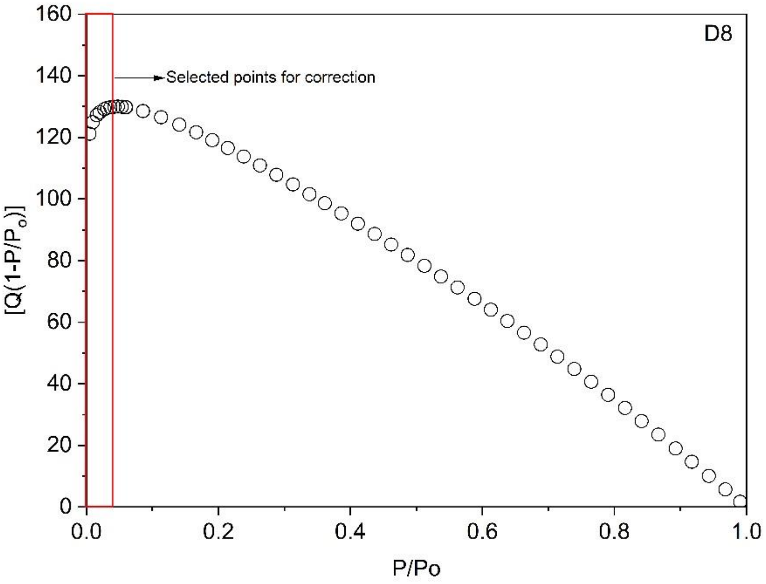

Figure G13 Plot of $Q(1-P/P_o)$ vs P/P_o for biochar D8 showing the range to which BET equation can be applied to obtain a positive 'C' constant and linear BET plot

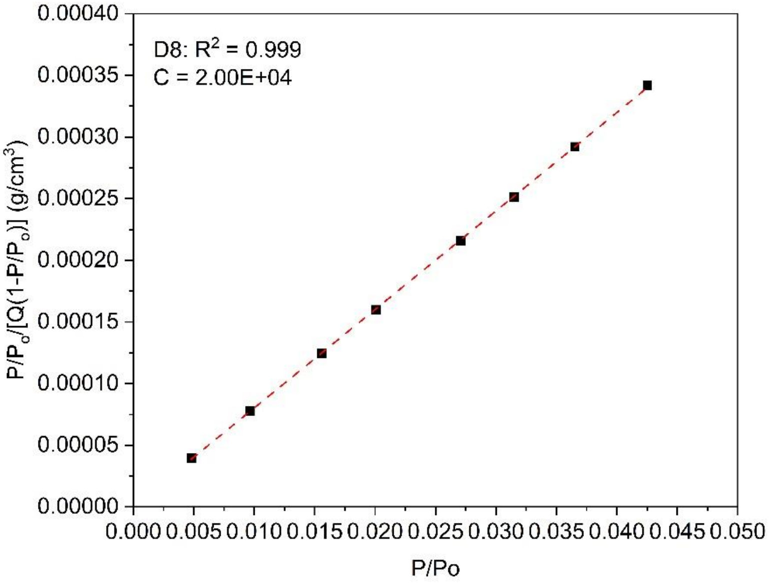

Figure G14 BET transform plot for D8 with a positive C-constant resulting from Rouquerol correction

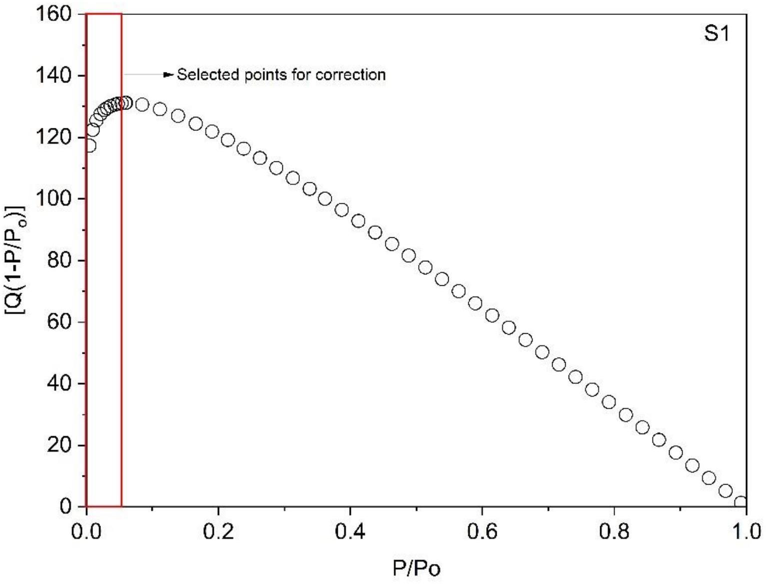

Figure G15 Plot of $Q(1-P/P_o)$ vs P/P_o for biochar S1 showing the range to which BET equation can be applied to obtain a positive 'C' constant and linear BET plot

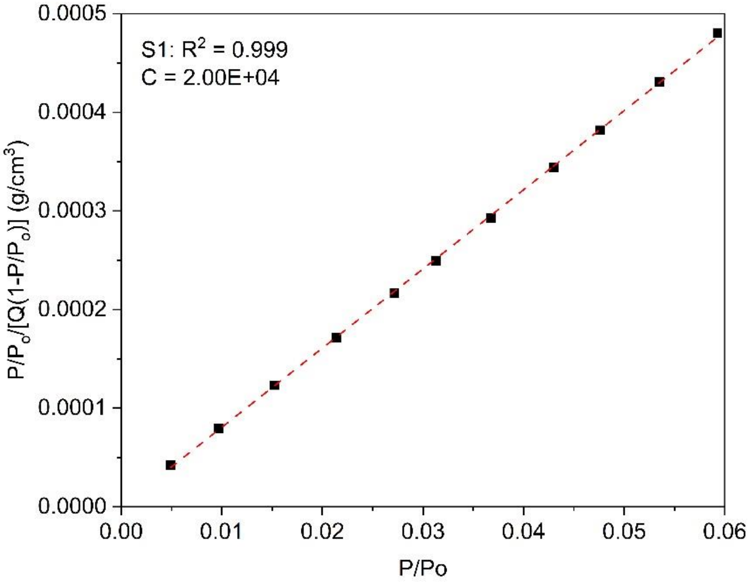

Figure G16 BET transform plot for S1 with a positive C-constant resulting from Rouquerol correction

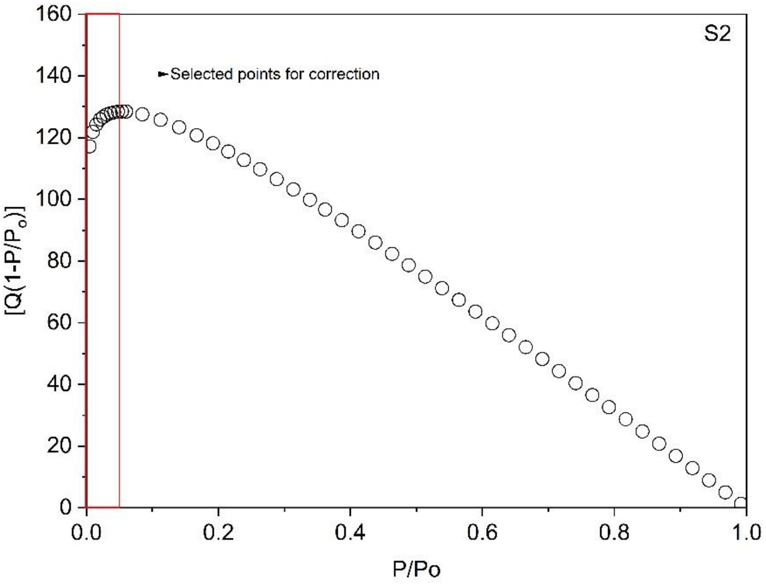

Figure G17 Plot of Q(1-P/P$_o$) vs P/P$_o$ for biochar S2 showing the range to which BET equation can be applied to obtain a positive 'C' constant and linear BET plot

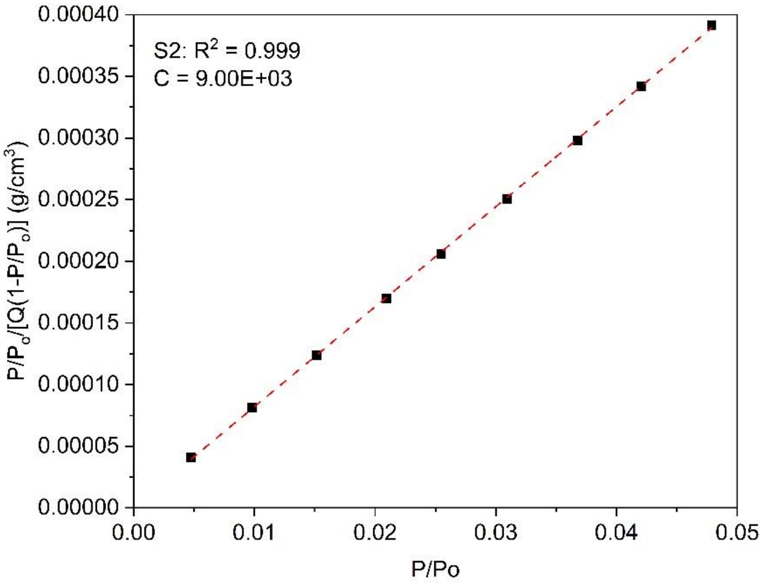

Figure G18 BET transform plot for S2 with a positive C-constant resulting from Rouquerol correction

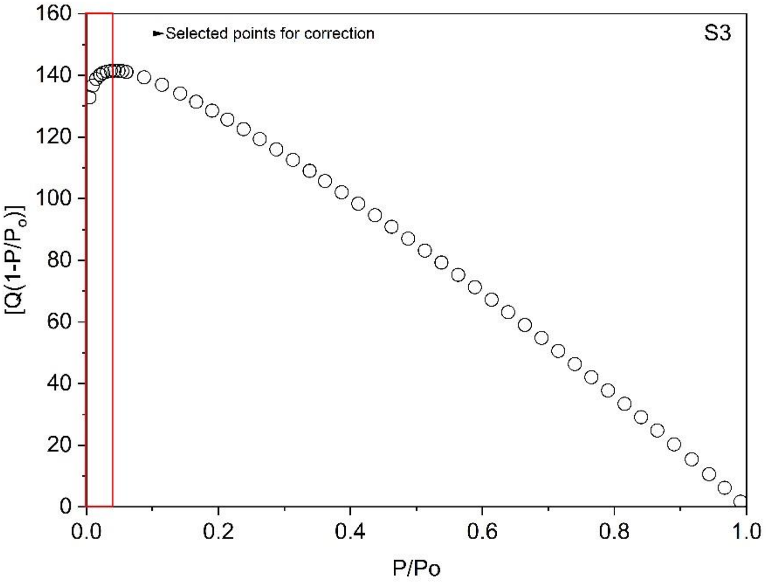

Figure G19 Plot of Q(1-P/P$_o$) vs P/P$_o$ for biochar S3 showing the range to which BET equation can be applied to obtain a positive 'C' constant and linear BET plot

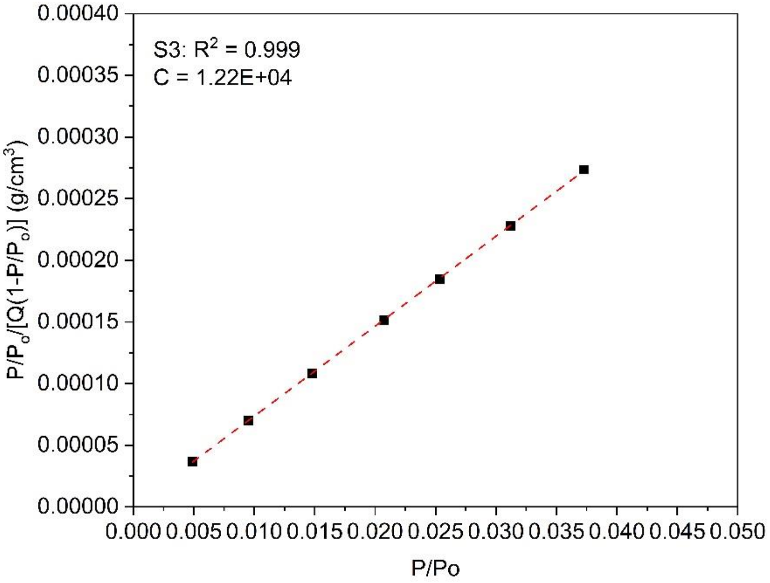

Figure G20 BET transform plot for S3 with a positive C-constant resulting from Rouquerol correction

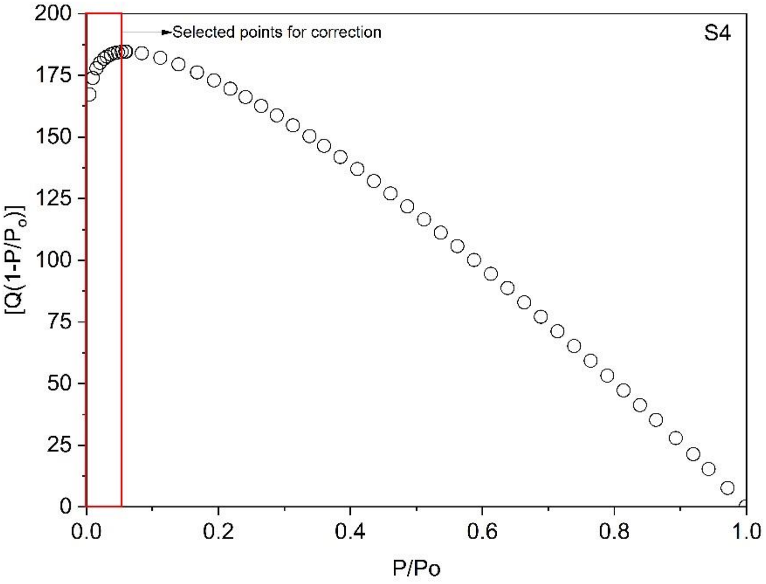

Figure G21 Plot of Q(1-P/P$_o$) vs P/P$_o$ for biochar S4 showing the range to which BET equation can be applied to obtain a positive 'C' constant and linear BET plot

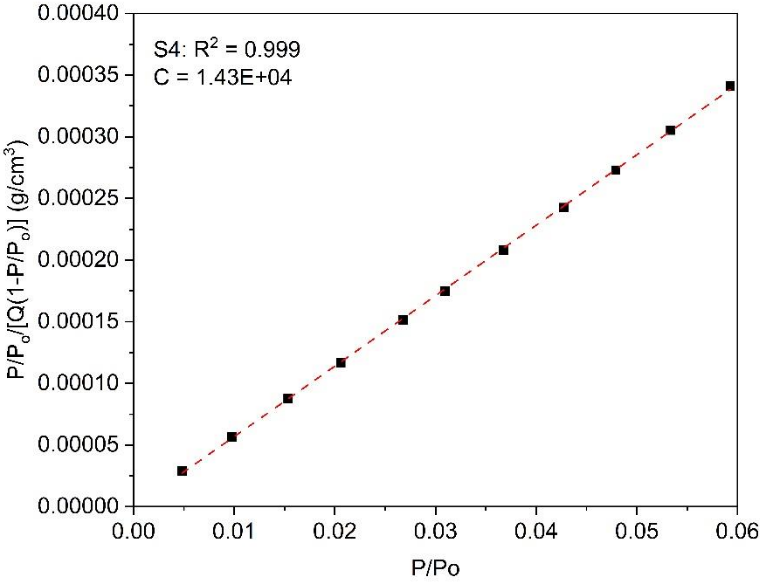

Figure G22 BET transform plot for S4 with a positive C-constant resulting from Rouquerol correction

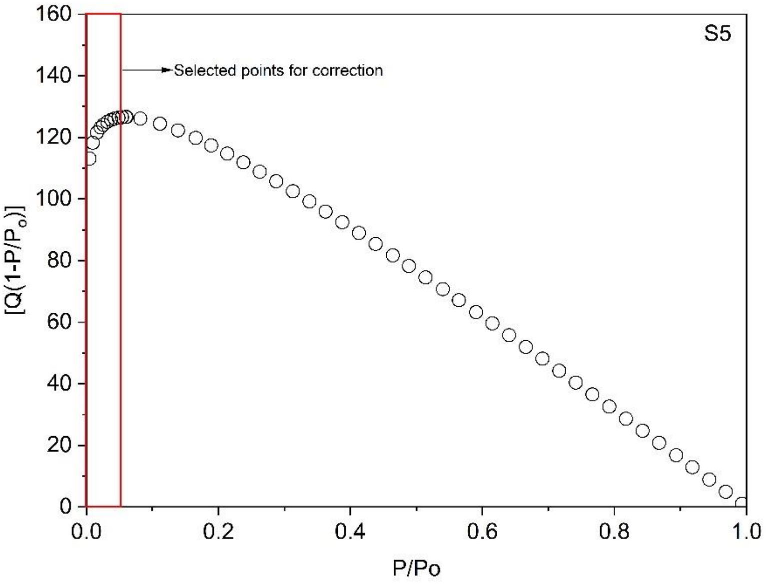

Figure G23 Plot of $Q(1-P/P_o)$ vs P/P_o for biochar S5 showing the range to which BET equation can be applied to obtain a positive 'C' constant and linear BET plot

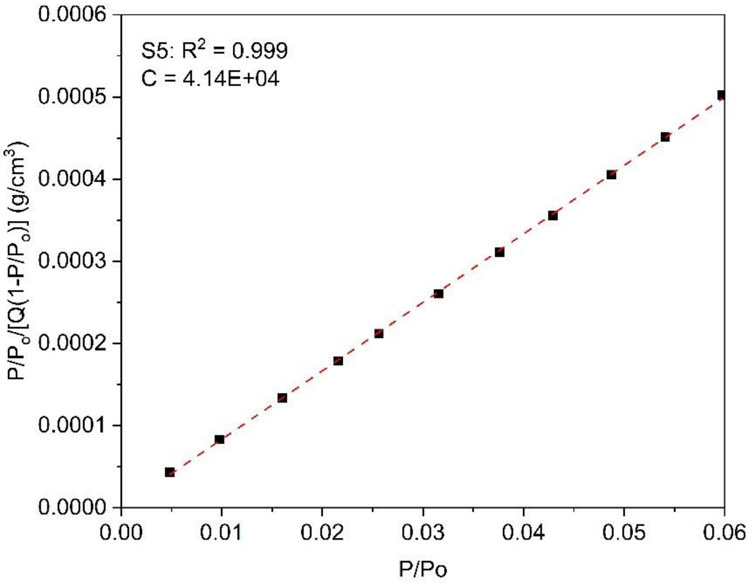

Figure G24 BET transform plot for S5 with a positive C-constant resulting from Rouquerol correction

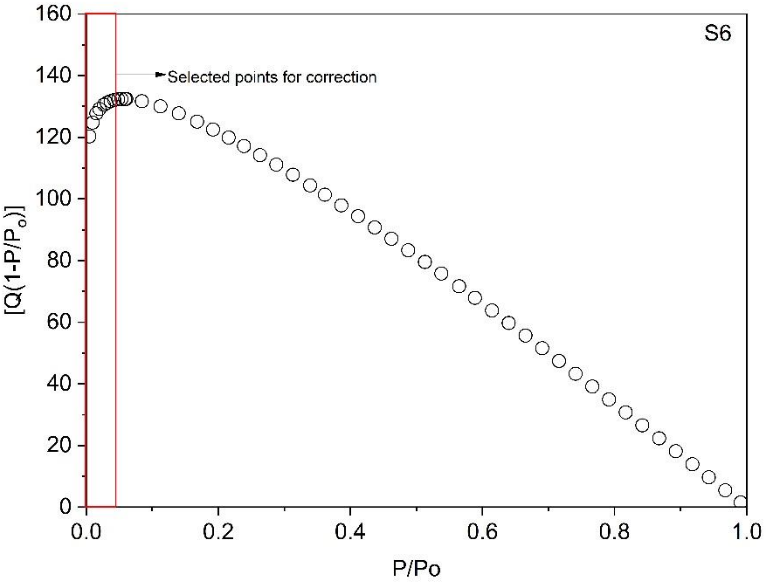

Figure G25 Plot of $Q(1-P/P_o)$ vs P/P_o for biochar S6 showing the range to which BET equation can be applied to obtain a positive 'C' constant and linear BET plot

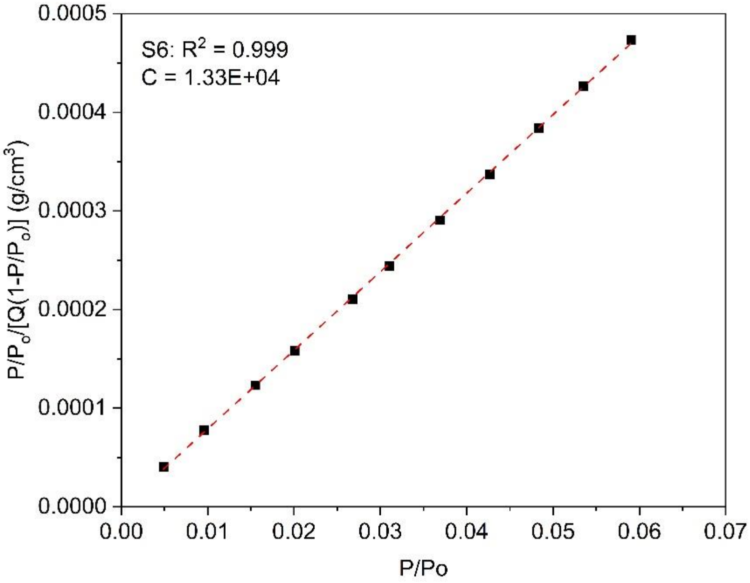

Figure G26 BET transform plot for S6 with a positive C-constant resulting from Rouquerol correction

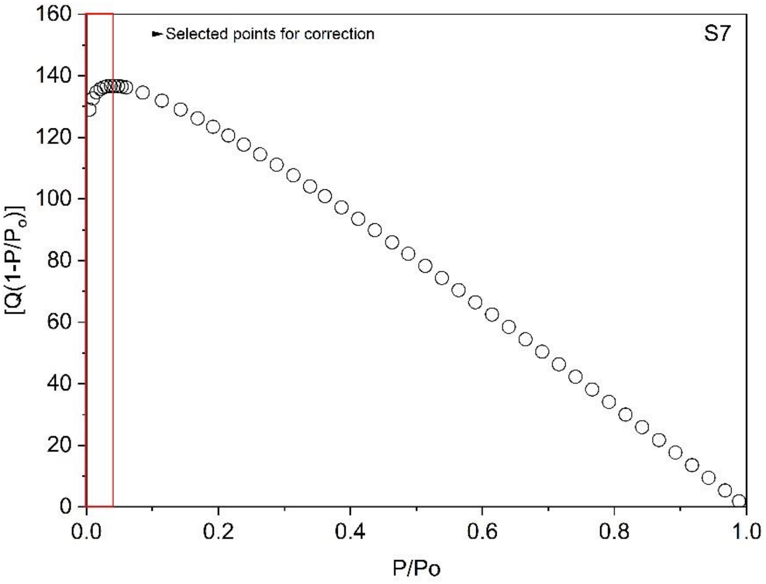

Figure G27 Plot of $Q(1-P/P_o)$ vs P/P_o for biochar S7 showing the range to which BET equation can be applied to obtain a positive 'C' constant and linear BET plot

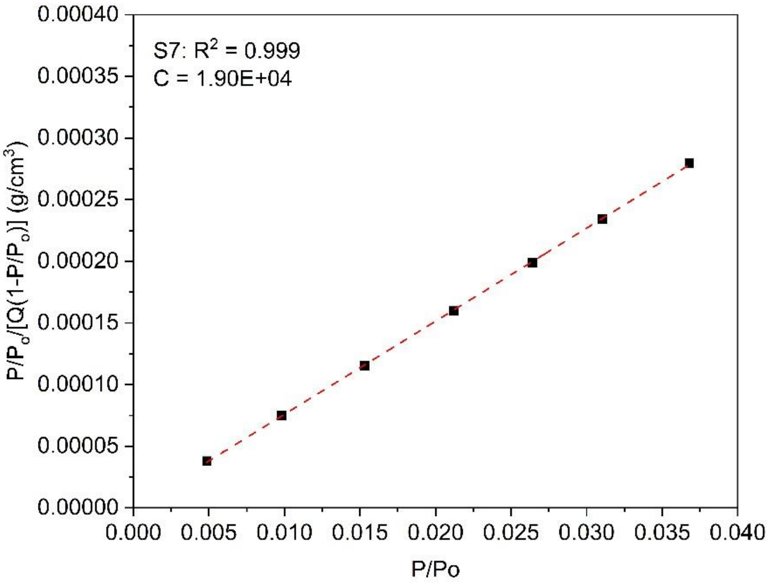

Figure G28 BET transform plot for S7 with a positive C-constant resulting from Rouquerol correction

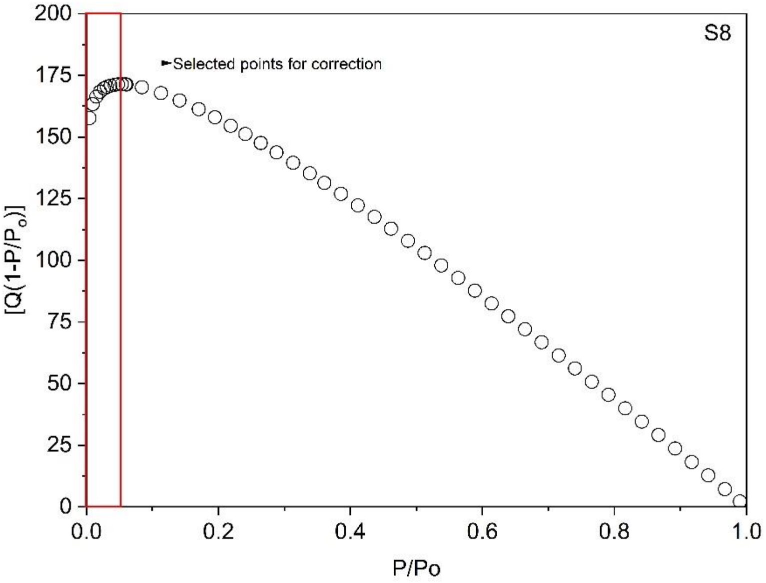

Figure G29 Plot of Q(1-P/P$_o$) vs P/P$_o$ for biochar S8 showing the range to which BET equation can be applied to obtain a positive ‘C’ constant and linear BET plot

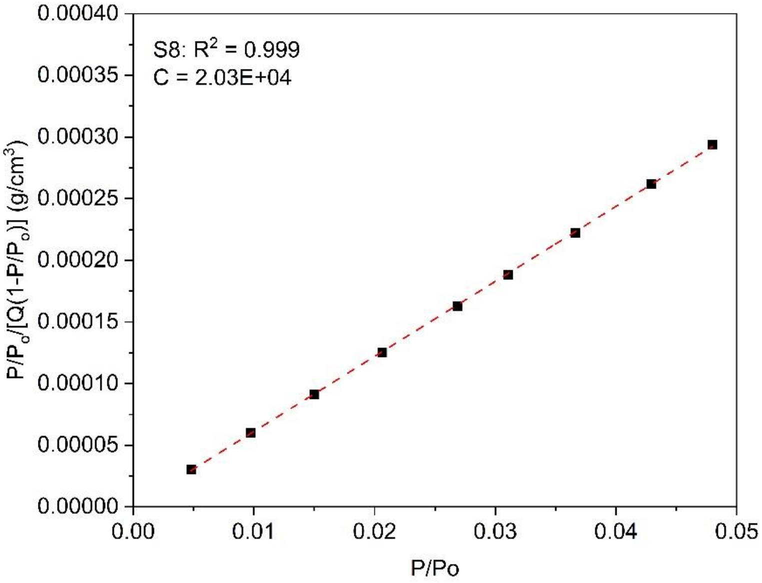

Figure G30 BET transform plot for S8 with a positive C-constant resulting from Rouquerol correction

Appendix H: Publications

BioEnergy Research
https://doi.org/10.1007/s12155-023-10595-6

Design of Experiments Study on Scottish Wood Biochars and Process Parameter Influence on Final Biochar Characteristics

Mohammad Umair Jamal[1] · **Ashleigh J. Fletcher**[1]

Received: 27 October 2022 / Accepted: 31 March 2023

Abstract

Native Scottish wood samples were investigated as potential, locally sourced, raw materials for biochar production. Screening experiments identified pure softwood as the preferable feedstock. Influence of operational parameters, i.e. activating gas flow rate (CO_2), heating ramp rate and contact time on final biochar characteristics, was investigated using design of experiments. Surface area and biochar yield were selected as response variables. Minitab was used to define experimental run conditions and suggested an optimal output at 60 min contact time and 15 °C/min ramp rate for maximum responses. The highest surface area (764 m^2/g) was achieved at 850 °C from softwood, albeit with a low yield of 15%. Under optimised conditions, the observed surface area was 613 m^2/g with ~ 18% yield. Pareto charts suggested no influence of gas flow rate on chosen responses, which correlated well with experimental data. Pore structure was a combination of micro- and mesopores with average pore widths of 3–5 nm and an average point of zero charge of 7.40 ± 0.02. Proximate analysis showed an increase in fixed carbon content from 20%, in the feedstock, to 80%, in the optimised biochar. Morphological analysis showed a layered carbon structure in the biochars. The results show the significance of the selected feedstock as a potential source of biochar material and the relevance of interplay of operational variables in biochar development and their final characteristics.

Keywords Pyrolysis · Minitab · DoE · Activated carbon · Wood · Surface area

Introduction

Biochar is the black carbonaceous residue formed from thermochemical conversion of biomass in an inert atmosphere, providing a mechanism to lock in the carbonaceous material rather than releasing greenhouse gas emissions in degradation pathways of the organic matter. These materials require similar or superior performance than commercially used activated carbons for their implementation across different applications, which is achieved by a combination of cheap availability of feedstock, accompanied by diverse physical and chemical properties, giving carbon-rich biochars the potential to be used in a range of applications, including soil amendment, such as enrichment fertilisers [1, 2], catalysts [3], adsorbents [1], and in energy storage [4]. Recent steps towards creating a circular economy has seen a drive to produce biochars from renewable sources, providing added value to waste streams; however, production is currently unregulated. Notably, biochar production offers scope for ad hoc production, with opportunity to tailor products to target applications. Such bespoke materials, manufactured from regenerative sources, with comparable characteristics to commercially produced activated carbons can potentially help to reduce the overall carbon footprint multiple industrial processes.

Biochars often have well-developed pore networks, ranging from micro- to macropores, and high surface areas that make them suitable for adsorption. The pore network extends throughout the material and provides active binding sites for heavy metals that readily sorb on the surface and within the pore network. Biochars made from renewable sources gave comparable adsorption capacities to commercial activated carbons, even though the surface areas are significantly smaller [5]. As a consequence of these characteristics, biochars produced from different feedstocks, such as walnut wood [6] and rosid angiosperm [7], have been used in water treatment applications. In addition to water

---

✉ Mohammad Umair Jamal
umair.jamal@strath.ac.uk

Ashleigh J. Fletcher
ashleigh.fletcher@strath.ac.uk

[1] Chemical and Process Engineering, University of Strathclyde, 75 Montrose Street, Glasgow G1 1XL, UK

treatment, biochars derived from rice husk have been used in acid catalysis [8], while pyrolysed hard wood biochars have found potential application in biodiesel production [9]; biochars as soil enhancement materials can maintain nutrients within soil and control cation exchange, which reduces nutrient leaching from soils [5], while potassium hydroxide-activated biochar offers potential within supercapacitors [10].

There are several parameters involved in the production of biochars: operating temperature, gas flowrate, residence time, furnace ramp rate, and pressure that can influence the yield and quality of the final product. Pyrolysis temperature is considered one of the key factors influencing the properties of biochars; the breakdown of heavy hydrocarbons decreases the quantity of the final product, as more volatiles are removed from the system [11]. Researchers have reported a reduction in biochar yield on increasing the pyrolysis temperature [12, 13], which is expected, as, at high temperatures, secondary reactions occur that further breakdown the char formed at initial temperatures into liquid and gaseous phases, i.e. releasing more volatile components [14]. While higher temperatures enable the development of micropores and an enhanced pore structure [15], a disadvantage of extreme temperatures is that the formation of ash hinders the growth of the pore network and surface area [16], and a fine balance exists in determining the optimal temperature for biochar formation. By contrast, too low a temperature can result in insignificant changes in pore volume and surface area, as the system is unable to completely devolatilise volatile constituents, and the final product may be subject to pore blockage and an underdeveloped pore network [17]. Previous studies indicate that a temperature range between 400 and 800 °C is most appropriate for biochar production. A low heating rate mitigates the possibility of thermal cracking of biomass and rules out secondary pyrolysis reactions to enhance the biochar yield [14]. A very high heating rate would melt the biochar particles and increase the gaseous and liquid components, thereby decreasing the quantity of the final product [18]. An excessive heating rate also results in accumulation within particles, resulting in blocked pore entrances, due to shortage of time for the volatile matter to diffuse [19], while depolymerisation of biomass and prevalence of secondary pyrolysis result in a reduced biochar yield [20] and can decrease surface area [21]. To avoid micropore coalescence or collapse of the carbon matrix altogether, a high rate of volatile matter generation must be avoided [18], which rules out the use of high heating rates; hence, an optimum range of 10 and 30 °C/min is preferred. Residence time is influenced by temperature, gas flowrate, and heating rate; to promote repolymerisation, and improve biochar yield, sufficient residence time is necessary for reaction [22]; however, several researchers have reported that the yield is not proportional to residence time [23, 24]. Residence times between 30 and 60 min have been reported to yield maximum pore volume for chemically activated biochars from corn cob [25], while an increase in the surface area was reported by for residence time increasing from 10 to 60 min [26]; however, further increase reduced surface area. Complications, arising from interaction between other process conditions and residence time, make it a challenging parameter to analyse; hence, it is a key component to investigate during biochar production with residence times between 20 and 60 min being of interest. By contrast, the influence of pressure on biochar production is relatively straightforward. Extreme, high pressures prevent the release of volatile matter from the system and result in the formation of spherical cavities [27], with continuous decrease in surface areas reported upon increasing the pressure from 1 to > 20 bar [27, 28]. Pressures slightly higher than atmospheric pressure can increase the residence time of reaction constituents, which assists char formation [29], and carbon content in the final product was suggested to be pressure dependent. During pyrolysis, vapours are formed, and these can participate in reactions with the char, modifying its characteristics if not purged from the system [14]. Carrier gases are used to ensure an inert atmosphere for pyrolysis, and nitrogen is the most common carrier gas used being cheaper and more readily available than other inert gases. Increased gas flowrate has been shown to marginally decrease the biochar yield, due to the removal of vapours from the system, preventing repolymerisation [14]; previous work has shown a reduction in yield from 28.4 to ~ 27% on increasing the nitrogen flowrate from 50 to 400 mL/min [30], with similar observations for other systems [5] suggesting that low to moderate flowrates will produce little effect on yield. By contrast, gas flowrate has been shown to markedly affect surface area and total pore volume, with an increase in nitrogen flowrate (50 to 150 mL/min) reported to cause an increase of > 300 m^2/g in surface area and a ten-fold increase in total pore volume for Algerian date pits derived activated carbon [31]. Notably, very high gas flowrates decrease biochar yield and pore volume [31, 32]; hence, moderate gas flowrates between 150 and 300 mL/min are suggested for optimum characteristics.

Previous studies have discussed the relationship between biochar performance and process parameters [33, 34]. However, there is a limitation and lack of understanding of the synergistic effects of these parameters on produced biochars. Feedstock with different physical and chemical compositions react differently to operational parameters and produce biochars with variability in characteristics [35]. Material selection is an important step prior to biochar production. Parent material characteristics can be influenced by climatic conditions [36]. To ensure profitability, the cost incurred in procuring the raw material and transforming it into bespoke materials for chosen applications should offer a reasonable benefit. In this study, the raw material utilised was native Scottish wood, and screening experiments assisted in the selection between hardwood and softwood, both abundantly available. Locally procured raw material provides a considerable reduction in carbon footprint associated with supply and transport, offering the potential for circularity in the formation of biochar materials for possible applications. This work adopts a design of experiments approach to develop an understanding of the synergistic effects of selected process conditions on biochar characteristics and inform biochar production for such wood sources.

Methodology

The wood samples used in this study were procured from Sustainable Thinking Scotland C.I.C. (Kinneil Estate, Bo'ness, Scotland) and obtained from a walled garden in a 200-acre estate. Wood samples included birch, oak, ash, Scots pine, Sitka spruce, and Western red cedar. Table 1 gives an overview of the sample mix used in the study.

Samples A and B were developed to give a comparison between biochars produced from soft and hardwoods. A design of experiments (DoE) approach was adopted, based on a comprehensive literature review. Screening experiments were performed on samples A and B to identify the type of wood to be used for the DoE study. The results of the preliminary runs on samples A and B were refined, and DoE was applied to sample C. Parameter scoping helped develop DoE runs to investigate a wider parameter space, utilising statistical analysis of variance (ANOVA) using Minitab to determine responses arising due to multiple factors changing simultaneously [37]. This provides a deeper understanding of the systematic factors that have statistical influence on the chosen responses.

Design of Experiments (DoE)

DoE is a multipurpose approach that helps in determining a relationship between input variables against a chosen response. Based on the situation, different design types can be applied to a system. *Comparison* investigates a single factor between different combinations using *t*-, *Z*-, or *F*-tests. *Variable screening* uses factorial designs to analyse the significance of input variables on the overall performance of a system or process. *Transfer function optimisation* allows study of the relationship between relevant input variables to the specified output. *System optimisation* uses the transfer function to improve the overall performance of the system. Finally, *robust design* is aimed at mitigating the effects of system variation without root cause elimination [38].

In this study, a full factorial design (FFD) which falls under variable screening was used to assess possible interactions of input variables as opposed to the traditional one factor at a time approach. The screening runs were based on three variables: contact time with activating agent (CO_2), flowrate of activating gas, and furnace temperature. Two temperatures (600 and 850 °C) were chosen based on a review of the literature, to study the difference in the types of

Table 1 Feedstock for biochar production

Sample	Wood type	Species
A	Predominantly softwood	Ash, birch, oak, Scots pine, Sitka spruce, Western red cedar
B	Predominantly hardwood	Ash, Downey birch, oak, Scots pine, Sitka spruce, Western red cedar
C	100% softwood	Scots pine, Sitka spruce, Western red cedar

Table 2 Process conditions, yields, and textural properties for biochars produced using wood samples A and B (ramp rate = 15 °C/min)

Exp	Sample code	CO_2 flow-rate (mL/min)	Temp (°C)	Contact time (min)	Biochar weight (g)	Yield (%)	Surface area (m^2/g)	Micropore volume (cm^3/g)	Total pore volume (cm^3/g)	Average pore width (nm)
S1	250S600-20A	250	600	20	6.53	21.8	544	0.18	0.26	3
S2	250S600-60A	250	600	60	6.20	20.7	538	0.18	0.25	3
S3	250S850-20A	250	850	20	5.30	17.7	597	0.20	0.29	3
S4	100S850-60A	100	850	60	4.41	14.7	764	0.22	0.42	5
S5	250H600-20B	250	600	20	7.59	25.3	525	0.17	0.25	3
S6	250H600-60B	250	600	60	6.96	23.2	544	0.18	0.27	3
S7	250H850-20B	250	850	20	5.16	17.2	573	0.19	0.26	3
S8	100H850-60B	100	60	100	4.54	15.1	714	0.23	0.34	4

produced biochars, as well as yields. Thermal CO_2 activation improves sorption characteristics of biochar and forms new functional groups, creating a more uniform porous structure, and is quicker than chemical activation. Flowrates of 100 or 250 mL/min were used with residence times of 20 and 60 min.

Screening identified softwood as a more desirable feedstock; hence, DoE (using FFD) was applied to pure softwood samples. A mean temperature of 725 °C was used with three variables: contact time (20 and 60 min), gas flowrate (100 and 250 mL/min), and the heating ramp up rate (15 and 30 °C/min) for the full factorial design (FFD). Minitab was used to generate the FFD, which resulted in a total of $2^3 = 8$ experiments for 3 factors with a high and low setting each [39]. The runs were randomised to minimise effects of factors that cannot be controlled. Centre points were omitted from the model to reduce excess material waste and minimise equipment usage and power consumption, but the model was allowed to run interactions up to third order. Biochar yield and surface area were considered as the two design responses as the economic feasibility and performance of the biochars are governed by these properties.

Nomenclature

Sample names were developed as per: The first three digits (e.g. 250 or 100) represent the gas flowrate. 'S' and 'H' denote either softwood or hardwood; the middle set of values (600, 850, 725) represent the pyrolysis temperatures, followed by residence time and sample category, e.g. 20A or 60C. Thus, the sample 250S725-60C represents a gas flowrate of 250 mL/min, for a softwood sample pyrolysed at 725 °C with a residence time of 60 min, from wood batch C. All experiments were conducted at a heating rate of 15 °C/min, with the exception of samples marked '/30', where the ramp rate was increased to 30 °C/min.

Pyrolysis

Prior to combustion, the wood samples were divided into cubes of sides ~ 5 cm. These smaller cubes were washed with de-ionised water to remove dust and oven dried at 100 °C for 24 h. For combustion, a precursor weight of 30 ± 0.1 g was used. The sample was equally distributed into four crucibles fitted with lids, all placed inside the Thermconcept KLS 10/12/WS muffle furnace. A CO_2 flow of 250 mL/min was maintained over the sample for 40 min to ensure an inert atmosphere and the furnace set to the corresponding temperature and dwell time. Following this, the gas flowrate was adjusted to the values detailed in Tables 2 and 3 and heating begun. After each run was complete, the flow of gas was switched off once the furnace reached room temperature, and the sample

Table 3 Process conditions, yields and textural properties for biochars produced wood sample C

Exp	Sample code	CO_2 flowrate (mL/min)	Temp (°C)	Contact time (min)	Biochar weight (g)	Yield (%)	Surface area (m^2/g)	Micropore Volume (cm^3/g)	Total pore volume (cm^3/g)	Average pore width (nm)	Fixed carbon (%)	Volatile matter (%)
	Feedstock										20.3	79.7
	Ramp rate = 15 °C/min											
D1	250S725-60C	250	725	60	5.30	17.7	613	0.19	0.36	3	80.0	20.0
D2	100S725-60C	100	725	60	5.27	17.6	613	0.19	0.35	3	86.0	14.0
D3	250S725-20C	250	725	20	6.08	20.3	558	0.18	0.29	4	80.5	19.5
D4	100S725-20C	100	725	20	6.31	21.0	581	0.19	0.29	5	80.0	20.0
	Ramp rate = 30 °C/min											
D5	250S725-60/30C	250	725	60	4.40	14.7	613	0.19	0.37	5	77.3	22.7
D6	100S725-60/30C	100	725	60	3.65	12.2	553	0.18	0.43	4	73.4	26.6
D7	250S725-20/30C	250	725	20	6.08	20.3	544	0.18	0.27	4	85.1	14.9
D8	100S725-20/30C	100	725	20	6.07	20.2	544	0.17	0.28	4	83.5	16.5

Table 4 Analysis of variance results for yield and surface area

Yield					
Source	DF	Adj SS	Adj MS	*F value*	*p value*
Model	3	5.9828	1.99427	25.88	0.004
Linear	2	5.3330	2.66650	34.61	0.003
Contact time	1	4.3808	4.38080	56.86	0.002
Ramp rate	1	0.9522	0.95220	12.36	0.025
2-way interactions	1	0.6498	0.64980	8.43	0.044
Contact time*ramp rate	1	0.6498	0.64980	8.43	0.044
Error	4	0.3082	0.07705		
Total	7	6.2910			
Surface area					
Model	2	4943	2471.6	5.96	0.048
Linear	2	4943	2471.6	5.96	0.048
Contact time	1	3403	3403.1	8.20	0.035
Ramp rate	1	1540	1540.1	3.71	0.112
Error	5	2075	414.9		
Total	7	7018			

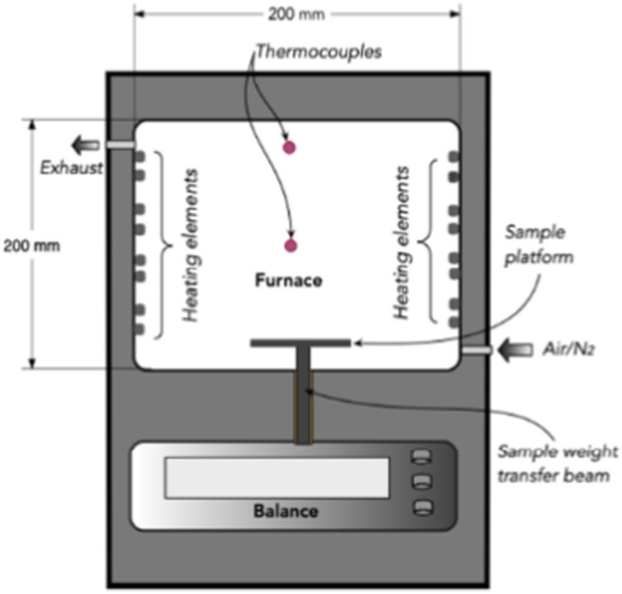

Fig. 1 Schematic diagram of muffle furnace equipped with a weighing system (licence number—5,501,811,254,585) [40]

was allowed to cool overnight. Figure 1 shows a schematic diagram of the muffle furnace used for pyrolysis.

Biochar weight was calculated once the samples had reached room temperature. The yield of the sample is calculated using Eq. 1:

$$Biochar\ yield\ (\%) = \frac{produced\ biochar\ weight\ (g)}{precursor\ weight\ (g)} * 100 \quad (1)$$

Analysis and Characterisation

Porous Structure Characterisation

The biochar sample was crushed to a powdered form prior to analysis, performed using nitrogen adsorption at – 196 °C on a Micrometrics ASAP 2420 system (99.99% nitrogen adsorbate). Degas was performed at 200 °C for 240 min (10 °C/min heating rate). A total of 49 points were taken on the adsorption branch and 30 on the desorption branch. Specific surface area and pore volume distribution of the samples were determined using Brunauer–Emmett–Teller (BET) model [41].

Fourier Transform Infrared Spectroscopy (FTIR)

The biochars were crushed to a powdered form, and a small amount of sample (~ 0.2 g) was placed on the sampling surface. An ABB IR Instrument MB 300 series was used to characterise the functional groups on the surface of the biochar samples using attenuated total reflectance (ATR) for analysis. A total of 32 scans were taken in transmittance mode. The spectra were recorded at 4 cm^{-1} resolution between 500 and 4000 cm^{-1}.

Proximate Analysis

Thermogravimetry was used to carry out proximate analysis of representative biochar samples. The technique employed [42] closely follows the British Standard (BS1016) method. Approximately 5–10 mg of crushed sample was placed in a crucible and analysed using a NETZSCH STA 449 F3 Jupiter system. The crucible was initially tared under a nitrogen gas flow of 50 mL/min, and the mass allowed to stabilise under the same gas flowrate and initial mass recorded. The sample was heated to 120 °C and allowed to stabilise. Subsequently, crucible mass was recorded, and the temperature increased to 920 °C, and held for 3 min, before the mass reading was recorded. Finally, the temperature was reduced to 820 °C, and the flowing gas switched to 50 mL/min of pressurised air. The crucible was allowed to stabilise, and a final mass reading was taken at ambient temperature.

Scanning Electron Microscopy (SEM)

SEM was used to capture the structural characteristics of the biochar surface. A small solid portion was clipped from a biochar cube and placed into the apparatus (Tungsten low-vacuum JEOL JSM-IT100 InTouchScope SEM). Images were captured at 10 µm with × 1000 magnification.

The beam current was kept constant at 35 with a voltage difference of 20 kV.

Point of Zero Charge (PZC)

Salt addition method was used to perform PZC analysis [43]. A 40-mL aliquot of 0.1 M $NaNO_3$ was adjusted to five pH values between 3 and 11. Solutions of 0.1 M NaOH and 0.1 M HCl were used to attain the desired pH. Powdered biochar (~ 0.2 g) was added to the beakers and agitated at 450 rpm for 24 h. The final solution was filtered and the pH of the permeate was measured. The difference between the initial and final pH values of the samples was calculated, and the change in pH versus initial value was plotted to identify the PZC.

Contact Angle Measurement

Sessile drop method [44] was used to determine the contact angle between the biochar surface and a water drop. Biochar samples were crushed, and a small amount of powder was placed on a microscopic glass slide. The lump was then smoothed by placing another slide on top which was removed before taking measurements. The analysis was performed on a Krüss Scientific Drop Shape Analyser DSA25B. To measure the contact angle, a small droplet of water (~ 0.5 mL) was dropped onto the sample from a height less than 1 cm, and photographs were taken at intervals of 1, 2, and 3 s using Krüss Advance software.

Results and Discussion

Minitab Outputs

Regression Analysis

Minitab was used to analyse the dataset obtained from the DoE runs. The regression equations for the two responses, yield (Y1) and surface area (Y2), are shown below in Eqs. 2 and 3, respectively. For analysis of the factorial design, a stepwise method was used, which works by combining forward selection and backward elimination procedures. The forward selection approach determines the variables to retain in a model. In forward selection, the added variable is never removed. By contrast, the backward elimination procedure removes terms from the initial model that have the smallest adjusted sum of squares. Determining whether a variable is added or removed from the model is based on the 'Alpha to enter' and 'Alpha to remove' value. If the *p value* of a variable is less than the 'Alpha to enter' value, it is retained in the model and vice versa. In this study, both alpha values were set to 0.15, which is the system default.

$$Yield(Y1) = 6.20 + 0.0058A + 0.0300C - 0.001900AC \tag{2}$$

$$\begin{aligned} Surface\ area\ (Y2) = 577.8 + 1.031\ Contact\ time\ (min) \\ - 1.85\ Ramp\ rate\left({}^{\circ}C/min\right) \end{aligned} \tag{3}$$

where *A* is contact time (min) and *C* is ramp rate (°C/min). Note that variable *B* (gas flowrate) was not found to be significant.

The coefficient of determination (R^2) for Eqs. 2 and 3 was equal to 0.95 and 0.70, respectively. The values indicate that the model can explain over 95% and 70% of variability in the responses of yield and surface area, respectively. The model also suggests that there is no notable variation in the obtained responses arising from changes in flow rate of the activating gas. Figure 2 shows the Pareto chart of standardised effects of variables on the responses.

Analysis of Variance (ANOVA)

Statistical analysis of the input variables, i.e. contact time, flow rate, and ramp rate, was performed to identify single or interaction effects on chosen responses. One way of checking the adequacy of the model uses the *p values* and the *F values* from the ANOVA table generated in Minitab. The data generated for yield and surface area is reported in Table 4. For a model to be significant, its *p value* should be less than the significance level (0.05 for a 95% confidence interval in this

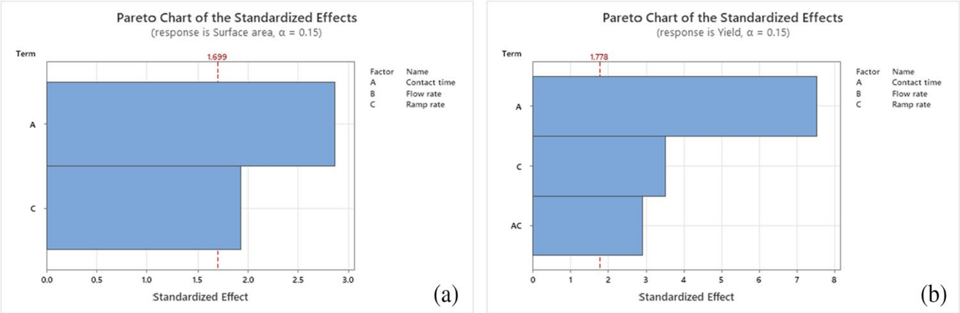

Fig. 2 Pareto chart for variable effects on a surface area and b yield

case), and it should have a high *F value* [45]. In both cases, the *p value* for the model is < 0.05, indicating the models are significant, the model for yield being considerably more accurate compared to the regression for surface area.

It can be seen from the table that contact time and ramp rate have determining effects on yield, with contact time in the furnace being the primary influencing factor with an *F value* of 56.7. There is also a noticeable two-way interaction between contact time and heating ramp rate on yield. The model also suggests no influence of the gas flow rate on biochar yield. For biochar surface area, contact time alone was predicted to be the influencing variable. The ramp rate *p value* was > 0.05 suggesting that this is not a significant variable in surface area determination. No influence of gas flow rate was predicted on surface area.

Response Optimisation

Based on the consideration of the model being statistically significant for both yield and surface area, an optimised response was generated using Minitab with the goal of maximising both of the selected responses. The suggested solution from Minitab included a contact time of 60 min and a ramp rate of 15 °C/min, with no specified value for the gas flow rate, resulting in a surface area of 612 m^2/g and a yield of 5.3 g. The generated solution had a desirability of 78%. The suggested solution was already a part of experiments D1 and D2, both run with a contact time of 60 min and ramp rate of 15 °C/min, with varying flow rates. The observed experimental values for surface area in both cases were 613 m^2/g. In addition, the yield for the two runs was approximately 5.3 g for both runs, which correlates closely to the theoretical predictions. Despite the close relation between theoretical and experimentally obtained data, the low accuracy of the surface area regression presents the need for further analysis of parameter influence on biochar characteristics. The model could be improved by running centre points; however, there is a need to minimise experimental runs to prevent resource utilisation and supplement the idea of sustainability. The following sections further analyse additional characterisation data obtained for the biochars and their relationship with the initial input process variables.

Biochar Yield

Table 2 shows the percentage yield of biochars produced from screening wood samples A and B, under different pyrolysis temperatures, and operating parameters. The trend in yield is as expected, with increasing pyrolysis temperatures resulting in lower quantities of produced biochars [7]. As the temperature is increased, more volatiles are removed from the system, thereby reducing the biomass within the system, hence the final mass of the biochar. It is evident that the final product is determined by a direct combination of the operating parameters. For the softwood chars (Sample A), a low contact time of 20 min and pyrolysis temperature of 600 °C, with a high gas flowrate of 250 mL/min, resulted in the highest biochar yield of 6.5 g. Increasing the contact time to 60 min and keeping the other two parameters constant resulted in a minor reduction in yield of less than 1%. The result suggests that the increment of contact time from 20 to 60 min does not have a significant impact on the product yield. A similar pattern was observed for the hardwood chars (sample B). A maximum yield of 7.6 g was obtained using a high gas flowrate, low pyrolysis temperature, and low contact time. The yield decreased slightly with increased contact time (~2%). The lowest yield was obtained at a temperature of 850 °C, with a 60 min residence time and low gas flowrate. Under similar conditions, hardwood samples gave higher yields than the softwood samples. For experiment S1, the softwood yield was 21.8%, and the hardwood biochar was 25.3% under similar parameters (S5). The difference in yield was not considerable for the other runs in both wood batches. This observation, combined with the specific surface areas obtained, indicated that 100% softwood samples were worthy of further investigation.

Table 3 shows the yield of produced biochars from DoE runs. In D1-4, temperature was fixed at 725 °C as an average between the two screening temperatures, and the ramp rate was kept at 15 °C/min. A contact time of 60 min, with both gas flowrates, gave an average yield of ~17.5%. This yield was slightly improved when the contact time was reduced to 20 min, giving ~20%. The ramp rate was increased to 30 °C/min for D5-8; combined with a high contact time, the yield was further reduced for runs 13 and 14 [18]. The high heating rate however did not seem to affect the yield with shorter residence times. The data suggests that temperature is the primary factor affecting the yield of biochars. There is a noticeable influence of contact time and ramp rate on the yield as previously suggested by the Minitab output, with no discernible influence from gas flow rate.

Porous Structure Characterisation

Figure 3a and b show the adsorption isotherms recorded in the screening study. Experiments S1-4 represent a type II isotherm, governed by adsorption onto microporous solids. The hardwood samples in experiments S5-8 also display an initial high uptake followed by a plateau. There is slight evidence of a final uptake at high relative pressure, which could be attributed to a type II isotherm and multilayer adsorption [46].

Adsorption isotherms obtained for the DoE biochars presented in Fig. 3c and d demonstrate a more prevalent type II/IVa isotherm behaviour with initial high uptakes, followed by a plateau and a slight update at high relative pressure

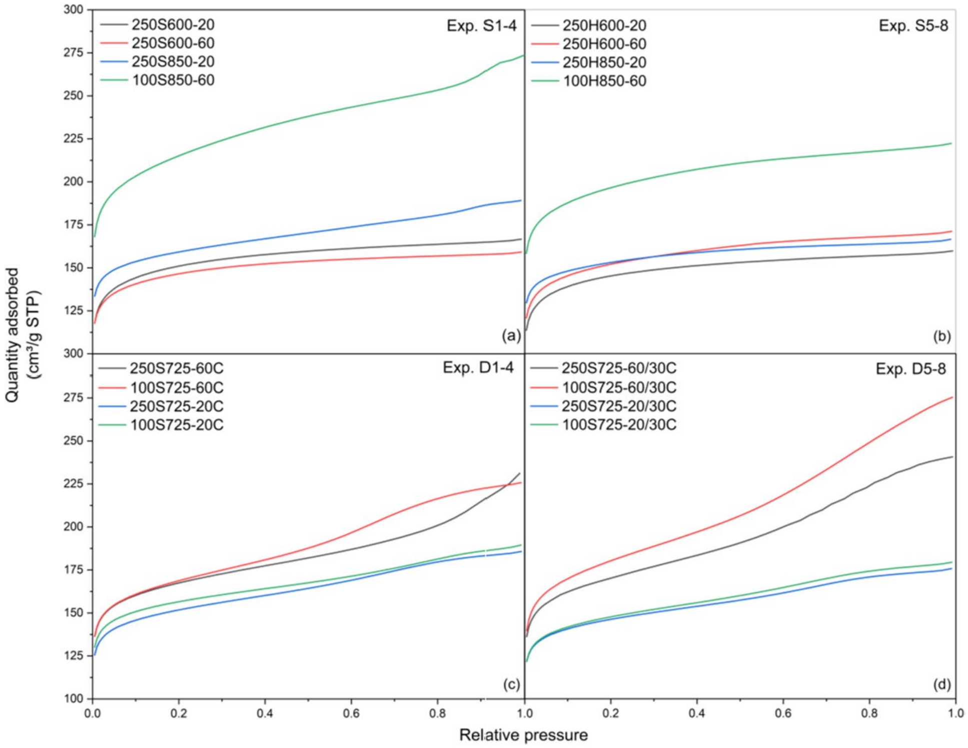

Fig. 3 Adsorption isotherms obtained for biochars

[46]. In general, the evidence of mesoporous nature is more prominent in pure softwood samples (sample C) in the latter experiments.

Table 2 shows the textural data obtained for the screening samples, comprising the surface area, micropore, and total pore volumes, as well as the average pore widths. Similar data on DoE samples is reported in Table 3. The total pore volume of samples is calculated using Eq. 4:

$$Total\ pore\ volume\ (TPV) = (Q_{Sat} * \mathrm{MW}/V_m)/\rho_{liq} \quad (4)$$

where.

Q_{sat} = maximum nitrogen adsorption (in cm^3/g, usually at relative pressure of 0.97 or above).

MW = molecular weight of N_2 (28 g/mol).

V_m = volume occupied by 1 mol of gas (22.4 L).ρ_{liq} = density of liquid N_2 at boiling point (808 g/L)

The *t* plot analysis, developed by Lippens and Boer [47], was used to determine the micropore volumes reported in Tables 2 and 3. It can be inferred that increasing pyrolysis temperatures caused an increase in microporosity. The ratio of micropore volume to TPV is highest in samples with low gas flowrates and higher residence times. At high gas flowrates, $V_{\mathrm{micropore}}/V_{\mathrm{total}}$ ratios are similar for experiments with 20 min hold time at high temperature. The evidence suggests an inverse relationship between microporosity development and residence time. Microporosity is suitable for interactions between small adsorbate species and adsorbents [7], so this can be a useful quantity to optimise. DoE experiments D5 and D6 indicate that a higher ramp rate combined with a longer hold time can enhance mesoporous nature in the biochars, which have previously been shown to be useful for aqueous phase applications [48].

Surface areas were calculated using BET analysis; however, such analysis is highly sensitive to the selected relative pressure range [49], particularly for microporous materials, and the optimal relative pressure range can be determined using the four consistency criteria suggested by Rouquerol et al. [50]: (1) only the range where the product of the adsorbate loading rate and 1 minus the relative pressure is increasing monotonically with the relative pressure should be chosen; (2) the value of BET 'C constant' must be positive. C constant quantifies the adsorbent and adsorbate interactions and is related to the energetics of adsorption in the first adsorbed layer [49]; (3) the selected linear region should encompass monolayer loading corresponding to the relative pressure; and (4) the relative pressure calculated in criterion 3 should be equal to the one calculated from BET theory consonant with monolayer loading with a 20% tolerance. Given the presence of significant microporosity reported in Tables 2 and 3, the Rouquerol correction was applied for all samples produced in this study. The maximum BET surface area was recorded for a pyrolysis temperature of 850 °C with a gas flowrate of 100 mL/min and 60 min residence time with softwood precursor (S4). Shorter residence times produced biochars with lower surface areas compared to those obtained under similar conditions but with longer hold time. Similar observations of improved surface areas with residence time were reported previously [26]. On average, pyrolysis runs performed at 725 °C produced biochars with higher surface areas. The intermediate temperatures also offered a reasonable trade-off between biochar yield and average pore widths. For DoE runs, lower ramp rates with high residence time can be inferred to be directly proportional to surface area. A reduction in $V_{\mathrm{micropore}}/V_{\mathrm{total}}$ ratio of these samples also suggests a more openly porous structure [7]. The highest biochar surface areas obtained for 100% softwood chars were higher than other wood-based biochars reported in the literature [7, 51]. As in the case of yield, observations made for surface area supplement the Minitab output with the exception of Experiment D6 where a high ramp rate has resulted in a reduced biochar surface area. This output could possibly be attributed to the reduced accuracy of the model.

Pore width data obtained from Barrett-Joyner-Halenda (BJH) analysis [52] (Tables 2 and 3) further confirms the predominantly microporous nature of the biochars. The average pore widths were largest for runs performed at 725 °C with high ramp rates. As stated above, shorter hold times resulted in increased microporosity, as well as narrower pore widths. Predominantly softwood biochars (S1-4) were almost as microporous as hardwood biochars (S5-8), and sample C (entirely softwood, D1-8) demonstrated the highest mesoporosity. The results indicate a possible application for sample A in the adsorption of small adsorptive species, mainly in gas phase [49], including in carbon capture [51].

Fourier Transform Infrared Spectroscopy

Figure 4a presents the FTIR spectrum obtained for softwood feedstock. In the fingerprint region, between 600 and 1500 cm^{-1}, there is evidence of $CH{=}CH_2$ vinyl terminals [53]. There is also evidence of loss of the peak from C–OH vibrations in the feedstock at 1000 cm^{-1} from pyrolysis treatment [7]. The heat treatment plays a crucial role in condensation of the carbonaceous skeleton and removes the hydroxyl groups from cellulosic compounds present in the precursors [54].

Figure 4b and c show the FTIR spectra for DoE biochar samples obtained using low and high ramp rates. The observed spectra look identical and not influenced by the change in ramp rates of the experimental runs. The peaks observed between regions 3800 and 3500 cm^{-1} indicate the presence of hydrogen bonds. This information is further supplemented by peaks between 1600 and 1300 cm^{-1}, as is the case with analysed biochar samples [53]. There are sharp peaks from the biochars between 3000 and 2600 cm^{-1} that could be due to C-H stretching bonds [7]. There is also strong evidence of $C{=}C$ bonds with symmetric and asymmetric vibrations and possible conjugation, as well as stretching vibrations with other structures such as oxygen and hydrogen ($C{=}O$, C-H) from the spectra in the

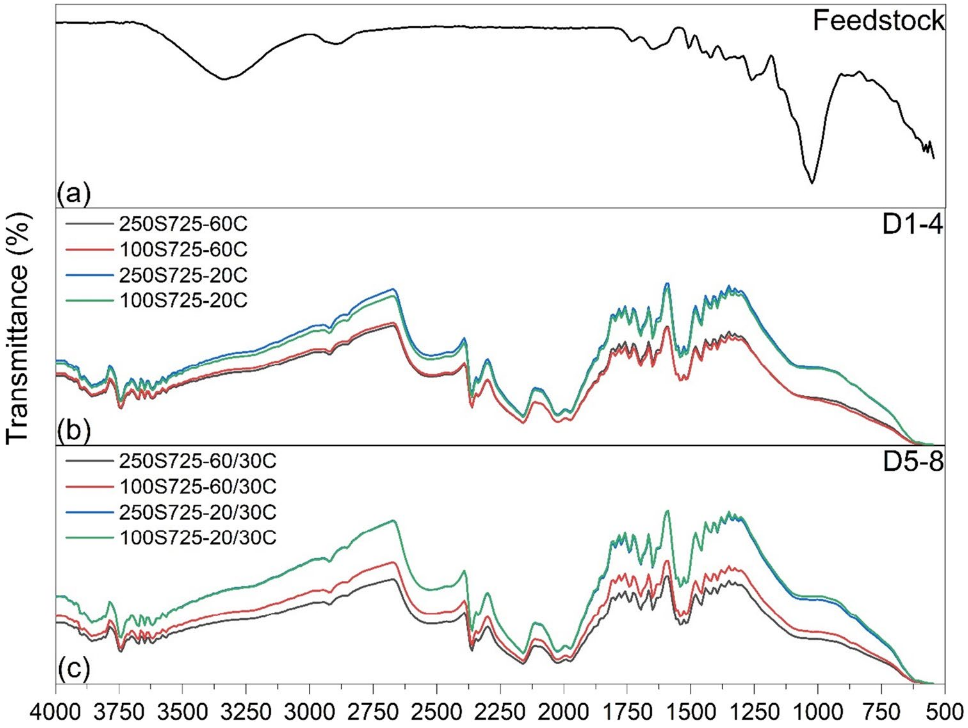

Fig. 4 FTIR spectrum of feedstock and DoE biochars

1600–1800 cm^{-1} region [53]. These functional groups could be the result of the presence of ketones, aldehydes, and carboxylic acids [55]. The results indicate the development of a layered, almost graphene-like carbon arrangement in the aromatic and aliphatic structures of the biochars [2]. There is no quantifiable influence of gas flowrate and residence time on the functional groups present in the samples. It can therefore be noted that temperature continues to be the primary influence on surface chemistry of produced biochars.

Proximate Analysis

The dry ash compositions of the feedstock and DoE biochars obtained from thermogravimetric analysis are reported in Table 3. The samples were treated on a dry basis to remove variability from moisture content and on an ash-free basis due to variability in inorganic forms from the natural precursor. A high contact time in experiments D1 and D2 resulted in a fixed carbon percentage of 80% and a volatile matter content of 20%. This was a significant increase from the fixed carbon content of 20.3% in the feedstock. For experiment D2, under a much lower gas flowrate, the carbon content was increased to 86% and volatiles reduced to 14%. The higher gas flowrate appears to have potentially decreased the temperature of the sample and affected the release of volatile matter as suggested previously [16]. For experiments D3 and D4, with shorter residence time, gas flowrates did not have a considerable impact on fixed carbon and volatile fractions. High heating rates combined with longer residence times result in accumulation of volatile matter [19]. The results obtained in D5 and D6 support this statement, with carbon percentages below 80 and higher volatile content, as opposed to their lower ramp rate counterparts. With a shorter hold period (D7 and D8), the percentages of volatiles reduced significantly, and a positive effect on fixed carbon content was also noted. Residence time was observed to be the key driver for fixed carbon and volatiles, with the fluctuations arising from variable gas flowrates being almost negligible. The results indicate that a higher ramp rate combined with a short residence time has the potential to produce biochars with high fixed carbon content and the lowest fraction of volatiles, albeit with a significant loss in yield.

Scanning Electron Microscopy

Figure 5a–d show the SEM images recorded for lower ramp rate biochars, and Fig. 5e–g display the observations for higher ramp rate biochars. There is evidence of a well-developed pore network in biochars produced at low and high ramp rates. The images at 10 μm and 1000 × magnification suggest that the high pyrolysis temperatures exposed the carbonaceous skeleton of the parent material encompassing an intricate network of pores [56]. A pyrolysis temperature that is sufficiently high is necessary for the removal of the outer biochar layer. The open structure of pores could be attributed to a lower ash content, which reduces the potential for clogging. There is no apparent evidence of influence from different ramp rates on the pore networks developed in the biochars.

Point of Zero Charge

The surface charge of chars produced under different operating conditions appears to be dependent on material origin and surface functional groups, as opposed to chosen DoE variables. The average PZC of the samples in this study was 7.40 ± 0.02. Pyrolysis temperatures influence the pH of wood-based biochars. High temperatures result in the loss of not only volatile matter but also acidic functional groups, i.e. phenols and carboxylic, thereby resulting in more alkaline surface charges [57]. For example, slow pyrolysis treatment of wood-based pellets at 200 °C produced biochars with pH 4.6. Upon increasing the temperature to 600 °C, the resulting biochar had a pH of 9.5 [58]. A similar observation on wood chip biochars pyrolysed at 500 °C was made with biochars having a pH(H_2O) of 8.58 ± 0.01 [59]. Having a neutral/slightly alkaline surface charge indicates potential application in drinking water systems that operate under acidic conditions without much alternation to target anionic species from effluents [57].

Contact Angle Measurement

Biochar wettability is a parameter that can be evaluated through contact angle (CA) measurement [60]. Figure 6a shows water droplet on a clear glass slide, and Fig. 6b shows a similar water droplet on a biochar film. Both images were taken 2 s after water contact. The measurement was repeated for all biochar samples and yielded similar observations. The absorption of water by prepared biochars was seemingly immediate, indicating hydrophilicity and high wettability [60]. Low CA (typically $< 90°$) are achieved in cases where water shows greater affinity to the solid surface [61]. The mechanism for this interaction could potentially be the formation of surface hydrogen bonds and the domination of adhesion forces over repulsive ones. This stabilisation of forces allows water to penetrate porous materials and wet larger surface areas [60]. This observed wettability in case of native Scottish biochars suggests a feasible application in drinking water treatment systems, allowing larger available surface areas for interaction between dissolved target species in water.

Discussion

Examination of the wide range of results obtained for the chars produced within this study suggests significant correlation of biochar properties with parameters used within their

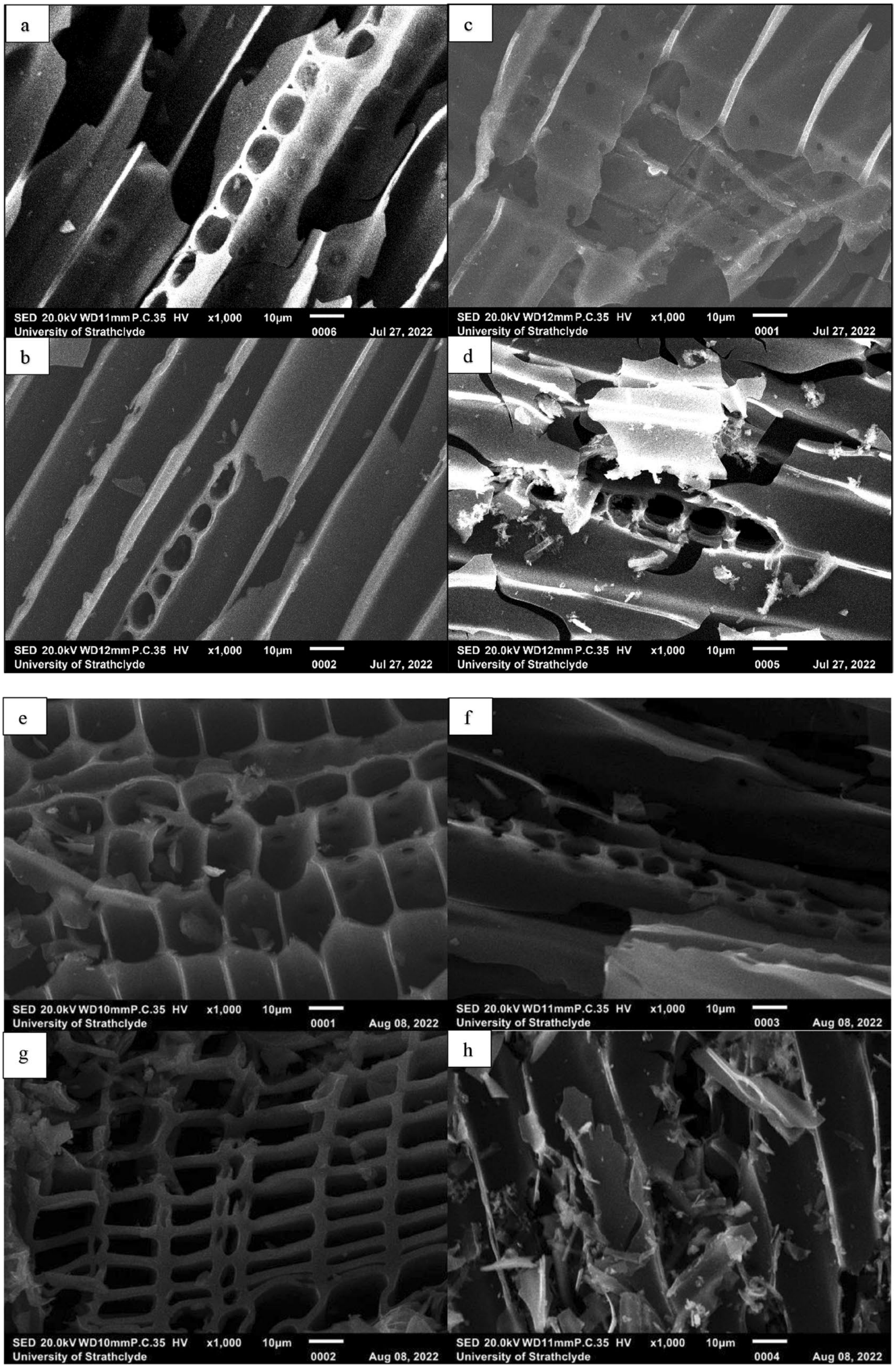

Fig. 5 a–d SEM of biochars with lower ramp rates; e–h SEM of biochars with higher ramp rates.

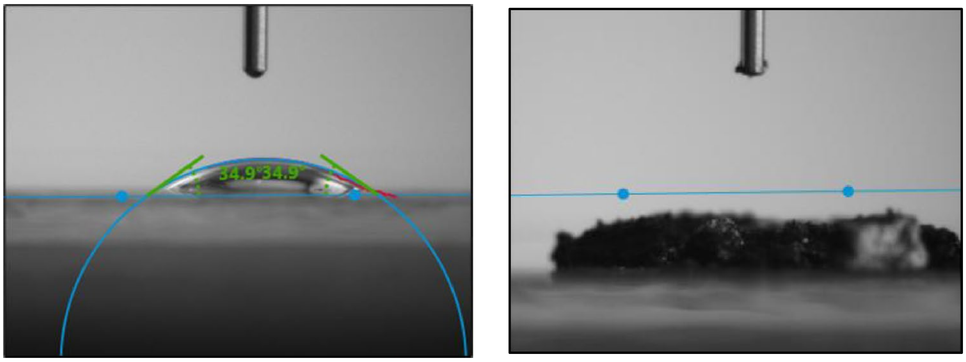

(a) Water droplet on a clear glass slide

(b) Water droplet on biochar surface

Fig. 6 a Water droplet on a clear glass slide. b Water droplet on biochar surface.

production. The surface areas of biochars reported in this study are higher than selected biochars reported in literature [57, 59]. The amount of fixed carbon in wood-based chars appears to be consistent, at around 80%, which was also observed for the DoE biochars. Temperatures above 400 °C were reported to produce a recalcitrant structure resulting from the loss of volatile matter, as well as alkyl and carboxylic groups [62]. The statement further supplements the chemical moiety information obtained from FTIR, suggesting a layered carbon structure. The concentric arrangement of pores in the carbonaceous skeleton is also visible in the SEM images.

Higher temperatures have also been reported to increase alkalinity of biochars [57]. DoE biochars in this work were determined to have an average PZC of 7.40 ± 0.02. In addition to a neutral pH, contact angle analysis of the biochars suggested hydrophilic character. Rattanakam et al. investigated the difference in hydrophilicity of oxidised and un-oxidised wood-based biochars [63], reporting an increase in the hydrophilic behaviour of oxidised biochars. Fir wood-derived biochars for perchlorate adsorption were contrastingly reported to provide a hydrophobic environment, as opposed to the hydrophilic biochars produced in this work [64]. The high surface areas, carbon content, and hydrophilic nature of the biochars produced in this work give them great potential for possible application in water and wastewater treatment systems [57]. Process parameter influence on biochar characteristics appears to be significant, as evidenced by the DoE study and could potentially provide a pathway to produce sustainable biochars catered to specific applications.

Conclusions

Biochars produced from native Scottish woods showed significant influence of pyrolysis operating parameters on the characteristics of the final products. The optimal solution for a design of experiments study on softwood closely resembled data obtained from experimental runs. Gas flow rates were noted as insignificant with contact time having the greatest impact on biochar characteristics. A high residence time not only produced an increase in observed surface area but also appeared to enhance mesoporosity within the pore structure. Spectroscopic analysis indicated the presence of a layered carbon structure in the biochars. The intricate pore network and graphene-like layered porous arrangement are also evident from morphological analysis. All biochars carry an almost neutral surface charge with a hydrophilic nature, indicating potential for application in water treatment systems. The results demonstrate the potential for native Scottish wood samples as a biochar material, with a requirement to consider the influence of manufacturing operating parameters on final biochar characteristics.

Supplementary Information The online version contains supplementary material available at https://doi.org/10.1007/s12155-023-10595-6.

Declarations

Conflict of Interest The authors declare no competing interests.

References

1. Manyà JJ (2012) Pyrolysis for biochar purposes: a review to establish current knowledge gaps and research needs. Environ Sci Technol 46:7939–7954. https://doi.org/10.1021/es301029g
2. Ahmad M, Rajapaksha AU, Lim JE et al (2014) Biochar as a sorbent for contaminant management in soil and water: A review. Chemosphere 99:19–33. https://doi.org/10.1016/j.chemosphere.2013.10.071
3. Lee J, Kim K-H, Kwon EE (2017) Biochar as a Catalyst. Renewable and Sustainable Energy Reviews 77:70–79. https://doi.org/10.1016/j.rser.2017.04.002
4. Liu W-J, Jiang H, Yu H-Q (2019) Emerging applications of biochar-based materials for energy storage and conversion. Energy Environ Sci 12:1751–1779. https://doi.org/10.1039/c9ee00206e
5. Ahmad J, Patuzzi F, Rashid TDU et al (2020) Exploring untapped effect of process conditions on biochar characteristics and applications. Environ Technol Innov 21:101310. https://doi.org/10.1016/j.eti.2020.101310
6. Ghaedi M, Mazaheri H, Khodadoust S et al (2015) Application of central composite design for simultaneous removal of methylene blue and Pb2+ ions by walnut wood activated carbon. Spectrochim Acta A Mol Biomol Spectrosc 135:479–490. https://doi.org/10.1016/j.saa.2014.06.138
7. Idowu GA, Fletcher AJ (2020) The manufacture and characterisation of rosid angiosperm-derived biochars applied to water treatment. Bioenergy Res 13:387–396. https://doi.org/10.1007/s12155-019-10074-x
8. Li M, Chen D, Zhu X (2013) Preparation of solid acid catalyst from rice husk char and its catalytic performance in esterification. Chinese Journal of Catalysis 34:1674–1682. https://doi.org/10.1016/S1872-2067(12)60634-2
9. Dehkhoda AM, West AH, Ellis N (2010) Biochar based solid acid catalyst for biodiesel production. Appl Catal A Gen 382:197–204. https://doi.org/10.1016/j.apcata.2010.04.051
10. Dehkhoda AM, Ellis N, Gyenge E (2014) Electrosorption on activated biochar: effect of thermo-chemical activation treatment on the electric double layer capacitance. J Appl Electrochem 44:141–157. https://doi.org/10.1007/s10800-013-0616-4

11 Roncancio R, Gore JP (2021) CO2 char gasification: a systematic review from 2014 to 2020. Energy Conversion and Management: X 10:100060. https://doi.org/10.1016/j.ecmx.2020.100060

12 Kyzas GZ, Deliyanni EA, Matis KA (2016) Activated carbons produced by pyrolysis of waste potato peels: cobalt ions removal by adsorption. Colloids Surf A Physicochem Eng Asp 490:74–83. https://doi.org/10.1016/j.colsurfa.2015.11.038

13. Marañón E, Sastre H (1991) Heavy metal removal in packed beds using apple wastes. Bioresour Technol 38:39–43. https://doi.org/10.1016/0960-8524(91)90219-A
14. Tripathi M, Sahu JN, Ganesan P (2016) Effect of process parameters on production of biochar from biomass waste through pyrolysis: a review. Renew Sustain Energy Rev 55:467–481. https://doi.org/10.1016/j.rser.2015.10.122
15. Lehmann J, Joseph S (2015) Biochar for environmental management, 2nd edn. Routledge, London

16 Luo L, Xu C, Chen Z, Zhang S (2015) Properties of biomass-derived biochars: combined effects of operating conditions and biomass types. Bioresour Technol 192:83–89. https://doi.org/10.1016/j.biortech.2015.05.054

17. Pallarés J, González-Cencerrado A, Arauzo I (2018) Production and characterization of activated carbon from barley straw by physical activation with carbon dioxide and steam. Biomass Bioenergy 115:64–73. https://doi.org/10.1016/j.biombioe.2018.04.015

18 Leng L, Xiong Q, Yang L et al (2021) An overview on engineering the surface area and porosity of biochar. Science of The Total Environment 763:144204. https://doi.org/10.1016/j.scitotenv.2020.144204

19. Angın D (2013) Effect of pyrolysis temperature and heating rate on biochar obtained from pyrolysis of safflower seed press cake. Bioresour Technol 128:593–597. https://doi.org/10.1016/j.biortech.2012.10.150

20 Ateş F, Pütün E, Pütün AE (2004) Fast pyrolysis of sesame stalk: yields and structural analysis of bio-oil. J Anal Appl Pyrolysis 71:779–790. https://doi.org/10.1016/j.jaap.2003.11.001

21 Chen D, Li Y, Cen K et al (2016) Pyrolysis polygeneration of poplar wood: effect of heating rate and pyrolysis temperature. Bioresour Technol 218:780–788. https://doi.org/10.1016/j.biortech.2016.07.049

22. Park HJ, Park Y-K, Kim JS (2008) Influence of reaction conditions and the char separation system on the production of bio-oil from radiata pine sawdust by fast pyrolysis. Fuel Processing Technology 89:797–802. https://doi.org/10.1016/j.fuproc.2008.01.003

23 Mohamed AR, Hamzah Z, Daud MZM, Zakaria Z (2013) The effects of holding time and the sweeping nitrogen gas flowrates on the pyrolysis of EFB using a fixed–bed reactor. Procedia Eng 53:185–191. https://doi.org/10.1016/j.proeng.2013.02.024

24 Tsai WT, Lee MK, Chang YM (2007) Fast pyrolysis of rice husk: product yields and compositions. Bioresour Technol 98:22–28. https://doi.org/10.1016/j.biortech.2005.12.005

25. Tsai WT, Chang CY, Lee SL (1997) Preparation and characterization of activated carbons from corn cob. Carbon N Y 35:1198–1200. https://doi.org/10.1016/S0008-6223(97)84654-4
26. Zhao B, O'Connor D, Zhang J et al (2018) Effect of pyrolysis temperature, heating rate, and residence time on rapeseed stem derived biochar. J Clean Prod 174:977–987. https://doi.org/10.1016/j.jclepro.2017.11.013
27. Cetin E, Gupta R, Moghtaderi B (2005) Effect of pyrolysis pressure and heating rate on radiata pine char structure and apparent gasification reactivity. Fuel 84:1328–1334. https://doi.org/10.1016/j.fuel.2004.07.016

28 Melligan F, Auccaise R, Novotny EH et al (2011) Pressurised pyrolysis of Miscanthus using a fixed bed reactor. Bioresour Technol 102:3466–3470. https://doi.org/10.1016/j.biortech.2010.10.129

29. Manyà JJ, Roca FX, Perales JF (2013) TGA study examining the effect of pressure and peak temperature on biochar yield during pyrolysis of two-phase olive mill waste. J Anal Appl Pyrolysis 103:86–95. https://doi.org/10.1016/j.jaap.2012.10.006

30 Ertaş M, Hakkı Alma M (2010) Pyrolysis of laurel (Laurus nobilis L.) extraction residues in a fixed-bed reactor: characterization of bio-oil and bio-char. J Anal Appl Pyrolysis 88:22–29. https://doi.org/10.1016/j.jaap.2010.02.006

31. Bouchelta C, Medjram MS, Zoubida M et al (2012) Effects of pyrolysis conditions on the porous structure development of date pits activated carbon. J Anal Appl Pyrolysis 94:215–222. https://doi.org/10.1016/j.jaap.2011.12.014
32. Lua AC, Lau FY, Guo J (2006) Influence of pyrolysis conditions on pore development of oil-palm-shell activated carbons. J Anal Appl Pyrolysis 76:96–102. https://doi.org/10.1016/j.jaap.2005.08.001

33 Hassan M, Liu Y, Naidu R et al (2020) Influences of feedstock sources and pyrolysis temperature on the properties of biochar and functionality as adsorbents: a meta-analysis. Science of The Total Environment 744:140714. https://doi.org/10.1016/j.scitotenv.2020.140714

34 Leng L, Huang H (2018) An overview of the effect of pyrolysis process parameters on biochar stability. Bioresour Technol 270:627–642. https://doi.org/10.1016/j.biortech.2018.09.030

35. Rehrah D, Bansode RR, Hassan O, Ahmedna M (2018) Short-term greenhouse emission lowering effect of biochars from solid organic municipal wastes. Int J Environ Sci Technol 15:1093–1102. https://doi.org/10.1007/s13762-017-1470-4

36. Seow YX, Tan YH, Mubarak NM et al (2022) A review on biochar production from different biomass wastes by recent carbonization technologies and its sustainable applications. J Environ Chem Eng 10:107017. https://doi.org/10.1016/j.jece.2021.107017
37. Deloach R Analysis of variance in the modern design of experiments. American Institute of Aeronautics and Astronautics
38. Durakovic B (2017) Design of experiments application, concepts, examples: state of the art. Periodicals of Engineering and Natural Sciences (PEN) 5 https://doi.org/10.21533/pen.v5i3.145
39. Barad M (2014) Design of experiments (DOE)—a valuable multi-purpose methodology. Appl Math (Irvine) 05:2120–2129. https://doi.org/10.4236/am.2014.514206
40. Cao W, Li J, Lin L, Zhang X (2021) Release of potassium in association with structural evolution during biomass combustion. Fuel 287:119524. https://doi.org/10.1016/j.fuel.2020.119524
41. Brunauer S, Emmett PH, Teller E (1938) Adsorption of gases in multimolecular layers. J Am Chem Soc 60:309–319. https://doi.org/10.1021/ja01269a023
42. Warne SSJ (1991) Proximate analysis of coal, oil shale, low quality fossil fuels and related materials by thermogravimetry. TrAC Trends in Analytical Chemistry 10:195–199. https://doi.org/10.1016/0165-9936(91)85021-I
43. Bakatula EN, Richard D, Neculita CM, Zagury GJ (2018) Determination of point of zero charge of natural organic materials. Environ Sci Pollut Res 25:7823–7833. https://doi.org/10.1007/s11356-017-1115-7
44. Usevičiūtė L, Baltrėnaitė E (2020) Methods for determining lignocellulosic biochar wettability. Waste Biomass Valorization 11:4457–4468. https://doi.org/10.1007/s12649-019-00713-x
45. El-Masry EH, Ibrahim HA, Abdel Moamen OA, Zaher WF (2022) Sorption of some rare earth elements from aqueous solutions using copolymer/activated carbon composite: multivariate optimization approach. Advanced Powder Technology 33:103467. https://doi.org/10.1016/j.apt.2022.103467
46. Thommes M, Kaneko K, Neimark AV et al (2015) Physisorption of gases, with special reference to the evaluation of surface area and pore size distribution (IUPAC Technical Report). Pure Appl Chem 87:1051–1069. https://doi.org/10.1515/pac-2014-1117
47 Lippens BC, de Boer JH (1965) Studies on pore systems in catalysts: V. The t method. J Catal 4:319–323. https://doi.org/10.1016/0021-9517(65)90307-6
48. Parsa M, Nourani M, Baghdadi M et al (2019) Biochars derived from marine macroalgae as a mesoporous by-product of hydrothermal liquefaction process: characterization and application in wastewater treatment. Journal of Water Process Engineering 32:100942. https://doi.org/10.1016/j.jwpe.2019.100942
49. Gómez-Gualdrón DA, Moghadam PZ, Hupp JT et al (2016) Application of consistency criteria to calculate BET areas of micro- and mesoporous metal–organic frameworks. J Am Chem Soc 138:215–224. https://doi.org/10.1021/jacs.5b10266
50. Sing KSW (2014) 7 - Assessment of surface area by gas adsorption. In: Rouquerol F, Rouquerol J, Sing KSW et al (eds) Adsorption by Powders and Porous Solids, 2nd edn. Academic Press, Oxford, pp 237–268
51. Kloss S, Zehetner F, Dellantonio A et al (2012) Characterization of slow pyrolysis biochars: effects of feedstocks and pyrolysis temperature on biochar properties. J Environ Qual 41:990–1000. https://doi.org/10.2134/jeq2011.0070
52. Barrett EP, Joyner LG, Halenda PP (1951) The determination of pore volume and area distributions in porous substances. I. Computations from Nitrogen Isotherms. J Am Chem Soc 73:373–380. https://doi.org/10.1021/ja01145a126
53 Nandiyanto ABD, Oktiani R, Ragadhita R (2019) How to read and interpret FTIR spectroscope of organic material. Indonesian Journal of Science and Technology 4:97. https://doi.org/10.17509/ijost.v4i1.15806
54. Lee JW, Kidder M, Evans BR et al (2010) Characterization of biochars produced from cornstovers for soil amendment. Environ Sci Technol 44:7970–7974. https://doi.org/10.1021/es101337x
55. Rey-Mafull CA, Tacoronte JE, Garcia R et al (2014) Comparative study of the adsorption of acetaminophen on activated carbons in simulated gastric fluid. Springerplus 3:48. https://doi.org/10.1186/2193-1801-3-48
56. Chaves Fernandes BC, Ferreira Mendes K, Dias Júnior AF et al (2020) Impact of pyrolysis temperature on the properties of eucalyptus wood-derived biochar. Materials 13:5841. https://doi.org/10.3390/ma13245841
57. Shaheen SM, Niazi NK, Noha E et al (2019) Wood-based biochar for the removal of potentially toxic elements in water and wastewater: a critical review. Int Mater Rev 64:216–247. https://doi.org/10.1080/09506608.2018.1473096
58. Zhang H, Voroney RP, Price GW (2015) Effects of temperature and processing conditions on biochar chemical properties and their influence on soil C and N transformations. Soil Biol Biochem 83:19–28. https://doi.org/10.1016/j.soilbio.2015.01.006
59. Pipíška M, Krajčíková EK, Hvostik M, et al (2022) Biochar from wood chips and corn cobs for adsorption of thioflavin t and erythrosine B. Materials 15
60. Bubici S, Korb J-P, Kučerik J, Conte P (2016) Evaluation of the surface affinity of water in three biochars using fast field cycling NMR relaxometry. Magn Reson Chem 54:365–370. https://doi.org/10.1002/mrc.4391
61. Yuan Y, Lee TR (2013) Contact angle and wetting properties. Springer, Berlin Heidelberg, pp 3–34
62. Jindo K, Mizumoto H, Sawada Y et al (2014) Physical and chemical characterization of biochars derived from different agricultural residues. Biogeosciences 11:6613–6621. https://doi.org/10.5194/bg-11-6613-2014
63. Rattanakam R, Pituya P, Suwan M, Supothina S (2017) Assessment of hydrophilic biochar effect on sandy soil water retention. Key Eng Mater 751:790–795. https://doi.org/10.4028/www.scientific.net/KEM.751.790
64. Fang Q, Chen B, Lin Y, Guan Y (2014) Aromatic and hydrophobic surfaces of wood-derived biochar enhance perchlorate adsorption via hydrogen bonding to oxygen-containing organic groups. Environ Sci Technol 48:279–288. https://doi.org/10.1021/es403711y

Article 2 was submitted to Adsorption Science & Technology on August 31st, 2023, and is currently under peer review.

Adsorption Science & Technology

Scottish softwood biochar for water remediation targeting selected persistent organic pollutants

Mohammad Umair Jamal*[1], Ashleigh Fletcher[1], Alan Baby[1], Isaac Maso[1], Lidija Šiller[2]
[1]Chemical and Process Engineering, University of Strathclyde, Glasgow, G1 1XL, UK
[2]School of Engineering, Newcastle University, Newcastle upon Tyne, NE1 7RU, UK

Correspondence should be addressed to **Mohammad Umair Jamal**; umair.jamal@strath.ac.uk

Abstract

A Scottish wood biochar sample was investigated for water remediation against persistent organic pollutants as a potential renewable material for adsorption processes. Textural characterisation gave a high surface area (588 m^2/g) and a mix of microporous and mesoporous nature with an average pore width of 4 nm. Morphological analysis revealed a layered carbon structure and spectroscopic analysis showed the presence of oxygen and nitrogen-based functionalities. The biochar had an average point of zero charge slightly above neutral. 3-4, DCA kinetic rates were rapid (<5 min), restricting kinetic analysis, while a pseudo second order kinetic model was best suited to represent the kinetic data for acetaminophen and carbamazepine, suggesting chemical control. The adsorption equilibria were most appropriately described by the Sips isotherm model, supplementing the chemical control theory for a multilayer system. Maximum adsorption capacity was relatively all three chemicals, and the biochar demonstrated good removal efficiency against all target species, showing potential as an adsorbent.

Keywords: Activated carbon, surface area, water treatment, pharmaceuticals, pesticides

Introduction

The demands on freshwater supplies to support growing populations and settlements is a key issue, particularly for communities located in water-stressed regions. Available freshwater amounts to 2.5% of total global water resources [1]; in 2018, an estimated two billion people were living in countries experiencing water scarcity [2]. Many also experience 'economic' water shortage, with ~1.6 million people residing in areas where water is physically available but there is an acute shortage of the required infrastructure required to access those water resources [2]. A significant disparity exists in gathering the required water quality data, due to a lack of monitoring and reporting, especially in developing nations.

Water quality has been severely affected by pollution via natural and anthropogenic factors. On a global scale, approximately 80% of industrial and municipal wastewater is discharged into the environment without undergoing any form of treatment beforehand. The risks associated with emerging pollutants, including micropollutants, have been recognized since the early 2000s [3]. Organic pollutants can be either synthetic compounds or oxygen demanding wastes produced from household or industrial activities. They contain compounds such as hydrocarbons, detergents, insecticides and herbicides, lubricants, endocrine disrupting chemicals (EDCs), pharmaceuticals, etc. that have detrimental effects on human and environmental health [4,5]. Among these, EDCs and pharmaceutical compounds are of growing concern due to release into the environment through engineered and natural pathways, without adequate monitoring systems. Such chemicals can mimic hormones within the body and interfere with the endocrine system and adversely affect bodily functions [6]. Even at low concentrations, prolonged exposure can result in adverse health effects. An EDC of particular concern is 3,4-Dicholoroaniline (3,4-DCA), a derivative of aniline with high global annual production [7] intermediate in the production of urea herbicides [8] in the synthesis of fabric pigments, and as a paint precursor [9,10]. Known to be toxic to aquatic organisms and humans, with the potential to cause long-term adverse effects in aquatic environments, the Predicted No-Effect Concentration (PNEC) for 3,4-DCA is 0.2 µg/L. In addition, the detection of Active Pharmaceutical Ingredients (APIs) in various surface waters has sparked concerns regarding their potential impact on the environment and living organisms and common pollutants in this category include acetaminophen (APAP) and carbamazepine (CBZ). APAP, commonly known as paracetamol, is an analgesic used to mitigate moderate to severe pain [11]. Healthcare facilities, improper household disposal, inadequate treatment and veterinary treatment provided to livestock are pathways for water contamination. APAP can accumulate in the tissues of aquatic organisms, posing risks to higher trophic levels in the food chain. In humans, it has been reported to cause acute liver failure, and is the second most frequent reason for liver transplantation in the US [12]. CBZ is extensively used worldwide as a multifunctional medication, serving both as an anticonvulsant and a pain-reliever [13] contamination pathways are similar to those for APAP, with a range of environmental and human health issues [14,15] CBZ is among the emerging organic contaminants detected at the highest concentration with highest concentration (~4.6 µg/L) [16]. All of these pollutant species pose a challenge for microbial degradation or decomposition in the environment, and it is necessary to develop new methods of removal from water streams; this is increasingly complex when designing systems that can target a range of species.

Adsorption is often used as an application for targeting persistent organic compounds owing to its ease of application and the availability of a range of materials as potential adsorbents. The choice of precursor is an important step in developing an effective adsorbent material. Biochar based adsorbents can be derived from a range of precursors and are also versatile in their field of application. [17] investigated 3,4-DCA removal using biomass fly ash and concluded that removal is regulated by boundary layer diffusion, while strong adsorbate-adsorbent interactions have been observed [18,19]. APAP adsorption appears to be controlled by the hydroxyl and amino functional groups acting as electron donors, augmenting the electron density on the aromatic ring [20], which may be influenced by the surface groups present on the biochar surface [21]. CBZ, on the other hand, is reported to interact through mechanisms including chemical bonding, π-π interaction, and Lewis Acid-Base interaction; and despite its weak hydrogen bonding, CBZ has been shown to chemical bond with biochar surfaces [22]. This indicates that, despite all being aromatic molecules, there is a range of interactions between these target molecules and a potential adsorbent material. The aim of this work is to investigate the removal of 3,4-DCA, APAP and CBZ from an aqueous system using biochar derived from native Scottish woods, analysed using thermodynamic and kinetic studies.

Materials and methods

The precursor used for making the biochar was procured from Sustainable Thinking Scotland C.I.C. (Kinneil Estate, Bo’ness, Scotland). Wood samples are taken from deforested wood in the walled garden of the 200-acre estate. The sample mix was pure softwood including species such as Scots pine, western red cedar, and Sitka spruce.

Pyrolysis

Previous results [23] indicated that, for the feedstock used, the optimum yield and surface area was obtained for a sample pyrolysed at 725 °C, with a hold time of 60 min and a heating rate of 15 °C/min (known as the optimised biochar). Before pyrolysis, wood samples were divided into small cubes, rinsed with DI water and oven dried for 24 h at 100 °C. A precursor weight of 30±0.1 g was distributed into three crucibles with a lid placed on top and pyrolysed inside a Thermconcept KLS 10/12/WS muffle furnace. An inert atmosphere was obtained inside the furnace using a CO_2 flowrate of 250 mL/min. The furnace was switched on at the designated temperature and dwell time conditions and at the end of each run, the flow of gas was switched off and samples were allowed to cool overnight before analysis. Figure 1 shows a schematic diagram of the muffle furnace used in this study.

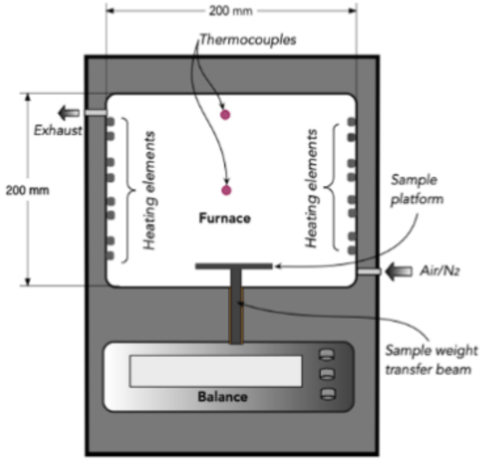

Figure 1 Schematic diagram of muffle furnace equipped with a weighing system (Licence number - 5501811254585) [24]

Biochar production was repeated twice to ensure the results fall within acceptable error margins.

Material Characterisation

Porous Structure Characterisation: Biochar specific surface area and pore size distribution were determined using Brunauer-Emmett-Teller (BET) [25] and Barrett-Joyner-Halenda (BJH) [26] models. Samples were crushed to a powdered form before analysis. A Micromeritics ASAP 2420 system was used to perform nitrogen adsorption at -196 °C. Sample degassing was performed at 200 °C for 4 h at a heating rate of 10 °C/min. The adsorption branch of the isotherm consisted of 49 points, with 30 points on the desorption branch.

Fourier Transform Infrared Spectroscopy (FTIR): Attenuated Total Reflectance (ATR) was used to study functional groups on the biochar surface. A small amount of powdered biochar was analysed using an ABB IR Instrument MB3000 series. The acquisition mode was set to transmittance, with a detector gain of 80% for increased accuracy. A total of 32 scans were taken between wavenumbers 500 and 4000 cm^{-1}, at 4 cm^{-1} resolution.

X-ray Photoelectron Spectroscopy (XPS): XPS analysis was used to determine the surface chemistry of the biochar sample and was performed by the NEXUS facility at Newcastle University. The biochar sample was crushed to a powdered form and analysed using a K-Alpha Photoelectron Spectrometer (Thermo Fisher) and electron detection using a hemispherical analyser. Measurements were taken with the flood gun on to lower charging with the beam energy at 40 eV and a step-size of 0.05 eV. The generated results were analysed using the Fityk program.

Point of Zero Charge (PZC): PZC analysis was performed using a salt addition method [27]. A 40 mL portion of a solution containing 0.1 M $NaNO_3$ was modified to reach five different pH levels ranging from 3 to 11. To achieve the desired pH, solutions of 0.1 M NaOH and 0.1 M HCl were utilized. Approximately 0.2 g of powdered biochar was introduced into the beakers and stirred at a speed of 450 rpm for 24 h. The resulting mixture was filtered, and the pH of the filtered liquid was measured. By calculating the difference between the initial and final pH values of the samples and plotting the change in pH against the initial value, the PZC value was determined.

Analytical Method

The experimental solutions were passed through Fisherbrand Grade 601 general purpose filter papers (125 mm diameter). Two filter papers were used for each filtration step to ensure the removal of all suspended particles from the permeate. For the target species in this work, calibration curves were plotted prior kinetic and adsorption experiments. The maximum adsorption wavelengths for 3,4-DCA, APAP and CBZ are 296, 243 and 285 nm respectively. For calibration, absorbance obtained by passing light of monochromatic radiation was plotted against concentration and a liner fit provided the required parameters of slope and intercept. The generated equation was then used to identify residual concentrations from experimental runs.

Adsorption Kinetics

Biochar samples (0.1 g) were added to 100 mL glass bottles and mixed with 50 mL of 100 mg/L solution of either APAP, CBZ or 3,4-DCA. The bottles were subsequently placed on an orbital shaker at 420 rpm for time steps 15, 30, 60, 120, 180, 240, 360 and 1440 min. Once completed, the solutions for each time step were double filtered using cellulose acetate filter papers to obtain a clear solution free of suspended biochar particles. The supernatants were analysed using UV-Vis spectroscopy. The amount of target species adsorbed was calculated using calibration curves run prior to kinetic and isotherm measurements. It should be noted that there was an exception in the case of 3,4-DCA kinetic analysis. The speed of adsorption was observed to be extremely fast, not allowing sufficient time to measure and analyse multiple samples. Hence, a reduction in temperature was used, using an ice bath (~2-3 °C) to slow the reaction process to obtain kinetic parameters. A series of kinetic models were applied to determine the most appropriate fit.

The pseudo first order (PFO) model was first proposed by Lagergren in 1898 [28]. The differential form of the model is given by Equation 1:

$$\frac{dq_t}{dt} = k_1(q_e - q_t) \tag{1}$$

Where k_1 is the rate constant for adsorption, and q_e and q_t are the adsorbate uptake amounts at equilibrium and a given time ‘t’, per mass of adsorbent, respectively. Integrating the above equation provides the linearized form of the model shown in Equation 2 [29]:

$$\ln(q_e - q_t) = lnq_e - k_1 t \tag{2}$$

Which upon rearranging gives the non-linear PFO model given by Equation 3:

$$q_t = q_e(1 - e^{-k_1 t}) \tag{3}$$

The physical meaning associated with the model has been suggested to be dependent on the initial solute concentration [30,31]. The PFO model is associated with a high initial solute concentration, the process being at the initial stage of adsorption, and availability of only a few active adsorbent sites [32].

Ho *et al.* [33], proposed the expression for the pseudo second order (PSO) model by integrating Equation 4:

$$\frac{dq_t}{dt} = k_2(q_e - q_t)^2 \tag{4}$$

And applying it to the adsorption of lead onto peat, to obtain the non-linear model displayed in Equation 5:

$$q_t = \frac{{q_e}^2 k_2 t}{1 + q_e k_2 t} \tag{5}$$

Where k_2 is the reaction rate constant, and all other terms are as defined for PSO. The linearised form of the model is given as shown in Equation 6:

$$\frac{t}{q_t} = \frac{1}{k_2 {q_e}^2} + \frac{t}{q_e} \tag{6}$$

PSO models are more commonly used to predict adsorption experiments as opposed to PFO models. The model signifies a low initial solute concentration, occurring within the final stages of the adsorption process, and an abundance of active sites on the adsorbent [32].

Adsorption Isotherms

Batch adsorption experiments were carried out using 0.1 g biochar in 50 mL solution of the target species. For APAP and 3,4-DCA, the concentrations used were 25, 50, 75, 100, 150, 200, 250 and 300 mg/L. For CBZ, the maximum solubility is 125 mg/L and, hence, the isotherm points were taken between 10-100 mg/L at intervals of 10 mg/L. Based on the kinetic data, 3,4-DCA isotherm solutions were filtered after 10 min. Experiments for APAP were run for 6 hours and CBZ experiments were allowed to run for 24 hours to allow for full equilibration of the samples. The permeate collection procedure was similar to that used within the kinetic measurements, where the solutions were double filtered using two cellulose acetate filter papers and the absorbance measured using UV-vis spectroscopy. The collected isotherm data was analysed using three adsorption isotherm models.

The non-linear form of Langmuir model [34] is given in Equation 7:

$$q_e = \frac{q_m K_L C_e}{1 + K_L C_e} \tag{7}$$

Where q_m is the maximum adsorption capacity in mg/g, C_e is the equilibrium concentration of the solute in mg/L, q_e is the amount of solute adsorbed in mg/g and K_L is the ratio between adsorption and desorption rates in L/mg. The model represents a chemical adsorption process with monolayer formation and homogenous adsorption [35].

The Freundlich model [36] is given in Equation 8:

$$q_e = K_F {C_e}^{1/n} \tag{8}$$

Where K_F is the rate constant in $L^{1/n}mg^{1-1/n}/g$ and n is a correction factor. The linearised form of the model can be obtained when n=1. All other terms are as defined above. This model represents nonlinear adsorption processes and can be treated as an empirical equation [35].

The Sips model [37] is often referred to as the Langmuir-Freundlich isotherm model and was developed in 1948. The non-linear form is shown in Equation 9:

$$q_e = \frac{q_{ms} K_S {C_e}^{n_S}}{1 + K_S {C_e}^{n_S}} \tag{9}$$

Where the maximum adsorbed amount is represented by q_{ms} in mg/g and K_S ($L^{ns}.mg^{-ns}$) and n_S are the Sips constants. When the value of n_S in the Sips model is equal to 1, the model simplifies to the Langmuir model. At low initial concentrations (C_0), the Sips model also resembles the Freundlich model. However, it is important to note that, unlike the Sips model, the Langmuir model satisfies Henry's law at low C_0. The model can be applied to homogeneous as well as heterogeneous systems and describes the adsorption process of a monolayer, where one adsorbate molecule is adsorbed onto $1/n_S$ adsorption sites [35].

Results

Material Characterisation

Figure 2 shows the adsorption-desorption isotherms obtained for the optimised biochar sample. The adsorption isotherm shows a high initial uptake at low relative pressures, followed by a plateau in the high relative pressure region, which can be attributed to the microporous and mesoporous nature of the material. This resembles a Type IV isotherm behaviour, as per the IUPAC classification of physisorption behaviour [38].

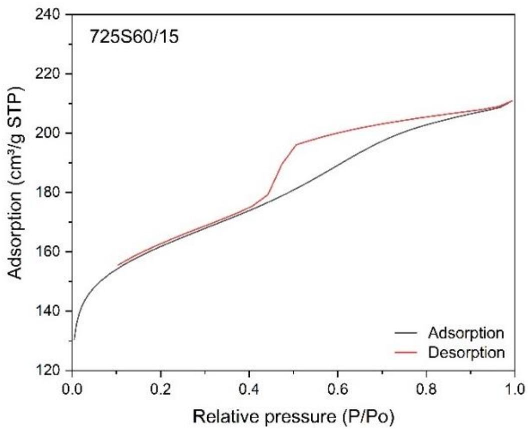

Figure 2 Nitrogen adsorption and desorption isotherms on the optimised biochar sample

The hysteresis loop resembles Type H4 where the adsorption branch is associated with micropore filling at low relative pressures as expected for microporous carbons [38], this is further supported by the ratio of micropore to total pore volume for the biochar sample, which was 55%. The micropore volume was calculated using the t plot method developed by Lippens and Boer [39]. Total pore volume (TPV) was calculated using Equation 10:

$$TPV = (Q_{sat} * \frac{MW}{V_m})/\rho_{liq} \tag{10}$$

Where, Q_{sat} is the maximum nitrogen adsorption in cm^3/g, MW is molecular weight of nitrogen (28 g/mol), V_m is volume occupied by 1 mol of gas (22.4 L) and ρ_{liq} is density of nitrogen at boiling point (808 g/L). The average pore width of the material was 4 nm, and the pore volume distribution is shown in Figure 3. It is evident from the distribution that the produced biochar material is highly microporous with a discrete pore size.

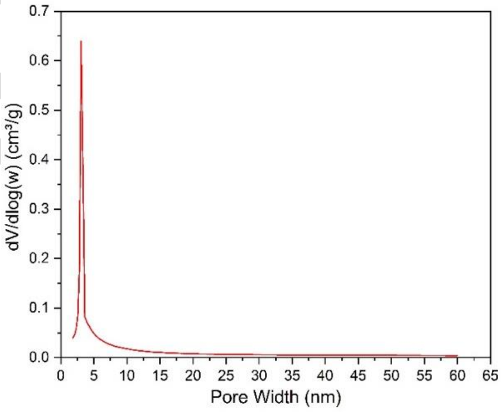

Figure 3 Pore volume distribution of the optimised biochar sample using BJH method [26]

The biochar surface area was calculated, using the BET method, to be 620 m^2/g. BET analysis, however, is sensitive to the selected relative pressure region [40]; specifically for microporous materials, the optimal range of relative pressure can be determined by applying the four consistency criteria proposed by Rouquerol *et al.* [41]. These criteria are as follows: (1): Only the range where the product of the adsorbate loading rate and the difference between 1 and the relative pressure exhibits a monotonic increase with the relative pressure should be selected, (2): The value of the BET 'C constant' should be positive. The C constant represents the interactions between the adsorbent and adsorbate and is linked to the energetic aspects of the first adsorbed layer [40], (3): The linear region chosen should include the loading corresponding to the monolayer at the given relative pressure, (4): The relative pressure obtained from Criterion 3 should be within a 20% tolerance of the relative pressure calculated from BET theory that aligns with monolayer loading. Upon applying the correction to the data obtained for this biochar sample, the ‘corrected’ surface area was calculated to be 588 m^2/g, which is larger than other wood based biochars reported in previous studies [42–44].

The FTIR spectra obtained for the wood feedstock and the optimised biochar are shown in Figure 4. The fingerprint region, observed between 600 and 1500 cm^{-1} shows the presence of vinyl terminals [45]. At 1000 cm^{-1}, there is evidence of a loss of the peak observed in the feedstock, due to heat treatment. The peak loss can be attributed to the removal of C-OH vibrations from dehydration during pyrolysis [44]. The process of heat treatment is essential in facilitating condensation of the carbonaceous skeleton and eliminating the hydroxyl groups found in the cellulosic compounds within the initial materials [46]. Overall, the feedstock and biochar spectra look comparable with the presence of C=C bonds with symmetric and asymmetric vibrations between 1600-1800 cm^{-1}.

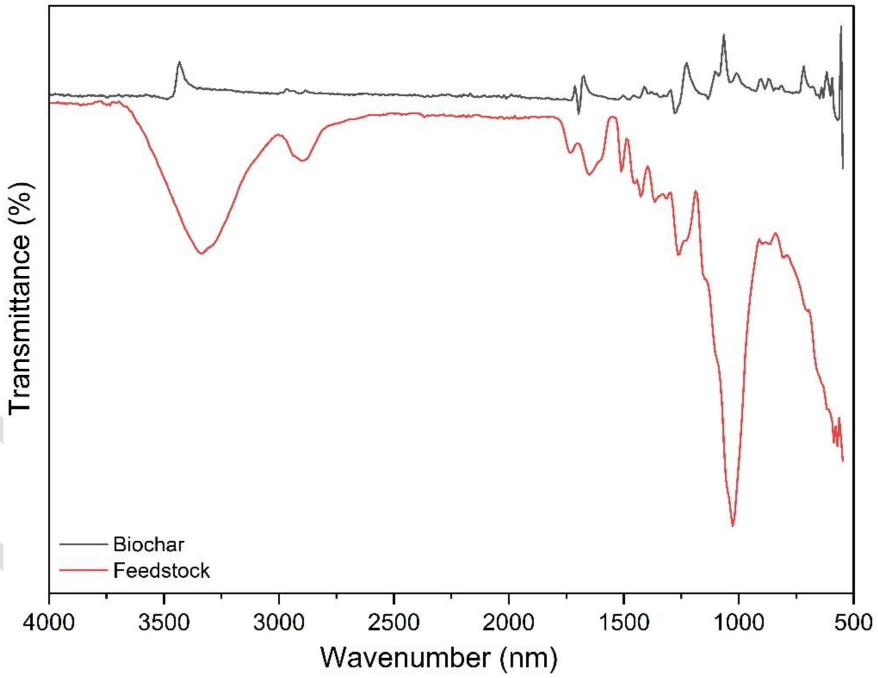

Figure 4 FTIR spectra of wood feedstock and biochar

The XPS spectra of the optimised biochar sample used are shown in Figure 5. The spectra show the presence of oxygen and nitrogen bonds, in addition to carbon with peaks at 532.5, 400 and 284.5 eV, respectively [47]. Peak deconvolution was achieved using the Fityk program, and the Voigt function assisted in the identification of the heteroatoms present in the biochar. The corresponding parameters are provided in Table S1 (Supporting Information). C1s peaks were deconvoluted into three peaks at 284.5 eV, suggesting a graphene like arrangement (C=C), at 285.6 eV indicating the presence of carbonyl bonds (C-O), and a third peak at 289.6 eV, which is ascribed to either carboxylic or pyridinic N bond functionalities (C=O/C-N) [48–51]. The area under the C=C peak is the largest indicating the preservation of the graphene-like arrangement in the wood samples post-pyrolysis. Peak convolution of O1s showed the presence of both carbonyl, as well as carboxyl groups, with peaks at 531.1 and 532.9 eV [51,52]. There were also trace amounts of nitrogen functionalities present in the sample and convolution of the N1s spectra suggested the presence of pyridinic (398.6 eV) as well as graphene N (400.2 eV) bonds in the sample [53]. The incorporation of O and N-based functional groups into the carbon framework enhances its wettability [47], which is further correlated with contact angle measurement presented in previous work [23], where biochar samples proved to be extremely hydrophilic. The calculation of the elemental compositions of C, N and O were performed as suggested by Alexander G. Shard [54]. Equation 11 works under the assumption that the sample is homogenous and a single phase within the penetration depth; where X represents the atomic fraction (in %), and I_P/S_P is the intensity divided by the sensitivity factor (S_P = 1, 1.8 and 2.93 for C, N and O respectively).

$$X = \frac{I_P/S_P}{\sum_j I_j/S_j} \tag{11}$$

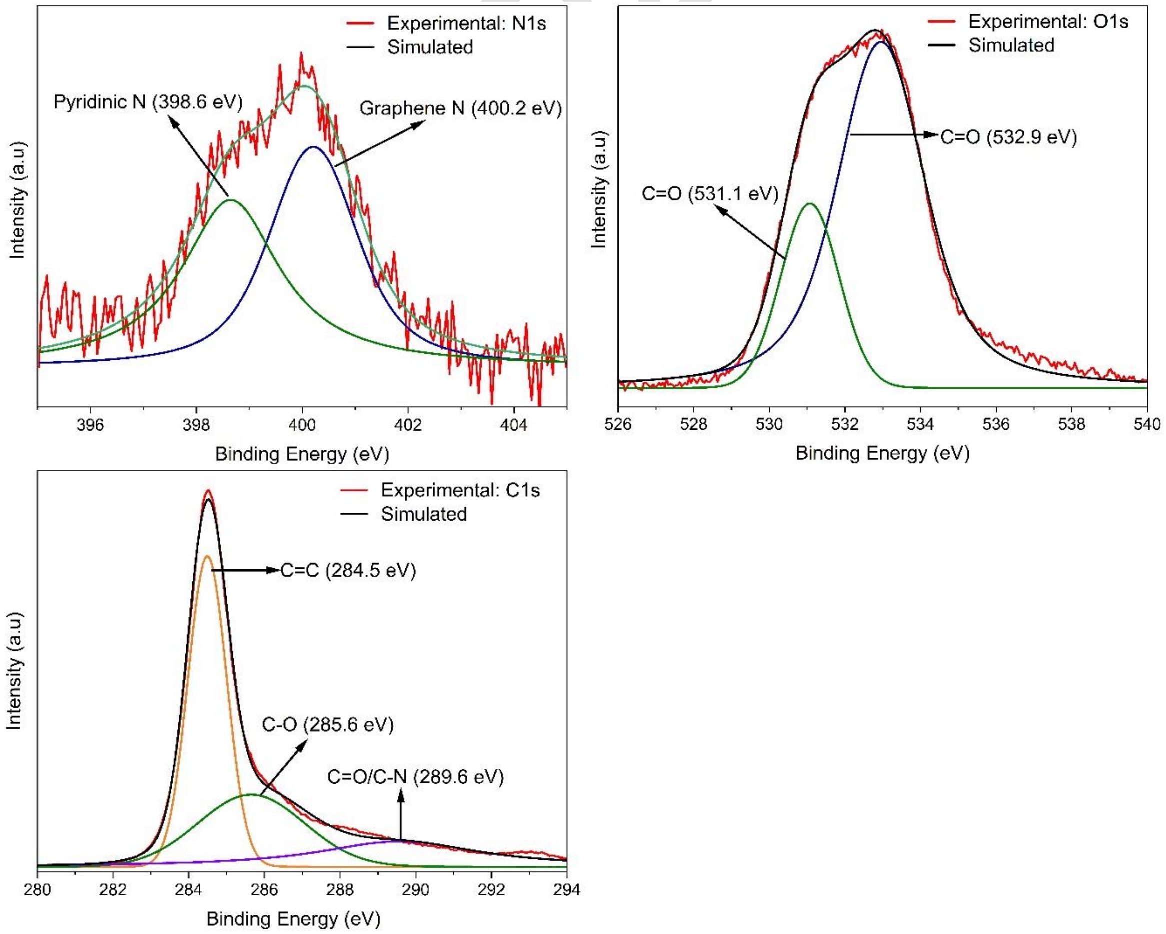

Figure 5 XPS spectra and Fityk simulated models showing N1s, O1s and C1s scans

The biochar sample used consisted of 80% C, 13% O and 7% N fractions. The findings again supplement the results obtained in the previous reported study, where thermogravimetric analysis of the samples showed 80% fixed C [23].

The PZC of the biochar was observed to be 7.44±0.2. The results are comparable to the previous study on parameter optimisation, where the DOE biochars had similar average PZC values [23]. PZC values are temperature dependent, and high temperatures result in a loss of volatile matter including acidic functional groups such as phenols and carboxyl, causing the resulting biochar to have a more alkaline nature [55]. PZC of wood pellet biochars was also reported to increase with increasing temperatures [56]; such alkaline/neutral PZC values make these biochars suitable for potential application in drinking water systems that operate naturally under slightly acidic conditions.

Adsorption Kinetics

Table 1 shows the parameters of kinetic models fitted to the data obtained for adsorption of APAP and CBZ onto the optimised biochar. Kinetic analysis of 3,4-DCA revealed fast adsorption rates, which could not be fitted to any kinetic models.

Table 1 Kinetic parameters of adsorption models fitted to acetaminophen (APAP) and carbamazepine (CBZ)

Model Parameters	APAP	Carbamazepine
Pseudo first order (non-linear)		
R^2 (COD)	0.461	0.460
R^2 adj.	0.371	0.371
qe (mg/g)	46.72±0.315	38.83±1.266
K_1 (min^{-1})	0.207±0.028	0.097±0.023
Pseudo second order (non-linear)		
R^2 (COD)	0.871	0.782
R^2 adj.	0.849	0.746
qe (mg/g)	47.32±0.199	40.56±1.001
K_2 (g/mg*min)	0.021±0.003	0.004±0.001
Pseudo second order (linear)		
R^2 (COD)	1	1
R^2 adj.	1	1
qe (mg/g)	47.62	46.86
K_3 (g/mg*min)	0.013	0.054

Data was obtained for 3,4-DCA adsorption on the optimised biochars at room temperature, for an initial concentration of 100 mg/L. Removal was observed to be 90% after 15 min, with a plateau thereafter. Readings were, therefore, taken at shorter time intervals, and also at lower temperature in an attempt to slow the kinetic process. Table 2 shows the removal percentages of 3,4-DCA at room temperature and in the ice bath. The data obtained confirms the rapid adsorption of 3,4-DCA onto the optimised biochar, even at the lower temperature, hence, it was not possible to monitor the adsorption in order to determine the kinetic parameters for 3,4-DCA.

Table 2 Biochar performance against 3,4-DCA at room temperature and in an ice bath

Time (min)	% Removal -> room temp.	% Removal -> 3±0.5°C
2	94	86
4	94	88
6	95	90
9	95	89

The results indicate that the interaction between the biochar surface and 3,4-DCA molecule is almost instant. An investigation into solution pH also yielded similar results with overnight runs at pH 6 and 9 resulting in 93% and 91% removal, respectively. Previous research into 3,4-DCA removal using adsorption suggested that the data followed a pseudo-second order kinetic model [57]. The observed reaction rates in this study are quicker than those previously reported. Experiments using kaolinite and montmorillonite to test removal of chloroanilines, including 3,4-DCA, were reported to achieve equilibrium in under 4 days [58]. Another study into 3,4-DCA removal from water using biomass fly ashes reported kinetic equilibrium at approximately 10 hours [17]. A selection of low-cost materials including corncob char, sugar beet pulp, perlite, and vermiculite were also tested against 3,4-DCA. The quickest reaction time to achieve maximum sorption percentage was 60 min using vermiculite [59]. The rates observed here indicate that there is significantly quicker adsorption for the biochars created in this work.

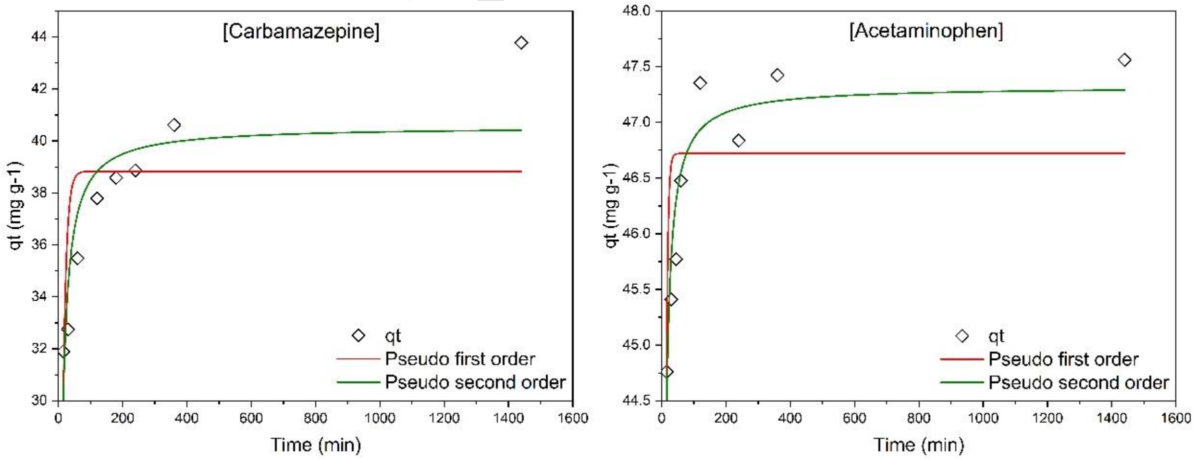

Figure 6 Non-linear kinetic model fittings for carbamazepine and acetaminophen on the optimised biochar

Figure 6 shows the kinetic data obtained for the sorption of CBZ and APAP on the biochar sample. Sorption kinetics for APAP showed rapid uptake with 90% removal achieved in 15 min followed by a gradual increase in the uptake, and equilibrium achieved after approximately 2 hours. For CBZ, the uptake was slower with just under 75% removal at 15 min and adsorption slowed considerably after 2 hours, with equilibrium achieved after 24 hours. The linearised pseudo second order rate equation showed a better fit for the data for both species compared to pseudo first order and non-linear second order kinetic models (Table 2). The adjusted R^2 values for both species was ≥0.99. The maximum adsorption capacity for APAP was 47.6 mg/g and 46.7 mg/g for CBZ. The second order rate constants show a quicker uptake rate for APAP than CBZ with the adsorption rate being 0.013 g/mg×min. The high R^2 values obtained for both species, with linear PSO model fitting, can be attributed to availability of abundant vacant active sites in the physically activated biochar and the adsorption process being ruled by chemisorption [32,60,61]. The mechanism could likely be attributed to hydrogen bonding between the species. Additionally, π- π interactions between the benzene ring in APAP and CBZ and the aromatics in biochar can influence the adsorption process [61].

Further analysis of the kinetic data was performed using the intraparticle diffusion model proposed by Weber and Morris [62], to understand the rate-controlling step in the adsorption process. The model equation is given below:

$$q_t = k_p t^{1/2} + C \tag{12}$$

Where k_p is the intraparticle diffusion rate constant in mg/g·min$^{1/2}$ and C is a constant that represents the boundary layer effect and initial adsorption. Linearised plots of the model are depicted in Figure 7.

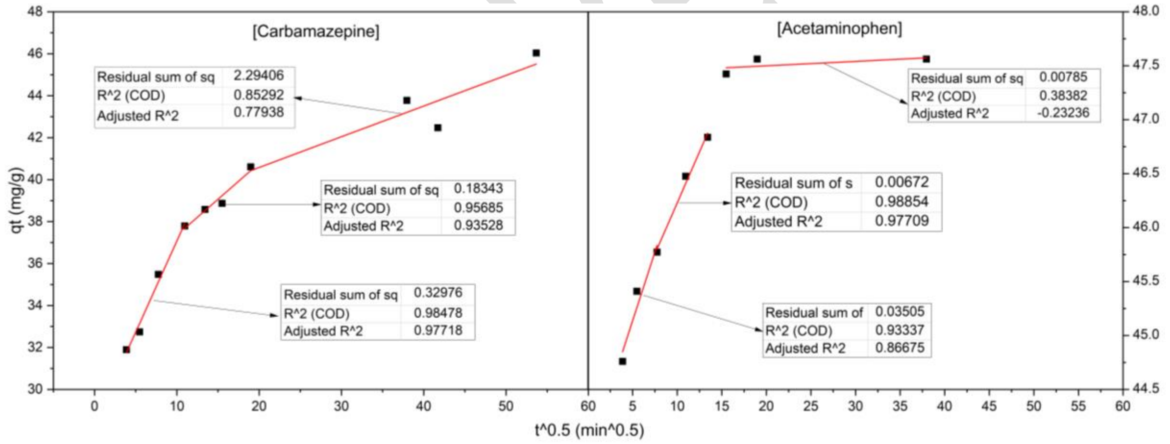

Figure 7 Intraparticle diffusion model fittings for acetaminophen and carbamazepine adsorption on the optimised biochar

The plots suggest that the adsorption process for both pharmaceutical species involved three diffusion steps. In both cases, liquid film diffusion was the dominating phase signifying rapid diffusion of molecules onto the active sites in the pores and voids of the biochar [63,64]. There is a hint of intraparticle diffusion in CBZ adsorption. This step involves the gradual diffusion of molecules into the micropores before the reaction proceeds to the equilibrium stage. For APAP however, the intraparticle diffusion phase is not as prevalent and the reaction appears to proceed rapidly to equilibrium after liquid phase diffusion. This also correlates with the longer time required by CBZ to reach equilibrium compared to APAP. The three target molecules have some similarities, allowing a comparison of their adsorption behaviour relative to their chemistry. All contain amine functionalities and benzene rings, with APAP/BBZ sharing carbonyl moieties and only 3,4-DCA containing halogenated species. The slower kinetics for CBZ could realistically be a consequence of the significantly larger relative size of the molecule (see Supporting Information), while the rapid adsorption of 3,4-DCA is likely a result of the comparatively increased electrostatic interactions, where the chlorine groups will be electron withdrawing from the benzene ring.

Adsorption Isotherms

Adsorption isotherms are of crucial importance in determining the maximum adsorption capacity of the adsorbent and understanding the adsorption equilibrium. The results of isotherm fittings for the Langmuir, Freundlich and Sips models are given in Table 3, and isotherm plots for the target species are shown in Figure 9. The results indicate that the adsorption uptake was significant at low pollutant concentrations. The data presented in Table 3 suggests that for CBZ and 3,4-DCA, the Sips model can be best used to describe the adsorption behaviour. This suggests that the adsorption process is a combination of physisorption at low concentrations and chemisorption at high initial C_o values with the formation of a monolayer on the adsorbent material. The maximum adsorption capacities for CBZ and 3,4-DCA, suggested by the Sips model, were 39.8 mg/g and 83.2 mg/g respectively. For APAP, both Langmuir and SIPS isotherm models demonstrated high R^2 values. A good fit to the Langmuir model assumes monolayer adsorption of the molecules on the biochar surface, with almost identical activation energies, albeit with the possibility of multilayer formation [60]. The maximum adsorption capacity for APAP is determined as 126 mg/g, much higher than the other two species, which may be reduced as a consequence of molecular size affecting packing in the case of CBZ and electrostatic repulsion in the case of 3,4-DCA. Since the two models exhibited a good fit to the experimental data for APAP, the value of the separation factor (R_L) suggested by Webber and Chakkravorti [65] was calculated to further verify the favourability of the Langmuir adsorption isotherm (see Supplementary Information). The separation factor is determined from Equation 13:

$$R_L = \frac{1}{1 + K_L C_o} \tag{13}$$

Table 3 Adsorption isotherm parameters obtained for acetaminophen (APAP), carbamazepine (CBZ) and 3,4-Dicholoroaniline (3,4-DCA) on the optimised biochar sample.

Isotherm Parameters	APAP	CBZ	3,4-DCA
Langmuir			
R^2 (COD)	0.976	0.907	0.905
R^2 adj.	0.972	0.895	0.893
q_m (mg/g)	118.9±5.910	59.84±9.694	110.9±15.36
K_L (L/mg)	0.204±0.036	0.182±0.065	0.028±0.010
Freundlich			
R^2 (COD)	0.929	0.801	0.797
R^2 adj.	0.915	0.772	0.769

q_m (mg/g)	32.62±4.966	11.77±2.679	9.771±4.409
K_F ($L^{1/n}mg^{1-1/n}/g$)	0.313±0.044	0.503±0.106	0.456±0.104
SIPS			
R^2 (COD)	0.977	0.968	0.939
R^2 adj.	0.967	0.959	0.922
q_m (mg/g)	126.2±19.81	39.77±2.105	83.20±7.025
K_S ($L^{ns}\cdot mg^{-ns}$)	0.214±0.046	0.065±0.032	0.002±0.003

The value for R_L was >1 for all C_o values suggesting unfavourable adsorption [35]. However, this could also be attributed to the limitations of the model assumptions, including homogenous adsorption sites and identical adsorption energies. The model is also limited to the assumption of monolayer adsorption, which can be overcome by the Sips model, which includes the possibility of multilayer formation. To conclude, APAP adsorption on the biochar surface is better represented by the Sips model.

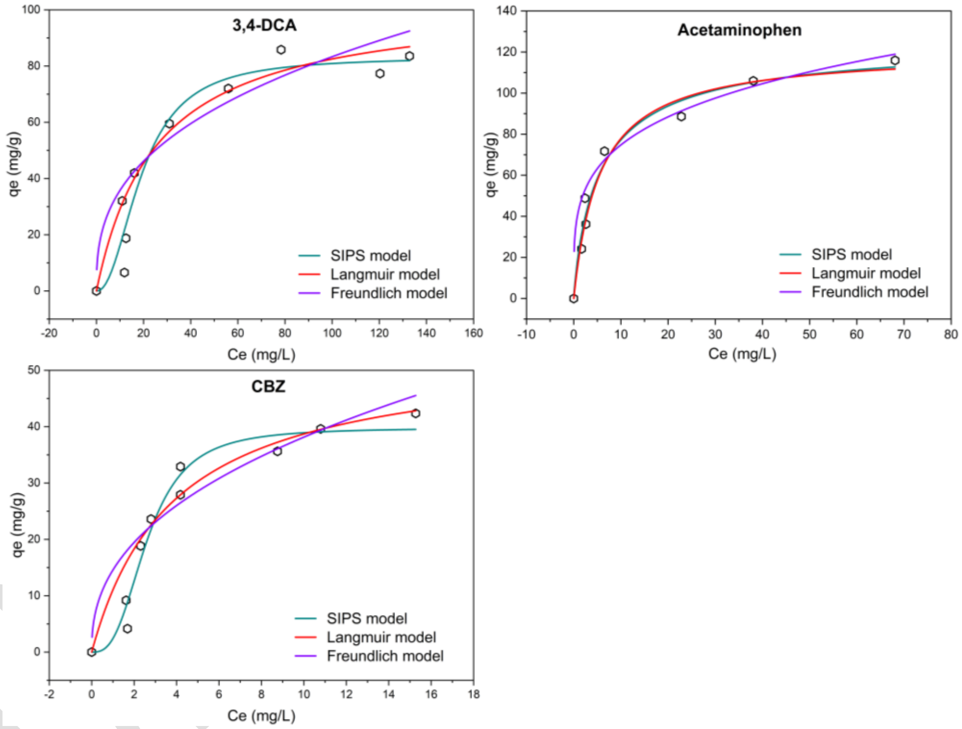

Figure 8 Adsorption isotherm models for target species

To further investigate the nature of adsorption sites, Scatchard plots were obtained from the adsorption data. The Scatchard equation is given in Equation 14.

$$\frac{q_e}{C_e} = Qb - q_e b \qquad (14)$$

Where the Scatchard adsorption constant Q is in mg/g and b is in L/mg. The nature of the material surface can be interpreted from the plot between q_e/C_e vs q_e. If the plot is linear, the material surface is expected to be homogeneous with a single type of binding site available. Contrary, a non-linear plot suggests heterogeneity and multiple binding sites [66].

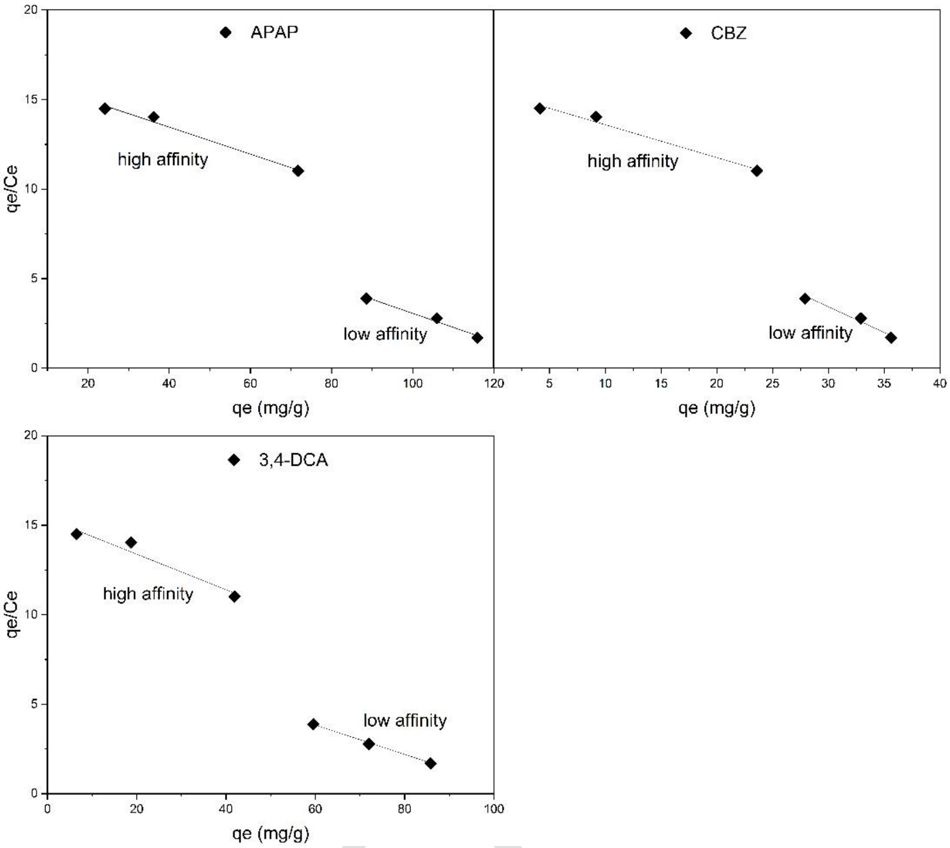

Figure 9 Scatchard plots target species adsorption using the optimised biochar

Figure 9 shows the Scatchard plots obtained for the adsorption of target species. It is evident from the plots that the adsorption behaviour deviates from linearity. The high and low binding affinities can be attributed to the presence of more than one type of binding sites, offering strong and weak interactions respectively. The high affinity binding sites can be attributed to chemical interactions between the biochar surface and the target compounds whereas the low affinity sites indicate weak physical bonds. The plots further supplement the observations from Sips isotherm indicating a heterogeneous material with multiple binding sites.

Discussion

The results obtained suggest potential for application of the optimised biochar in water remediation, targeting persistent organic pollutants. The biochar surface area was higher than those reported for many wood-based biochars reported in literature [44,67]. The sample presents a mixed microporous-mesoporous structure, as observed from the nitrogen isotherms with an average pore width of 4 nm, indicating that the mesopores present in the sample are narrow. Biochars pyrolysed at higher temperatures are linked with alkaline surface character [55], which fits with the PZC value obtained for the biochar produced at 725 °C (7.44±0.2). FTIR analysis suggested a layered carbon structure with the presence of oxygen and nitrogen chemical moieties. These findings were further assisted by XPS analysis presenting a graphene-like arrangement, and 80% atomic carbon fraction. Additionally, the presence of oxygen and nitrogen-based functionalities was confirmed from XPS data. These chemical moieties assist the hydrophilic nature of the biochar and provide a potential avenue for application in water remediation.

Table 4 Maximum uptake capacities of different adsorbents for acetaminophen (APAP), carbamazepine (CBZ) and 3,4-DCA

Adsorbent	**Species**	**q_{max} (mg/g)**	**Reference**
AC from wood	APAP	87	[68]
AC from coconut shell	APAP	135	[68]
AC from orange peels	APAP	118	[60]
Biochar from Scottish softwood	APAP	126	This study
Peanut shells biochar	CBZ	4.96	[69]
Pine sawdust biochar	CBZ	5.25	[70]
AC from Argan tree nutshells	CBZ	71.4	[71]
Biochar from Scottish softwood	CBZ	40	This study
Kaolinite	3,4-DCA	0.311	[8]
Montmorillonite	3,4-DCA	0.077	[8]
Greenhouse biomass fly ash	3,4-DCA	0.125	[17]
Biochar from Scottish softwood	3,4-DCA	83	This study

The application of biochar against 3,4-DCA, APAP and carbamazepine resulted in efficient removal of the species from an aqueous system. 3,4-DCA removal was characterised with fast removal rates and a very short equilibrium time of around 6 min and a maximum adsorption capacity of 83 mg/g. Although the maximum removal capacity was lower than some activated carbons reported in the literature, adsorption rates were far superior in achieving acceptable removal overall [72]. Adsorption of APAP and CBZ was best explained by the linearised pseudo second order model indicating the formation of chemical bonds as the rate limiting step. The maximum adsorption capacities for APAP and CBZ were 126 and 40 mg/g, respectively and these were superior or on par with those reported in Table 4. The presence of nitrogen and oxygen functionalities on the surface of the biochars present possible hydrogen bonding or π-π interactions between the benzene rings in the target elements and the biochar surface, as a possible removal mechanism. Overall, the optimised biochar sample selected for application from the design of experiments optimisation study conducted previously [23], provided fast adsorption kinetics and high adsorption capacities against the identified target molecules. The results provide an attractive avenue for biochar application for water remediation targeting a range of pollutants in aqueous media.

Conclusions

The optimised biochar produced from Scottish softwood showed good performance against selected pollutant species. The material was characterised with a high surface area and mixed microporous/mesoporous nature. Point of zero charge analysis indicated a neutral surface charge and X-ray photoelectron spectroscopy data suggested a hydrophilic nature and potential for application in water remediation. The material showed great performance against 3,4-dichloroaniline with rapid equilibrium proving difficult to perform a kinetic analysis. For acetaminophen and carbamazepine, adsorption followed a pseudo second order kinetic model. Adsorption isotherms were best explained by the Sips model for all three species suggesting the formation of an initial monolayer with chemical bonding as the rate limiting step. The highest adsorption capacity was noted in the case of acetaminophen. Scatchard plots suggested a heterogeneous surface with multiple binding sites. Ultimately, the results indicate a potential application of the softwood biochar as a renewable adsorbent in water remediation.

Data Availability

All data generated in this study are included in this article. No AIF related data was generated in this study. Access to previous publication can be found using the DOI: https://doi.org/10.1007/s12155-023-10595-6

Conflicts of Interest

The authors declare no conflict of interests.

Funding Statement

This research did not receive any specific grant from funding agencies in the public, commercial, or not-for-profit sectors.

Acknowledgements

The authors would like to acknowledge Sustainable Thinking Scotland C.I.C for supplying the raw wood feedstock for biochar production and Kiran Kumar Reddy Reddygunta for their assistance in the analysis of XPS data.

Supplementary Materials

The supplementary document contains information on XPS peak deconvolution parameters and values of separation factor against initial APAP concentrations to assess the favourability of Langmuir isotherm model. It also includes the chemical structures of the target species along with linear kinetic PSO model fittings for CBZ and APAP.

References

[1] International Energy Agency, Water-Energy Nexus, Paris, 2017. https://www.iea.org/reports/water-energy-nexus.

[2] United Nations Educational Scientific and Cultural Organization, The United Nations World Water Development Report 2021: Valuing water, Water Politics. (2021) 206. https://unesdoc.unesco.org/ark:/48223/pf0000375724 (accessed July 10, 2023).

[3] N. Bolong, A.F. Ismail, M.R. Salim, T. Matsuura, A review of the effects of emerging contaminants in wastewater and options for their removal, Desalination. 239 (2009) 229–246. https://doi.org/10.1016/J.DESAL.2008.03.020.

[4] Jr., G.A. Burton, R. Pitt, Stormwater Effects Handbook : A Toolbox for Watershed Managers, Scientists, and Engineers, Stormwater Effects Handbook. (2001). https://doi.org/10.1201/9781420036244.

[5] A.W. Verla, C.E. Enyoh, E.N. Verla, K.O. Nwarnorh, Microplastic–toxic chemical interaction: a review study on quantified levels, mechanism and implication, SN Appl Sci. 1 (2019) 1–30. https://doi.org/10.1007/S42452-019-1352-0/FIGURES/8.

[6] T.M. Crisp, E.D. Clegg, R.L. Cooper, W.P. Wood, D.G. Andersen, K.P. Baetcke, J.L. Hoffmann, M.S. Morrow, D.J. Rodier, J.E. Schaeffer, L.W. Touart, M.G. Zeeman, Y.M. Patel, Environmental endocrine disruption: an effects assessment and analysis., Environ Health Perspect. 106 (1998) 11. https://doi.org/10.1289/EHP.98106S111.

[7] A.G. Livingston, A. Willacy, Degradation of 3,4-dichloroaniline in synthetic and industrially produced wastewaters by mixed cultures freely suspended and immobilized in a packed-bed reactor, Appl Microbiol Biotechnol. 35 (1991) 551–557. https://doi.org/10.1007/BF00169767.

[8] A. Luca Tasca, A. Fletcher, Journal of Environmental Science and Health, Part A Toxic/Hazardous Substances and Environmental Engineering State of the art of the environmental behaviour and removal techniques of the endocrine disruptor 3,4-dichloroaniline, (2017). https://doi.org/10.1080/10934529.2017.1394701.

[9] M. Nurul, H. Bhuiyan, H. Kang, J. Choi, S. Lim, Y. Kho, K. Choi, Effects of 3,4-dichloroaniline (3,4-DCA) and 4,4 0-methylenedianiline (4,4 0-MDA) on sex hormone regulation and reproduction of adult zebrafish (Danio rerio), Chemosphere. 269 (2021) 128768. https://doi.org/10.1016/j.chemosphere.2020.128768.

[10] M.A. Ibrahim, S.Z. Zulkifli, M.N.A. Azmai, F. Mohamat-yusuff, A. Ismail, Reproductive Toxicity of 3,4-dichloroaniline (3,4-DCA) on Javanese Medaka (Oryzias javanicus, Bleeker 1854), Animals (Basel). 11 (2021) 1–12. https://doi.org/10.3390/ANI11030798.

[11] O.M. Rodriguez-Narvaez, J.M. Peralta-Hernandez, A. Goonetilleke, E.R. Bandala, Treatment technologies for emerging contaminants in water: A review, Chemical Engineering Journal. 323 (2017) 361–380. https://doi.org/10.1016/J.CEJ.2017.04.106.

[12] A.M. Larson, J. Polson, R.J. Fontana, T.J. Davern, E. Lalani, L.S. Hynan, J.S. Reisch, F. V. Schiødt, G. Ostapowicz, A.O. Shakil, W.M. Lee, Acetaminophen-induced acute liver failure: results of a United States multicenter, prospective study, Hepatology. 42 (2005) 1364–1372. https://doi.org/10.1002/HEP.20948.

[13] M.A. Décima, S. Marzeddu, M. Barchiesi, C. Di Marcantonio, A. Chiavola, M.R. Boni, A Review on the Removal of Carbamazepine from Aqueous Solution by Using Activated Carbon and Biochar, Sustainability 2021, Vol. 13, Page 11760. 13 (2021) 11760. https://doi.org/10.3390/SU132111760.

[14] J.K. Harvey, Pollution Sources: Point and Nonpoint - river, temperature, important, salt, types, system, plants, oxygen, human, Water Encyclopedia. (n.d.). http://www.waterencyclopedia.com/Po-Re/Pollution-Sources-Point-and-Nonpoint.html (accessed July 11, 2023).

[15] A. Vaseashta, Nanomaterials for Chemical—Biological — Physical Integrity of Potable Water, (2009) 1–16. https://doi.org/10.1007/978-90-481-3497-7_1.

[16] R. Loos, R. Carvalho, D.C. António, S. Comero, G. Locoro, S. Tavazzi, B. Paracchini, M. Ghiani, T. Lettieri, L. Blaha, B. Jarosova, S. Voorspoels, K. Servaes, P. Haglund, J. Fick, R.H. Lindberg, D. Schwesig, B.M. Gawlik, EU-wide monitoring survey on emerging polar organic contaminants in wastewater treatment plant effluents, Water Res. 47 (2013) 6475–6487. https://doi.org/10.1016/J.WATRES.2013.08.024.

[17] M. Quirantes, R. Nogales, E. Romero, Sorption potential of different biomass fly ashes for the removal of diuron and 3,4-dichloroaniline from water, J Hazard Mater. 331 (2017) 300–308. https://doi.org/10.1016/J.JHAZMAT.2017.02.047.

[18] C.J. van Oss, A review of: “Active Carbon.” R.C. Bansal, J.B. Donnet and F. Stoeckli; Marcel Dekker, New York, 1988. pp. 482, $135.00., Http://Dx.Doi.Org/10.1080/01932699008943255. 11 (2007) 323–323. https://doi.org/10.1080/01932699008943255.

[19] L.P. Bakhaeva, G.K. Vasilyeva, E.G. Surovtseva, V.M. Mukhin, Microbial degradation of 3,4-dichloroaniline sorbed by activated carbon, Microbiology (N Y). 70 (2001) 277–284. https://doi.org/10.1023/A:1010495025794/METRICS.

[20] P.S. Pauletto, S.F. Lütke, G.L. Dotto, N.P.G. Salau, Adsorption mechanisms of single and simultaneous removal of pharmaceutical compounds onto activated carbon: Isotherm and thermodynamic modeling, J Mol Liq. 336 (2021) 116203. https://doi.org/10.1016/J.MOLLIQ.2021.116203.

[21] H.N. Tran, F. Tomul, N. Thi Hoang Ha, D.T. Nguyen, E.C. Lima, G.T. Le, C.T. Chang, V. Masindi, S.H. Woo, Innovative spherical biochar for pharmaceutical removal from water: Insight into adsorption mechanism, J Hazard Mater. 394 (2020) 122255. https://doi.org/10.1016/J.JHAZMAT.2020.122255.

[22] G. Liang, Z. Hu, Z. Wang, X. Yang, X. Xie, J. Zhao, Effective removal of carbamazepine and diclofenac by CuO/Cu2O/Cu-biochar composite with different adsorption mechanisms, Environ Sci Pollut Res Int. 27 (2020) 45435–45446. https://doi.org/10.1007/S11356-020-10284-3.

[23] M.U. Jamal, A.J. Fletcher, Design of Experiments Study on Scottish Wood Biochars and Process Parameter Influence on Final Biochar Characteristics, Bioenergy Res. 1 (2023) 1–14. https://doi.org/10.1007/S12155-023-10595-6/FIGURES/6.

[24] W. Cao, J. Li, L. Lin, X. Zhang, Release of potassium in association with structural evolution during biomass combustion, Fuel. 287 (2021) 119524. https://doi.org/https://doi.org/10.1016/j.fuel.2020.119524.

[25] S. Brunauer, P.H. Emmett, E. Teller, Adsorption of Gases in Multimolecular Layers, J Am Chem Soc. 60 (1938) 309–319. https://doi.org/10.1021/ja01269a023.

[26] E.P. Barrett, L.G. Joyner, P.P. Halenda, The Determination of Pore Volume and Area Distributions in Porous Substances. I. Computations from Nitrogen Isotherms, J Am Chem Soc. 73 (1951) 373–380. https://doi.org/10.1021/ja01145a126.

[27] E.N. Bakatula, D. Richard, C.M. Neculita, G.J. Zagury, Determination of point of zero charge of natural organic materials, Environmental Science and Pollution Research. 25 (2018) 7823–7833. https://doi.org/10.1007/s11356-017-1115-7.

[28] S.L.-K. svenska vetenskapsakademiens. Handlingar, undefined 1898, Zur theorie der sogenannten adsorption geloster stoffe, Cir.Nii.Ac.Jp. (n.d.). https://cir.nii.ac.jp/crid/1572824501080908544 (accessed July 17, 2023).

[29] H. Moussout, H. Ahlafi, M. Aazza, H. Maghat, Critical of linear and nonlinear equations of pseudo-first order and pseudo-second order kinetic models, Karbala International Journal of Modern Science. 4 (2018) 244–254. https://doi.org/10.1016/J.KIJOMS.2018.04.001.

[30] Y. Liu, L. Shen, From Langmuir kinetics to first- and second-order rate equations for adsorption, Langmuir. 24 (2008) 11625–11630. https://doi.org/10.1021/LA801839B/ASSET/IMAGES/MEDIUM/LA-2008-01839B_0004.GIF.

[31] S. Azizian, Kinetic models of sorption: a theoretical analysis, J Colloid Interface Sci. 276 (2004) 47–52. https://doi.org/10.1016/J.JCIS.2004.03.048.

[32] J. Wang, X. Guo, Adsorption kinetic models: Physical meanings, applications, and solving methods, (2020). https://doi.org/10.1016/j.jhazmat.2020.122156.

[33] Y.S. Ho, G. McKay, Sorption of dye from aqueous solution by peat, Chemical Engineering Journal. 70 (1998) 115–124. https://doi.org/10.1016/S1385-8947(98)00076-X.

[34] I. Langmuir, The constitution and fundamental properties of solids and liquids. Part I. Solids, J Am Chem Soc. 38 (1916) 2221–2295. https://doi.org/10.1021/JA02268A002.

[35] J. Wang, X. Guo, Adsorption isotherm models: Classification, physical meaning, application and solving method, Chemosphere. 258 (2020) 127279. https://doi.org/10.1016/J.CHEMOSPHERE.2020.127279.

[36] H. Freundlich, Über die Adsorption in Lösungen, Zeitschrift Für Physikalische Chemie. 57U (1907) 385–470. https://doi.org/10.1515/ZPCH-1907-5723/HTML.

[37] R. Sips, On the Structure of a Catalyst Surface, J Chem Phys. 16 (1948) 490–495. https://doi.org/10.1063/1.1746922.

[38] M. Thommes, K. Kaneko, A. V Neimark, J.P. Olivier, F. Rodriguez-Reinoso, J. Rouquerol, K.S.W. Sing, IUPAC Technical Report Physisorption of gases, with special reference to the evaluation of surface area and pore size distribution (IUPAC Technical Report), (2015). https://doi.org/10.1515/pac-2014-1117.

[39] B.C. Lippens, J.H. de Boer, Studies on pore systems in catalysts: V. The t method, J Catal. 4 (1965) 319–323. https://doi.org/https://doi.org/10.1016/0021-9517(65)90307-6.

[40] D.A. Gómez-Gualdrón, P.Z. Moghadam, J.T. Hupp, O.K. Farha, R.Q. Snurr, Application of Consistency Criteria To Calculate BET Areas of Micro- And Mesoporous Metal–Organic Frameworks, J Am Chem Soc. 138 (2016) 215–224. https://doi.org/10.1021/jacs.5b10266.

[41] K.S.W. Sing, 7 - Assessment of Surface Area by Gas Adsorption, in: F. Rouquerol, J. Rouquerol, K.S.W. Sing, P. Llewellyn, G. Maurin (Eds.), Adsorption by Powders and Porous Solids (Second Edition), Academic Press, Oxford, 2014: pp. 237–268. https://doi.org/https://doi.org/10.1016/B978-0-08-097035-6.00007-3.

[42] S. Kloss, F. Zehetner, A. Dellantonio, R. Hamid, F. Ottner, V. Liedtke, M. Schwanninger, M.H. Gerzabek, G. Soja, Characterization of Slow Pyrolysis Biochars: Effects of Feedstocks and Pyrolysis Temperature on Biochar Properties, J Environ Qual. 41 (2012) 990–1000. https://doi.org/10.2134/jeq2011.0070.

[43] K. Jindo, H. Mizumoto, Y. Sawada, M.A. Sanchez-Monedero, T. Sonoki, Physical and chemical characterization of biochars derived from different agricultural residues, Biogeosciences. 11 (2014) 6613–6621. https://doi.org/10.5194/bg-11-6613-2014.

[44] G.A. Idowu, A.J. Fletcher, The Manufacture and Characterisation of Rosid Angiosperm-Derived Biochars Applied to Water Treatment, Bioenergy Res. 13 (2020) 387–396. https://doi.org/10.1007/s12155-019-10074-x.

[45] A.B.D. Nandiyanto, R. Oktiani, R. Ragadhita, How to Read and Interpret FTIR Spectroscope of Organic Material, Indonesian Journal of Science and Technology. 4 (2019) 97. https://doi.org/10.17509/ijost.v4i1.15806.

[46] J.W. Lee, M. Kidder, B.R. Evans, S. Paik, A.C. Buchanan Iii, C.T. Garten, R.C. Brown, Characterization of Biochars Produced from Cornstovers for Soil Amendment, Environ Sci Technol. 44 (2010) 7970–7974. https://doi.org/10.1021/es101337x.

[47] K.K.R. Reddygunta, A. Callander, L. Šiller, K. Faulds, L. Berlouis, A. Ivaturi, Sono-exfoliated graphene-like activated carbon from hazelnut shells for flexible supercapacitors, Int J Energy Res. 46 (2022) 16512–16537. https://doi.org/10.1002/ER.8314.

[48] K.L. Smith, K.M. Black, Characterization of the treated surfaces of silicon alloyed pyrolytic carbon and SiC, Journal of Vacuum Science & Technology A. 2 (1984) 744–747. https://doi.org/10.1116/1.572562.

[49] J.B. Lhoest, P. Bertrand, L.T. Weng, J.L. Dewez, Combined Time-of-Flight Secondary Ion Mass Spectrometry and X-ray Photoelectron Spectroscopy Study of the Surface Segregation of Poly(methyl methacrylate) (PMMA) in Bisphenol a Polycarbonate/PMMA Blends, Macromolecules. 28 (1995) 4631–4637. https://doi.org/10.1021/MA00117A038/ASSET/MA00117A038.FP.PNG_V03.

[50] K. Wagener, C. Batich, B. Kirsch, S. Wanigatunga, Chain propagation/step propagation polymerization. III. An XPS investigation of poly(oxyethylene)-b-poly(pivalolactone) telechelomer, J Polym Sci A Polym Chem. 27 (1989) 2625–2631. https://doi.org/10.1002/POLA.1989.080270811.

[51] G. Beamson, D. Briggs, High Resolution XPS of Organic Polymers: The Scienta ESCA300 Database, J Chem Educ. 70 (1992) A25. https://doi.org/10.1021/ED070PA25.5.

[52] G.P. López, D.G. Castner, B.D. Ratner, XPS O 1s binding energies for polymers containing hydroxyl, ether, ketone and ester groups, Surface and Interface Analysis. 17 (1991) 267–272. https://doi.org/10.1002/SIA.740170508.

[53] NIST X-ray Photoelectron Spectroscopy (XPS) Database, Version 3.5, (n.d.). https://srdata.nist.gov/xps/ (accessed August 1, 2023).

[54] A.G. Shard, Practical guides for x-ray photoelectron spectroscopy: Quantitative XPS, Journal of Vacuum Science & Technology A: Vacuum, Surfaces, and Films. 38 (2020) 41201. https://doi.org/10.1116/1.5141395/246897.

[55] S.M. Shaheen, N.K. Niazi, E. Noha, I. Bibi, H. Wang, Daniel, Y.S. Ok, N. Bolan, J. Rinklebe, Wood-based biochar for the removal of potentially toxic elements in water and wastewater: a critical review, International Materials Reviews. 64 (2019) 216–247. https://doi.org/10.1080/09506608.2018.1473096.

[56] H. Zhang, R.P. Voroney, G.W. Price, Effects of temperature and processing conditions on biochar chemical properties and their influence on soil C and N transformations, Soil Biol Biochem. 83 (2015) 19–28. https://doi.org/https://doi.org/10.1016/j.soilbio.2015.01.006.

[57] S. Angioi, S. Polati, M. Roz, C. Rinaudo, V. Gianotti, M.C. Gennaro, Sorption studies of chloroanilines on kaolinite and montmorillonite, Environmental Pollution. 134 (2005) 35–43. https://doi.org/https://doi.org/10.1016/j.envpol.2004.07.018.

[58] S. Polati, F. Gosetti, V. Gianotti, M.C. Gennaro, Sorption and desorption behavior of chloroanilines and chlorophenols on montmorillonite and kaolinite, J Environ Sci Health B. 41 (2006) 765–779. https://doi.org/10.1080/03601230600805774.

[59] D. Huguenot, P. Bois, K. Jézéquel, J.Y. Cornu, T. Lebeau, Selection of low cost materials for the sorption of copper and herbicides as single or mixed compounds in increasing complexity matrices, J Hazard Mater. 182 (2010) 18–26. https://doi.org/10.1016/J.JHAZMAT.2010.05.062.

[60] M. El Saied, · Seham, A. Shaban, · Mohsen, S. Mostafa, A.O. Abo, E. Naga, Efficient adsorption of acetaminophen from the aqueous phase using low-cost and renewable adsorbent derived from orange peels, Biomass Convers Biorefin. 1 (n.d.) 3. https://doi.org/10.1007/s13399-022-02541-x.

[61] N. Abd, E. Youssef, E. Amer, A.O. Abo, E. Naga, S.A. Shaban, Molten salt synthesis of hierarchically porous carbon for the efficient adsorptive removal of sodium diclofenac from aqueous effluents, (2020). https://doi.org/10.1016/j.jtice.2020.07.018.

[62] W.J. WeberJr., J.C. Morris, Kinetics of Adsorption on Carbon from Solution, Journal of the Sanitary Engineering Division. 89 (1963) 31–59. https://doi.org/10.1061/JSEDAI.0000430.

[63] Z. Zhao, W. Sun, M.B. Ray, Adsorption isotherms and kinetics for the removal of algal organic matter by granular activated carbon, Science of The Total Environment. 806 (2022) 150885. https://doi.org/10.1016/J.SCITOTENV.2021.150885.

[64] Y. Wang, C. Lin, X. Liu, W. Ren, X. Huang, M. He, W. Ouyang, Efficient removal of acetochlor pesticide from water using magnetic activated carbon: Adsorption performance, mechanism, and regeneration exploration, Science of The Total Environment. 778 (2021) 146353. https://doi.org/10.1016/J.SCITOTENV.2021.146353.

[65] T.W. Weber, R.K. Chakravorti, Pore and solid diffusion models for fixed-bed adsorbers, AIChE Journal. 20 (1974) 228–238. https://doi.org/10.1002/AIC.690200204.

[66] T.S. Anirudhan, P.S. Suchithra, Equilibrium, kinetic and thermodynamic modeling for the adsorption of heavy metals onto chemically modified hydrotalcite, Indian Journal of Chemical Technology. 17 (2010) 247–259.

[67] G. Bataillou, C. Lee, V. Monnier, T. Gerges, A. Sabac, C. Vollaire, N. Haddour, Cedar Wood-Based Biochar: Properties, Characterization, and Applications as Anodes in Microbial Fuel Cell, Appl Biochem Biotechnol. 194 (2022) 4169–4186. https://doi.org/10.1007/S12010-022-03997-3.

[68] I. Quesada-Peñate, C. Julcour-Lebigue, U.J. Jáuregui-Haza, A.M. Wilhelm, H. Delmas, Degradation of paracetamol by catalytic wet air oxidation and sequential adsorption – Catalytic wet air oxidation on activated carbons, J Hazard Mater. 221–222 (2012) 131–138. https://doi.org/10.1016/J.JHAZMAT.2012.04.021.

[69] J. Chen, D. Zhang, H. Zhang, S. Ghosh, B. Pan, Fast and slow adsorption of carbamazepine on biochar as affected by carbon structure and mineral composition, Science of The Total Environment. 579 (2017) 598–605. https://doi.org/10.1016/J.SCITOTENV.2016.11.052.

[70] G. Chu, J. Zhao, Y. Liu, D. Lang, M. Wu, B. Pan, C.E.W. Steinberg, The relative importance of different carbon structures in biochars to carbamazepine and bisphenol A sorption, J Hazard Mater. 373 (2019) 106–114. https://doi.org/10.1016/J.JHAZMAT.2019.03.078.

[71] E.M. El Mouchtari, C. Daou, S. Rafqah, F. Najjar, H. Anane, A. Piram, A. Hamade, S. Briche, P. Wong-Wah-Chung, TiO2 and activated carbon of Argania Spinosa tree nutshells composites for the adsorption photocatalysis removal of pharmaceuticals from aqueous solution, J Photochem Photobiol A Chem. 388 (2020) 112183. https://doi.org/10.1016/J.JPHOTOCHEM.2019.112183.

[72] L.P. Bakhaeva, G.K. Vasilyeva, E.G. Surovtseva, V.M. Mukhin, Microbial degradation of 3,4-dichloroaniline sorbed by activated carbon, Microbiology (N Y). 70 (2001) 277–284. https://doi.org/10.1023/A:1010495025794/METRICS.